Auxetic Behaviour in High Pressure Polymorphs of CO_2 and H_2O: A Computational Chemistry Study

Ph.D. Thesis

by

Darryl Gambin

Supervised by: Prof. Ruben Gatt

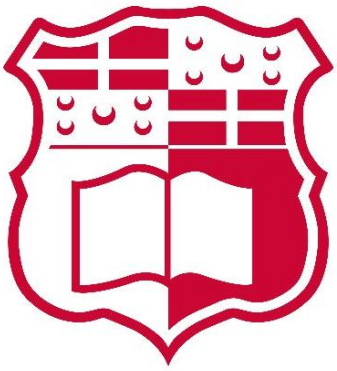

University of Malta

2022

L-Università ta' Malta

University of Malta Library – Electronic Thesis & Dissertations (ETD) Repository

The copyright of this thesis/dissertation belongs to the author. The author's rights in respect of this work are as defined by the Copyright Act (Chapter 415) of the Laws of Malta or as modified by any successive legislation.

Users may access this full-text thesis/dissertation and can make use of the information contained in accordance with the Copyright Act provided that the author must be properly acknowledged. Further distribution or reproduction in any format is prohibited without the prior permission of the copyright holder.

Acknowledgements

I would like to thank my supervisor, Prof. Ruben Gatt, for all the help and patience shown throughout my studies. His help and guidance helped to shape this work. I am truly grateful for all the feedback given. My thanks also goes to Prof. Joseph N. Grima for all the advice and words of encouragement given. I would also like to thank Dr. Daphne Attard for all the help and support shown throughout the project. I would like to thank Prof. Miroslav Dudek for his help on this project. I would like to thank Dr. Krzysztof Dudek and Dr. Luke Mizzi and the other member of the metamaterials unit for their help and support. I would like to thank the Doctoral Faculty Board for their understanding and allowing me to extend my studies. I wish to acknowledge the anonymous reviewers who have gone over the papers submitted and provided valuable feedback.

Finally, I would like to thank my parents for all their support throughout the years. This project would not have been possible without their help.

Abstract

In this work, a detailed study of the mechanical properties of the single crystal and polycrystalline aggregate of high-pressure polymorphs of H_2O and CO_2 will be carried out, paying particular attention to Poisson's ratio of these systems. Using first principles density functional theory (DFT) calculations, this work will show for the first time that the **high-pressure polymorphs ice VIII, ice X, CO_2-V and CO_2-II have the potential to exhibit a negative Poisson's ratio** with the auxetic behaviour of these systems increasing with increasing hydrostatic pressure. To adequately study these systems using DFT simulations, detailed convergence and benchmarking studies will be carried out. It will be shown that contrary to the single crystal, the Poisson's ratio of the polycrystalline aggregate of these systems exhibits a positive Poisson's ratio which increases with increasing hydrostatic pressure. The deformation mechanism for ice X, ice VIII and CO_2-V will be studied through the application of stress, with the proposed mechanism being consolidated through the use of spectroscopy. In the case of ice X and ice VIII, the auxetic behaviour will be rationalised by studying the deformation of two orthogonally interpenetrating rhombi on application of a stress. In the case of CO_2-V, the auxeticity will be explained from a 2D perspective by the relative rotation of semi-rigid projected squares which both rotate and deform on application of a stress. It will also be shown that these 2D squares are projections of 3D CO_4 tetrahedra which rotate relative to each other whilst stretching and deforming. In the case of CO_2-II, it will be shown that the application of a stress results in a non-continuous change in the structural parameters studied. Thus, a novel approach will be developed in this thesis, where the auxetic behaviour of the system will be rationalised by studying the variation of the Raman active and infrared active modes with varying hydrostatic pressure and comparing any shifts observed in these modes with shifts in the Poisson's ratio.

Table of Contents

List of Figures

List of Tables

List of abbreviations

Abbreviation	Meaning
THO	Thomsonite
NAT	Natrolite
EDI	Edingtonite
BCC	Body-centred cubic
FCC	Face-centred cubic
HCP	Hexagonal close packed
DAC	Diamond anvil cell
NMR	Nuclear magnetic resonance
CASTEP	Cambridge Serial Total Energy Package
DFT	Density-functional theory
GGA	Gereralized gradient approximation
PBE	Perdew-Burke-Ernzerhof
PBE-TS	Perdew-Burke-Ernzerhof -Tkatchenko-Scheffler
PBE-Grimme	Perdew-Burke-Ernzerhof-Grimme
PBESOL	Perdew-Burke-Ernzerhof for solids
PW91	Perdew-Wang 1991
PW91obs	Perdew-Wang 1991-Ortmann, Bechstedt- Schmidt
HSE06	Heyd-Scuseria-Ernzerhof-2006
SCF	Self-consistent field
DFPT	Density-functional perturbation theory

Chapter 1: Introduction

Simple molecular compounds composed of light elements such as H_2O and CO_2, in their various forms have enthralled scientists with their anomalous and intriguing properties, particularly, when subjected to high pressures. CO_2 and H_2O are not only found on Earth, but also in our galaxy[1–9]. Their study has been described as challenging since both have a complex phase diagram[10–15]. In the case of solid water, at least nineteen different stable and metastable forms have been identified through experimental and theoretical works[11,12,16–20]. Similarly, in the case of solid CO_2 at least seven phases have been characterized[21–26].

The study of these molecular crystals is of great importance to a number of disciplines including planetary and geo-sciences[27–33]. For instance, Neptune and Uranus are thought to possibly contain internal layers composed of molecular ices which form due to the pressures found within these planets[8,34–36]. However, the occurrence of these ices is not only limited to such planets and in fact, they are also found on Earth. For example, the presence of a high pressure phase of H_2O ice (ice VII) has been reported in portions of the coldest slabs in the oceanic lithosphere, which might eventually lead to the dwindling or termination of the tectonic activity[4]. Another example is the possible presence of a high-pressure phase of carbon dioxide, CO_2 phase V (CO_2-V) in the deep lower mantle of Earth[37].

In addition to being of interest to planetary sciences, the study of substances at high pressure is also of interest to researchers in other fields such as physics and chemistry[11,38–44]. In particular, high pressures could lead to the formation of atypical compounds[45]. For example,

at high pressures substances typically composed of discrete molecules can form macromolecular compounds such as ice X[46,47] and CO_2-V[48,49].

Even though high pressure polymorphs of ice have been studied for over a hundred years, with the first experiments on H_2O ice being conducted in the 1900s[50,51], our understanding of the phase diagrams of CO_2 and H_2O ice and all their polymorphs is still incomplete, particularly at low temperatures and high pressures. In particular, studies which have focused on the elastic properties of high-pressure phases of CO_2 and H_2O ices are relatively few. For example, some of the investigations which have been published have generally focused on the bulk elastic properties (such as Young's modulus, the average acoustic velocity, and bulk modulus) of polycrystalline specimens, with some studies employing Brillouin spectroscopic techniques [47,52] and ultrasonic techniques [53]. Recently, some theoretical studies have determined the elastic constants of H_2O and CO_2 phases at higher pressures[54–57].

One fundamental material property is the Poisson's ratio which describes the change in size of a system in a direction perpendicular to an applied stress. The Poisson's ratio ν_{ij} may be defined mathematically as the negative ratio of the transverse and lateral strains in the $Ox_i - Ox_j$ plane for loading in the Ox_i direction:

$$\nu_{ij} = -\frac{\varepsilon_j}{\varepsilon_i} \qquad \textbf{1.1}$$

where ε_i and ε_j are the strains in the Ox_i and Ox_j directions respectively.

Most materials get thinner when uniaxially stretched, and hence have a Poisson's ratio which is positive. Though not common in nature, materials with a negative Poisson's ratio[58,59] have been reported and are collectively termed auxetic materials[59]. Contrary to intuition, these materials get fatter, rather than thinner when stretched, see Figure 1.1.

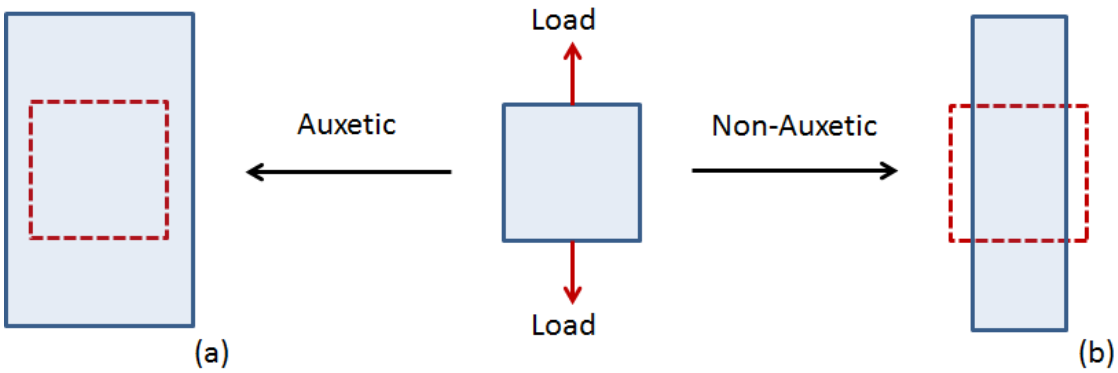

Figure 1.1: An illustration of the behaviour observed when (a) auxetic materials and (b) non-auxetic materials are stretched, with the former getting fatter while the latter getting thinner when subjected to a uniaxial tensile load.

Auxetic behaviour has been reported in myriad of materials, such as naturally occurring silicates, e.g. α–cristobalite[60–63], β–cristobalite[63–65] and zeolites e.g. THO, NAT and EDI[66–69]. The auxetic behaviour has been attributed to the way the framework deforms when subjected to a stress. Studies on naturally occurring systems made it possible for scientists to design man-made molecular-level auxetics, i.e. the molecular structure mimics the framework of naturally occurring systems or an auxetic macrostructure which exhibit a negative Poisson's ratio. Having a system tailor-made to exhibit pre-defined mechanical properties would then make it better suited for a particular application. For auxetic behaviour to take place there is no size requirement on the structural motifs, i.e. auxetic behaviour is a scale independent property since the Poisson's ratio is normally unaffected by the scale at which a particular 'deformation mechanism' takes place.

Even though a few studies have focused on the mechanical properties of high-pressure H_2O and CO_2 polymorphs, detailed studies on the Poisson's ratio and auxetic potential of these systems is lacking. In fact, the Poisson's ratio of single crystal, high-pressure phases of both

H_2O and CO_2 polymorphs have not been described in the literature. Literature on the deformation mechanisms of high-pressure crystals is also lacking. Furthermore, numerous debates are present in literature pertaining to the stability of a number of high-pressure H_2O and CO_2 polymorphs at certain pressures.

This thesis aims to address these lacunae by studying the mechanical properties of various solid phases of CO_2 and H_2O ices. The pressure dependence of the mechanical properties of several polymorphs of CO_2 and H_2O ices namely, ice X, ice VIII, CO_2-V and CO_2-II will be investigated. The phonon stability for each of these polymorphs will also be investigated in order to assess their stability in the pressure ranges used in this study. For each polymorph and pressure range studied, the Poisson's ratio will be determined. Furthermore, deformation mechanisms that leads to the measured Poisson's ratio will also be investigated through direct microstructural measurements (where possible) as the systems deforms under a uniaxial stress. The deformation mechanism will also be studied through the use of vibrational spectra taken at different hydrostatic pressures. To achieve all this, the thesis will be subdivided as into seven chapters. Following the introduction (Chapter 1), a literature review addressing the studies relevant to this thesis will be presented in Chapter 2. The aim of the first part of this chapter is to introduce the reader to the polymorphism of H_2O and CO_2 and discuss the studies carried out on the polymorphs which are the main focus of this thesis namely ice X, ice VIII, CO_2-V and CO_2-II. Following this, a discussion on auxetic materials is given. The main deformation mechanisms leading to a negative Poisson's ratio and systems exhibiting auxetic behaviour will be discussed. This will then be followed by a detailed explanation of the scope of this work where the main aim and objectives of this work will be presented.

The first high-pressure polymorph to be studied in this thesis is the macromolecular ice X, which study is carried out in the pressure range of 150 GPa to 300 GPa. The work on this polymorph is presented in Chapter 3. In particular, the mechanical properties of both the single

crystal and the polycrystalline aggregate in the pressure range of the study will be determined. The deformation of the system on the application of stress will be then studied in detail in order to propose a deformation mechanism rationalizing the predicted Poisson's ratio and the pressure dependence of this property. The proposed deformation mechanism will be consolidated through the use of Raman spectroscopy.

Another high-pressure polymorph of H_2O ice which is also known to be stable at low temperatures is ice VIII. In fact, the ice X polymorph can be formed from ice VIII through the application of pressure. Thus, following the work on ice X, Chapter 4 will delve into the mechanical properties of ice VIII. Employing the methodology developed in the previous chapter, detailed convergence testing and benchmarking of the methodology will be carried out. After validating the methodology, the structural, mechanical and vibrational properties of this system will be determined. In particular, the Poisson's ratio together with the effect of pressure on the Poisson's ratio will be studied. The Poisson's ratio of this system will be rationalised by studying the deformation of the system under the application of stress and through the use of Raman and IR spectroscopy.

Following the study of two high-pressure polymorphs of H_2O ice, the focus of this thesis will shift on the high-pressure polymorphs of CO_2. Similar to ice X, the high-pressure polymorph CO_2-V is also a macromolecular phase. Thus, in Chapter 5 the structure and mechanical properties of CO_2-V are studied in the pressure range of 40 GPa to 60 GPa, following detailed convergence and benchmarking studies. A two-dimensional and a three-dimensional approach will be taken in order to rationalize the measured Poisson's ratio. The proposed three-dimensional deformation mechanism will then be ascertained through the use of Raman and IR spectroscopy.

CO_2-V can be formed from CO_2-II through the application of pressure. Thus, as was the case with ice VIII and ice X, it would be interesting to investigate the mechanical properties of CO_2-II, which system is found at relatively lower pressures than CO_2-V. In view of this, in Chapter 6 the CO_2-II polymorph will be studied. In particular, this chapter will investigate the mechanical properties of the polycrystalline aggregate and the single crystal. Based on the methodology developed in the previous chapters, the Poisson's ratio of the CO_2-II system will be rationalised by carefully studying the variation of the Raman and IR active modes with pressure.

Finally, Chapter 7 presents a general discussion on the work carried out in this thesis. The main findings will be summarized and further studies which can build on the work carried out in this thesis will be suggested.

Chapter 2: Literature Review

This chapter aims to introduce the reader to the subject matter of this thesis, and thus it will be divided into two main parts, the first part discussing the literature on H_2O and CO_2 ice, while the second part will present an introduction on negative Poisson's ratios.

2.1 H_2O Ice

H_2O is one of the most abundant substances found on Earth making up about 70% of the Earth's surface[70] and one of the most common molecular species present in the universe[71]. It is an essential chemical without which life on Earth could not be possible[72]. Water has a myriad of indispensable functions such as providing a home for aquatic organisms and making up a large proportion of living cells, thus providing a medium in which biological reactions may take place. Its excellent solvent properties make it ideal as a transport medium in both plants and animals[70]. It also takes part in a number of biologically important reactions such as acting as the source of hydrogen in photosynthesis. Being such an essential substance for our existence it comes as no surprise that behaviour of water is widely studied in a number of different fields such as chemistry, astrophysics and geoscience[73–78]. In particular the behaviour of water on changing conditions of temperature and pressure has attracted the attention of scientists for over a hundred years[50,51].

On cooling at ambient pressures water crystallises to a polymorph of ice known as hexagonal ice commonly referred to as ice I*h*, a substance which though very common in everyday life, has a number of unusual properties[79–85]. An example of this includes the fact that

ice I*h* is less dense than liquid water, a property which allows ice to float on water. This property is anomalous since the density of almost all solids is greater than the liquid (other exceptions include arsenic, bismuth, gallium and germanium). Another interesting property is the fact that ice I*h* exhibits negative thermal expansion at temperatures below circa 70 K[86–89]. In addition to this, ice I*h* was one of the first materials reported to undergo pressure-induced amorphisation with ice I*h* transforming into high-density amorphous ice when compressed above 1 GPa at 77 K[80,81].

The existence of numerous crystalline phases of ice, a phenomenon known as polymorphism, is also considered an anomaly[84], with around nineteen crystalline[1] phases being reported in the literature[11,12,19,84,90–92], resulting in water having an extremely rich phase diagram. At this stage it should also be mentioned that ice is also known to have three amorphous forms, a phenomenon known as 'polyamorphism'[84].

In view of the above, the aim of this section is to give a brief review of the crystalline phases of ice. This will be followed by a more detailed review of the studies conducted on the low temperature polymorphs of ice, which polymorphs are the most relevant to this dissertation.

2.1.1 Nomenclature of ice phases

Some of the first studies conducted on the phases of ice date back to the early 20th century[50]. At this stage, it was already apparent that numerous phases of ice could be discovered, thus a convention was established to name the crystalline phases of ice which convention specifies that newly discovered ice phases are labelled with Roman numerals according to the chronological order of their discovery[50,51]. It was later argued that this

[1] 'it is not clear how many condensed phases of water can be distinguished' [84]

convention may only be utilised for crystalline phases that are fully characterised through experimental studies, for example by using crystallographic techniques[93].

2.1.2 Crystal structure of ices

In crystalline ice structures, each water molecule is hydrogen bonded to four different water molecules with the crystalline structure being dictated by the Bernal-Fowler rules[94]. These rules state that two hydrogen atoms must be covalently bonded to each oxygen atom, thus maintaining the stoichiometry of the H_2O molecule, and that only one proton must be involved in each hydrogen bond. Despite these rules, the water molecule can be found in six different molecular orientations as shown in Figure 2.1.

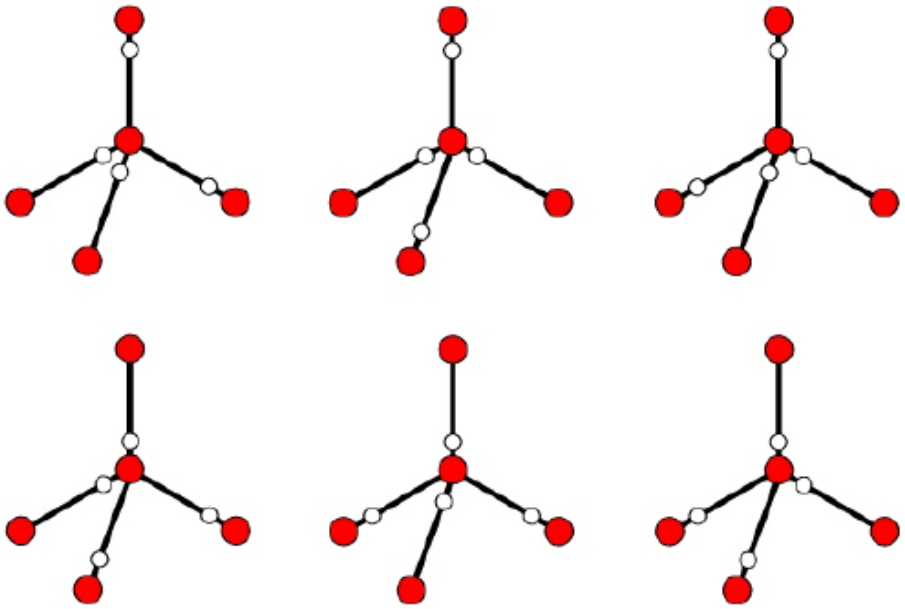

Figure 2.1: Illustration of the six possible configurations of a central water molecule in ice where the oxygen atoms are shown in red and the hydrogen atoms are shown in white. Diagram taken from[84]

The structural configuration of the ice phases may be divided into two main groups, the proton ordered structures and the proton disordered structures. In the latter case, each water molecule may assume any of the orientations shown in Figure 2.1 at any given time with equal

probability. Thus, in such a structure only long-range order of the oxygen atoms is observed while in a proton-ordered ice phase, long-range order of both the oxygen and hydrogen atoms are observed. A number of the ice phases can be grouped into a proton ordered-disordered pair where in each pair, the polymorphs possess the same lattice of oxygen atoms but however differ in the orientational order of the water molecules[83].

To date six pairs of proton disordered-ordered ice phases have been identified namely ice I*h*-XI[95–98], ice III-IX[98–102], ice V-XIII[103–105], ice VI-XV[20,104,106], ice VII-VIII[96,97,107,108], ice XII-XIV [109–111] where the phase mentioned first is the proton-disordered form. In addition to this, it has also been shown that ice III, V and XIX[112] display partial hydrogen order. It possible to convert a proton disordered phase to an ordered one by lowering the temperature, as hydrogen disordered phases are usually associated with higher temperatures, since the water molecules have sufficient thermal energy to assume any of the six possible molecular configurations. Moreover, this exothermic phase transition is usually associated with a change in the symmetry group[83]; an illustration of this being the conversion of ice VII with symmetry group $Pn\bar{3}m$ to ice VIII with symmetry group $I4_1/amd$ [16,99,107,108,113]. A notable exception is the pair of ice III and IX[99,100,102,114,115] which phases belong to the same symmetry group namely $P4_12_12_1$.

2.1.3 Phase diagram of water

The relatively complex water phase diagram (see Figure 2.2) consists of a number of interesting features such as the numerous crystalline phases present and the number of triple points including solid-solid-solid triple points where three solid polymorphs may be found and solid-solid-liquid triple points. Another interesting feature of the phase diagram is the course taken by the melting line, a spectacle rarely seen in other one-component systems[84]. As can be seen from the phase diagram, the melting line is initially negatively sloped and then at around

210 MPa and 251 K suddenly becomes positively sloped. In the negatively sloped region the pressure induced melting may be observed while in the positively sloped region pressure-induced crystallisation may take place[84]. A number of studies have focused on understanding this melting line of ice where it was shown that there are five solid-solid-liquid triple points along this line[84].

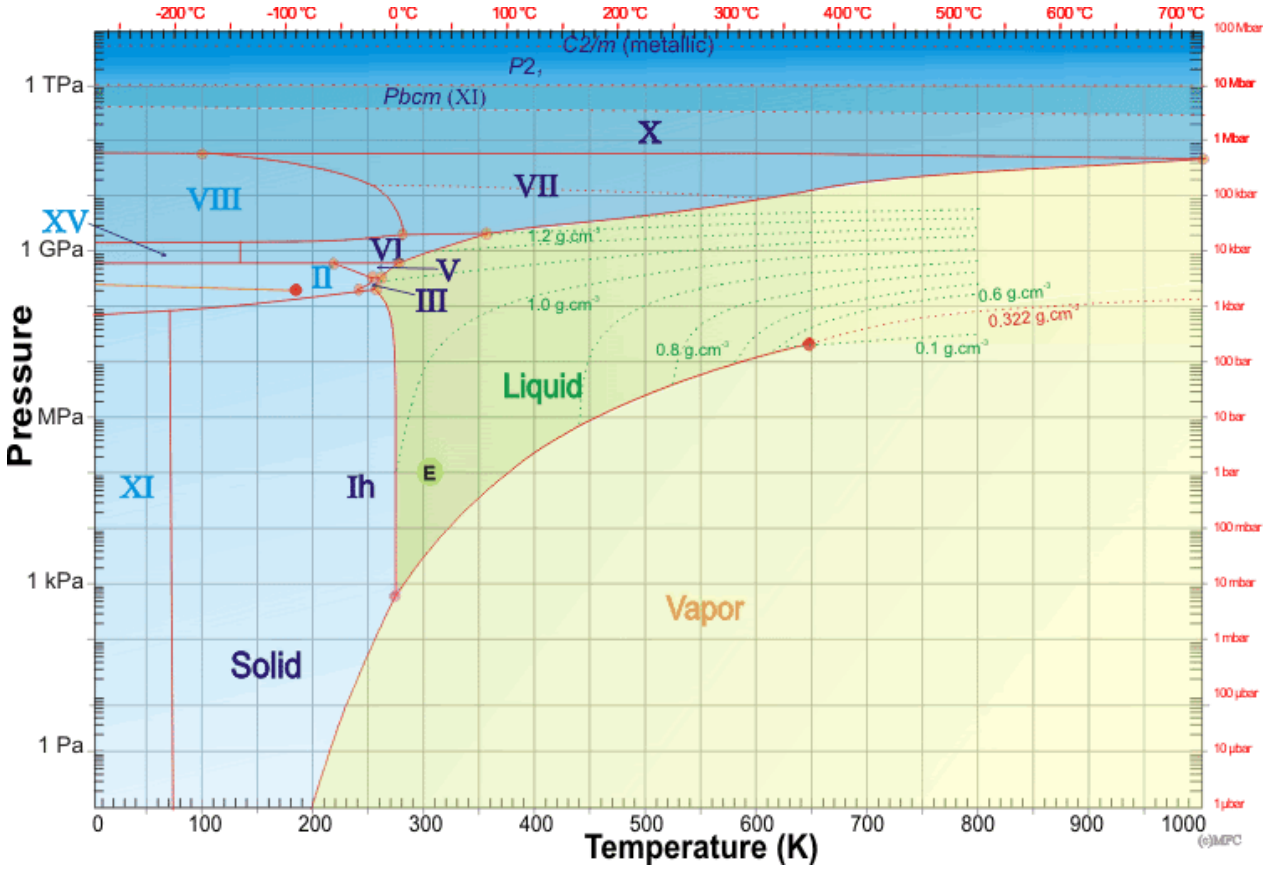

Figure 2.2: Water phase diagram taken from[116].

2.1.4 Low temperature and high-pressure phases of ice

The most important phases of ice above 2 GPa are ice VII, ice VIII, and ice X[47,117–120] with ice X being found in the higher pressure range. At even higher pressures, ice X is thought

to undergo a further phase change. In the following sections, namely 2.1.5 to 2.1.7, a review of the H_2O ice polymorphs discussed in this thesis, namely ice VIII and ice X, will be given. This will be followed by a brief overview of the possible post ice X phases.

2.1.5 Ice VIII

A number of theoretical [96,121–132] and experimental studies [16–18,108,113,117,118,133–137] have been conducted on ice VIII, see Figure 2.3, from which it has been described as a proton ordered high pressure polymorph of ice [16,113] having a molecular crystal containing 8 water molecules per unit cell, where all the H_2O molecules obey the ice rules[94]. It has also been shown through neutron diffraction studies that ice VIII is composed of two interpenetrating hydrogen-bond networks with a body centred tetragonal unit cell, belonging to the $I4_1/amd$ space group [16]. The dipole moments of the water molecules in one network are equal and opposite to the dipole moment of the water molecules in the second network resulting in an overall antiferroelectric structure. A ferroelectric variant to the ice VIII structure has been proposed with this structure being slightly less stable than the antiferroelectric ice VIII [125]. However, a recent neutron diffraction study under high pressure and high electric field could not yet find sufficient evidence for this ferroelectric variant of ice VIII [138].

Ice VIII can be obtained from its proton disordered counterpart, ice VII, by lowering the temperature of ice VII below approximately 270 K without utilising any dopant [137]. X-ray diffraction[139] and infrared absorption[118] studies have shown that the ice VII-VIII phase boundary is at 273 K up to 12 GPa and then exhibits a rapid decreases to 0 K at approximately 60 GPa. This phase transition has also been subjected to a number of theoretical studies where Monte Carlo simulations[96,97] predict a phase transition taking place at 228 K and ab initio simulations[140] were able to qualitatively reproduce the trends observed experimentally. On

increasing the hydrostatic pressure ice VIII may undergo a phase transition from a molecular crystal into the macromolecular ice X.

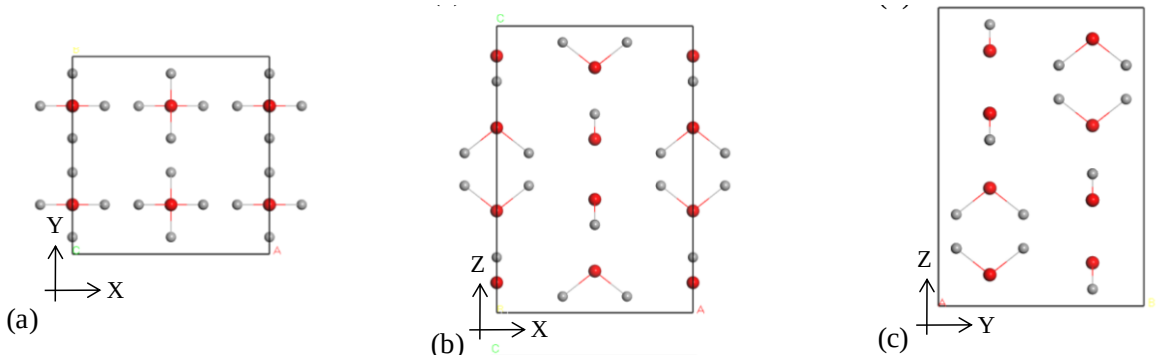

Figure 2.3: The unit cell projections of ice VIII in the (a) (001), (b) (010) and (c) (100) planes.

2.1.6 Ice X

Ice X belongs to the cubic space group Pn$\bar{3}$m. Its structure is composed of a BCC packing of oxygen atoms, each of which is connected to four hydrogen atoms which are located midway between two neighbouring oxygen atoms, see Figure 2.4. Each hydrogen atom in the structure therefore has two symmetric O-H bonds to two different oxygen atoms. This leads to the molecular character seen in previous phases of ice disappearing in ice-X[46,47,120,141–149]. This phase of ice is unique in that it is the only experimentally determined crystalline phase of ice which is not composed of well-defined water molecules which are bonded together by hydrogen bonds. In ice X the H atoms are found exactly halfway between the two O-atoms, commonly referred to as the 'halfway position'. Thus, this polymorph may be considered as an atomic crystal composed of one-third oxygen atoms and two-thirds H-atoms[150], hence it also known as 'symmetric ice' [143,151,152].

The symmetric structure of ice X was initially predicted by Holzapfel[147] and later inferred through experimental studies. Hirsch and Holzapfel[148,149] construed that the changes in the Raman spectrum of ice VII in the pressure range of approximately 35-50 GPa were

consistent with hydrogen-bond symmetrisation and hence ice X formation. Brillouin scattering studies of ice VII[47] in the 35-50 GPa pressure range also gave results which suggest a phase transition, possibly to ice X. In addition to these, infrared absorption studies have also given results which are consistent with the notion of hydrogen-bond symmetrisation[46,142,153].

Two 'forms' for the structure of ice X have been proposed namely the 'disordered ice X' and the 'ordered ice X'. In disordered ice X the hydrogen atoms can be found in a double-well potential where the hydrogen atoms can tunnel back and forth between the two minima. Thus, the hydrogen atoms can be found in two energetically equivalent sites. In this case the 'halfway position' is a result of statistically averaging hydrogen atoms which are delocalized in a shallow double-well potential. As the pressure is increased the O-O distance decreases and the double-well potential transforms into a single well potential, giving rise to the ordered ice X where the hydrogen atoms can be found in one position, with the hydrogen atom being localized in a single-well potential[120,143]. The BCC oxygen lattice is maintained in both structures. The phase transition sequence at low temperatures is thought to follow the route ice VIII—disordered ice X—ordered ice X[120].

The pressure at which ordered ice X is formed is under debate. Caracas[120] had shown that the ordered structure for ice X is obtained at pressures higher than 120 GPa. This was consistent with a Raman spectroscopic study which also suggested that the symmetric hydrogen bonded ice X does not exist below 120 GPa[146] and a first principles DFT study which has shown that ice X is formed at 120 GPa[154]. Nevertheless, a subsequent NMR study has shown that proton ordered ice X should be present at 90 GPa[145]. In addition to this, a theoretical study had suggested that ice X is stable from 110 GPa[144].

2.1.7 Post ice X phases

Our understanding of the region above ice X in the phase diagram is still incomplete with a number of post-ice X phases being predicted (see Figure 2.4) in the literature though no experimental evidence is available for any of these phases. Work conducted by Demontis *et al.* suggests that ice X undergoes a phase transformation to an antiflouorite structure with *Pm-3m* symmetry with this transition being initially predicted using constant pressure molecular-dynamics calculations to occur at approximately 100 GPa[155]. The calculation was based on a primitive ionic model consisting of O^{2-} ions and H^{+} ions. However, diamond anvil studies did not give any indication of a phase transition occurring at this pressure[156], which lead Demontis et al. to refine their calculations to include short-range repulsions between the O^{2-} ions with this work suggesting that the phase transition occurs at a pressure of approximately 330 GPa[157]. However, using DFT simulations Benoit et al. suggest that at ice X undergoes a phase transition at a pressure greater than 300 GPa to form an orthorhombic structure belonging to the *Pbcm* space group with 12 atoms per unit cell[119]. DFT studies suggest that the phase transition is due to dynamic instabilities in ice X[120,158].

More recently molecular dynamic simulations using the VASP density functional theory code predicts that ice X may form a crystal structure with *Pbca* symmetry at 760 GPa and a crystal structure with *Cmcm* symmetry at 1550 GPa [159]. Moreover, similar to ice VII, VIII, X and *Pbcm*, the predicted *Pbca* phase consists of two interpenetrating hydrogen bonded networks while on the other hand the *Cmcm* phase is composed of corrugated sheets of oxygen and hydrogen atoms. In addition to this, it should be noted that band structure calculations suggest that the *Cmcm* phase is metallic while the *Pbca* phase is an insulator.

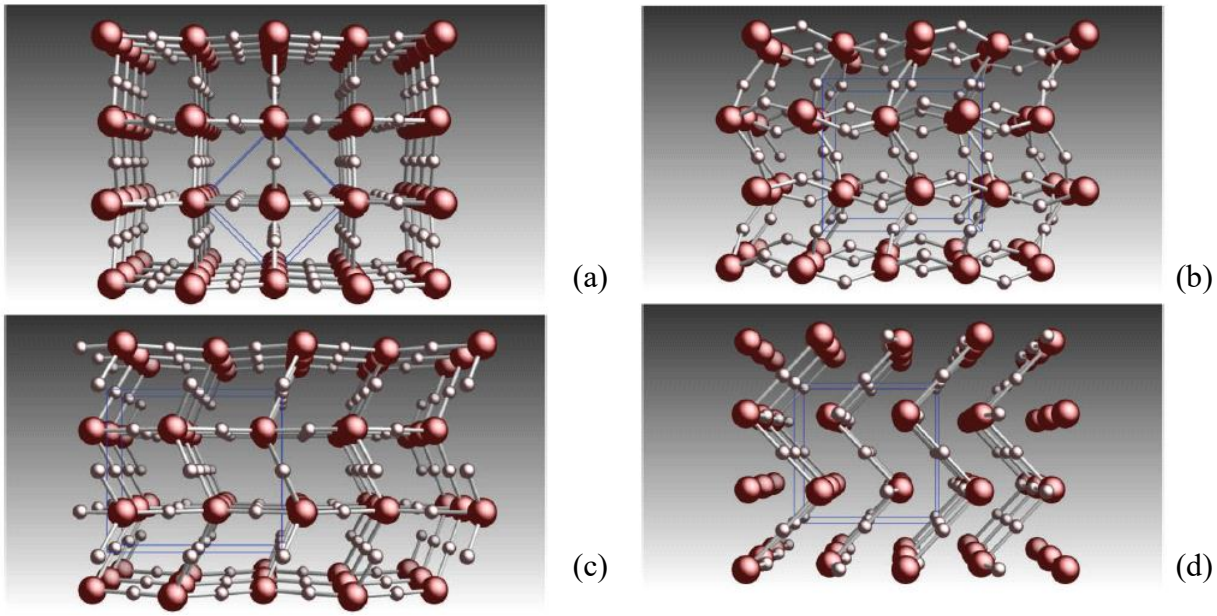

Figure 2.4: Diagrams illustrating the structures of ice X (a), predicted Pbcm phase (b), predicted Pbca phase (c) and the predicted Cmcm phase. Oxygen atoms are represented by large spheres while the hydrogen atoms are shown as small spheres. The thin blue line represents the unit cell. Diagram adapted from[84].

2.2 Carbon dioxide

2.2.1 Introduction

Carbon dioxide, a simple covalent molecule at ambient conditions, has an extremely rich phase diagram. In fact, CO_2 has a number of high-pressure solid polymorphs including both molecular and macromolecular phases[1,3,10,24,26,37,56,160–173]. This polymorphism has attracted the attention of several scientists due to its importance in the fields of geophysics and planetary science [1,2,164]. Indeed, the high pressure polymorphs of CO_2 ice can be found in the interior of a number of planets[1,2,27,28,174] such as Earth, Venus and Mars making the study of such high pressure polymorphs essential to understand the dynamics of planet interiors [3]. In addition to this, the field of high-pressure polymorphism of CO_2 ice has also intrigued scientist due to the transition of simple molecular CO_2, which is present under ambient conditions, to non-molecular CO_2 at high pressure. This has led to a number of

experimental[24,26,37,160,162,163,165,166,172,175] and theoretical studies[10,28,56,167,168,174,176,177] being conducted on the high-pressure polymorphs of CO_2 ice. The study of the phase diagram of carbon dioxide is relatively complex with a number of controversies surrounding the stability window of the various CO_2 solid polymorphs. A recent phase diagram for carbon dioxide is shown in Figure 2.5. The polymorphs which will be the focus of this thesis are CO_2 phase II and CO_2 phase V. These polymorphs are found at relatively high pressures as discussed in the following sections.

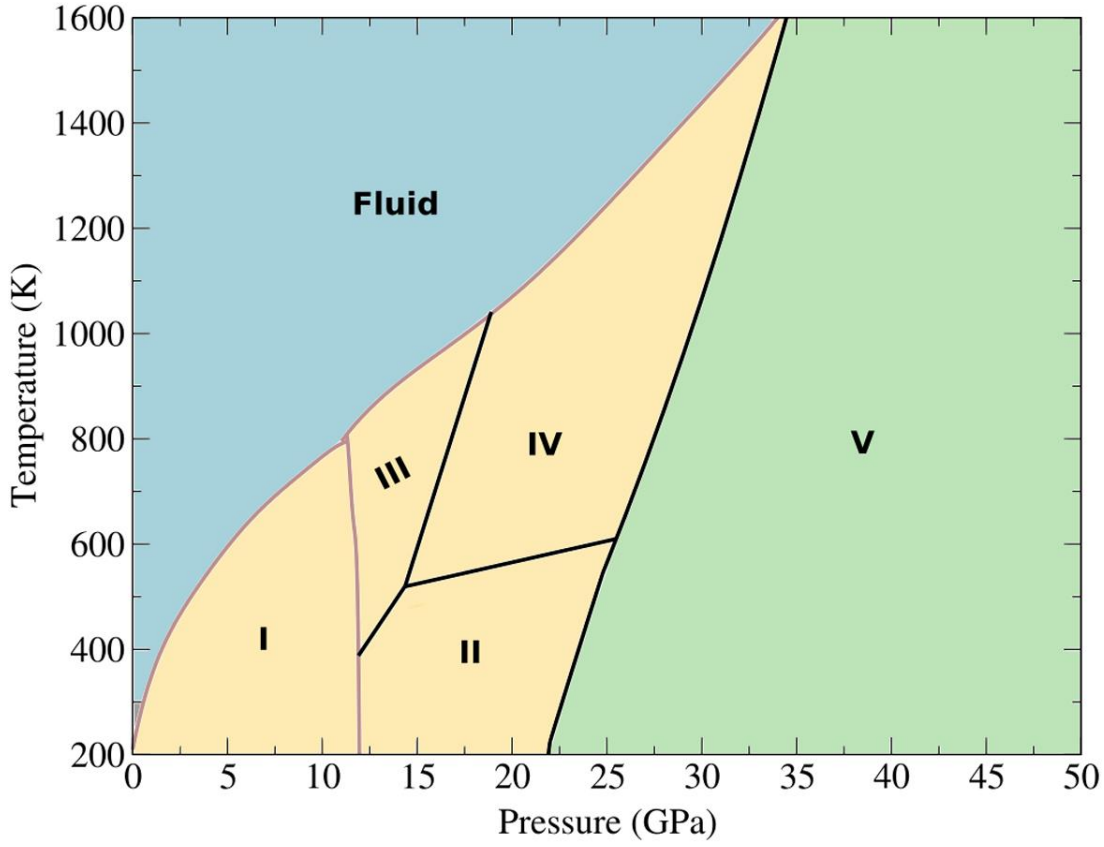

Figure 2.5: Recent phase diagram for carbon dioxide. Taken from[176].

2.2.2 CO_2-II

CO_2-II, shown in Figure 2.6, was formed by heating CO_2-III above ~500 K at 19 GPa[178] with the $P4_2/mnm$ symmetry of this system being determined in ensuing studies[57,171,179]. The transition of CO_2-III to CO_2-II was not reversible on lowering the temperature with CO_2-II being recovered at ambient temperature above 10 GPa which suggested that CO_2-III is a metastable phase [178] with CO_2-II being more stable than CO_2-III at ambient temperatures and below. This view has recently been challenged by a recent theoretical study which showed that CO_2-III is more stable than phase II at lower temperature and high pressure[15]. However, this claim has been disputed by an ensuing study[176] which has showed that CO_2-II is the more stable phase at lower temperatures while CO_2-III is more stable than CO_2-II at higher temperatures.

Initial work on the structure of CO_2-II at high pressures and high temperatures employing angle-resolved X-ray diffraction suggested that the carbon atoms in this polymorph are pseudo-six-fold coordinated by oxygens with two oxygen atoms at an elongated intramolecular C=O distance and four non-bonding oxygen atoms of the nearest CO_2 molecules at a collapsed intermolecular distance [179]. On the basis of the aforementioned distances the CO_2-II system was described as an intermediate state between molecular and nonmolecular solids[179]. This intermediate state was however disputed by subsequent theoretical[15,171] and experimental[57] work which did not find evidence for this intermediate state and instead suggested a molecular structure for this system. The pressure at which CO_2-II transforms into CO_2-V is a also source of debate[15,171,176,178,180] with a recent theoretical study suggesting that CO_2-II should undergo a phase transition to the macromolecular CO_2-V at 21.5 GPa at 0 K[176].

Work involving the mechanical properties of CO_2-II is mostly limited to experimental [57,179] or theoretical [56,167,171] determination of the bulk modulus, with some theoretical studies also determining the elastic constants [56,57] of this system.

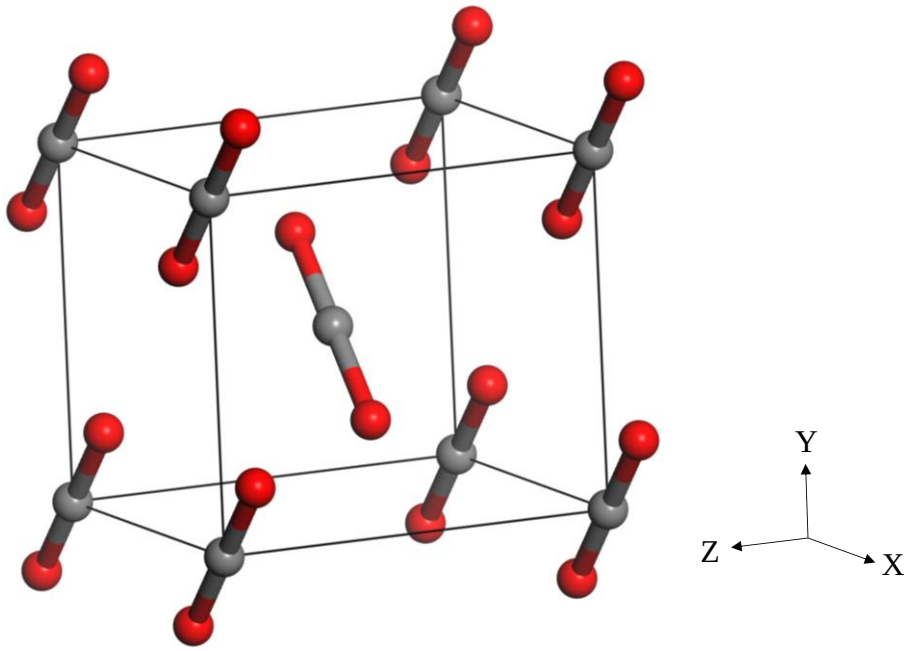

Figure 2.6: An illustration of the structure of CO2-II. Carbon atoms are shown as grey spheres while oxygen atoms are shown as red spheres.

2.2.3 CO_2-V

A macromolecular phase of CO_2 that has attracted particular attention is phase V, shown in Figure 2.7. CO_2-V has been synthesised from CO_2-III through laser heating above 40 GPa and 1800 K in a diamond anvil cell (DAC)[48,166]. The structure of CO_2-V has been shown to be that of partially collapsed tetragonal β-cristobalite with $I\bar{4}2d$ space group composed of corner sharing CO_4 tetrahedra with the carbon atoms forming a diamond network [26,162]. It has been suggested that at high pressures and temperatures CO_2-V dissociates into elemental carbon (diamond) and oxygen (ε-O_2)[2,181]. This has been disputed in recent work[37,176,182] on the phase stability of CO_2-V which has shown that CO_2-V does not undergo such disproportionation and is stable at pressures as high as above 100 GPa. It was demonstrated that CO_2-V is stable in the thermodynamic conditions of the deep lower mantle and thus, studies on this system could be beneficial in understanding carbon distribution in the layers of Earth[37]. The elastic constants of CO_2-V have also been calculated from 0 GPa to circa 40 GPa[56].

Further work on the higher pressure polymorphs of CO_2 suggested the presence of macromolecular phases with six-fold coordianated carbon atoms (CO_2-VI)[25] and an ionic crystal form (*i*-CO_2) [183]. This work was then disputed by other research groups who argued that these are kinetically trapped metastable phases that convert to CO_2-V on annealing[184]. CO_2-V has been the subject of a number of theoretical studies involving DFT[56,162,168,174,176,185] where the structure[185], stability[176], vibrational properties[162] and mechanical properties[56] have been studied.

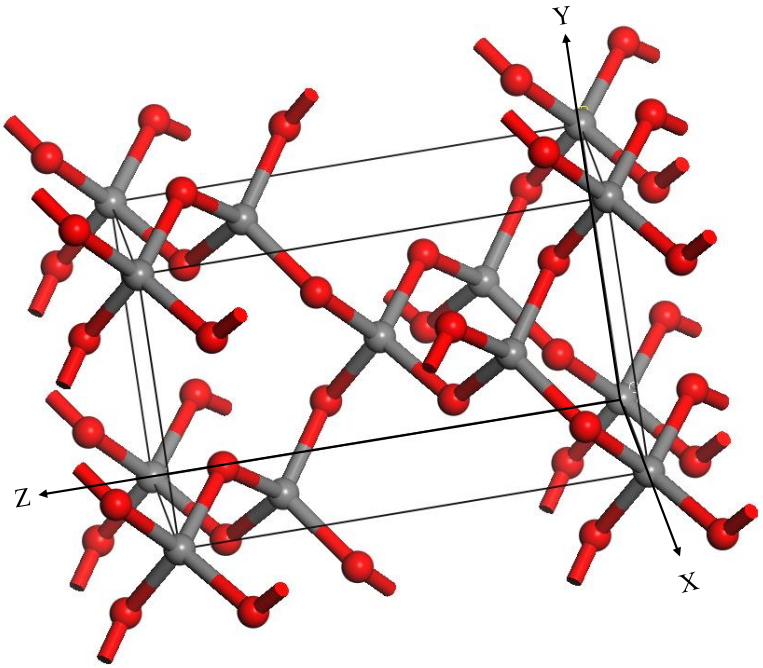

Figure 2.7: An illustration of the structure of CO_2-V. Carbon atoms are shown as grey spheres while oxygen atoms are shown as red spheres.

2.3 Negative Poisson's ratios: Mechanisms and nano-structured systems

In this section, an overview of the geometries / deformation mechanisms which give rise to a negative Poisson's ratio will be discussed. A vast number of such models are present in the literature, and thus, the most fundamental geometries / deformation mechanisms or those which are the most relevant to this work will be described. This will be followed by a brief review on molecular level auxetics, which were proposed, or found to exhibit auxetic behaviour. Finally, some uses of auxetic materials will also be described.

2.3.1 Auxetic Mechanisms

2.3.1.1 Re-Entrant Honeycombs

The re-entrant honeycomb was the first structure that was shown, through analytical modelling, to exhibit a negative Poisson's ratio when deforming via flexure of ribs[186,187]. Following these initial studies, the honeycomb structure attracted the attention of a number of scientists, with research being conducted on 2-D and 3-D systems utilising both analytical models and finite element analysis[188–191]. The re-entrant systems have also been investigated for acoustic[192], thermal[193] properties together with potential applications in composites[194–196].

The work conducted by Masters and Evans [188,189] and subsequently by Gibson and Ashby [197] on the mechanical properties of both re-entrant and non-re-entrant honeycombs is a good illustration of how the Poisson's ratio of a system is dependent on both the geometry and the deformation mechanism of the system. It was shown that re-entrant honeycombs which deform via stretching (or dilation) exhibits a positive Poisson's ratio, while non re-entrant honeycombs (commonly referred to as conventional honeycombs) deforming via stretching would exhibit a negative Poisson's ratio. On the other hand, it was also shown that conventional honeycombs deforming via hinging or flexing would exhibit a positive Poisson's ratio while re-entrant honeycombs would exhibit a negative Poisson's ratio (see Figure 2.8).

A number of studies have focused on the superior properties of re-entrant honeycombs when compared to their non-re-entrant counterparts. Such studies examined the effect of varying geometric parameters, such as aspect ratio and rib thickness of the honeycomb, on the in-plane mechanical properties of these systems [190,193,198–201]. These studies suggest that re-entrant honeycombs usually exhibit superior properties when compared to their conventional counterparts, including enhanced crushworthiness[202,203], improved density specific buckling [204], improved bending stiffness due to a larger out-of-plane shear modulus[199], and superior performance during thermal loading in a confined space[205].

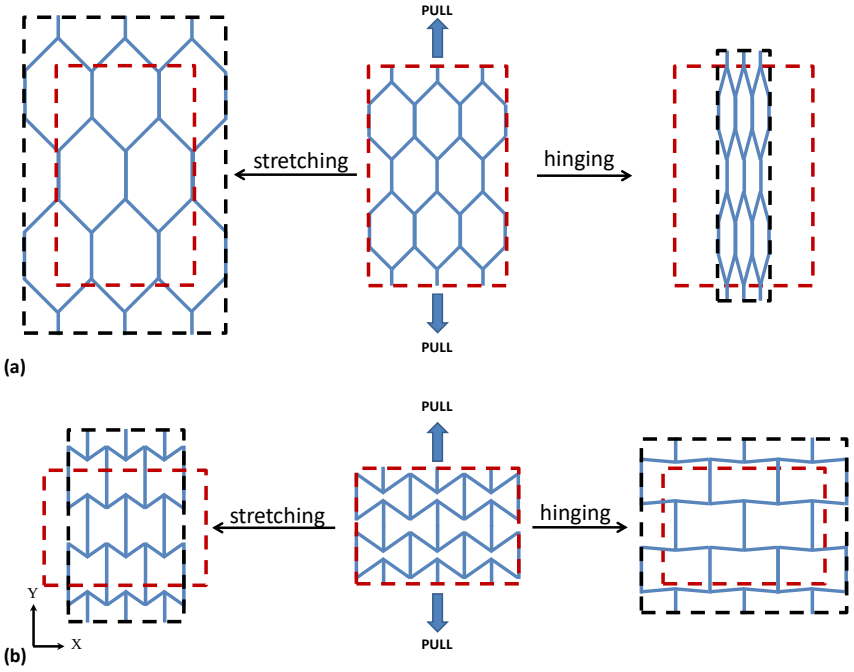

Figure 2.8:(a) Non-re-entrant honeycombs (b) re-entrant honeycombs. Taken from[206]

Other work focusing on the mechanical properties of hexagonal honeycombs included studies of the off-axis deformation[189,207] and response to large stresses[205]. Research has also focused on the manufacture of re-entrant honeycomb systems, with one particular study analysing the use of recycled rubber for their production. Apart from the enhanced properties associated with re-entrant conformations this would also be beneficial from an environmental

point of view due to problems related to the disposal of rubber waste[208]. Analytical and finite element studies suggest that the introduction of edged corners in the honeycomb's framework could potentially provide an easier route for the manufacture of these structures. In addition, this would enable the designer to adjust the Young's modulus of the structure without altering the Poisson's ratio[191,209]. Furthermore such re-entrant systems have also been studied for their utilisation in tubular structures[210] and in composites[195,211]

It should be noted that even though auxetic re-entrant honeycomb systems are very prominent in the literature, there are various other re-entrant systems with the potential to exhibit a negative Poisson's ratio. An example of this is the STAR-n systems[212], which systems are composed of re-entrant arrow-shaped units joined together through a rotational symmetry of 3, 5 or 6 forming star shaped system.

2.3.1.2 Rotating Units

The first model which attempted to explain auxetic behaviour through the use of rotating rigid units was that proposed by Sigmund[213]. However, this model proved to be too complex to predict auxetic behaviour in natural or synthetic materials. Subsequently, a much simpler 2D model (see Figure 2.9) which could be easily used to rationalise auxetic behaviour in a number of molecular systems was developed by Grima et al.[214,215]. The rotating squares model proposed by Grima consisted of rigid squares connected together from their vertices. On application of a uniaxial stress the system deforms by the rotation of the squares relative to each other. Analytical work on the rotating rigid squares system has shown that this system exhibits a Poisson's ratio of -1, and is also isotropic [215,216].

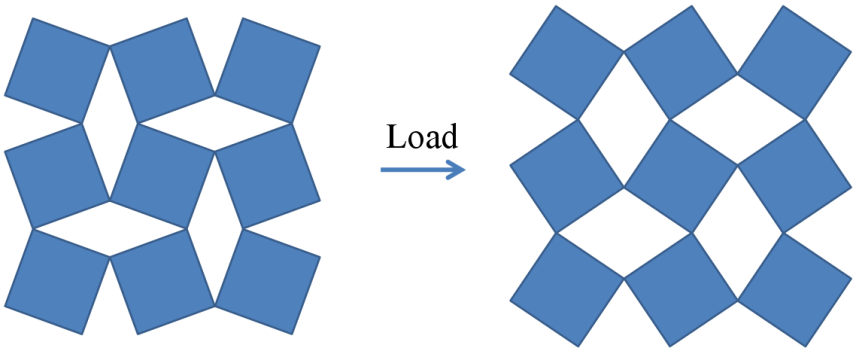

Figure 2.9: Representation of the rotating squares mechanism. Taken from [206].

The notion of rotating squares was subsequently extended to other rotating polygons such as rectangles[217,218], parallelograms[219,220], triangles[221–224] and rhombi[219,225] (see Figure 2.10). Studies on these systems have shown that the Poisson's ratio varies according to the shape of the polygon and the way that these polygons are connected. For example, for a system of rotating rectangles there are two ways in which the rectangles can be connected. These are referred to as the Type I and Type II conformations, which conformations are shown in Figure 2.9. In the former case the rectangles are connected in such a way that the long side of one rectangle is connected to the long side of another rectangle. This results in a system with anisotropic properties, in which the Poisson's ratio may be both positive or negative, depending on both the angle between the rectangles and the size of the rectangles themselves[226].

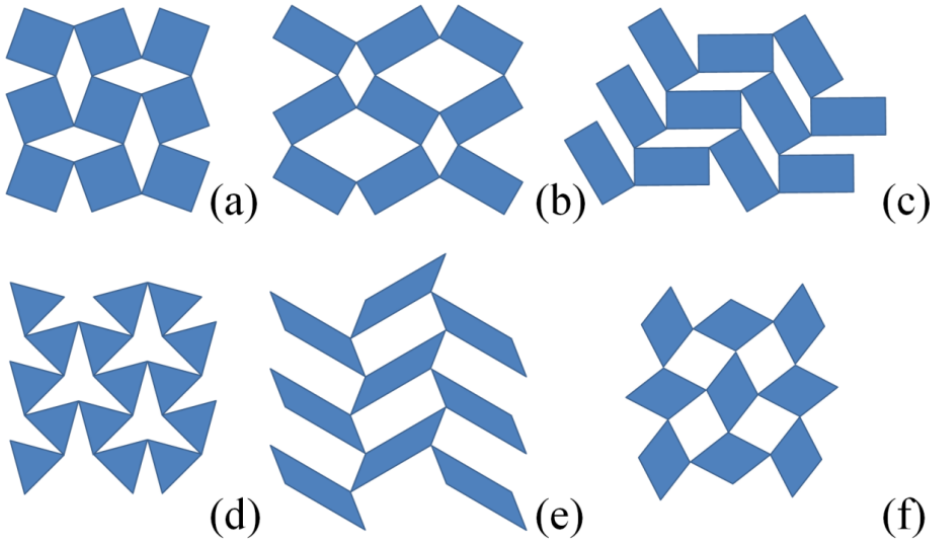

Figure 2.10: Illustration of some of the rotating rigid units (a) rotating squares (b) type I rotating rectangles, (c) type II rotating rectangles, (d) rotating triangles, (e) rotating parallelograms and (f) rotating rhombi systems. Taken from [206].

In the Type II rotating rectangles the longer sides of one rectangle is connected to the shorter side of the next rectangle, giving a system with an isotropic Poisson's ratio of -1. In this case the Poisson's ratio is independent of the degree of openness of the system[217,226]. Subsequent studies on these systems focused on structures which are not fully rigid (see Figure 2.11) where the squares not only rotate but also deform through other mechanisms, such as concurrent rotation and stretching[227,228] and rotation together with square deformation[229,230].

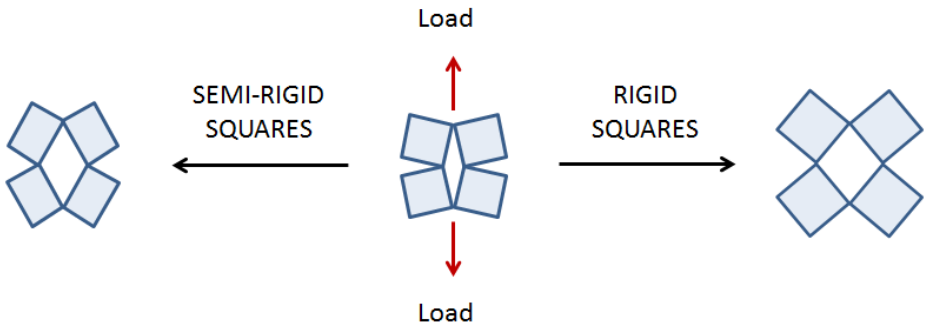

Figure 2.11: The rigid-squares and semi-rigid rotating squares model.

The rotating polygons mechanism has been used to rationalise the auxetic behaviour of numerous species. Examples of this are the rotating triangles model, which has been used to explain the negative Poisson's ratio found in auxetic foams[231] and the rotating Type II rectangles model which rationalises the auxetic behaviour in silicates such as α-cristobalite[226]. It should be noted that in addition to these 2D models, 3D models have also been developed to explain the auxetic behaviour in silicates[61,63,232–234].

2.3.1.3 Dilating Systems

Another mechanism which could result in auxetic behaviour is the dilating mechanism. The basis of this mechanism is that the ribs of the system are allowed to shorten or elongate whilst it is not allowed to distort. This mechanism was first described by Rothenburg[235], who proposed a triangular system (see Figure 2.12) which exhibits a negative Poisson's ratio when subjected to a uniaxial load. Following this initial report, several other dilating systems have been proposed such as sliding rigid rods[236], sliding wedges[237] and stretching squares[228].

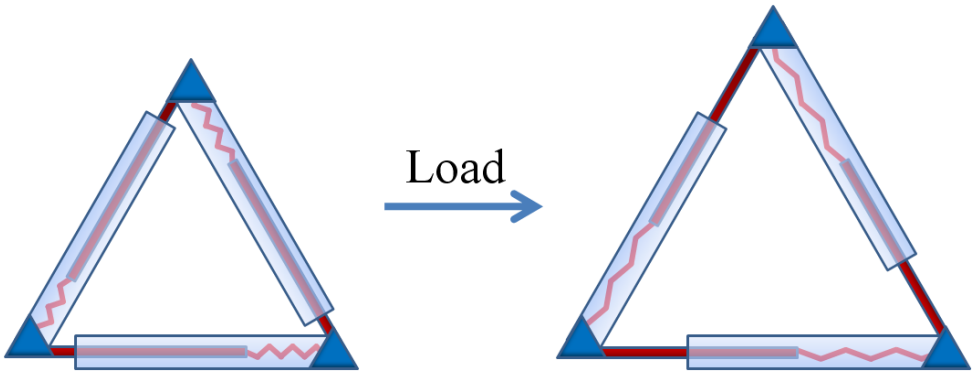

Figure 2.12: An illustration of the dilating triangular system proposed by Rothenburg. Taken from [206].

2.3.1.4 Chirals

Chiral systems are another important class of structures which have the ability to exhibit a negative Poisson's ratio. These systems were first described by Wojciechowski[238] and later implemented as a structure by Lakes[239] where a hexagonal chiral system, also known as hexachiral, was proposed. Chiral systems derive their name from the fact that such systems may be constructed in a left handed or right handed manner, where the two systems are non-superimposable. A hexachiral system is composed of a central cylinder (node) with six tangentially attached ligaments (also referred to as ribs), see Figure 2.13. The deformation mechanism of such a system involves the rotation of the central cylinder on the centre of its own axis, whilst the ribs which join the cylinders are allowed to roll over the central cylinder. Analytical and experimental studies of hexachiral systems have shown that such systems possess an isotropic Poisson's ratio of -1[240]. Chiral honeycombs have been proposed for a number of potential applications[241] such as their use in stents[242].

In subsequent studies, Sigmund *et al.*[243,244] developed a similar system composed of a square node instead of a cylindrical one, with each square being connected to four ligaments. In this system the adjacent chiral units are mirror images of each other rather than units with the same chirality, which was consequently described as being an anti-tetrachiral honeycomb[237], see Figure 2.13.

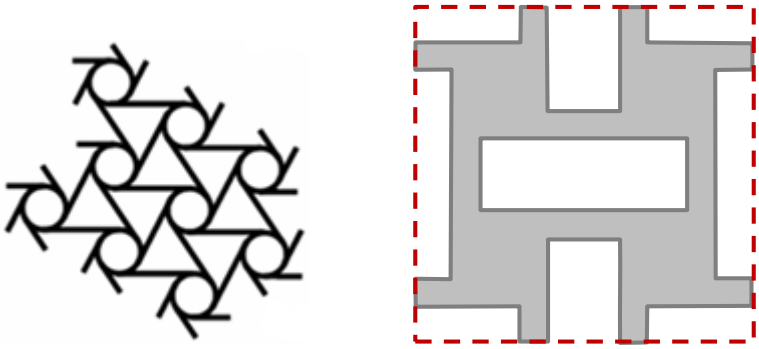

Figure 2.13: (a) The hexachiral system studied by Lakes [239] and (b) the anti-tetrachiral system. Adapted from [206].

2.3.2 Molecular level auxetics

Since the main focus of this dissertation is molecular level systems, particularly their mechanical properties, a review of the advances in the field of molecular level auxetics will be given. Before this however, it should be noted that auxetic behaviour is scale independent. Thus, when one is studying molecular level auxetics one should keep in mind that the mechanism utilised to explain the auxetic behaviour could be applied on the macroscale.

2.3.2.1 Auxetic Inorganic Molecular systems

A large number of studies have focussed on analysing the mechanical properties, in particular the Poisson's ratio, of inorganic molecular systems**.** In the work conducted by Grima et al. [66–68] force-field based simulations were utilised to determine the Poisson's ratio of the idealised silicon equivalents frameworks of the zeolites THO, NAT and EDI (see Figure 2.14), which simulations have shown that these systems are auxetic in the (001) plane, with the value of the Poisson's ratio depending on the force-field used and the zeolite under study.

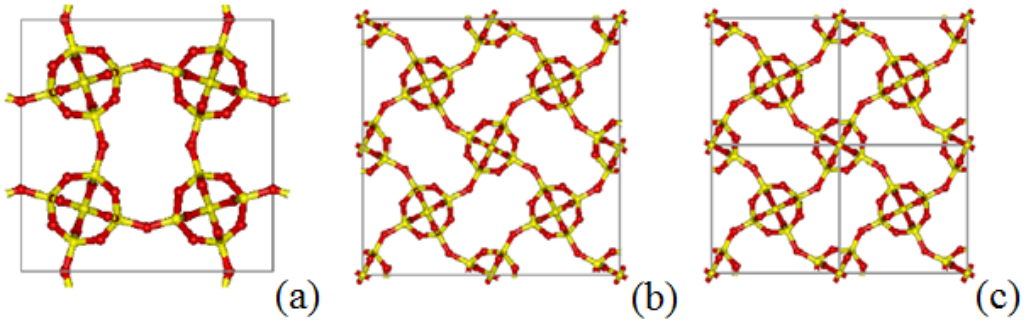

Figure 2.14: The SiO_2 equivalent frameworks of THO (a) NAT (b) and EDI (c), in the (001) plane where such systems exhibit a negative Poisson's ratio.

This behaviour was initially rationalised by utilising the rotating rigid squares mechanism (see Figure 2.15). However analytical studies of the equivalent mechanical systems predict a Poisson's ratio of -1 which is more negative than the values obtained through force-field simulations[66]. This was later explained by utilising the 'semi-rigid rotating squares' deformation mechanism[230]. Experimental studies[245] on the mechanical properties of NAT confirmed that this system has the ability to exhibit auxetic behaviour.

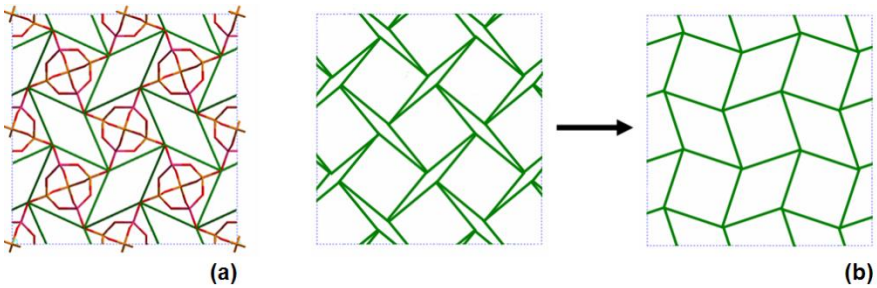

Figure 2.15: (a) The connected squares in natrolite at zero stress. (b) The behaviour of the connected squares upon stretching. Taken from [206]

Further studies on the SiO_2 equivalent frameworks of NAT, EDI and THO suggested that the Poisson's ratio of these species is affected by hydrostatic pressure, with maximum auxeticity being reported at positive external hydrostatic pressure of around 2-8% of the bulk modulus[246].

Apart from zeolites, silicates have also been subjected to a number of studies in order to determine if such molecular systems have the potential to exhibit a negative Poisson's ratio. In fact the silicate α-cristobalite was subjected to a number of experimental and modelling studies [60,62,64,233,247–250]. The first reported case of α-cristobalite exhibiting a negative Poisson's ratio was through the Brillouin spectroscopy study conducted by Yeganeh-Haeri *et al.*[60], where maximum auxetic behaviour was observed in the (010) and (100) planes with maximum auxeticity, $\nu_{23} \approx -0.5$, being reported at *c.* 42° to the z-axis. Yeganeh-Haeri *et al.* explained that these observations could be due to the bending of the Si—O—Si angle, which results in the inwards rotation of the SiO_4 tetrahedra, see Figure 2.16.

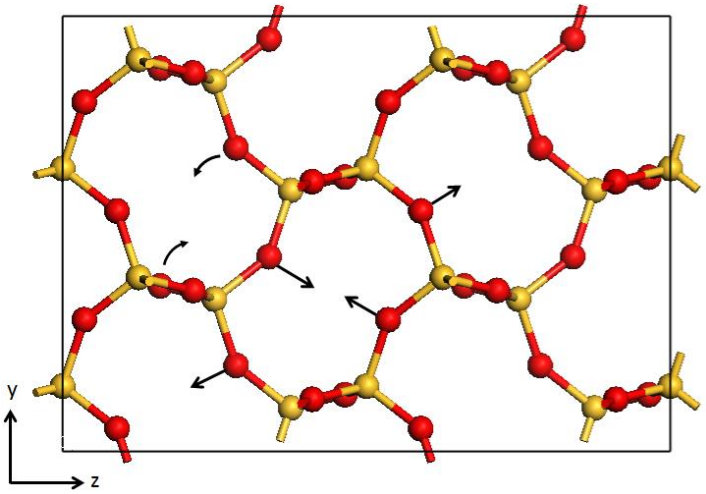

Figure 2.16: The Yeganeh-Haeri deformation mechanism[60].

Following this work, first principles calculations conducted by Keskar and Chelikowsky [247] also suggested that this silicate has the ability to exhibit a negative Poisson's ratio with the auxetic behaviour being rationalised by to the rotation of rigid SiO_4 tetrahedra, a mechanism similar to that suggested by Yeganeh-Haeri.

These initial reports led to a number of studies on the mechanical properties and deformation mechanism of α-cristobalite[61–63,234]. In their work Alderson and co-workers used a 3D approach to rationalise this auxetic behaviour. Their approach involved the interplay of rotation and dilation of the SiO_4 tetrahedra, see Figure 2.17. Through their work these authors have developed three main deformation mechanisms [61,63,232–234,251] namely:

- Rotating tetrahedral model (RTM): where the tetrahedra rotate relative to each other, but remain rigid internally, and thus dilation or deformation of the tetrahedra does not take place. The rotation of the tetrahedra can take place relative to the a-axis, which is known as RTM1, or relative to the c-axis, which is known as RTM2.
- Dilation tetrahedral model (DTM): where the tetrahedra may not rotate relative to each other but are allowed to dilate. It was shown that for such a system the Poisson's ratio in any plane was equal to -1[232].
- Concurrent tetrahedral model (CTM): where both dilation and rotation of the tetrahedra take place. The value of the Poisson's ratio in this model is dependent on the relative extent of dilation and rotation as it has been shown that these mechanisms have the potential to function against each other, to the extent that a positive Poisson's ratio can be obtained[233].

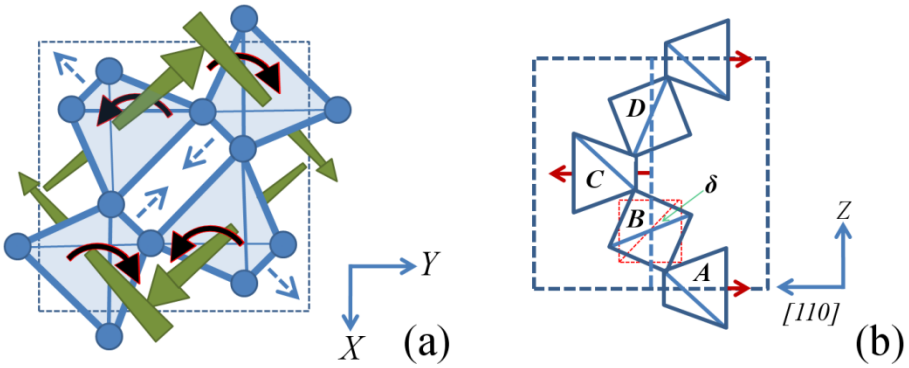

Figure 2.17: Illustration of the (001) plane (a) and the Z-[110] in α-cristobalite (b) Depiction of how the tetrahedra rotate in plane as suggested by Alderson. Taken from[206] .

Grima et al. [62] proposed an alternative approach to explain the auxeticity in α-cristobalite which behaviour was explained by using a rigid rotating 2D model, see Figure 2.18. It was postulated that the negative Poisson's ratio in the (100) and (010) planes can be explained in terms of the Type II rotating rectangles mechanism.

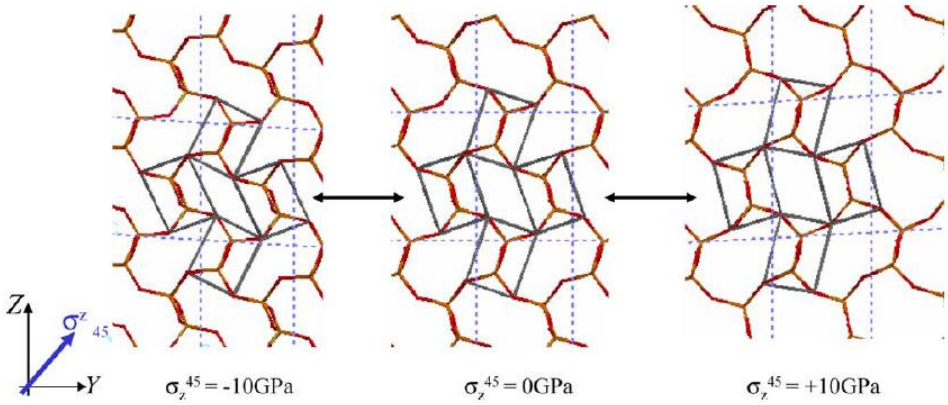

Figure 2.18: The 'rotating rectangles' in α-cristobalite. Adapted from [62].

It has been shown that α–cristobalite can undergo a phase change to form β–cristobalite. Research has shown that β–cristobalite demonstrates maximum auxeticity in the (001) plane when loaded on axis, and unlike α–cristobalite it does not exhibit auxetic behaviour in the (001) and (100) planes[234]. It has been suggested that this apparent loss in

auxeticity is due to the fact that the Type II rectangles responsible for the auxetic behaviour in α–cristobalite are in their fully open state in β–cristobalite. Moreover, it has also been postulated that the auxeticity of the WL β–cristobalite in the (001) plane may be explained through a rotating squares mechanism.

Gatt[206] subsequently reported a positive Poisson's ratio for β–cristobalite in the (100) and (010) planes when loaded in the [001] direction, which results were obtained by using both CVFF and Compass force-fields. It was suggested that in the (100) and (010) planes the rectangles no longer rotate relative to each other, but rather the rectangles themselves deform via a 'defective wine-rack mechanism'. In this mechanism the diagonals of the rectangles (the elements making up the wine-rack, see Figure 2.19) stretch and rotate with respect to each other. Systems which deform through this mechanism exhibit a Poisson's ratio of about 0.6.

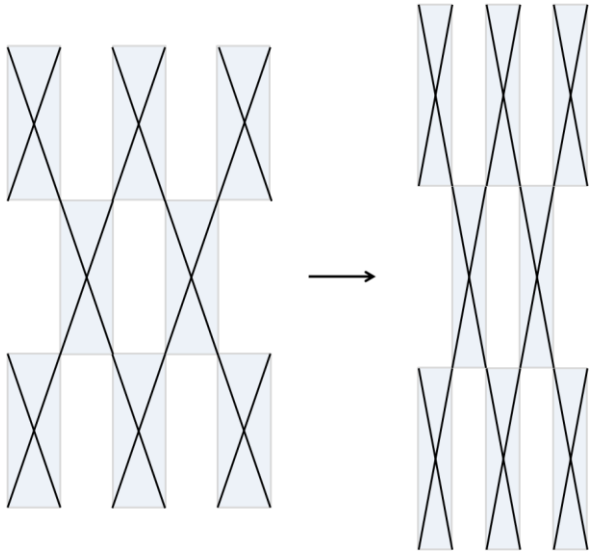

Figure 2.19: Representation of the 'defective wine rack' mechanism, where the elements of the 'wine rack' (black lines) hinge relative to each other as well as stretch. Taken from[206].

Auxetic behaviour was also reported in stishovite[252,253], a rutile-type polymorph of SiO_2. It was shown that this system exhibits a negative Poisson's ratio was in the (100), (010) and (001) planes. Through the use of first principles density functional theory (DFT) calculations, it was shown that stishovite is auxetic in the (001) plane with an increase in

hydrostatic pressure in the range of 0-30 GPa resulting in a decrease in auxetic potential, where a nearly zero Poisson's ratio is recorded at 30 GPa. The direction of maximum auxetic behaviour is circa 45 ° to the [001] axis in the pressure range studied.

In the (100) plane stishovite exhibits an increase in auxetic behaviour with a positive value being recorded at 0 GPa and a decrease in Poisson's ratio being recorded on increasing pressure from 0 GPa to 30 GPa. The auxetic behaviour exhibited in the (010) plane is identical to the (100) plane with a minimum value of circa -0.2 being recorded at 30 GPa. The direction of minimum Poisson's ratio exhibits a shift with increasing hydrostatic pressure, with the minimum Poisson's ratio being recorded at circa 45 ° to the [010] axis at 0 GPa shifting to circa 49 ° at 30 GPa.

The auxetic behaviour of stishovite was explained through deformation mechanisms involving rotations and distortions of the constituting octahedra. In particular, it was shown that octahedral distortions play an important role on the observed Poisson's ratio. In the (001) plane scissoring distortions decrease with increasing pressure, when the system is loaded in direction of maximum auxeticity, which is associated which was associated with the minimum Poisson's ratio becoming more positive. In addition to this, on increasing the hydrostatic pressure, an increase in scissoring distortions was noted when the system is loaded at 45 ° to the [010] axis in the (100) plane, which was associated with the Poisson's ratio becoming more negative.

Other molecular systems which have been studied for their auxetic behaviour include black phosphorus[254,255], boron arsenate [256,257] and 2D systems[258,259] such as graphene[260–263] and interconnected shurikens[264]. Other auxetic systems are inspired by various geometries[211,265–267]. Recently materials have been shown to exhibit 'half-auxetic' effect, where the material will

expand on both compression and stretching. This effect has been reported in 2D monolayer 2D boron sheets[268] and TiSe[269].

2.3.2.2 Auxetic Organic Molecular systems

One of the first organic molecular level systems was that proposed by Evans[59], which consisted of a theoretical 2-D network based on re-entrant honeycomb systems, with the deformation of re-entrant systems leading to auxetic behaviour. This framework is composed of a network of benzene rings interconnected via acetylene chains[59]. Networks based on re-entrant systems are known as (n,m)-reflexynes (see Figure 2.20) where m is the number of links on the vertical branches and n is the number of acetylene links on the diagonal branches. Varying the values of m and n will alter the anisotropy and Poisson's ratio of the system, illustrating how the mechanical properties of a system can be tailor-made through careful design of the molecular structure. It should be noted though that such systems are very difficult to reproduce experimentally.

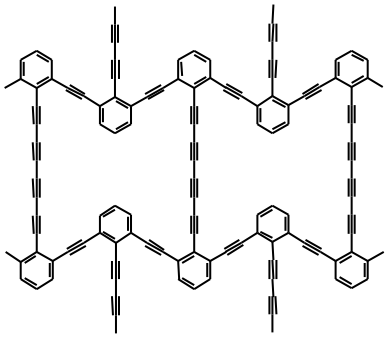

Figure 2.20: 1,4-reflexyne molecular systems.

Following Evans' seminal work[59], a number of researchers studied the mechanical properties of such systems through force-field based simulations, with the results obtained suggesting that such frameworks have the potential to exhibit auxetic behaviour in the *YZ* and *ZY* planes[188,270,271]. Nevertheless, this auxetic behaviour is limited for loading on-axis up to a

maximum of around 10 º off-axis. In fact, when studying the off-axis Poisson's ratio of reflexynes it was shown that such systems are characterised by non-auxetic behaviour, exhibiting very high positive off-axis Poisson's ratios, with the maximum value being reported at *circa* 0.85 when loading at 45º to the *Y*- and *Z*- directions[271]. This lack of off-axis auxeticity in 'flexing re-entrant' honeycombs is in agreement with Gibson and Ashby's model of idealised honeycombs[187,272] and is due to the fact that honeycombs are very weak in shear when compared to the uniaxial on-axis stretching.

In addition to studying the mechanical properties of such systems, the mass transport properties of such frameworks have also attracted the attention of several scientists for their potential application in molecular sieves. In fact, research suggests that the (2,8)-reflexyne has the potential for tunable size selectivity. Thus, it may act as a sieve for C60 and C70 molecules which may be introduced into the sieve as the framework deforms, with the subsequent release of the guest molecules being dependent on variations in the size and shape of the pores of the sieve[273]. In addition to this, since auxetic sieves exhibit an almost linear correlation with the applied strain, these sieves would exhibit higher tenability when compared to non-auxetic sieves. Thus, a particular application of such molecular sieves would be their use in smart bandages and filters, where for example biochemicals can be filtered whilst blocking nanoscale impurities[274].

Apart from exhibiting a negative Poisson's ratio, it was shown that polyphenylacetylene networks designed to mimic the geometry of honeycombs which have both non-re-entrant and re-entrant features, referred to as the 'semi re-entrant honeycombs', also have the potential to exhibit the not so common property of a near-zero Poisson's ratio[275]. This anomalous mechanical property means that the material will not contract or expand laterally when it is compressed or stretched. Such a characteristic is particularly desirable in applications where changes in the lateral dimensions are detrimental to a system's performance. Moreover

materials which exhibit a zero Poisson's ratio would be particularly useful in the manufacture of cylindrical surfaces[275].

Another molecular 2-D framework which is predicted to exhibit auxetic behaviour is that of a triangular network composed of polyphenylacetylene units[276] (see Figure 2.21a). Such a system would be referred to as polytriangles-*n*-yne where *n* indicates the acetylene links which are present. This system was made to mimic the auxetic behaviour exhibited by rotating triangles model, which model predicts a constant isotropic Poisson's ratio of -1[221]. Molecular modelling studies of the polytriangles-*n*-yne systems have shown that if more than two acetylene links are present, the system will exhibit six mutually orthogonal negative Poisson's ratios[221]. Force-field based simulations, utilising the PCFF[271] and DREIDING force-fields[276], carried out on such systems predict that these are auxetic in the *YZ* and *ZY*-planes. In addition to this it was also predicted that the auxeticity increases as the acetylene chains are made longer. It was also shown through molecular modelling that such systems exhibit negative off-axis Poisson's ratios very similar to those observed on-axis, i.e. the networks are *quasi* isotropic, a property which is typical for systems which exhibit hexagonal symmetry.

It should be noted that the Poisson's ratio obtained for the polytriangles system through molecular modelling was not identical to that of the idealised 'rotating triangles' model. This phenomenon was rationalised[271] by the fact that the molecular level networks are more complex, even in shape, than the idealised model. In addition to this, in the case of the idealised 'flexing rotating triangles' model the sides of the triangles are composed of simple beams, whilst in the case of the molecular polytriangles they are two benzene rings linked together by an acetylene chain. In such a network, it is primarily the acetylene chains, particularly the longer ones, which mimic the behaviour of the beams. Thus, as the system gets smaller, the deviation from the idealised Poisson's ratio of -1 gets larger. Another notion which is important to consider is that such molecular level systems are characterised by non-bond interactions

which give rise to interactions between the different beams in the system, which non-bond interactions increases as the separation between the atoms is reduced. Thus, less dense systems will exhibit less of the non-bond interactions per unit volume when compared to an equivalent denser system. This is another factor which contributes to the fact that smaller systems exhibit a larger deviation from the idealised Poisson's ratio when compared to a larger system[271].

Another set of systems which have attracted the attention of researchers for their potential to exhibit a negative Poisson's ratio are the calixarenes[271,277,278], which are systems composed of aromatic compounds consisting of carbon, hydrogen and oxygen and assume a nanoscopic conformation reminiscent to that of a cup (thus the term calix), see Figure 2.21b. The nomenclature for such systems is calix[*n*]arene where *n* indicates the number of aromatic rings between the cup-like structures. The molecular system proposed by Grima *et al.*[277] is composed of alternate facing 'four-legged claws', composed of benzene rings, arranged on a square grid. This system is made to mimic the behaviour of an 'egg rack' macrostructure which structure was shown to open up in all directions when loaded in tension, giving rise to auxetic behaviour. Similarly, when subjecting calixarene systems to a load in tension, the connectivity of the 'claws' forces the structure to open in all directions like an umbrella giving rise to a negative Poisson's ratio[271,277]. Force-field based simulations predict that this system will exhibit auxetic behaviour in the *ZY* and *YZ* planes[271]. In addition to exhibiting auxetic behaviour, such a deformation mechanism will also lead to a large positive Poisson's ratio in the out-of-plane direction, which property could potentially be useful in a number of applications.

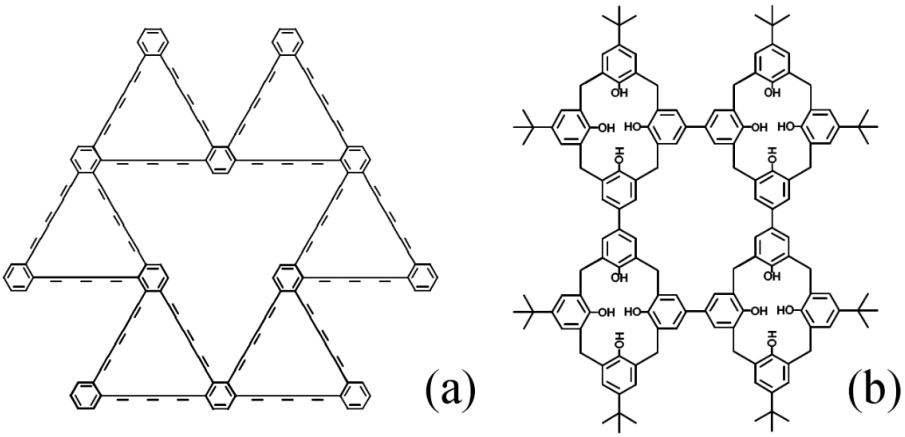

Figure 2.21: Illustration of polytriangles-3-yne (a) and calixarene (b) systems.

The idealised model for calixarene systems predicts an in-plane on-axis Poisson's ratio of -1, which value was not predicted by force-field simulations. The arguments utilised to rationalise this phenomenon are very similar to those used to explain the deviation from ideality of polytriangles i.e. that smaller networks deviate more from the ideal model the system is meant to mimic when compared to an equivalent larger system. Moreover, it was also argued that the egg-rack / umbrella model is not an adequate enough representation of the double calix systems. In fact, it was speculated that these systems resemble structures whose joints are replaced by rhombic units. In such an arrangement two deformation mechanisms take place when the system is subjected to a stress, with the combined effect of these two mechanisms giving rise to the actual value of the Poisson's ratio[271].

One of the mechanisms taking place involves the deformation of the rhombi, which deformation leads to a positive Poisson's ratio. The second mechanism acts on the 'arms' of the system by opening the structure in a manner which is reminiscent of opening an umbrella and flattening out the whole structure, leading to a negative Poisson's ratio. The two aforementioned mechanisms act concurrently, resulting in the net Poisson's ratio being less negative than expected, with the actual value depending on the relative magnitude of the

mechanisms which in turn is dependent on the relative size of the rhombi when compared to the arms. In fact smaller systems, where the rhombi are more predominant, would exhibit a more positive Poisson's ratio than larger systems where the umbrella arms are more predominant[271].

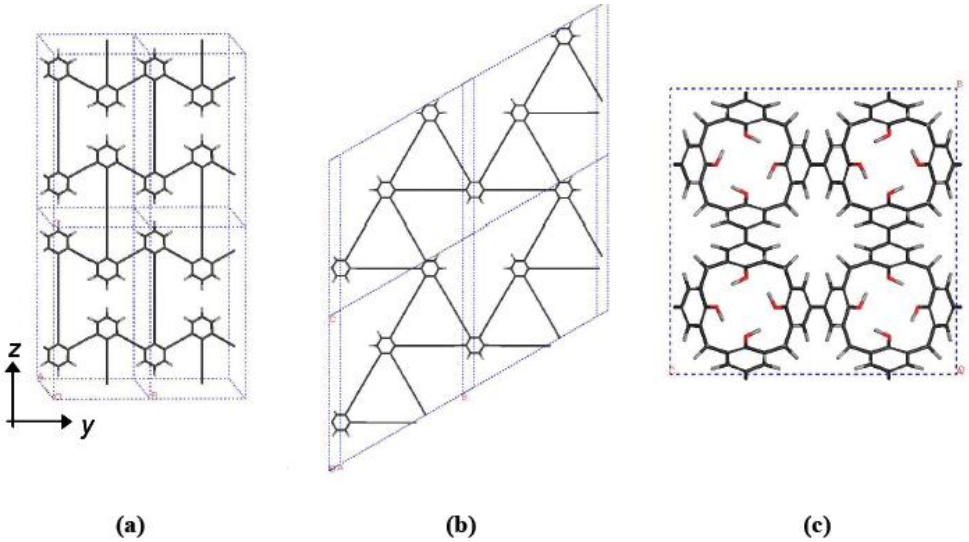

Figure 2.22: An illustration of reflexynes (a), polytriangles (b) and calyxarines (c) Taken from [271].

In addition to 2-D networks, 3-D organic molecular systems which exhibit a negative Poisson's ratio have also been reported. In fact, in 1993, Baughman proposed a hypothetical molecular level system with a (10,3)-*b* topology[279] known as 'twisted-chain auxetics' or (10,3) – *b* networks, see Figure 2.23. The auxetic behaviour predicted for these systems would arise due to shear deformation in the helical polyacetylene chains. Following this work, Gardner proposed that systems similar to those described by Baughman could be synthesised from existing starting materials[280].

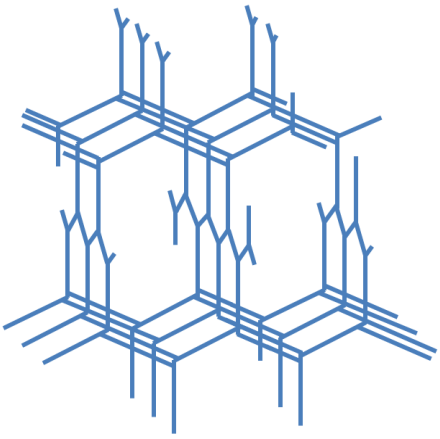

Figure 2.23: An illustration of the theoretical (10,3) – b networks proposed by Baughman.

Another field of study which is important to discuss when considering molecular level auxetics is that of the design and synthesis of liquid crystalline polymers with a negative Poisson's ratio, which field of research is a still a relatively new niche of study. Work on these systems was only initiated in the 1990s, and is presently still in its development stage. Much of the strides made in this field can be attributed to the pioneering work conducted by A.C. Griffin *et al.* at the Georgia Institute of Technology.

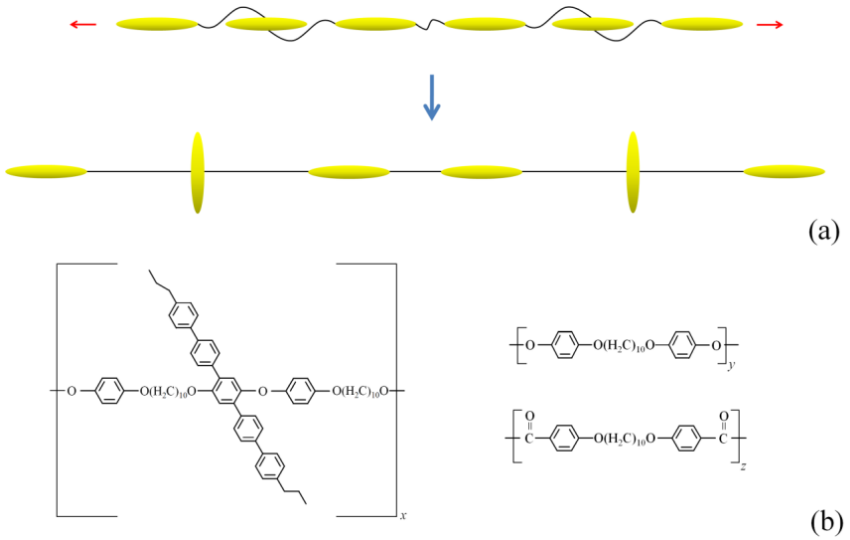

Figure 2.24: (a) The auxetic behaviour in LCPs as proposed by Griffin and co-workers. (b) The co-polymer with a pentaphenyl rod suggested by Griffin and co-workers. Adapted from[281].

In their work, Griffin and co-workers suggested a number of LCPs which were specifically designed to exhibit negative Poisson's ratios[281–284]. Griffin's LCPs are composed of long and thin rigid units, such as terphenyl[283] and pentaphenyl[284], which rigid units can be connected together, either end-to-end or side-to-side, by flexible spacers, see Figure 2.24.

It was suggested that auxetic behaviour can be achieved in such species through a side-connectivity driven rod reorientation mechanism in main-chain liquid crystalline polymers[285]. X-ray scattering experimental data revealed that the long axes of the rigid units tend to align parallel to each other when present in the nematic phase. However, when stress is applied, the rigid units will rotate, resulting in the parallel chains attempting to move into each other and giving rise to transverse displacements[281,284,285]. It was also shown that oligo-paraphenyls are capable of exhibiting such behaviour[281]. Nevertheless, despite the experimental evidence that the aforementioned deformation mechanism is taking place, which mechanism would lead to auxetic behaviour, the room temperature experimentally measured Poisson's ratio of these systems has been reported to be anisotropic and positive. These results were rationalised by Griffin and co-workers by the fact that as the system is loaded, the chains slip past each other, which leads to a reduction in the cross-sectional area of the sample, which phenomenon will counteract the auxetic effect of the molecular expansion[281]. To date only positive values for Poisson's ratio have been recorded in such materials[286].

Experimental work has shown auxetic behaviour in a synthetic non-porous liquid crystal elastomer. For strains above circa 0.8 applied perpendicular to the liquid crystal director (i.e. perpendicular to the alignment direction) a negative Poisson's ratio is recorded [286,287].

2.3.2.3 Auxetic Metallic Molecular and related systems

Auxetic behaviour has also been reported in a number of metallic molecular systems. In fact one of the earliest reports of systems exhibiting a negative Poisson's ratio were the metallic species antimony, arsenic, cadmium and zinc single crystals[288,289]. In addition to this, a number of other studies have focused on the auxetic behaviour of cubic systems [290–305].

Body centred cubic (BCC) and face centred cubic (FCC) phases are usually auxetic in non-axial directions [290,292,304]. Hexagonal close packed (HCP) metals zinc and beryllium have also been shown to be auxetic[304]. Analytic expressions of the extreme values of Poisson's ratio over all possible directions for cubic materials were derived[306]. It has also been shown how elastic constants can be utilised for the classification of any cubic materials as auxetic, directional auxetics and non-auxetics[303,305,307].

The list of systems which are complete auxetics is limited with Ba, $Sm_{0.7}Y_{0.3}S$, $Sm_{0.75}Y_{0.25}S$, $Sm_{0.75}La_{0.25}S$, $Sm_{0.65}La_{0.35}S$, $Sm_{0.75}La_{0.25}S$ being shown to have a negative Passion's ratio for all directions of applied strain. However, it should be noted that some results show that $Sm_{0.7}Y_{0.3}S$, $Sm_{0.75}Y_{0.25}S$, Ba are complete auxetics while other show that they are partial auxetics[291]. There are extensive tables of recorded Poisson's ratios of different cubic systems [290–292,298].

In the work carried out by Baughman et al., it was shown that 69 % of the sample of cubic elemental metals studied have a negative Poisson's ratio when stretched along the [110] direction[304]. Referring to the two adjacent unit cells of a body centred cubic metal shown in Figure 2.25, application of force in the [110] direction results in a decrease in the acute angles in rhombus denoted by atoms 1-4. This results in a decrease in distance between atoms 1 and 3 in rhombus denoted by atoms 1, 3, 5, 6 which leads to an increase in distance between atoms 5 and 6 leading to a negative Poisson's ratio.

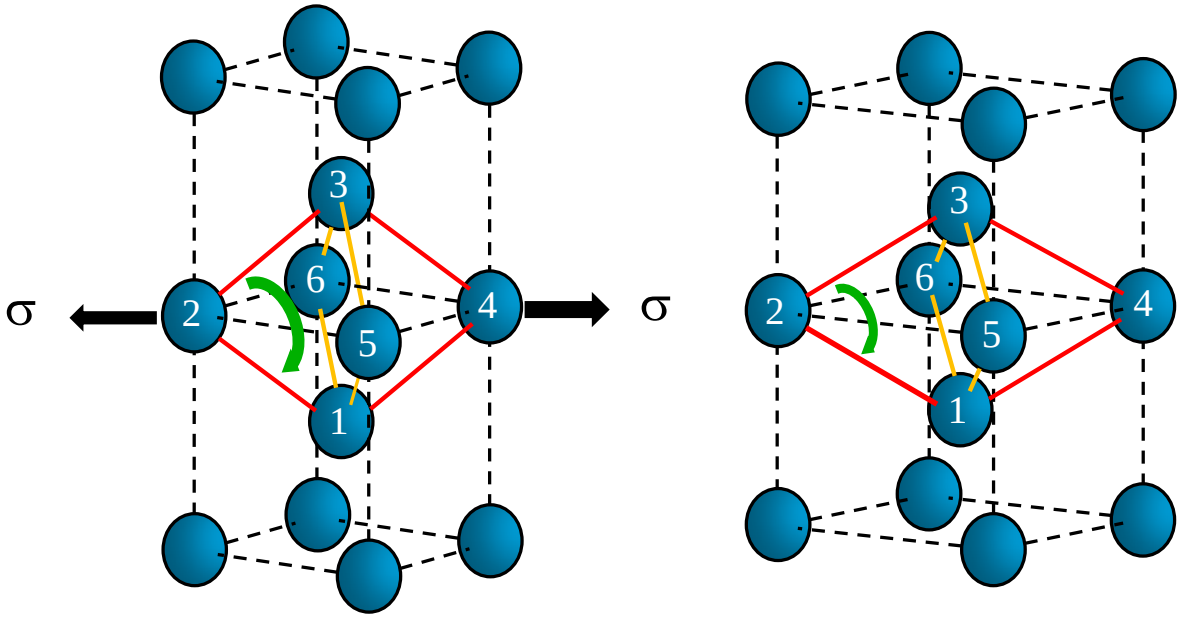

Figure 2.25: Illustration of the deformation mechanism leading to auxetic behaviour in body centred cubic metals as proposed by Baughman [304].

2.3.3 Properties and Applications of Auxetics

When "conventional materials" are subjected to an out-of-plane bending force they attain a saddle-shaped conformation (anticlastic curvature). Auxetic materials on the other hand adopt a dome-shaped form (synclastic curvature), see Figure 2.26. One of the first studies to predict this interesting feature was conducted by O'Donnell[308], when his team were carrying out studies on perforated steel plates. This property has subsequently attracted the attention of a number of researchers[309–311] and it was shown that due to this phenomenon auxetic materials could potentially be better suited to adopt the curves of the human body than "conventional materials". This has led to a number of potential applications for soft auxetic materials in mattresses and ergonomic cushions[312], since cushions made of auxetic foams could potentially enhance comfort and reduce the risk of bed-sores[313,314].

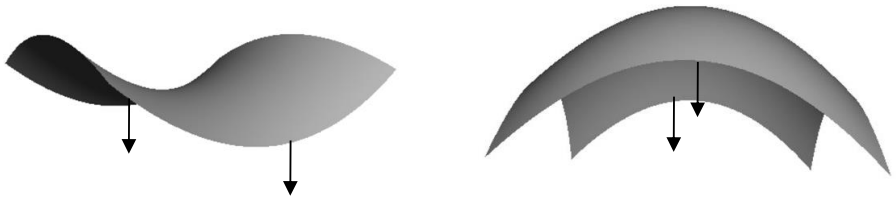

(a) **(b)**

Figure 2.26: (a) saddle-shaped conformation adopted by "conventional materials" compared to dome-shaped conformation adopted by auxetic materials when both materials are subjected to an out-of-plane bending force. Taken from [206].

Another property which could potentially give auxetic materials an advantage over conventional materials with respect to application in cushions is that of increased densification of auxetic materials at a point of impact. This counterintuitive property, which has been reported in materials such as foams[315–319], ultra-high molecular weight polyethylene[320,321], honeycomb structures[322,323] and composites[324,325], results in higher indentation resistance when compared to "conventional materials", see Figure 2.27. This property, combined with the ability of auxetic material to adopt a dome-shaped conformation, makes auxetic materials ideal for use in safety equipment such as crash helmets, knee and elbow-pads and bullet proof vests [326–330].

Auxetic materials may also be utilised in biomedical applications such as smart bandages, where scientists can take advantage of the fact that numerous auxetic systems have increased porosity compared to "conventional materials". Such bandages have an advantage over "conventional bandages" in that they can release a dose of medicine which is directly proportional to the swelling. Such bandages are composed of a textile having a porous auxetic framework which is impregnated with medicine, whose pores open as the swelling increases, resulting in the release of medicine. Conversely as the swelling decreases the pores close, resulting in the administration of a controlled dose of medicine[331].

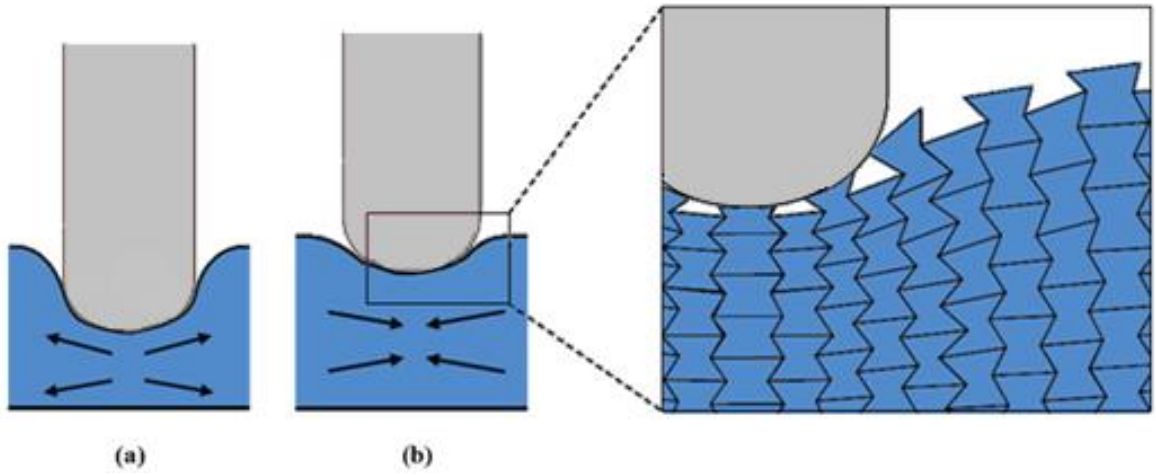

Figure 2.27: A comparison of the material response of (a) conventional material and (b) auxetic material when subjected to a stress. Auxetic materials exhibits increased densification at the point of impact. Adapted from[331].

Porous auxetic systems may also be applied in smart filters where the pore size of the filter is strain dependent. Thus, a single filter may be used to separate differently sized particles within the same mixture by adjusting the applied strain. It has also been shown that such filters are easier to clean than "conventional filters", since by the application of a known strain the pores of the filter may be fully opened[332–336].

Another useful property of auxetic systems is their ability to contract under compression and expand under tension. This particular property has attracted the attention of scientists for numerous potential applications, ranging from use in construction materials[337] to biomedical applications[338]. An ingenious application of this property is using auxetic systems in rivets, press-fit fasteners and nails which are easier to insert but harder to remove than "conventional" materials. For example, conventional nails tend to get fatter when being hammered i.e. when they are under compression. This will reduce the pressure the nail exerts on the wall, making it harder to hammer in. The opposite should take place with auxetic nails[337], since these get thinner when under compression, resulting in an increase in the pressure exerted

by the nail on the wall making it is easier to insert. In addition to this, auxetic nails would expand under tension making such nails harder to remove[339]. The fact auxetic materials expand under tension also makes them ideal candidates for seat belts, since this would reduce the stress applied on the passenger upon impact since the surface area of the belt increases[340].

Potential biomedical applications[338,341,342] include the use of auxetic stents[343–345], auxetic neck brace[346] and auxetic microporous polymers as artery dilators[331,347]. Since auxetic materials tend to expand in all directions when under tension, it has been suggested that these materials pose a smaller chance of causing failure of the blood vessel on insertion, thus making them safer than 'conventional materials'[331].

2.4 Scope of thesis

As detailed in the literature review, CO_2 and H_2O in their various forms, have been the subject of a myriad of theoretical and experimental studies[1,18,26,57,96,98,162,348–351] due to their importance[1,2,164] on Earth and in the universe. Both CO_2 and H_2O have extremely rich phase diagrams[121,127,129,352] boasting numerous solid polymorphs, some of which, have been studied for over a hundred years[50,51]. In an attempt to fully characterise the high-pressure polymorphs of H_2O and CO_2, researchers have focused on several different aspects such as studying the structural properties[16,56,57,129,167,171,353,354], vibrational properties[57,120,124,127,171,355] and mechanical properties[54,56,57,130] of these systems.

A number of studies have focused on the phase transitions which take place at extreme conditions of pressure and temperature, where for example, it has been reported that the proton order-disorder phase change in H_2O ice may be brought about by lowering the temperature of the disordered phase usually in the presence of a dopant[20,111,356]. A number of studies have also focused on the pressure induced phase transitions of CO_2 and H_2O ice polymorphs[176,354,357], with examples including the pressure induced phase transition of ice VIII to ice X[47,117,358] and the pressure-induced phase transitions of CO_2 phase II to the CO_2-V[48,49,176]. Pressure induced phase transitions have intrigued a number of researchers by the novel phenomena observed. For example, simple molecular species at ambient conditions can form non-molecular phases by the application of high external hydrostatic pressures, such as in the case of symmetric ice X[46,47] and the polymeric CO_2-V[48,49].

A few studies have also investigated the mechanical properties of the high-pressure polymorphs of H_2O and CO_2 ices. These studies focused mainly on the bulk elastic properties of the polymorphs found at relatively lower pressures [47,52,53]. For instance, the elastic constants of single crystals of ice polymorphs such as ice-III, ice-V and ice-VI [359–363], which are stable

at a pressure of only around 1 GPa, have been investigated. Recently, some work has determined the elastic constants of H_2O and CO_2 polymorphs at higher pressures[54–57].

Despite all of this, there are a number of open questions, particularly with respect to the study of the low temperature and high-pressure phases of these ices. For instance, the stability windows of the high-pressure polymorphs of H_2O and CO_2 are under debate. For example, some studies suggest that CO_2-V should break down at high pressures and temperatures into carbon and oxygen (ε-O_2)[2,181] while other studies did not find evidence for this[37,176,182]. Another example, is the debate on the pressure at which ice VIII should undergo a phase change to ice X[145,146,154]. Moreover, no studies have focused primarily on examining the mechanical properties of the high-pressure single crystal phases of H_2O and CO_2 polymorphs. In order to fully characterise the high-pressure polymorphs of H_2O and CO_2 detailed understanding of their mechanical properties is important.

Detailed studies on the Poisson's ratio and auxetic potential of high-pressure polymorphs are also lacking. It would thus, be interesting to investigate the auxetic potential of these systems and study the effect of varying hydrostatic pressure on the auxetic behaviour of these systems, something which to date has not been tackled. In relation to this, a detailed study rationalising anomalous mechanical properties of these high-pressure polymorphs, together with the pressure dependence of the auxetic behaviour, is also lacking in the literature.

Furthermore, in the case of molecular modelling studies, analysis of the Poisson's ratio of nanoscale auxetics is usually rationalised by investigating the changes in bond length, bond angles and/or their projections in particular planes when a stress is applied in a particular direction[67,68,256,364]. Although this technique has been found to produce reliable results, there may be circumstances where such method cannot be utilised, for example, when the application of stress results in non-continuous change in the structural parameters studied. To date, no

attempts have been made to employ other techniques such as spectroscopy to study the deformation mechanisms. The use of spectroscopy to investigate the deformation mechanisms in crystals would also make it easier to study deformation mechanisms experimentally and compare molecular modelling results with experimental results.

In view of the above, this thesis aims **to study the mechanical properties, with particular emphasis on the Poisson's ratio, of high-pressure phases of H_2O and CO_2 ice, specifically, ice X, ice VIII, CO_2-II and CO_2-V through first principles DFT calculations**. This aim will be achieved by fulfilling the following objectives.

- Use of first principles DFT calculations to study ice X, ice VIII, CO_2-II and CO_2-V.
- Produce detailed convergence studies to ensure that the simulation parameters chosen are adequate to optimally simulate the structures and properties of the aforementioned ice polymorphs.
- Benchmark the properties obtained through DFT calculations with experimental and other theoretical results present in the literature to validate the methodology employed.
- Use of phonon dispersion relations to study the stability of the high-pressure phases of H_2O and CO_2 ice polymorphs in the pressure range of the study.
- Investigate the mechanical properties of the single crystal and polycrystalline aggregate of the high-pressure polymorphs in order to study the Young's modulus, shear modulus, bulk modulus, Pugh ratio and Poisson's ratio.
- Rationalise the calculated Poisson's ratios by investigating the deformation mechanism through:
    - the study of nanoscale changes in various bond lengths, angles and/or their projections in particular planes when a stress is applied

- the use of spectroscopic techniques to study the deformation mechanism of auxetic nanoscale systems. The use of spectroscopic techniques such as infrared and Raman spectroscopy conducted at different pressures will be used to give an insight into changes in molecular vibrations which, when coupled with changes in mechanical properties, are envisaged to give an indication of which deformations are important to achieve a negative Poisson's ratio.

Chapter 3: *An investigation of the mechanical properties of ice X

3.1 Introduction

Water, a key component of life as we know it, has enthralled scientists with its anomalous properties[351,365–367]. H_2O in its various forms is found abundantly on Earth and throughout the cosmos[348]. As detailed in Chapter 2, H_2O ice has a complex phase diagram, with numerous different stable and metastable solid phases which have been identified through experimental and theoretical works[16,18,20,159,368–379]. The most important phases of ice above 2 GPa are ice VII, ice VIII, and ice X[47,117–120] with ice X being found in the higher pressure range. Ice X is macromolecular phase of ice which belongs to the cubic space group $Pn\bar{3}m$. The ice X structure is composed of a BCC packing of oxygen atoms, where each oxygen atom is covalently bonded to four hydrogen atoms, with the hydrogen atom being located midway between two neighbouring oxygen atoms. As a consequence, the molecular character seen in lower pressure phases of ice is lost in ice X[46,47,120,142–149].

Despite numerous studies on ice X, studies on the mechanical properties of this system are limited. Recently, simulations utilising first principle calculations have been carried out to predict the elastic constants of ice X[54,130]. Nevertheless, detailed studies on the Poisson's ratio are lacking. In view of this, the work presented here investigates the mechanical properties of ice X and the variation of these properties with pressure in

*The contents of this chapter have been published in the peer-reviewed Journal of Physics and Chemistry of Solids: Gambin, D., Dudek, K. K., Dudek, M. R., Grima, J. N. & Gatt, R. The mechanical properties of ice X with particular emphasis on its auxetic potential. *J. Phys. Chem. Solids* **150**, 109717 (2021).

the range of 150 GPa to 300 GPa. The mechanical properties of the ice X single crystal and of the polycrystalline aggregate will be investigated. The Poisson's ratio will be studied in detail and geometries/deformation mechanisms will be investigated in order to rationalise any anomalous mechanical properties.

In order to achieve this, this chapter will be subdivided into two sections. In the first part, the methodology employed will be validated through a detailed convergence and benchmarking study. In the second part, the properties of ice X will be determined, paying particular attention to the Poisson's ratio of this system.

3.2 Convergence and benchmarking study for ice X

3.2.1 Introduction

The macromolecular ice X structure has been the subject of a number of DFT studies, where for example, the structure[139], stability[120,144], vibrational[380] and mechanical properties[54,130] have been investigated. The simulation parameters employed have varied in the different studies and thus, in order to choose appropriate simulation parameters to study ice X, a convergence and benchmarking study will be conducted. This will validate the methodology utilised and ensure that the results obtained are not an artefact of calculation parameters employed but an appropriate representation of the ice X system.

3.2.2 Methodology

The crystal structure of ice X as obtained from the literature[120,381] was constructed within the CASTEP[382] modelling platform as implemented in Materials Studio. The Pn$\bar{3}$m space group of ice X was set to P1 in order to eliminate symmetry constraints, apart from those imposed by the unit cell itself, during the minimisation

process. This increases the simulation time but allows all the elements within the cell to act independently. The DFT simulations were carried out utilising GGA functionals on a 1 x 1 x 1 unit cell employing periodic boundary conditions throughout. GGA functionals are widely used in the study of the polymorphs of ice, including ice X[54,120,130,144,154,381,383]. The performance of a number of GGA functionals namely PBE[384], PBE-TS[385], PBE-Grimme[386], PBESOL[387], PW91[388], PW91obs[389], was tested. For each functional geometry optimisation was performed using a cut-off energy ranging from 400 eV to 1200 eV in steps of 200 eV. For each cut-off energy used, different refinements of the Brillouin zone sampling were tested by utilising a Monkhorst-Pack grid [390,391] with varying mesh size, namely 3×3×3, 5×5×5, 7×7×7, 9×9×9, 11×11×11 which are equivalent to a separation of 0.12 $Å^{-1}$, 0.07 $Å^{-1}$, 0.05 $Å^{-1}$, 0.04 $Å^{-1}$ and 0.03 $Å^{-1}$ respectively. These calculations were conducted at 128 GPa and 300 GPa. The DFT simulations were carried out utilising norm conserving pseudopotentials. The geometry optimizations were carried out by employing the BFGS algorithm as this allows for relaxation of both the internal degrees of freedom and the cell parameters. Stringent convergence criteria were employed. These included an energy cut-off of 5.0 x 10^{-6} eV/atom, a maximum force of 0.01 eV/Å, a maximum stress of 0.02 GPa and maximum displacement of 5.0 x 10^{-4} Å.

Most experimental studies on ice X were carried out between 50 GPa and 120 GPa[5,46,47,117,118,139,142,145,146,148,149,152,153,156,392–396]. Within this pressure range, Caracas[120] described the structure of ice X as being ‘disordered’. Caracas[120] further argued that the ordered structure for ice X is obtained at pressures higher than 120 GPa. Raman spectroscopic measurements also suggest that the symmetric hydrogen bonded ice X does not exist below 120 GPa[146]. However, a more recent NMR study has shown that proton ordered ice X should be present at 90 GPa[145]. A phonon dispersion study has

also shown that ice X is stable from 110 GPa (with imaginary phonon frequency being calculated below this pressure) up to a pressure of 420 GPa, with a transition to orthorhombic Pbcm phase being predicted above this pressure[144] while a DFT-PBE study has shown that ice X is formed at 120 GPa [154].

In this study, we are interested in elucidating the mechanical behaviour of ordered ice X, thus, simulations for the mechanical properties were carried out using pressures higher or equal to 150 GPa up to 300 GPa, in increments of 50 GPa using DFT calculations, which pressure range is well within the stability field of ordered ice X (see section 3.3). Having said this, due to the lack of experimental studies for ice X at pressures higher or equal to 150 GPa, preliminary simulation within the pressure range of 98 GPa and 128 GPa were carried out in order to benchmark the methodology used.

The molar cell volume computed in this work in the pressure range of 98 GPa to 128 GPa was compared to the data available in the literature. The molar cell volume, V_m, was calculated by using the following relation:

$$V_m = \frac{N_A V_{cell}}{Z} \qquad \textbf{3.1}$$

where N_A is the Avogadro constant and Z is the number of formula units per unit cell. Ice X has two H_2O molecules per unit cell.

3.2.3 Results and discussion

All functional considered in this work correctly predicted the $Pn\bar{3}m$ cell symmetry of ice X, which symmetry is reported in the literature[118,381]. In order to determine suitable simulation parameters for the ice X system, convergence tests at pressures of 128 GPa and 300 GPa have been carried out. The lattice parameters obtained from each combination of the energy cut-off and the Monkhorst-Pack k-point grid[390,391] tested were compared to those obtained using an energy cut-off of 1200 eV and a Monkhorst-Pack k-point grid with 11×11×11 mesh size. From the results obtained, see Figure 3.1 and Figure 3.2, it may be inferred that the cut-off energy is sufficient at 800 eV, whilst the Brillouin zone sampling, conducted by means of a Monkhorst-Pack grid is sufficient with a mesh size of 5 × 5 × 5 at both 128 GPa and 300 GPa, as further refinements in simulation parameters did not significantly change the lattice parameters obtained. From the results obtained for the lattice parameters, O—H bond length and HOH bond angle, see Table 3.1 and Table 3.2, it can be noted that the functionals assessed, namely PBE[384], PBE-TS[385], PBE-Grimme[386], PBESOL[387], PW91[388], PW91obs[389] mostly give equivalent results.

Table 3.1: A comparison of the lattice parameters as simulated by different GGA functionals, with and without VDW corrections. Note that this data was obtained using a cut-off energy of 1200 eV, a Monkhorst-Pack grid of 11x11x11 and a pressure of 128 GPa.

GGA functional	**a**	**b**	**c**
PBE	2.61	2.61	2.61
PBE GRIMME	2.61	2.61	2.61
PBE TS	2.60	2.60	2.60
PBESOL	2.60	2.60	2.60
PW91	2.61	2.61	2.61
PW91-OBS	2.57	2.57	2.57

Table 3.2: A comparison of the different O—H bond lengths and HOH bond angles calculated utilising different GGA functionals, with and without VDW corrections. Note that this data was obtained using a cut-off energy of 1200 eV, a Monkhorst-Pack grid of 11x11x11 and a pressure of 128 GPa. It can be seen that the different functionals give very similar results.

GGA functional	**O—H bond length**	**HOH bond angle**
PBE	1.13	109.471
PBE GRIMME	1.13	109.471
PBE TS	1.126	109.471
PBESOL	1.127	109.471
PW91	1.13	109.471
PW91-OBS	1.114	109.471

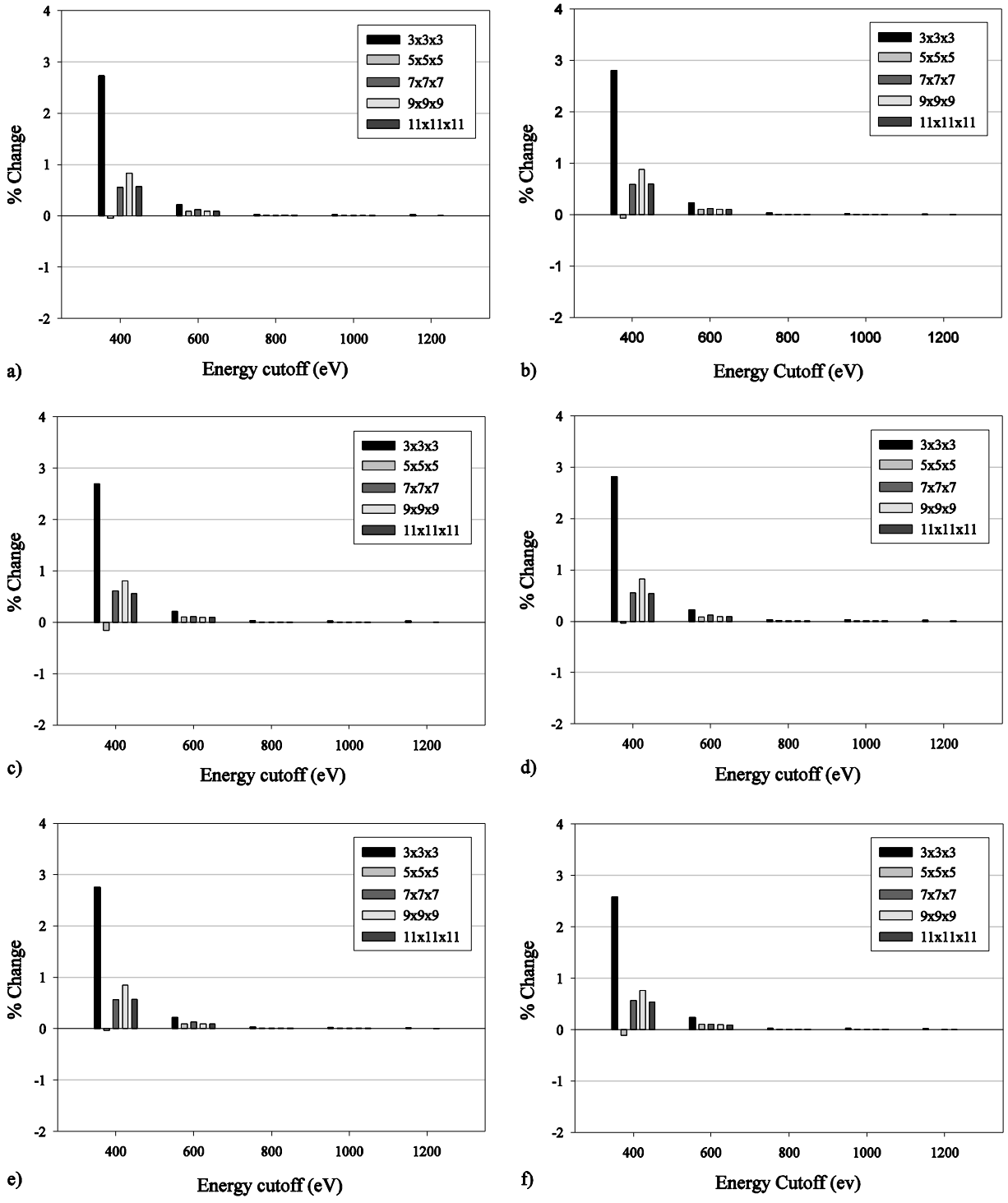

Figure 3.1: The convergence test carried out on ice X, using (a) GGA-PBE (b) GGA-PBE-Grimme (c) GGA-PBE-TS (d) GGA-PBESOL (e) GGA-PW91 and (f) GGA-PW91-OBS when subjected to a hydrostatic pressure of 128 GPa. Note that the Y axis give the percentage deviation from the simulation carried out using a cut-off energy of 1200eV and a Monkhorst-Pack grid of 11x11x11, whilst the legend indicates the Monkhorst-Pack grid used. Percentage change refers to the percentage change in lattice parameters.

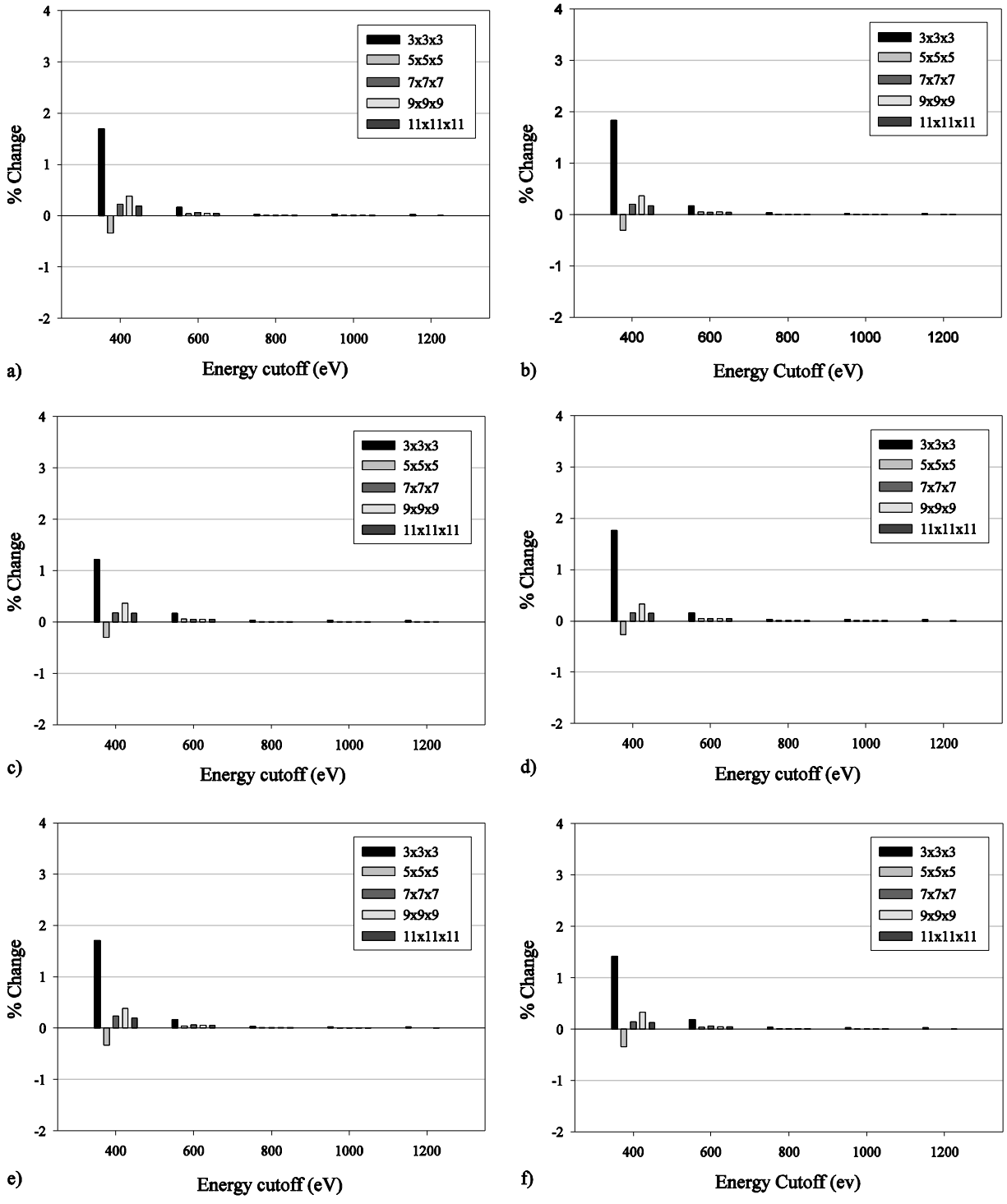

Figure 3.2: The convergence test carried out on ice X, using (a) GGA-PBE (b) GGA-PBE-Grimme (c) GGA-PBE-TS (d) GGA-PBESOL (e) GGA-PW91 and (f) GGA-PW91-OBS when subjected to a hydrostatic pressure of 300 GPa. Note that the Y axis give the percentage deviation from the simulation carried out using a cut-off energy of 1200eV and a Monkhorst-Pack grid of 11x11x11, whilst the legend indicates the Monkhorst-Pack grid used. Percentage change refers to the percentage change in lattice parameters.

In order to benchmark the methodology used, a number of parameters were determined employing the PBE functional and compared to data available in the literature. The molar volume calculated in this work is compared with those obtained in other studies in Table 3.3. The molar volume of ice X obtained from the simulations carried out were 5.65 cm^3 mol^{-1} at 98 GPa, 5.43 cm^3 mol^{-1} at 120 GPa and 5.36 cm^3 mol^{-1} at 128 GPa. These values were comparable with the ones determined experimentally by Hemley and co-workers[156], who determined the molar volume of ice X to be 5.57 ± 0.01 cm^3 mol^{-1} at 98.0 ± 0.7 GPa, 5.33 ± 0.01 cm^3 mol^{-1} at 120.0 ± 1.0 GPa and 5.20 ± 0.01 cm^3 mol^{-1} at 128.0 ± 2.0 GPa. It should be highlighted that the difference between the simulations in this work and the experimentally derived data increased as the reported experimental error increased. Moreover, the results obtained in this study also show very good agreement with other theoretical studies with a deviation of less than 0.8%[130,381].

Table 3.3: Calculated cell volumes at different pressures compared with data available in the literature. It can be seen that the DFT simulations in this work can accurately reproduce experimental [156] *and theoretical work* [130,381].

Pressure (GPa)	**Molar cell volume (cm^3mol^{-1}) (this work)**	**Molar cell volume (cm^3mol^{-1}) (Literature)**	**Percentage difference (%)**
98	5.65	5.57 [156]	1.43
100	5.63	5.66 [130]	-0.558
105	5.58	5.62 [381]	-0.773
120	5.43	5.33 [156]	1.85
128	5.35	5.52 [156]	-3.11

To consolidate the work done, the refractive index determined in this work employing the PBE functional was compared to experimentally determined values available in the literature. The refractive index of the simulated structure at 110.5 GPa and 120.5 GPa were found to be within a maximum deviation of 6×10^{-3} from the experimentally derived values[392], see Table 3.4.

Table 3.4: Comparison of the simulated refractive index and the experimentally determined value at 110.5 GPa and 120.5 GPa [392]. It can be seen that the DFT simulations can accurately reproduce the experimentally determined refractive index with a maximum deviation of 6×10^{-3}.

Pressure (GPa)	**Experimental work (at 630 nm)[392]**	**This work**
110.5	1.880	1.886
120.5	1.882	1.879

Taken together, the verifications of the simulated structure against experimentally derived values suggest that the methodology employed in this study reliably determines the structure and properties of ice X. All the above suggests that the structure and properties of the ice X system can be adequately studied employing the PBE functional. This is in agreement with other theoretical studies[54,120,130,139,144] on ice X.

3.2.4 Conclusion

From the work carried out in this section it was determined that the ice X system can be adequately studied utilising the PBE functional with an energy cut-off of 800 eV and a Monkhorst-Pack grid with a 5 x 5 x 5 mesh. These parameters will used throughout the rest of the study unless otherwise stated.

3.3 Studying the properties of ice X

3.3.1 Introduction

In this section the properties of ice X will be studied in the pressure range of 150 GPa to 300 GPa employing the calculation parameters determined in the previous section. Firstly, the stability of ice X in the pressure range of this study will be assessed through the use of lattice dynamic calculations. This will be followed by determination of the elastic constants of ice X. The mechanical properties of the polycrystalline aggregate and the single crystal will then be studied. Any anomalous mechanical properties will be investigated through the direct measurement of the nanoscale deformation of the ice X system. This work will be consolidated through the use of spectroscopy.

3.3.2 Methodology

Unless specified otherwise, the DFT calculations were carried out employing the PBE functional with an energy cut-off of 800 eV and a Monkhorst-Pack grid with a 5 x 5 x 5 mesh as determined from the work carried out in the previous section. The methodology employed to study the properties of ice X is detailed below.

3.3.2.1 Phonon dispersion

Phonon dispersion curves were calculated at 150 GPa and 300 GPa using the finite displacement method. For this method, a supercell was defined by a cut-off radius of 6.5 Å that is equivalent to a supercell volume of 128 times that of the original unit cell. This represents a circa 4 × 4 × 4 supercell. Convergence for the phonon dispersion curves was also achieved by systematically increasing the energy cut-off, Monkhorst-Pack grid and radius cut-off.

3.3.2.2 Mechanical properties

The elastic constants were determined by utilising the constant-strain method for which a linear stress-strain relationship was achieved. Utilising the calculated stiffness matrix [C], the auxetic potential of ice X together with the direction of maximum auxeticity was determined by calculating and plotting the off-axis Poisson's ratio. This was carried out by employing standard axis transformation techniques[237,397]. This was repeated for all the different hydrostatic pressures considered during this study. The mechanical properties obtained were also verified by using the hybrid functional HSE06[398] and through dispersion-corrected functionals GGA-PBE-TS, GGA-PBE-Grimme. The computed elastic constants were also utilised to calculate the maximum and minimum bounds of Poisson's ratio, bulk and shear moduli for ice X polycrystalline aggregate. The maximum and minimum values of the Poisson's ratio for an isotropic polycrystalline aggregate can be calculated utilising the equations below, which equations assume that the crystal domains in the sample are arranged in such a way that the material is isotropic.

$$\nu^{\max} = \frac{3K^{Voigt} - 2G^{Reuss}}{6K^{Voigt} + 2G^{Reuss}} \qquad \textbf{3.2}$$

$$\nu^{\min} = \frac{3K^{Reuss} - 2G^{Voigt}}{6K^{Reuss} + 2G^{Voigt}} \qquad \textbf{3.3}$$

where K^{Voigt} is greatest possible bulk polycrystalline modulus and G^{Voigt} is greatest possible shear polycrystalline modulus, both moduli being determined utilising the Voigt method [399,400] shown below:

$$K^{Voigt} = \frac{A+2B}{3} \quad \textbf{3.4}$$

$$G^{Voigt} = \frac{A-B+3C}{5} \quad \textbf{3.5}$$

where:

$$A = \frac{1}{3}(c_{11}+c_{22}+c_{33}) \quad \textbf{3.6}$$

$$B = \frac{1}{3}(c_{23}+c_{31}+c_{12}) \quad \textbf{3.7}$$

$$C = \frac{1}{3}(c_{44}+c_{55}+c_{66}) \quad \textbf{3.8}$$

whilst K^{Reuss} is lowest possible polycrystalline bulk modulus and G^{Reuss} is the lowest possible shear modulus, both moduli being determined employing the Reuss method [400,401]

$$K^{Reuss} = \frac{1}{3a+6b} \quad \textbf{3.9}$$

$$G^{Reuss} = \frac{5}{4a-4b+3c} \quad \textbf{3.10}$$

where:

$$a = \frac{1}{3}(s_{11} + s_{22} + s_{33}) \quad \textbf{3.11}$$

$$b = \frac{1}{3}(s_{23} + s_{31} + s_{12}) \quad \textbf{3.12}$$

$$c = \frac{1}{3}(s_{44} + s_{55} + s_{66}) \quad \textbf{3.13}$$

The bulk modulus for ice X polycrystalline aggregate can be calculated using Voigt-Reuss-Hill approximation. For a cubic system the bulk modulus K^{Voigt} is equal to K^{Reuss} with the value of the Voigt-Reuss-Hill average for the bulk modulus being calculated as shown below:

$$K = \frac{1}{2}(K^{Voigt} + K^{\text{Reuss}}) \quad \textbf{3.14}$$

Similarly, the Voigt-Reuss-Hill average for the shear modulus is calculate as shown below:

$$G = \frac{1}{2}(G^{Voigt} + G^{\text{Reuss}}) \quad \textbf{3.15}$$

3.3.2.3 Deformation mechanism

To rationalise the calculated Poisson's ratio, simulations were carried out to deduce the deformation mechanism. The ice X system was subjected to a series of both

positive and negative uniaxial stresses up to 0.5% of the Young's modulus in the direction of maximum auxeticity, i.e. applied at 45° to the z-axis in the (010) plane. The stresses applied were in the form of:

$$\begin{pmatrix} \cos(\zeta) & 0 & -\sin(\zeta) \\ 0 & 1 & 0 \\ \sin(\zeta) & 0 & \cos(\zeta) \end{pmatrix} \begin{pmatrix} 0 & 0 & 0 \\ 0 & 0 & 0 \\ 0 & 0 & \sigma \end{pmatrix} \begin{pmatrix} \cos(\zeta) & 0 & -\sin(\zeta) \\ 0 & 1 & 0 \\ \sin(\zeta) & 0 & \cos(\zeta) \end{pmatrix}^{T}$$

where ζ, the in-plane rotation, was set to 45° in order to load the structure in the direction of maximum auxetic potential. Bond lengths and bond angles were measured in order to elucidate the deformation mechanism as shown in Figure 3.3.

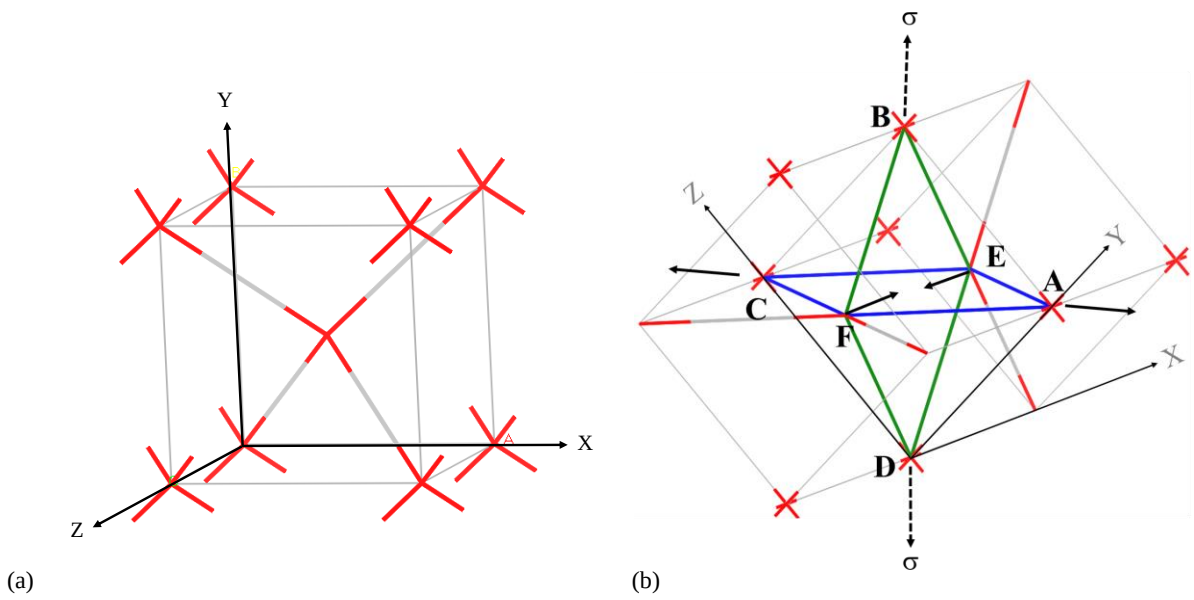

Figure 3.3: (a) The unit cell of ice X illustrating the BCC arrangement of the oxygen atoms (shown in red), where each oxygen atom is covalently bonded to four hydrogen atoms (shown in grey). (b) The structure of ice X showing two adjacent ice X unit cells with two orthogonally interconnected rhombi, BEDF (shown with a green line) and ECFA (shown with a blue line). The applied stress on rhombus BEDF results in an increase in distance CA leading to a negative Poisson's ratio. The stress is being applied at 45° to the [001] direction in the (010) plane.

3.3.2.4 Spectroscopy

In order to consolidate the deformation mechanism, the Raman spectra of ice X in the pressure range of 150-300 GPa at intervals of 50 GPa were calculated as implemented in CASTEP which determines the Raman tensors by utilising a combined DFPT and finite displacement approach. Convergence for the Raman spectra has been also achieved by systematically increasing the energy cut-off and the Monkhorst-Pack grid.

3.3.3 Results and discussion

This work has shown that ice X has the potential to exhibit auxetic behaviour for loading at 45° off-axis in the (100), (010) and (001) planes. Studying the deformation of two orthogonally interconnected rhombi has shown that this predicted negative Poisson's ratio can be attributed to the interplay between distortion and hinging of these rhombi. Moreover, it has been shown that the auxetic potential of ice X increases with an increase in hydrostatic pressure, which behaviour is explained by the rhombi approaching quasi-perfect behaviour resulting in a decrease in the distortion of the rhombi and an increase in hinging mechanism. A detailed discussion of the results obtained is given in the following sections.

3.3.3.1 Dynamic Lattice calculations

In order to further consolidate the simulated ice X structure obtained, lattice dynamics calculations were performed at number of different pressures namely 150 GPa and 300 GPa (see Figure 3.4). The phonons obtained at both pressures were all in the positive region, which indicates that the structure of ice X simulated is stable or metastable at these pressures in accordance with the work conducted by Caracas[120] where static phonon dispersion studies have shown that ice X is stable in the 120-400 GPa pressure range.

To assess that the simulation parameters determined in section 3.2 are suitable to calculate the phonon dispersion relations of ice X, the calculation was repeated by systematically increasing the energy cut-off, Monkhorst-Pack grid and radius cut-off at 300 GPa. The phonon dispersion curves obtained, see Figure 3.5, show that increasing the aforementioned simulation parameters has no effect on the results obtained. This ensures that the phonon dispersion curves obtained are not an artefact of the simulation parameters employed.

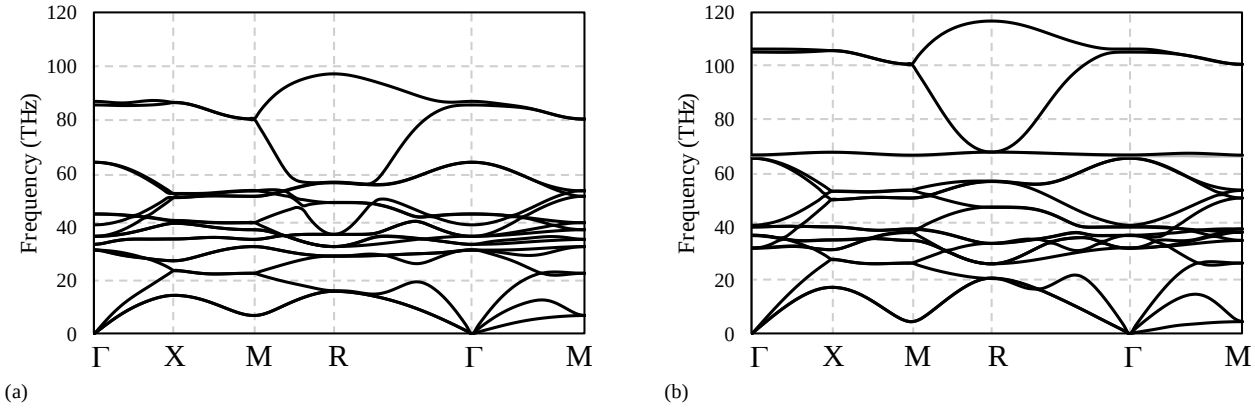

Figure 3.4: Phonon dispersion spectra calculated utilising GGA-PBE functional at different hydrostatic pressures namely (a) 150 GPa and (b) 300 GPa. The absence of imaginary modes shows that the structure of ice X is stable or metastable at both pressures in accordance to Caracas[120].

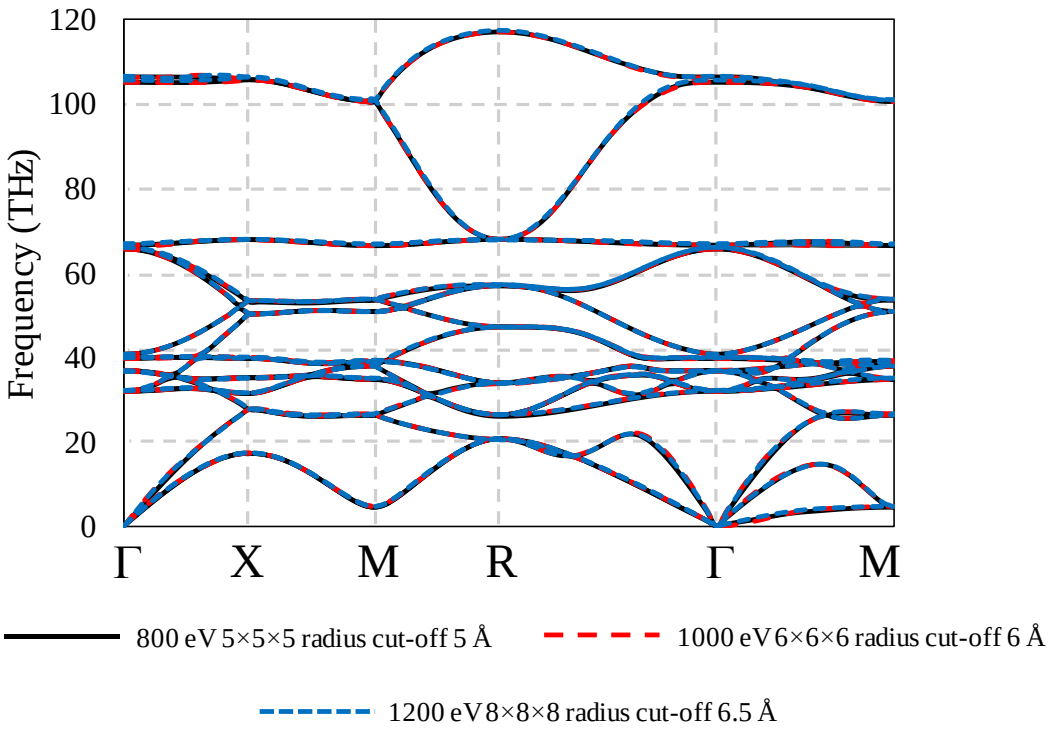

Figure 3.5: Convergence of phonon dispersion curves of ice X at 300 GPa utilising the finite displacement method. It can be seen that an increase in the energy cut-off, Monkhorst-Pack grid and radius cut-off has no effect on the dispersion curve obtained.

3.3.3.2 Elastic constants

The elastics constants of ice X at 150 GPa were then calculated. First of all, it is important to note that the elastic constants obtained from this study are in very good agreement (with a maximum variation of 0.7%) with those derived by Tsuchiya and co-workers[130] who also employed a theoretical approach (see Table 3.5). The stiffness and compliance matrices obtained for ice X show the expected symmetry for a cubic system whereby $c_{11} = c_{22} = c_{33}$, $c_{44} = c_{55} = c_{66}$ and $c_{12}=c_{13}=c_{23}$.

Table 3.5: A comparison of the elastic constants calculated at 150 GPa in this work with those obtained in other theoretical studies[130] at the same hydrostatic pressure where it can be seen that the results obtained are very similar.

Reference	**c_{11} (GPa)**	**c_{12} (GPa)**	**c_{13} (GPa)**	**c_{44} (GPa)**
[130]	751.2	636.3	636.3	441.5
This work	750.25	631.9	631.9	441.5

The mechanical properties obtained from the compliance matrices (see Figure 3.6) show that ice X has the potential of exhibiting a negative Poisson's ratio of around -0.4 at 45° to [100] direction in the (001) plane, at 45° to [010] direction in the (100) plane and at 45° to [001] direction in the (010) plane. An analysis of the shear and Young's modulus also reveals that loading in the direction of maximum auxeticity results in a minimum value for the shear modulus and a maximum value for the Young's modulus, see Figure 3.6. It is very interesting to note that as the hydrostatic pressure is increased, the minimum Poisson's ratio becomes more negative i.e. the auxetic potential of ice X increases with an increase in hydrostatic pressure. At the same time, the maximum positive Poisson's ratio increases to a lesser degree. Similar to the Poisson's ratio, the on-axis shear modulus tends to increase with increasing hydrostatic pressure, while the off-axis shear modulus decreases. On the other hand, as the hydrostatic pressure is increased both the on-axis and off-axis Young's modulus are observed to decreases.

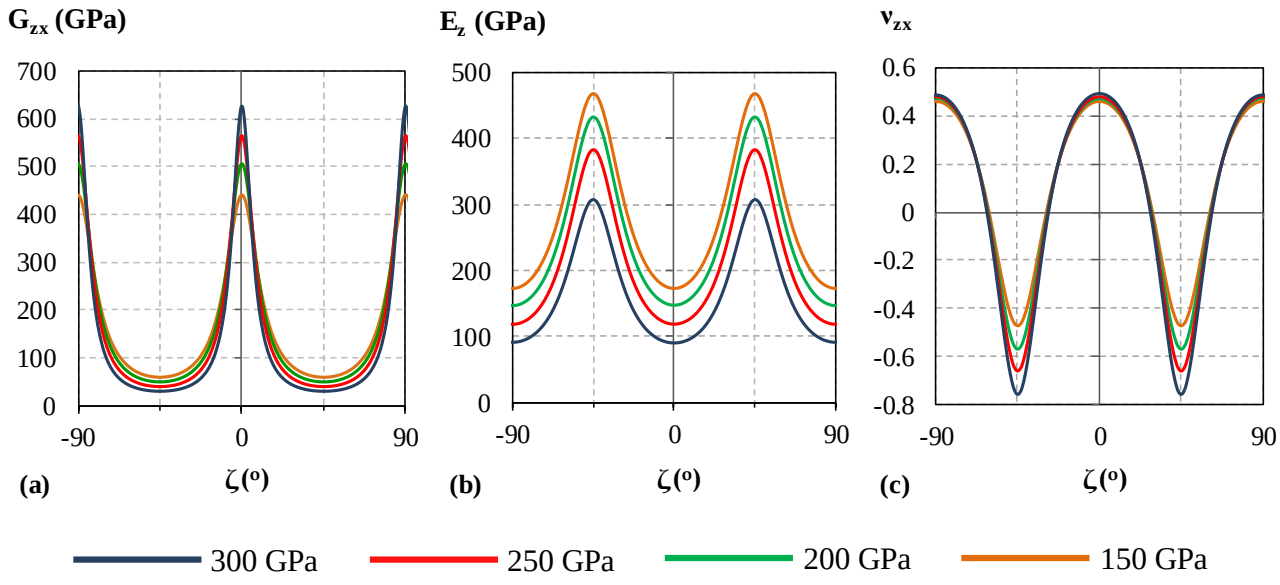

Figure 3.6: The variation of the shear modulus (a), Young's modulus (b) and Poisson's ratio (c) with angle of rotation, ζ, in the (010) plane for ice X at different hydrostatic pressures when simulated utilising GGA-PBE functional. Poisson's ratio is pressure dependant with the auxetic potential of ice X increasing with an increase in hydrostatic pressure.

In order to confirm the simulated mechanical properties of ice X, the elastic constants of this system were simulated utilising the dispersion corrected functionals PBE-TS and PBE-Grimme and the hybrid functional HSE06 at 300 GPa. The mechanical properties derived from the elastic constants are plotted in Figure 3.7. The auxetic potential of ice X is confirmed with all functionals used. In particular, it can be seen that there is very good agreement between the PBE functional used in this study, dispersion corrected functional PBE-TS and the hybrid functional. Therefore, one may infer that the results obtained are not an artefact of the functional being used with the Poisson's ratios obtained through the use of PBE functional, the dispersion corrected functionals and the hybrid functional being very similar. This is further confirmed by simulating mechanical properties of ice X at 150 GPa using the dispersion corrected functionals which are shown in Figure 3.8. The trends in the mechanical properties obtained are similar irrespective of the functional used.

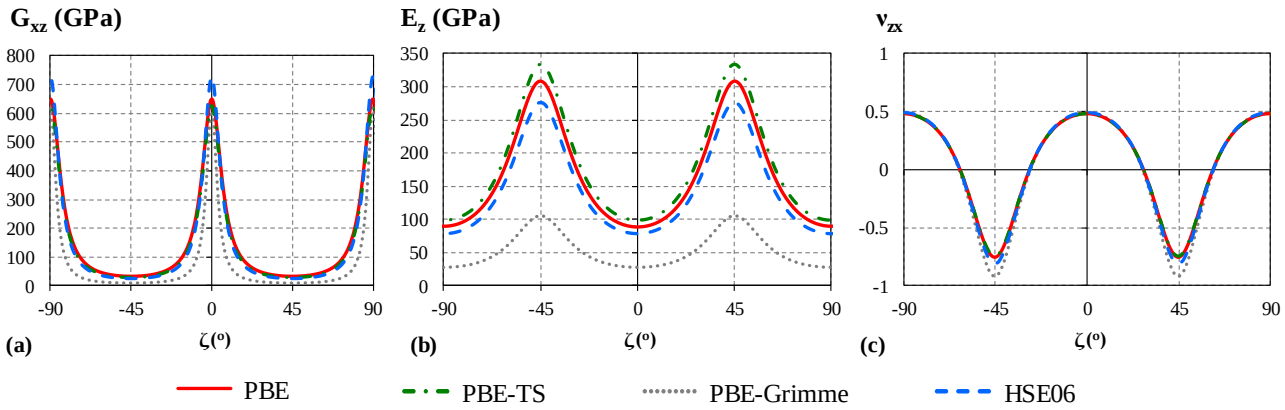

Figure 3.7: The variation of the shear modulus (a), Young's modulus (b) and Poisson's ratio (c) with angle of rotation, ζ, in the (010) plane for ice X at 300 GPa utilising PBE, the dispersion corrected functionals PBE-TS, PBE-Grimme and the hybrid functional HSE06. It can be seen that similar trends are obtained irrespective of the functional used.

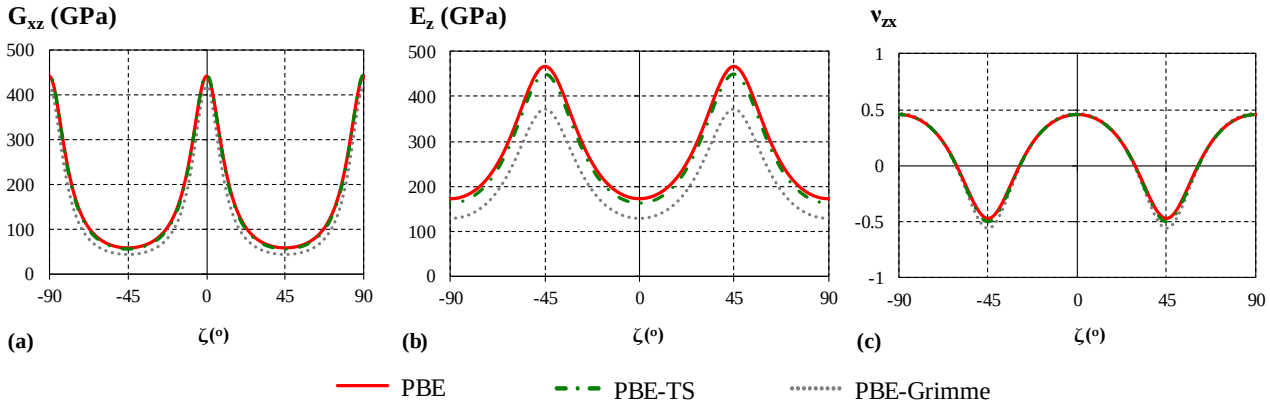

Figure 3.8: The variation of the shear modulus (a), Young's modulus (b) and Poisson's ratio (c) with angle of rotation, ζ, in the (010) plane for ice X at 150 GPa utilising PBE and the dispersion corrected functionals PBE-TS and PBE-Grimme. It can be seen that similar trends are obtained irrespective of the functional used.

3.3.3.3 Polycrystalline properties

The elastic constants of the ice X system may be employed to determine the mechanical properties of the polycrystalline aggregate as detailed in the methodology section. Calculation of the maximum and minimum values of the Poisson's ratio show that the polycrystalline aggregate is expected to exhibit a positive Poisson's ratio in the pressure range of this study, with the value of the Poisson's ratio increasing with an increase in hydrostatic pressure as shown in Table 3.6. This is in sharp contrast to the auxetic behaviour predicted for the ice X single crystal.

Table 3.6: The maximum and minimum bounds of Poisson's ratio for ice X polycrystalline aggregate at various hydrostatic pressures.

Pressure (GPa)	ν^{max}	ν^{min}
150	0.414	0.312
200	0.436	0.324
250	0.453	0.334
300	0.468	0.339

As shown in Table 3.7, an increase in hydrostatic pressure also results in an increase in the value of the bulk and shear modulus of polycrystalline ice X. The K/G ratio, known as the Pugh ratio[402], gives an indication of the ductility or brittleness of a material with a K/G value exceeding 1.75 indicating that the material is ductile. The K/G ratio calculated at 150 GPa is 3.26 illustrating the ductile nature of ice X at this pressure. In addition to this, the DFT simulations have predicted an increase in the K/G ratio with increasing pressure, showing that the ductility of the material increases with pressure.

Table 3.7: The pressure dependence of the maximum and minimum bounds for the bulk moduli ($K^{Reuss} = K^{Voigt}$ denoted by K) and shear moduli for ice X polycrystalline aggregate together with the K/G ratio of the polycrystalline aggregate.*

Pressure (GPa)	K* (GPa)	G^{Voigt} (GPa)	G^{Reuss} (GPa)	G (GPa)	K/G
150	671	289	123	206	3.26
200	812	323	109	216	3.76
250	948	355	91	223	4.25
300	1080	388	71	230	4.70

3.3.3.4 Deformation mechanism

Having established the potential of ice X to exhibit auxetic behaviour, it is important to determine the origins of this behaviour. Baughman et al.[304] showed that most cubic metals can exhibit a negative Poisson's ratio when stretched in the [110] lattice direction and explained this behaviour using a simple geometrical model composed of two orthogonally interconnected rhombi. In the case of ice X, referring to Figure 3.3, the oxygen atoms between two subsequent unit cells may also be seen to form such orthogonally interconnected rhombi. In this case however, the sides of the rhombi are not identical wherein for each rhombus, two sides are composed of O-H-O interactions, whilst the other two sides are composed of O:O non-bond interaction. Hence in the case of ice X a similar mechanism may be responsible for the predicted negative Poisson's ratio. Referring to Figure 3.3 and Figure 3.9, application of a stress (σ) along the direction of maximum auxeticity (at 45° to the [001] direction in the case of Figure 3.3 and Figure 3.9) results in a decrease in the acute angle EBF in the rhombus BEDF. Due to this, bond angle CEA in the rhombus ECFA is geometrically bound to increase,

resulting in an increase in the distance between positions C and A. This increased distance between positions C and A results in the simulated negative Poisson's ratio in the (010) plane. Furthermore, during this deformation, the distance between the oxygen atoms in both rhombi only change to a small degree. Due to the cubic nature of the structure a similar deformation mechanism can be used to explain the predicted negative Poisson's ratios in the (100) and (001) planes. It is important to note that the fact that ice X is achieving its auxeticity through a Baughman-like deformation mechanism confirms the strength of this classical mechanism in generating auxetic behaviour.

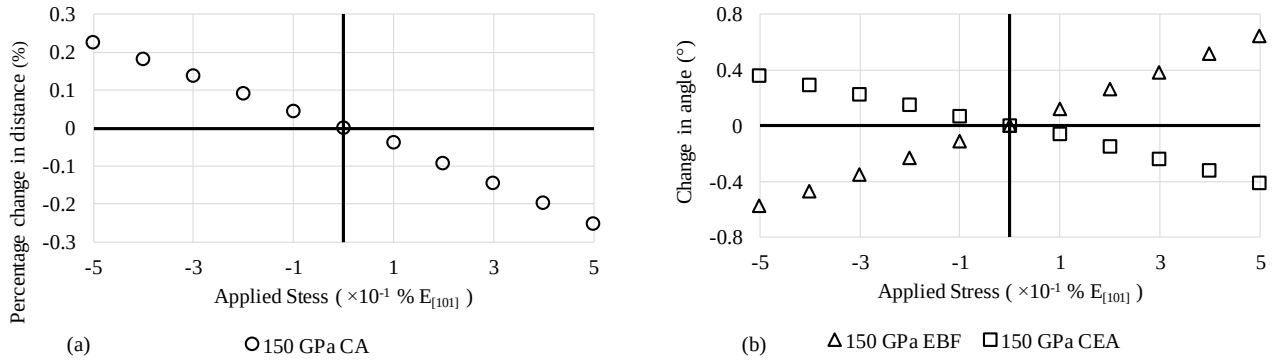

Figure 3.9: (a) The percentage change in distance CA at 150 GPa and (b) the change in bond angles EBF and CEA at 150 GPa.

The mechanical properties of ice X were then studied at higher pressures, up to 300 GPa as detailed in the methodology section. An analysis of how the structure of ice X changes with increasing pressure shows that an increase in pressure is accompanied with a decrease in the O-H bond length and hence a decrease in the O-H-O distances. The O:O distances also decrease to the same extent when the pressure is increased. These are shown in Table 3.8. This can also be shown when taking into consideration the Raman active O-O mode of the non-molecular ice X system whereby the T_{2g} interaction is observed to shift to higher wavenumbers as the pressures is increased as shown in Figure 3.10, with this positive pressure shift is also reported in the literature[5] albeit at lower pressures.

Table 3.8: The variation of O-H bond length and O:O distance with an increase in pressure.

Pressure (GPa)	O-H bond length (Å)	O:O distance (Å)
150	1.118	2.235
200	1.093	2.185
250	1.072	2.144
300	1.055	2.109

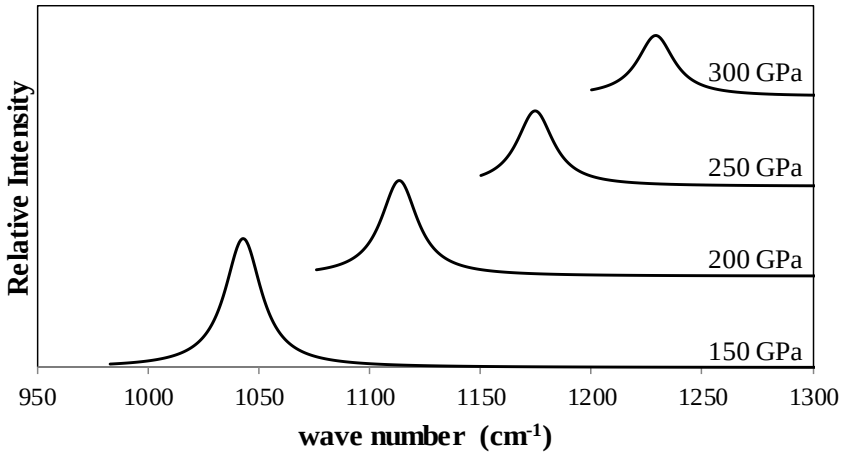

Figure 3.10: The simulated Raman spectra for ice X at pressures ranging from 150 GPa to 300 GPa.

To confirm that the simulation parameters chosen in section 3.2 can adequately determine the Raman spectrum of ice X, the calculation was repeated using more stringent simulation criteria. Referring to Figure 3.11, it can be noted that an increase in cut-off energy and an increase the in mesh of the Monkhorst-Pack grid had no significant effect on the spectrum obtained.

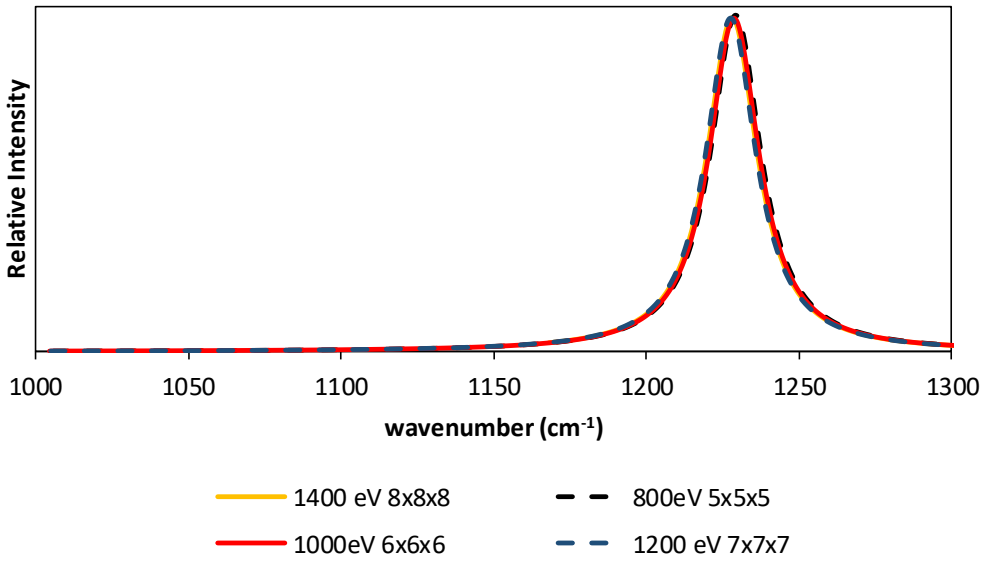

Figure 3.11: Convergence of Raman spectrum for ice X at 300 GPa. It can be seen that convergence is achieved at 800 eV and a Monkhorst-Pack grid with a 5 × 5 × 5 mesh.

The mechanical properties of ice X where then derived at pressures up to 300 GPa. The symmetry of the compliance and stiffness matrices obtained were still representative of a cubic system. In the case of the Poisson's ratio, an increase in hydrostatic pressure produced similar results to those obtained at 150 GPa (see Figure 3.6) in that, the maximum auxeticity is shown at 45° to the [001] direction in the (010) plane.

At this point, it is interesting to re-analyse the deformation mechanism of ice X at different hydrostatic pressures in order to determine what brings about the increase in auxeticity when the hydrostatic pressure is increased. It is known that the auxetic potential of a system may be explained in terms of an interplay between two or more different deformation mechanisms where it is possible that one mechanism leads to a positive Poisson's ratio while another leads to a negative value with the overall value of the Poisson's ratio being a result of the interplay between these mechanisms. Thus, in order to fully rationalise the predicted auxetic potential, the distortion and hinging of the rhombi was studied as a function of pressure.

Taking into consideration the two orthogonally interconnected rhombi, which were deemed to be responsible for the observed negative Poisson's ratio (see Figure 3.3), one notes that in the case of rhombus EDFB, sides EB and ED (O-H-O interactions) always change to a higher degree when compared to a change in length of sides FB and DF (the O:O non-bond interaction), irrespective of the hydrostatic pressure, see Figure 3.12 and Figure 3.13. This means that when a stress is applied, to ice X in the [101] direction, rhombus EDFB tends to distort to form a parallelogram. However, it is important to note that the distortion of rhombus EDFB (as a response to a stress in the [101] direction) becomes smaller as the hydrostatic pressure increases. For example, referring to Figure 3.12, when ice X is loaded in the [101] direction, the rate of change in length of side EB was measured to be 0.0361 %/GPa at a hydrostatic pressure of 150 GPa which decreased to 0.0165 %/GPa when ice X was studied at a hydrostatic pressure of 300 GPa.

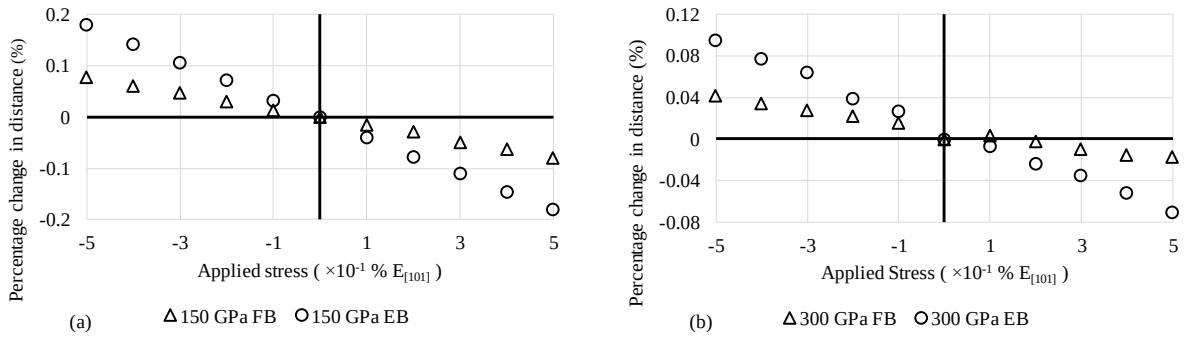

Figure 3.12: A comparison of the change in length of sides EB and FB at 150 GPa (a) and 300 GPa (b) for rhombus EDFB. It can be seen that side EB always changes to a larger extent than side FB. At each pressure, side ED gives an identical plot to that of side EB while side DF gives an identical plot to side FB. Thus, to ensure clarity, sides DF and ED are not shown, these are shown in Figure 3.13.

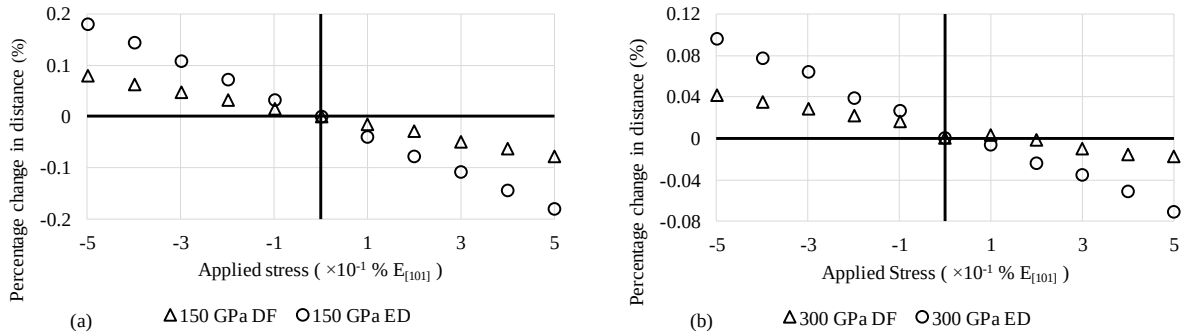

Figure 3.13: A comparison of the percentage change in length of sides ED and DF at 150 GPa (a) and 300 GPa (b). It can be seen that side ED always changes to a larger extent than side DF.

In the case of rhombus EAFC, sides EA and CE do not change appreciably when ice X is loaded in the [101] direction (see Figure 3.14). On the other hand, the rate of change in length of sides FA and FC was found to decrease with an increase in hydrostatic pressure. For instance, the rate of change in side FA was measured to be 0.0203 %/GPa at a hydrostatic pressure of 150 GPa which decreased to 0.0105 %/GPa when ice X was studied at a hydrostatic pressure of 300 GPa, see Figure 3.15. This shows that rhombus EAFC also tends to distort to a higher degree at lower pressures when ice X is loaded in the [101] direction.

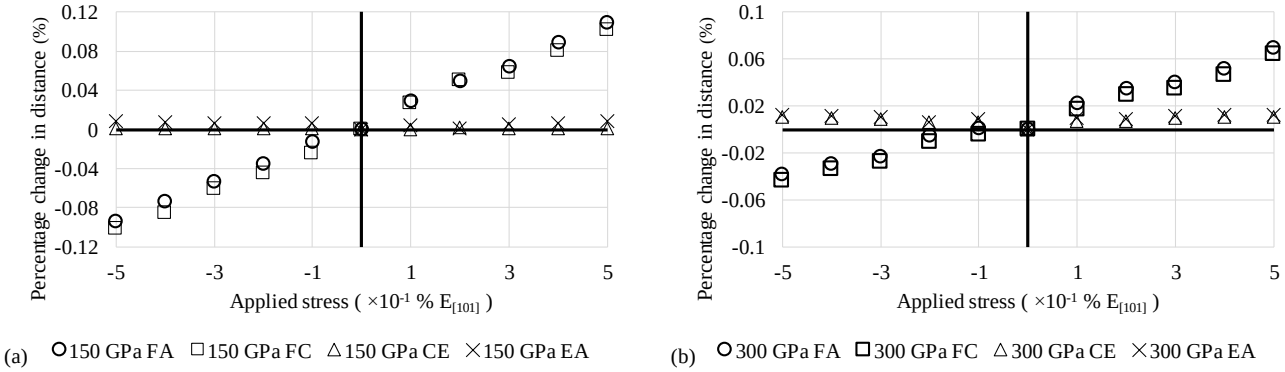

Figure 3.14: A comparison of the percentage change in length of the sides of the rhombus EAFC at 150 GPa (a) and 300 GPa (b). It can be seen that sides EA and CE do not change appreciably when ice X is loaded in the [101] direction.

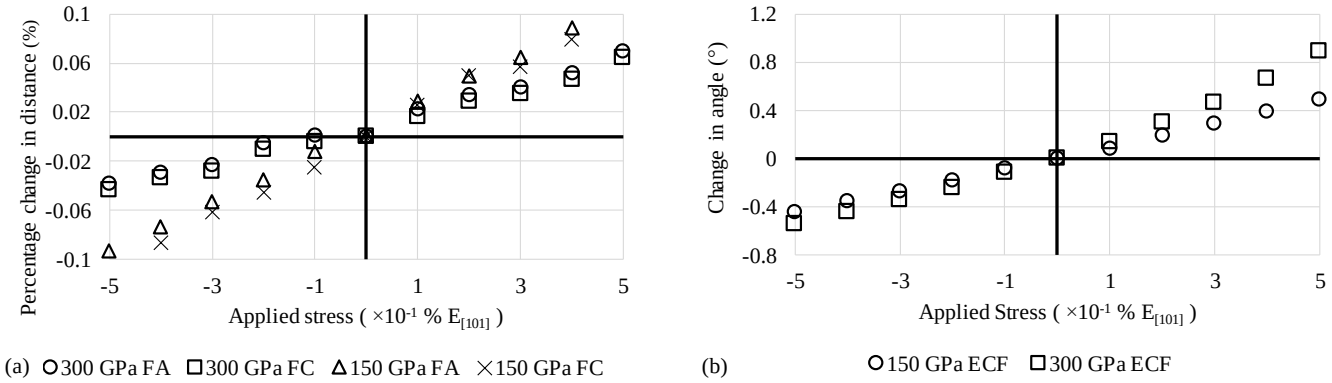

Figure 3.15: (a) Comparison of the percentage change in length of sides FA and FC at 150 GPa and 300 GPa. It can be seen that the percentage change is greater at 150 GPa than at 300 GPa for both FA and FC. It can also be seen that FA and FC exhibit similar percentage change in length. (b) Comparison of the change in bond angle ECF at 150 GPa and 300 GPa. It can be seen that rate of change of angle ECF is greater at 300 GPa than at 150 GPa.

When a stress is applied to ice X, the identified rhombi (see Figure 3.16) undergo distortion due to the fact that the change in length is different for different sides of the rhombi. In rhombus BEDF sides BE and DE increase in length more than sides BF and DF. In the case of rhombus EAFC sides FC and FA decrease in length while EC and EA do not undergo a significant change in length. As the hydrostatic pressure is increased this distortion decreases whilst the hinging of the rhombi increases (see Figure 3.12 and Figure 3.15). This coupled with the observed increase in auxeticity with an increase in hydrostatic pressure indicates that the distortion of the rhombi leads to a decrease in auxeticity.

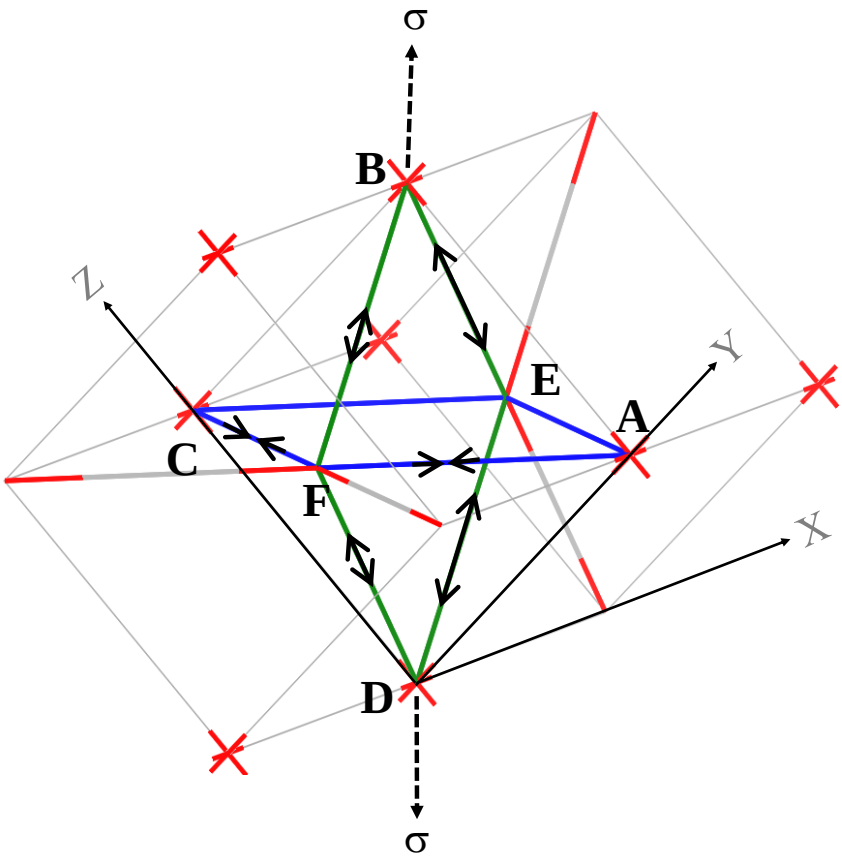

Figure 3.16: A diagrammatic representation of the distortion in the two orthogonally interconnected rhombi, BEDF (shown with a green line) and EAFC (shown with a blue line) when a stress is applied at 45° to the [001] direction in the (010) plane.

When considering the hinging of rhombi EAFC and EDFB one finds out that upon loading uniaxially, the changes in angle increase with an increase in hydrostatic pressure. For example, referring to Figure 3.15, it was found that angle ECF changes at a rate of 0.0933 °/GPa when ice X is loaded in the [101] direction at 150 GPa, whilst the same angle changes a rate of 0.1395 °/GPa when ice X is uniaxially loaded at a hydrostatic pressure of 300 GPa. From the above, it may be deduced that the increase in auxeticity of ice X upon an increase in hydrostatic pressure is due to an increase in hinging of the rhombi and a decreased distortion of the rhombi. Thus, the predicted auxetic behaviour may be attributed to interplay between hinging and distortion of the rhombi with the prevalent mechanism being the hinging mechanism. It may also be inferred that distortion of the rhombi leads to a positive Poisson's ratio while hinging

leads to a negative Poisson's ratio. As pressure is increased the rhombi tend to approach quasi-perfect behaviour with only slight distortion being predicted at higher pressures. The increase in rigidity of the rhombi can also be inferred from Figure 3.10, where an increase in strength of the O-O interaction with increasing pressure is shown by the shift to higher wavenumbers of the T_{2g} interaction. Thus, it may be inferred that the increased auxetic potential on increasing hydrostatic pressure is due to the increased rigidity of the sides of the rhombus while the bond angle becomes easier to change.

3.3.4 Conclusion

This work has shown that ice X has the potential of exhibiting auxetic behaviour at 45° off-axis in all three principle crystallographic planes. Moreover, it has also been shown that Poisson's ratio is pressure dependent with an increase in hydrostatic pressure resulting in an increase in auxetic potential. This behaviour has been rationalised by studying the deformation of two orthogonally interconnected rhombi. It has been shown that these rhombi may undergo hinging and distortion on application of a stress in the direction of maximum auxeticity, with the prevalent mechanism being the hinging mechanism. As the pressure is increased, hinging becomes more prevalent than distortion of the rhombus, with the rhombi approaching quasi-perfect rhombi at higher hydrostatic pressures.

Chapter 4: [*]An investigation of the mechanical properties of ice VIII

4.1 Introduction

The work carried out in the previous chapter has shown that ice X has the potential to exhibit auxetic behaviour. Following this work, it would now be interesting to analyse the properties of another high-pressure polymorph of ice. As discussed in Chapter 2, ice VIII is a high-pressure proton ordered phase of ice which has been the focus of a number of theoretical[96,121–132] and experimental studies[16–18,108,113,117,118,133–137]. Neutron diffraction studies have shown that ice VIII is composed of two interpenetrating hydrogen-bond networks with a body centred tetragonal unit cell, belonging to the $I4_1/amd$ space group[16]. This molecular crystal contains 8 water molecules per unit cell, with all water molecules obeying the ice rules[94].

Ice VIII can be formed from its proton disorder counterpart, ice VII, by decreasing the temperature of the ice VII system below approximately 270 K without employing any dopant[137]. On increasing the hydrostatic pressure, the ice VIII system can undergo a pressure induced phase transition to the macromolecular ice X. Studies on the mechanical properties of this system are rather limited. Recently, theoretical studies employing first principle calculations have been carried out to simulate the elastic constants of ice VIII[130]. In addition to this, some theoretical studies have analysed the bulk modulus of ice VIII[129,134]. Nevertheless,

[*] The contents of this chapter have been published in the peer-reviewed Journal of Physics and Chemistry of Solids: Gambin, D., Vella Wood, M., Grima, J. N. & Gatt, R. Unusual mechanical properties of ice VIII: Auxetic potential in a high pressure polymorph of ice. *J. Phys. Chem. Solids* **169**, 110755 (2022).

detailed studies which have focused on the Poisson's ratio of ice VIII single crystals are lacking.

In view of the above, this work aims to study the mechanical properties of ice VIII and their variation with hydrostatic pressure utilising DFT simulations. In particular, this work will involve a detailed study on the Poisson's ratio of ice VIII single crystal and its pressure dependence. In order to rationalise the Poisson's ratio of ice VIII, its deformation will be studied by utilising direct measurements of bond lengths and bond angles, as well as through the use of spectroscopic techniques. To this end, this chapter will be divided into two sections as carried out in Chapter 3. In the first section the methodology employed will be validated through convergence and benchmarking studies. In the second section the properties of the ice VIII system will be studied, paying particular attention to the Poisson's ratio.

4.2 Convergence and benchmarking study for ice VIII

4.2.1 Introduction

Ice VIII has been the subject of a number of theoretical studies employing DFT simulations[124,127,130,354,403,404]. For example, the structure[403,404], stability[127], mechanical properties[130] and vibrational properties[124,354] of the ice VIII system have been investigated. The theoretical studies carried out on this system have utilised different simulation parameters. Thus, in order to determine suitable simulation parameters for the ice VIII system, convergence tests at pressures of 2.4 GPa and 40 GPa will be carried out. This will be followed by benchmarking of the methodology by comparing the results obtained in this work with those present in the literature.

4.2.2 Methodology

The experimental crystal structures of ice VIII as obtained from the literature[16] was constructed within the CASTEP [382] modelling platform as implemented in Materials Studio. The crystal lattice was aligned in such a way that the *c* crystal direction was parallel to the global *z*-axis while the *b* crystal direction was aligned in the global *yz*-plane and no constraints were imposed on the *a* crystal direction. All simulations were carried out employing density functional theory (DFT) [405,406] utilising full periodic boundary conditions on a 1 × 1 × 1 unit cell.

Geometry optimisation of the ice VIII crystal structure was carried out by firstly setting the $I4_1/amd$ symmetry of ice VIII to P1 in order to remove symmetry constraints on the system, apart from those imposed by the unit cell itself, during the minimisation process. This has the benefit of allowing all the elements within the cell to act independently albeit resulting in an increased simulation time. The performance of a number of GGA functionals namely PBE[384], PBE-TS[385], PBE-Grimme[386], PBESOL[387], PW91[388] and PW91obs[389], was tested in order to determine the appropriate cut-off energy and separation for the Monkhorst-Pack grid.

This was achieved by carrying out geometry optimisation of the ice VIII system at 2.4 GPa and 40 GPa while systematically increasing the cut-off energy from 400 eV to 1200 eV and decreasing the spacing for the Monkhorst-Pack grid from 0.08 $Å^{-1}$ to 0.02 $Å^{-1}$ whilst checking if these changes had a significant effect on the structural parameters obtained. This was carried out at 2.4 GPa and 40 GPa. The structural parameters assessed were the lattice parameters, the O-H bond length, the length of the O-H:O interaction (lengths O3-O2 and O1-O2 in Figure 4.1) and the angle of the O-H:O:H-O interaction (angle O1-O2-O3 in Figure 4.1).

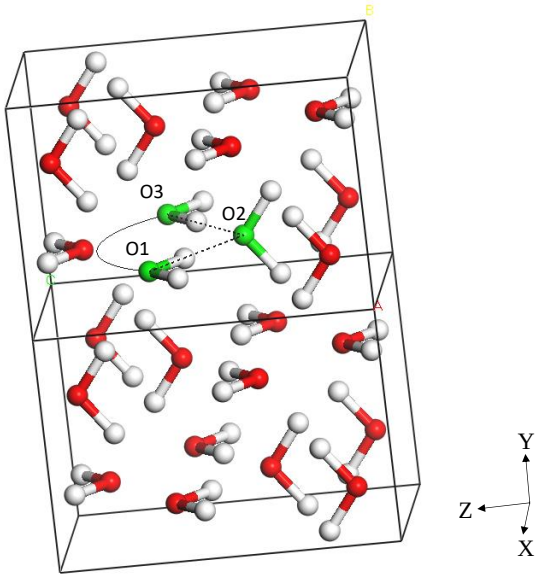

Figure 4.1: An illustration of the ice VIII structure. The O-H:O:H-O angle is illustrated above as O1-O2-O3 while the O-H:O length is shown as O1-O2 (or O2-O3). The hydrogen atoms are shown in white while the oxygen atoms are shown in red. The oxygen atoms denoted as O1, O2 and O3 are shown in green in order to facilitate viewing.

The DFT calculations were carried out employing norm conserving pseudopotentials and an SCF tolerance of 5 x10^{-7} eV/atom. Geometry optimisation was carried out utilising the Broyden-Fletcher-Goldfarb-Shanno (BFGS) algorithm employing the line search method. This algorithm allows for relaxation of both the cell parameters and the internal degrees of freedom. Stringent convergence criteria were utilised including a maximum force of 0.01 eV/Å, an energy cut-off of 5.0 ×10^{-6} eV/atom, a maximum stress of 0.02 GPa and maximum displacement of 5.0 ×10^{-4} Å.

Following the determination of the appropriate simulation parameters, the methodology employed was benchmarked by comparing the structural properties obtained with experimental data available in the literature. The structural properties assessed were the lattice parameters, cell volumes, and various lengths and angles as available in the literature.

4.2.3 Results and discussion

Although GGA functionals have been used in a number of different studies involving the properties of ice VIII[124,127,130,354,403,404], a convergence study and benchmarking of the methodology using different functionals has been conducted in order to ensure that the simulation parameters employed in this work can adequately represent the ice VIII system. Convergence testing was carried out at 2.4 GPa and 40 GPa utilising a number of different GGA functionals namely PBE[384], PBE-TS[385], PBE-Grimme[386], PBESOL[387], PW91[388] and PW91obs[389]. The cell symmetry obtained from all the simulations carried out, $I4_1/amd$, coincides with that present in the literature [16].

The results obtained for the convergence testing of the lattice parameters are summarised in Figure 4.2 to Figure 4.7. In particular, Figure 4.3 and Figure 4.6 show the effect of the cut-off energy and the spacing for the Monkhorst-Pack grid on the a/b ratio, which for ice VIII (a tetragonal system) is expected to be 1. It can be seen that an a/b value of 1 is obtained for most simulations carried out for both hydrostatic pressures utilised expect for some instances where a lower energy cut-off was been used (see Figure 4.3 and Figure 4.3b).

The *a*-lattice parameter and c-lattice parameter obtained from each combination of the energy cut-off and the Monkhorst-Pack k-point grid tested were compared to those obtained using an energy cut-off of 1200 eV and a Monkhorst-Pack k-point grid spacing of 0.02 $Å^{-1}$. Referring to Figure 4.2, Figure 4.4, Figure 4.5 and Figure 4.7 it can be inferred that when considering the lattice parameters, a cut-off energy of 1000 eV and a spacing for Monkhorst-Pack grid 0.03 $Å^{-1}$ can be used to adequately simulate the ice VIII structure at 2.4 GPa and 40 GPa as a further increase in the cut-off energy and decrease in the Monkhorst-Pack grid had no significant effect on the results obtained and hence convergence has been achieved.

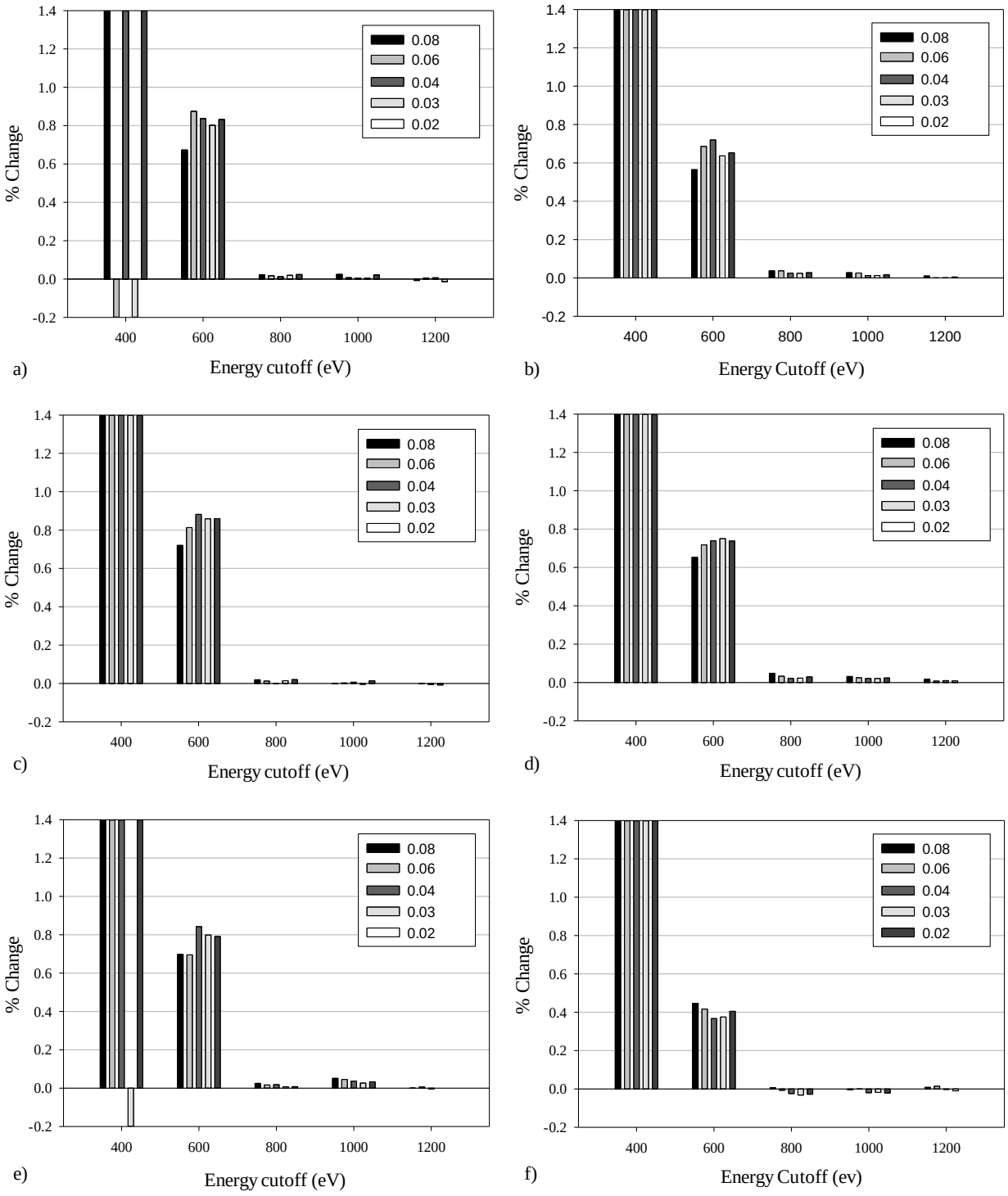

Figure 4.2: The convergence test carried out on ice VIII for the a-lattice parameter, using (a) GGA-PBE (b) GGA-PBE-Grimme (c) GGA-PBE-TS (d) GGA-PBESOL (e) GGA-PW91 and (f) GGA-PW91-OBS when subjected to a hydrostatic pressure of 2.4 GPa. Note that the Y axis give the percentage deviation for the a-lattice parameter when compared to the a-parameter obtained when the simulation is carried out using a cut-off energy of 1200 eV and a spacing of 0.02 Å^{-1} for the Monkhorst-Pack grid, whilst the legend indicates the spacing used (in Å^{-1}) for the Monkhorst-Pack grid. The scale of the graph is truncated to 1.4 and -0.2.

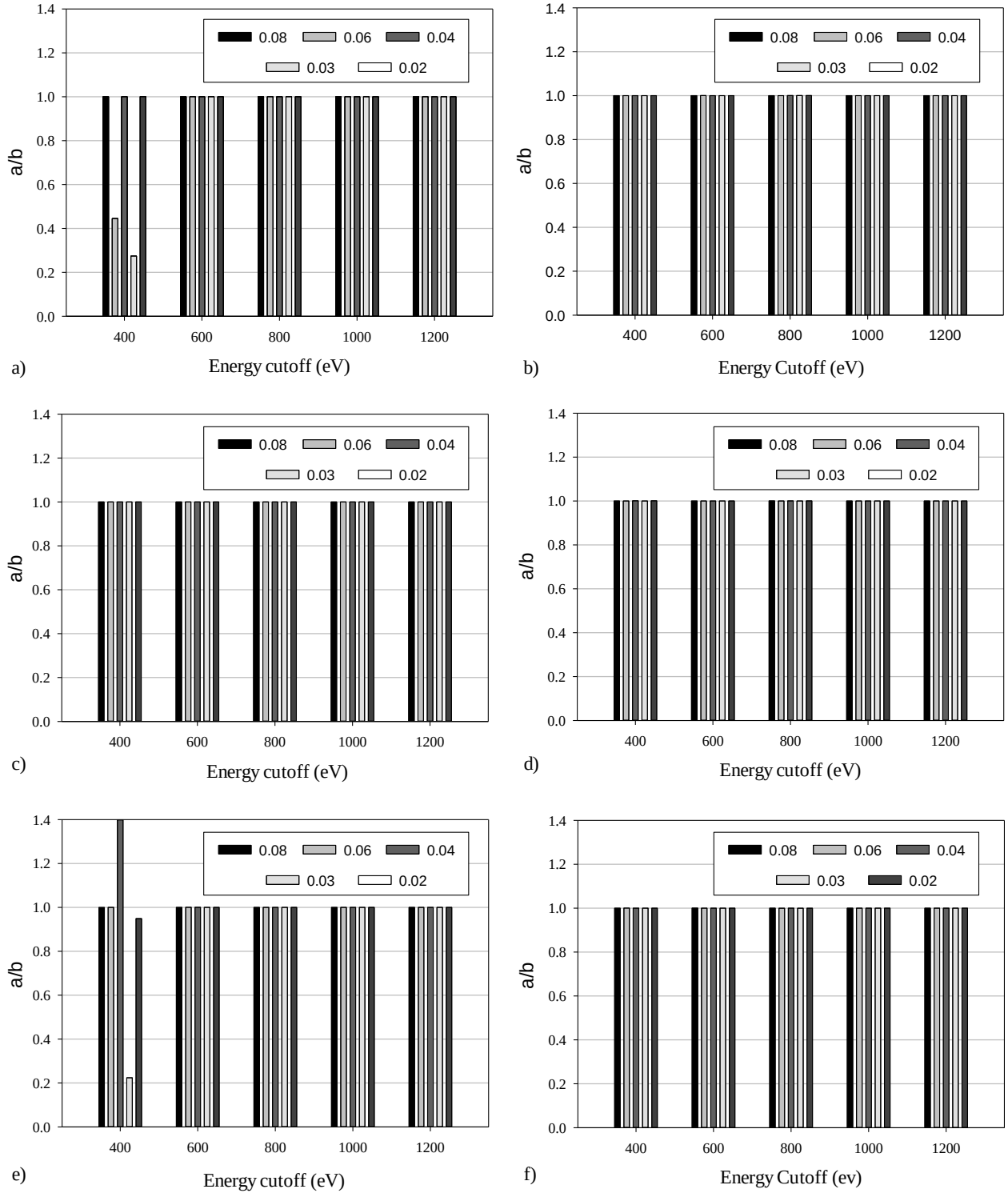

Figure 4.3: The convergence test carried out on ice VIII for the ratio of a/b lattice parameters, using (a) GGA-PBE (b) GGA-PBE-Grimme (c) GGA-PBE-TS (d) GGA-PBESOL (e) GGA-PW91 and (f) GGA-PW91-OBS when subjected to a hydrostatic pressure of 2.4 GPa. Since ice VIII is a tetragonal system, a=b and hence the a/b ratio should be equal to 1. The legend indicates the spacing used (in $Å^{-1}$) for the Monkhorst-Pack grid.

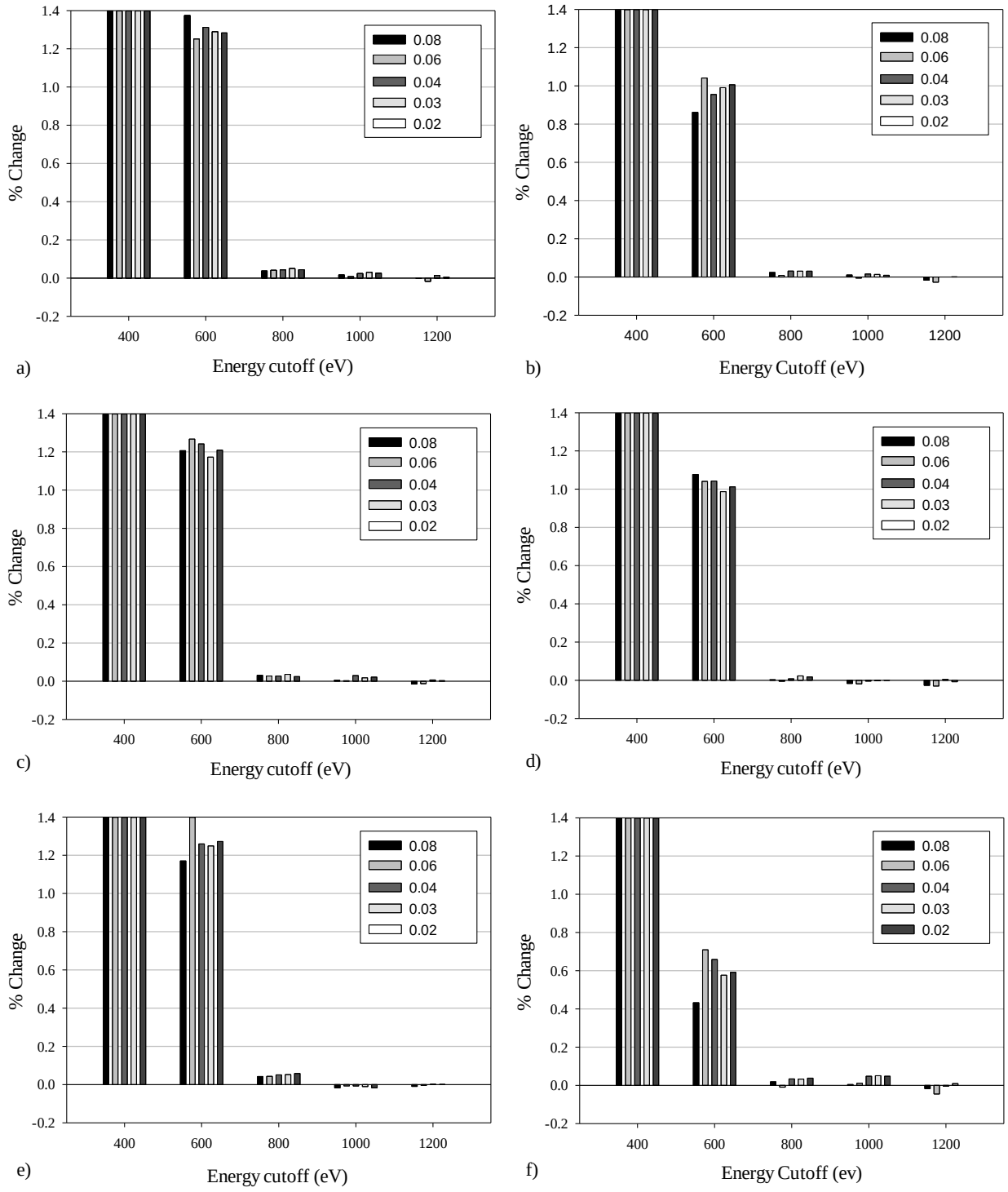

Figure 4.4: The convergence test carried out on ice VIII for the c-lattice parameter, using (a) GGA-PBE (b) GGA-PBE-Grimme (c) GGA-PBE-TS (d) GGA-PBESOL (e) GGA-PW91 and (f) GGA-PW91-OBS when subjected to a hydrostatic pressure of 2.4 GPa. Note that the Y axis give the percentage deviation for the c-lattice parameter when compared to the c-parameter obtained when the simulation is carried out using a cut-off energy of 1200 eV and a spacing of 0.02 $Å^{-1}$ for the Monkhorst-Pack grid, whilst the legend indicates the spacing used (in $Å^{-1}$) for the Monkhorst-Pack grid. The scale of the graph is truncated to 1.4.

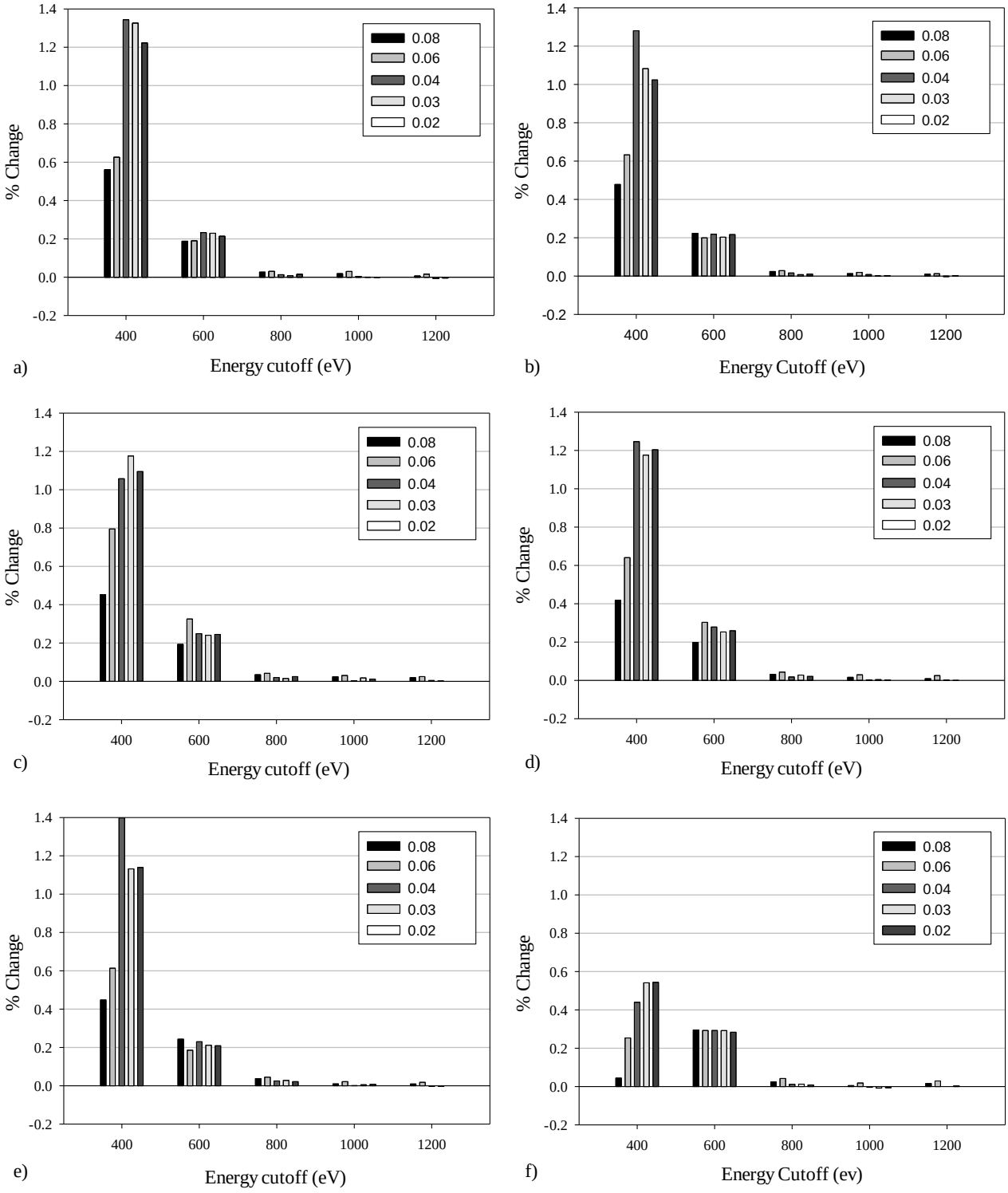

Figure 4.5: The convergence test carried out on ice VIII for the a-lattice parameter, using (a) GGA-PBE (b) GGA-PBE-Grimme (c) GGA-PBE-TS (d) GGA-PBESOL (e) GGA-PW91 and (f) GGA-PW91-OBS when subjected to a hydrostatic pressure of 40 GPa. Note that the Y axis give the percentage deviation for the a-lattice parameter when compared to the a-parameter obtained when the simulation is carried out using a cut-off energy of 1200 eV and a spacing of 0.02 Å^{-1} for the Monkhorst-Pack grid, whilst the legend indicates the spacing used (in Å^{-1}) for the Monkhorst-Pack grid. The scale of the graph is truncated to 1.4.

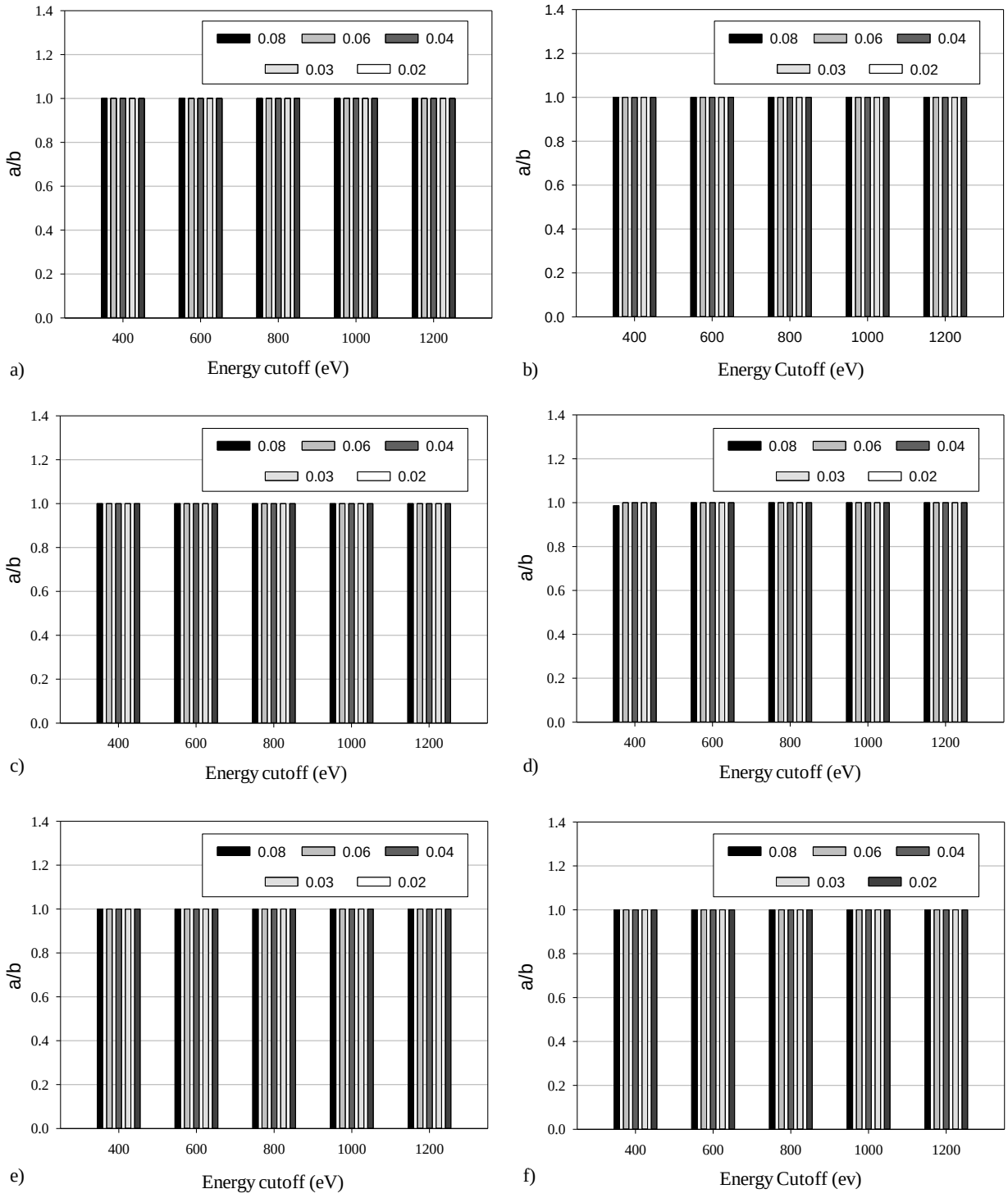

Figure 4.6: The convergence test carried out on ice VIII for the ratio of a/b lattice parameters, using (a) GGA-PBE (b) GGA-PBE-Grimme (c) GGA-PBE-TS (d) GGA-PBESOL (e) GGA-PW91 and (f) GGA-PW91-OBS when subjected to a hydrostatic pressure of 40 GPa. Since ice VIII is a tetragonal system, a=b and hence the a/b ratio should be equal to 1. The legend indicates the spacing used (in $Å^{-1}$) for the Monkhorst-Pack grid.

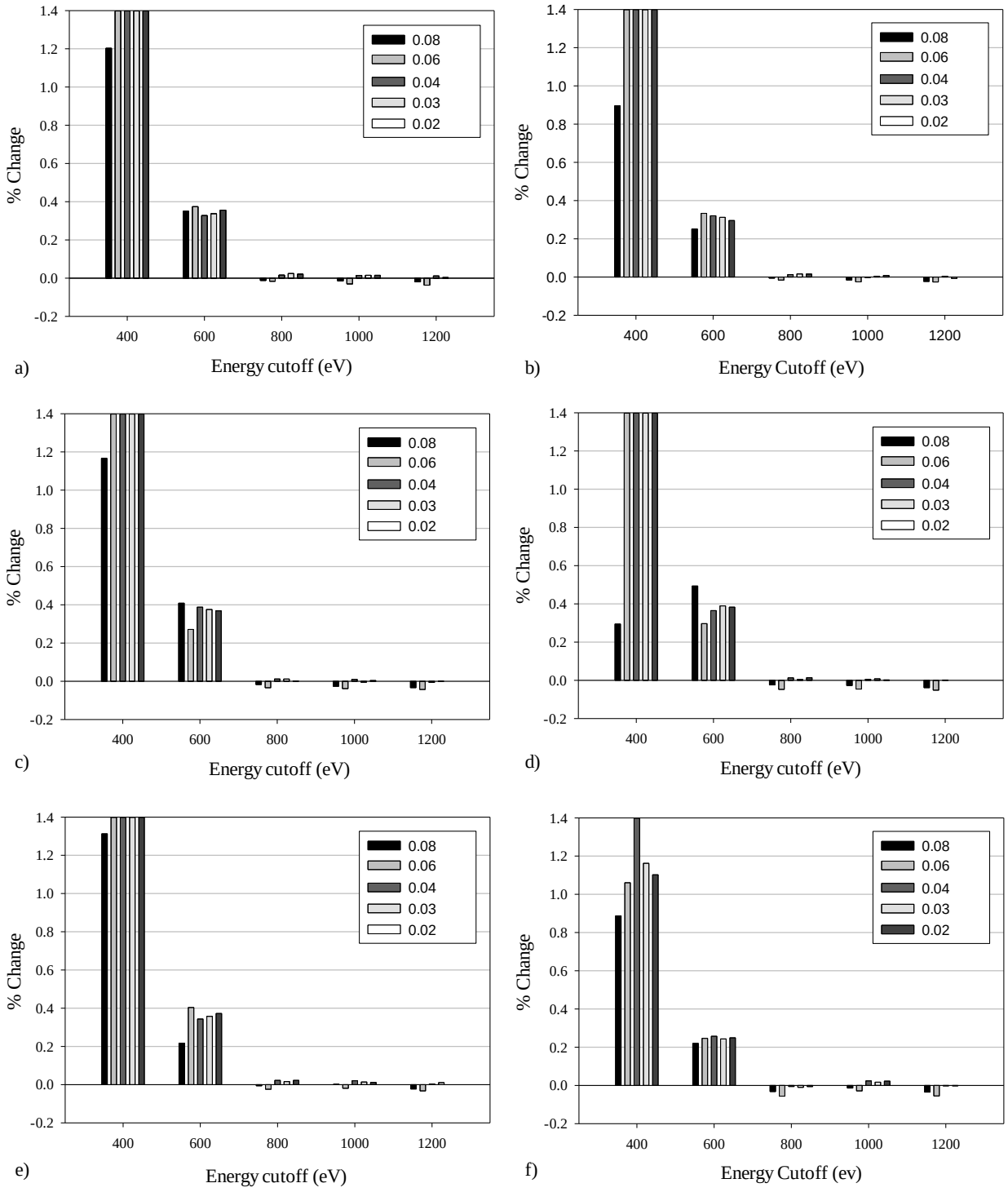

Figure 4.7: The convergence test carried out on ice VIII for the c-lattice parameter, using (a) GGA-PBE (b) GGA-PBE-Grimme (c) GGA-PBE-TS (d) GGA-PBESOL (e) GGA-PW91 and (f) GGA-PW91-OBS when subjected to a hydrostatic pressure of 40 GPa. Note that the Y axis give the percentage deviation for the c-lattice parameter when compared to the c-parameter obtained when the simulation is carried out using a cut-off energy of 1200 eV and a spacing of 0.02 Å^{-1} for the Monkhorst-Pack grid, whilst the legend indicates the spacing used (in Å^{-1}) for the Monkhorst-Pack grid. The scale of the graph is truncated to 1.4.

In order to consolidate the fact that the simulation parameters chosen are enough to correctly represent the structure of ice VIII, the effect of systematically increasing the energy cut-off and decreasing the spacing of the Monkhorst-Pack grid, on various bonded and non-bonded interactions as predicted for ice VIII at 2.4 GPa and 40 GPa was examined. The O-H bond length, the length of the O-H:O interaction (lengths O3-O2 and O1-O2 in Figure 4.1) and the angle of the O-H:O:H-O interaction (angle O1-O2-O3 in Figure 4.1) were investigated. The results obtained for convergence testing of these parameters at 2.4 GPa and 40 GPa are shown in Figure 4.8 to Figure 4.13. These results confirm that an energy cut-off of 1000 eV and a Monkhorst-Pack grid with a 0.03 $Å^{-1}$ spacing is enough to represent the structure of ice VIII accurately as a further refinement in the simulation parameters had no significant effect on the structural parameters obtained.

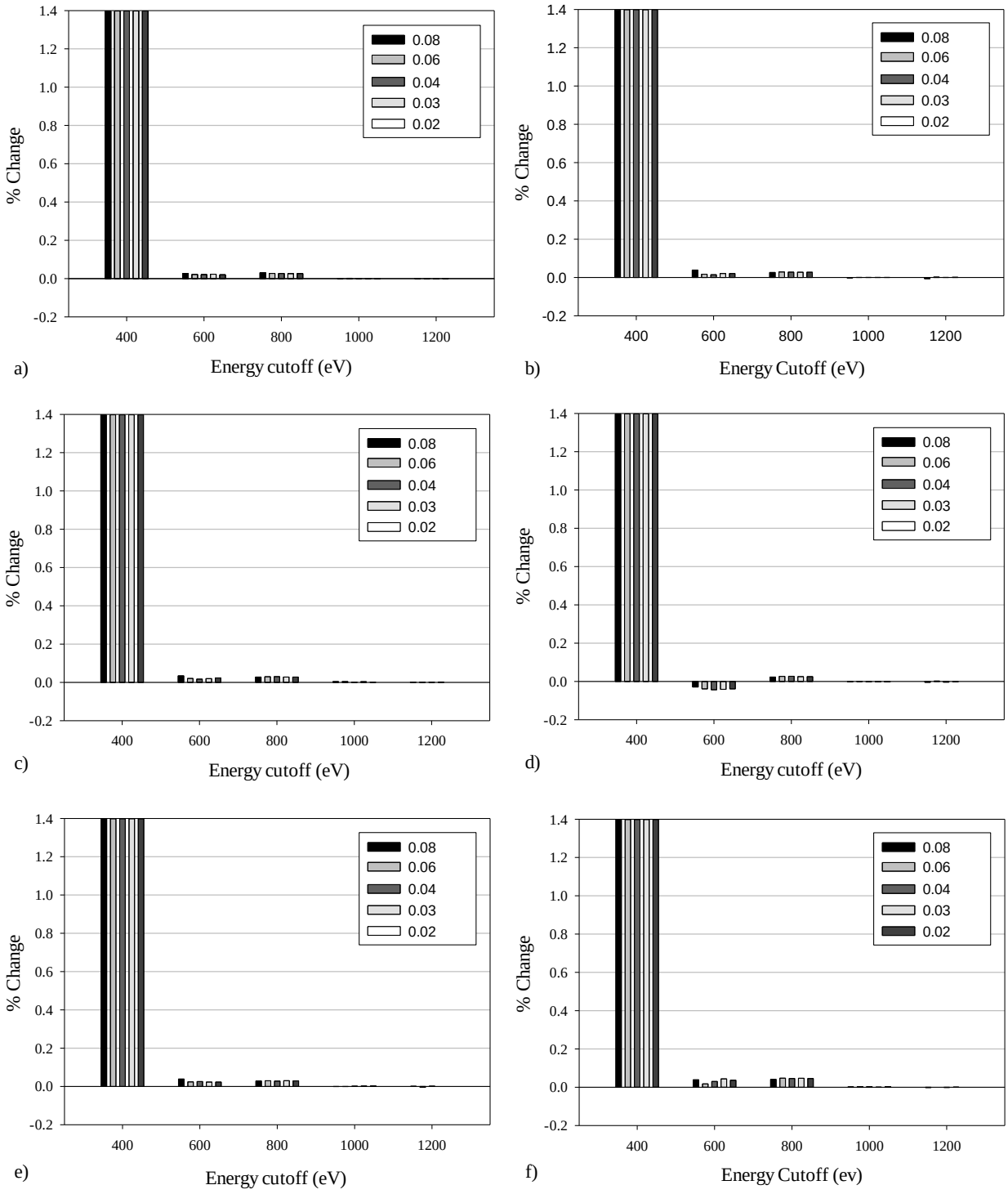

Figure 4.8: The convergence test carried out on ice VIII for the O-H bond length, using (a) GGA-PBE (b) GGA-PBE-Grimme (c) GGA-PBE-TS (d) GGA-PBESOL (e) GGA-PW91 and (f) GGA-PW91-OBS when subjected to a hydrostatic pressure of 2.4 GPa. Note that the Y axis give the percentage deviation for the O-H bond length when compared to the O-H bond length obtained when the simulation is carried out using a cut-off energy of 1200 eV and a spacing of 0.02 Å^{-1} for the Monkhorst-Pack grid, whilst the legend indicates the spacing used (in Å^{-1}) for the Monkhorst-Pack grid. The scale of the graph is truncated to 1.4.

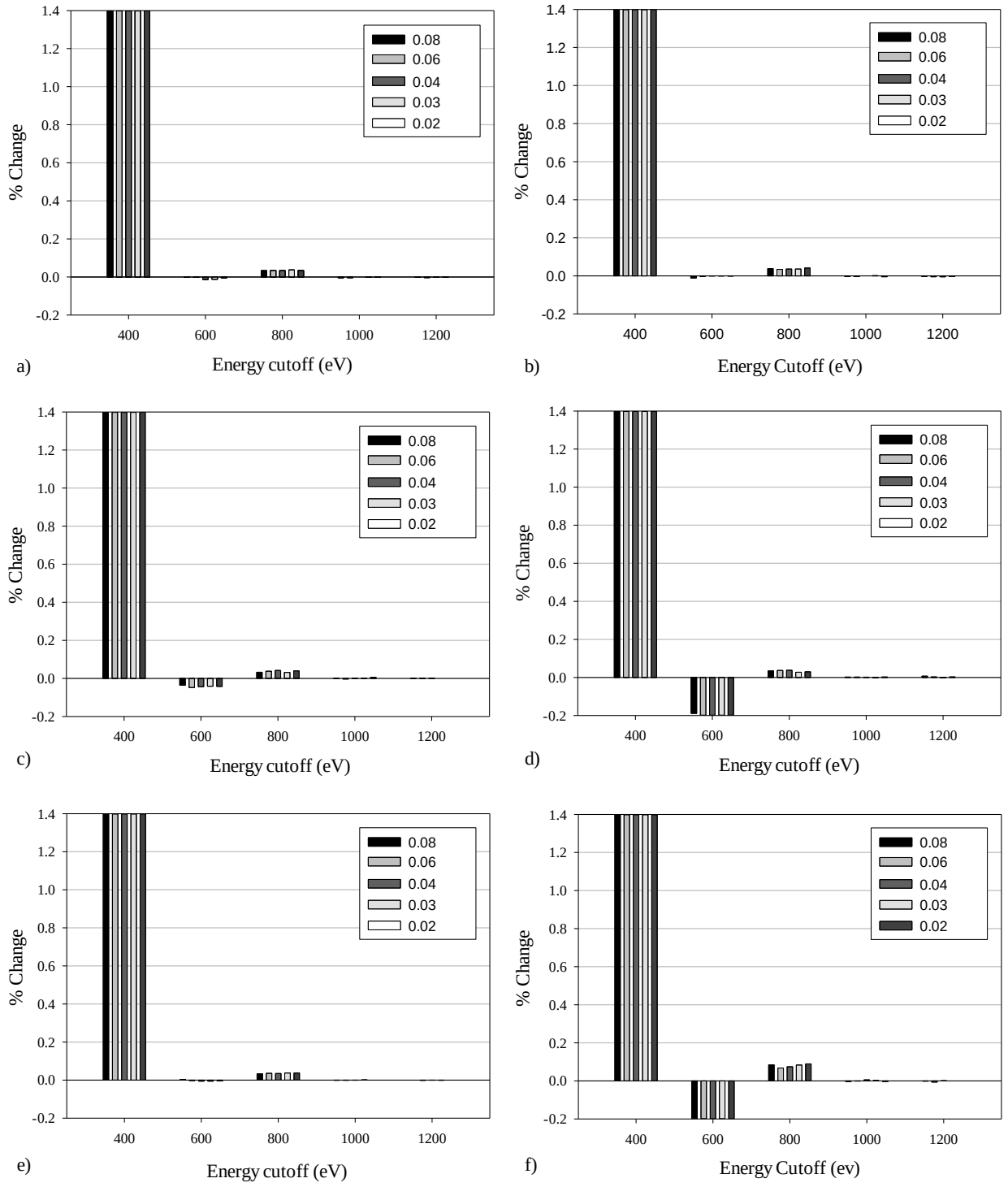

Figure 4.9: The convergence test carried out on ice VIII for the O-H bond length, using (a) GGA-PBE (b) GGA-PBE-Grimme (c) GGA-PBE-TS (d) GGA-PBESOL (e) GGA-PW91 and (f) GGA-PW91-OBS when subjected to a hydrostatic pressure of 40 GPa. Note that the Y axis give the percentage deviation for the O-H bond length when compared to the O-H bond length obtained when the simulation is carried out using a cut-off energy of 1200 eV and a spacing of 0.02 Å^{-1} for the Monkhorst-Pack grid, whilst the legend indicates the spacing used (in Å^{-1}) for the Monkhorst-Pack grid. The scale of the graph is truncated to 1.4 and -0.2.

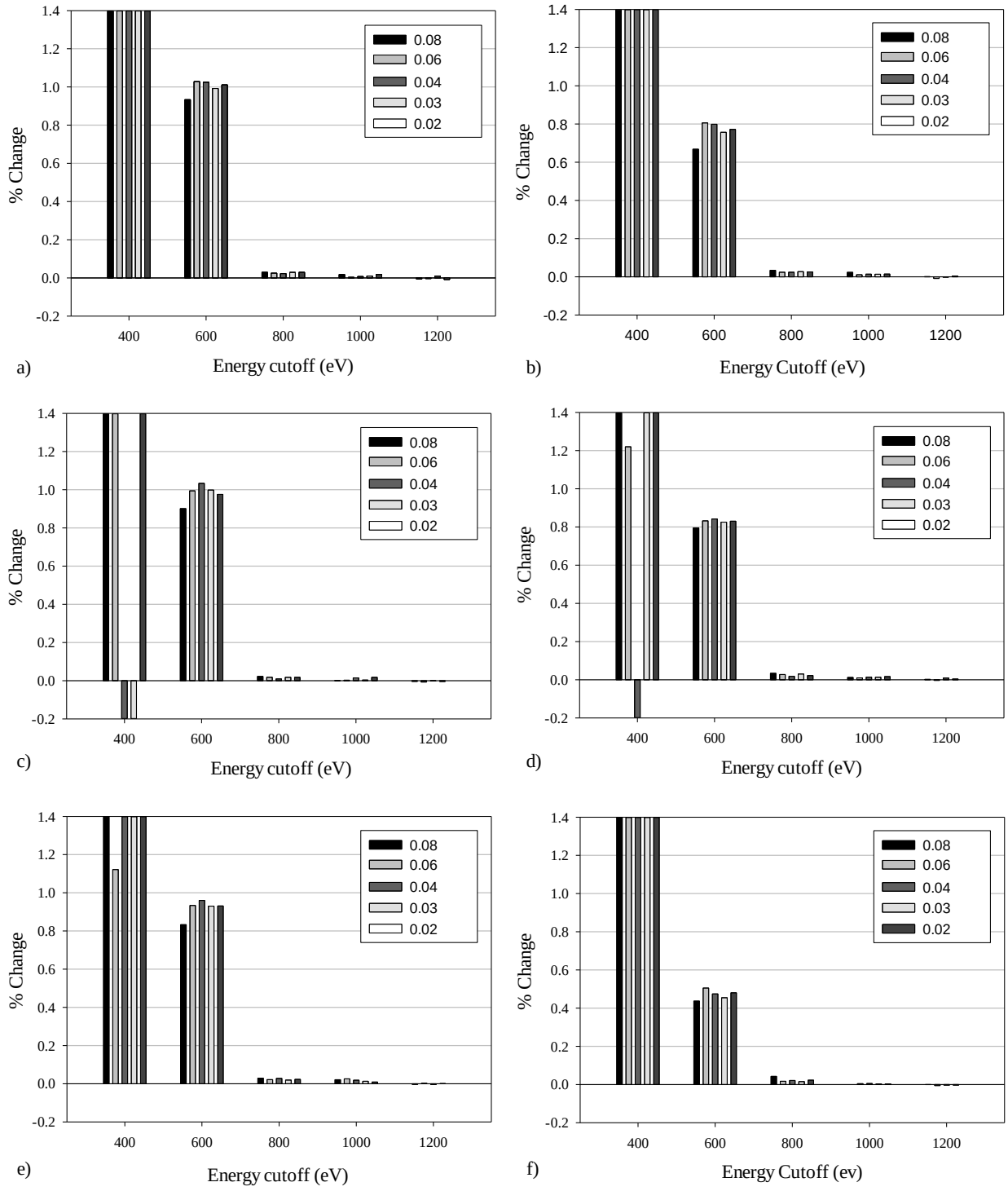

Figure 4.10: The convergence test carried out on ice VIII for the O-H:O length, using (a) GGA-PBE (b) GGA-PBE-Grimme (c) GGA-PBE-TS (d) GGA-PBESOL (e) GGA-PW91 and (f) GGA-PW91-OBS when subjected to a hydrostatic pressure of 2.4 GPa. Note that the Y axis give the percentage deviation for the O-H:O length when compared to the O-H:O length obtained when the simulation is carried out using a cut-off energy of 1200 eV and a spacing of 0.02 $Å^{-1}$ for the Monkhorst-Pack grid, whilst the legend indicates the spacing used (in $Å^{-1}$) for the Monkhorst-Pack grid. The scale of the graph is truncated to 1.4 and -0.2.

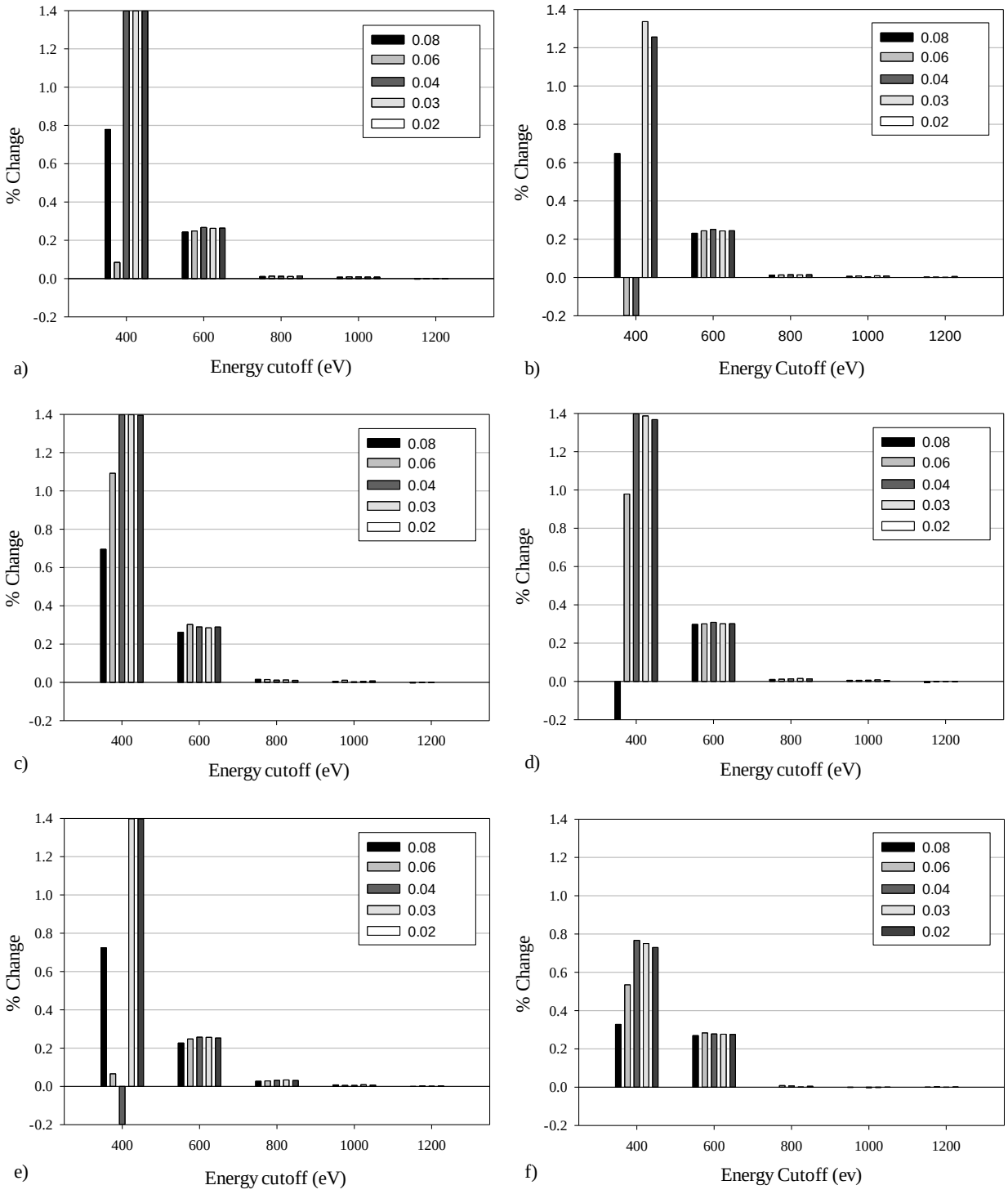

Figure 4.11: The convergence test carried out on ice VIII for the O-H:O length, using (a) GGA-PBE (b) GGA-PBE-Grimme (c) GGA-PBE-TS (d) GGA-PBESOL (e) GGA-PW91 and (f) GGA-PW91-OBS when subjected to a hydrostatic pressure of 40 GPa. Note that the Y axis give the percentage deviation for the O-H:O length when compared to the O-H:O length obtained when the simulation is carried out using a cut-off energy of 1200 eV and a spacing of 0.02 $Å^{-1}$ for the Monkhorst-Pack grid, whilst the legend indicates the spacing used (in $Å^{-1}$) for the Monkhorst-Pack grid. The scale of the graph is truncated to 1.4 and -0.2.

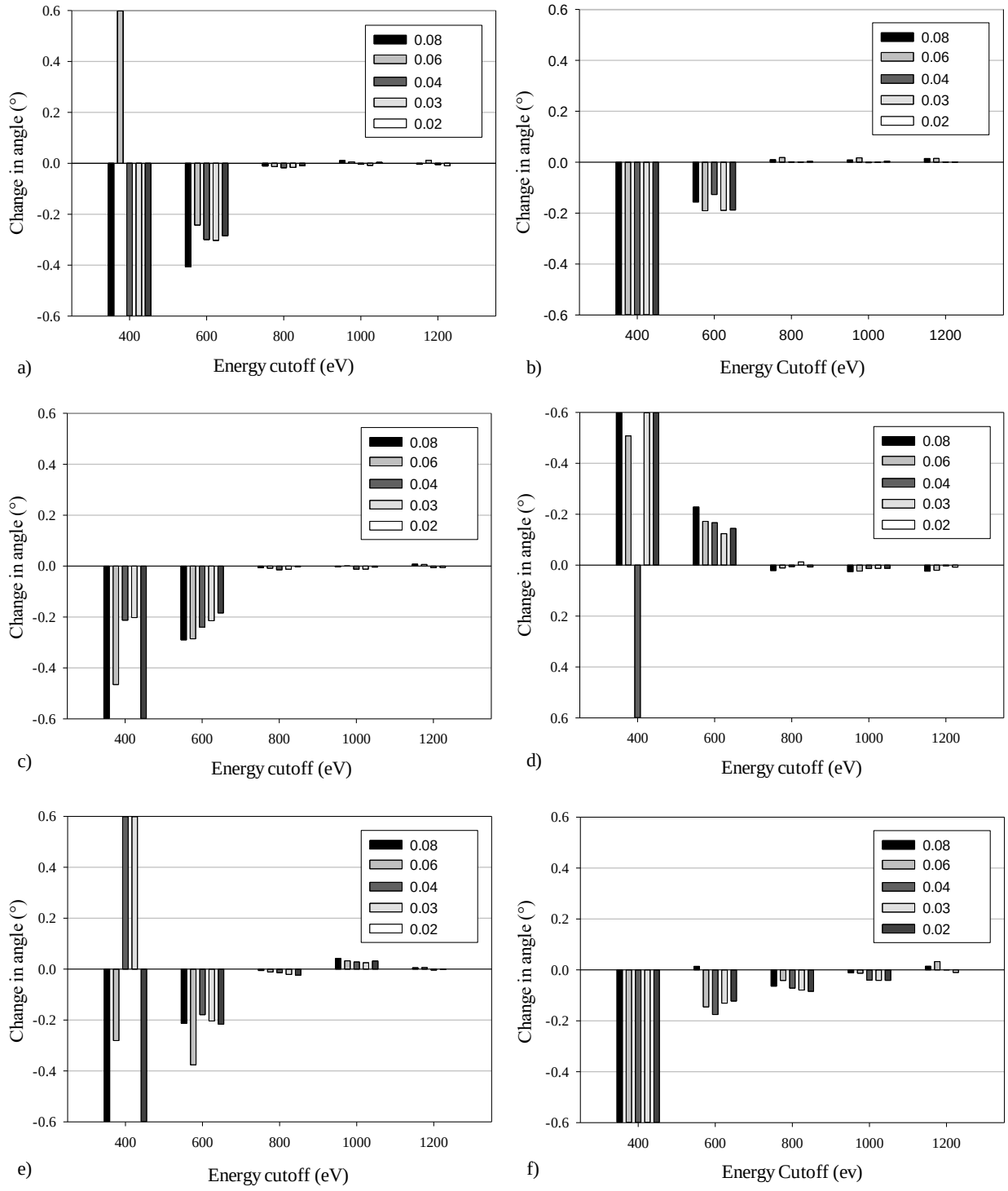

Figure 4.12: The convergence test carried out on ice VIII for the O-H:O:H-O angle, using (a) GGA-PBE (b) GGA-PBE-Grimme (c) GGA-PBE-TS (d) GGA-PBESOL (e) GGA-PW91 and (f) GGA-PW91-OBS when subjected to a hydrostatic pressure of 2.4 GPa. Note that the Y axis give the change in angle (°) for the O-H:O:H-O angle when compared to the O-H:O:H-O angle obtained when the simulation is carried out using a cut-off energy of 1200 eV and a spacing of 0.02 Å^{-1} for the Monkhorst-Pack grid, whilst the legend indicates the spacing used (in Å^{-1}) for the Monkhorst-Pack grid. The scale of the graph is truncated to 0.6 and -0.6.

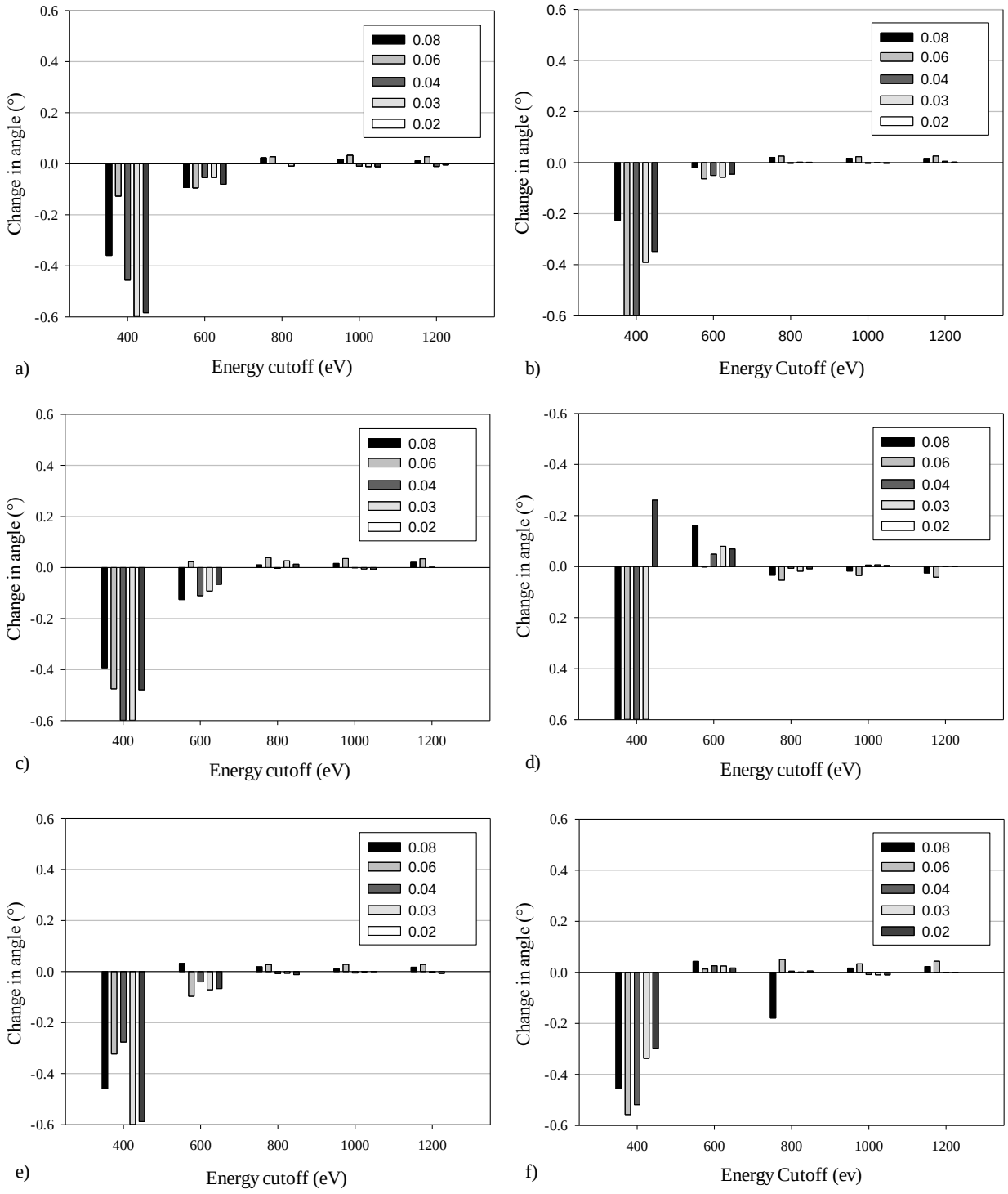

Figure 4.13: The convergence test carried out on ice VIII for the O-H:O:H-O angle, using (a) GGA-PBE (b) GGA-PBE-Grimme (c) GGA-PBE-TS (d) GGA-PBESOL (e) GGA-PW91 and (f) GGA-PW91-OBS when subjected to a hydrostatic pressure of 40 GPa. Note that the Y axis give the change in angle (°) for the O-H:O:H-O angle when compared to the O-H:O:H-O angle obtained when the simulation is carried out using a cut-off energy of 1200 eV and a spacing of 0.02 Å^{-1} for the Monkhorst-Pack grid, whilst the legend indicates the spacing used (in Å^{-1}) for the Monkhorst-Pack grid. The scale of the graph is truncated to 0.6 and -0.6.

In order to choose an appropriate functional, the lattice parameters as obtained from the first principles DFT simulations were compared to experimental data conducted by Kuhs *et al.*[16]. The experimental data and simulations were conducted at a hydrostatic pressure of 2.4 GPa. As indicated in Table 4.1, the lattice parameters obtained using the PBE functional are in agreement with those obtained experimentally, with a maximum deviation of 0.65 %. On the other hand, the PBE-TS, PBE-Grimme, PW91 and PBESOL were less accurate in predicting the lattice parameters of ice VIII and underestimated the lattice parameters by a maximum of 1.30 %, 4.18 %, 1.17 % and 4.62% respectively.

The worst result was obtained by the PW91-OBS functional which underestimated the lattice parameters of ice VIII to a large degree, with a minimum difference of 7.96 % (for the a and b lattice parameters) and a maximum difference of 11.95 % (for the c lattice parameter). At this point, it must be highlighted that a slight difference between the results obtained in this work and the experimental results found in the literature is expected due to the difference in temperature, with the simulations carried out in this work taking a static approach.

Table 4.1: A comparison of the lattice parameters as simulated by different GGA functionals, with and without VdW corrections and the experimental data obtained by Kuhn et al.[16]*. Note that this data was obtained using a cut-off energy of 1200 eV and a spacing of 0.02 Å^{-1} for the Monkhorst-Pack grid at a hydrostatic pressure of 2.4 GPa.*

		This work					
	Kuhs *et al.* [16]	**PBE**	**PBE-TS**	**PBE-Grimme**	**PW91-OBS**	**PW91**	**PBESOL**
a (Å)	4.656	4.667	4.636	4.513	4.285	4.647	4.503
b (Å)	4.656	4.667	4.636	4.513	4.285	4.647	4.503
c (Å)	6.775	6.731	6.687	6.492	5.966	6.696	6.462

The cell volumes of ice VIII as simulated by the PBE functional at 2.75 GPa and 11.48 GPa were then compared to the cell volume of ice VIII obtained experimentally by Klotz and co-workers [16,134] at the same pressure. Referring to Table 4.2, it may be observed that the calculated cell volume utilising the PBE functional is also in agreement with the experimental data with a maximum percentage difference of less than 0.7 % being recorded.

Table 4.2: Comparison of the calculated cell volume of ice VIII with the experimentally determined cell volume by [134]. The experimental study was conducted at a temperatures of 93 K.

Pressure (GPa)	**Cell Volume (Å^3) (this work)**	**Cell Volume (Å^3) [134]**	**Percentage Difference (%)**
2.75	144.94	143.97	0.67
11.48	120.86	121.42	-0.46

In order to further consolidate the benchmarking process, a number of experimental determined structural parameters[16] were compared to the DFT derived structural parameters with the results obtained being shown in Table 4.3. It can be seen that although most functionals gave good results, in most cases, the PBE functional had the best performance between the experimentally derived lengths and angles and the ones obtained from our DFT simulations. In fact, bond lengths and bond angles obtained when utilising the PBE functional compare well with those derived experimentally with a maximum deviation of less than 2 % in the case of the bond lengths and 0.5 ° in case of angles. This once more confirms that the PBE functional can be used to simulate the properties of ice VIII. In addition to this, as shown in Figure 4.14(b), the fractional co-ordinates obtained in this work through the use of the PBE functional only vary within $\pm 6.71\times10^{-3}$ of the experimentally derived fractional coordinates[16].

Table 4.3*: Comparison of the calculated lengths and angles utilising different functionals with the experimentally derived structural parameters*[16]*. Shown in brackets is the reported experimental uncertainty.*

Atoms	**Distance (Å) or angle (°) (literature)[16]**	**Distance (Å) or angle (°) (PBE)**	**Distance (Å) or angle (°) (PBE Grimme)**	**Distance (Å) or angle (°) (PBE-TS)**	**Distance (Å) or angle (°) (PBESOL)**	**Distance (Å) or angle (°) (PW91)**	**Distance (Å) or angle (°) (PW91-OBS)**
O-H:O	2.879(1)	2.877	2.780	2.858	2.771	2.863	2.611
O:O	2.743(9)	2.763	2.695	2.737	2.667	2.754	2.560
O-H	0.9685(71)	0.986	0.991	0.987	1.002	0.987	1.007
H-O-H	105.61(1.06)	105.433	105.806	105.495	105.619	105.552	107.489
O:H-O-H: O	107.92(3)	108.404	108.554	108.403	108.682	108.455	110.324
O:H-O:H-O	110.25(1)	110.017	109.931	110.003	109.867	109.969	109.044
O-H:O:H-O	107.92(3)	108.404	108.554	108.403	108.682	108.455	110.324
O-H:O	178.25(70)	177.731	177.861	177.767	177.602	177.795	177.670

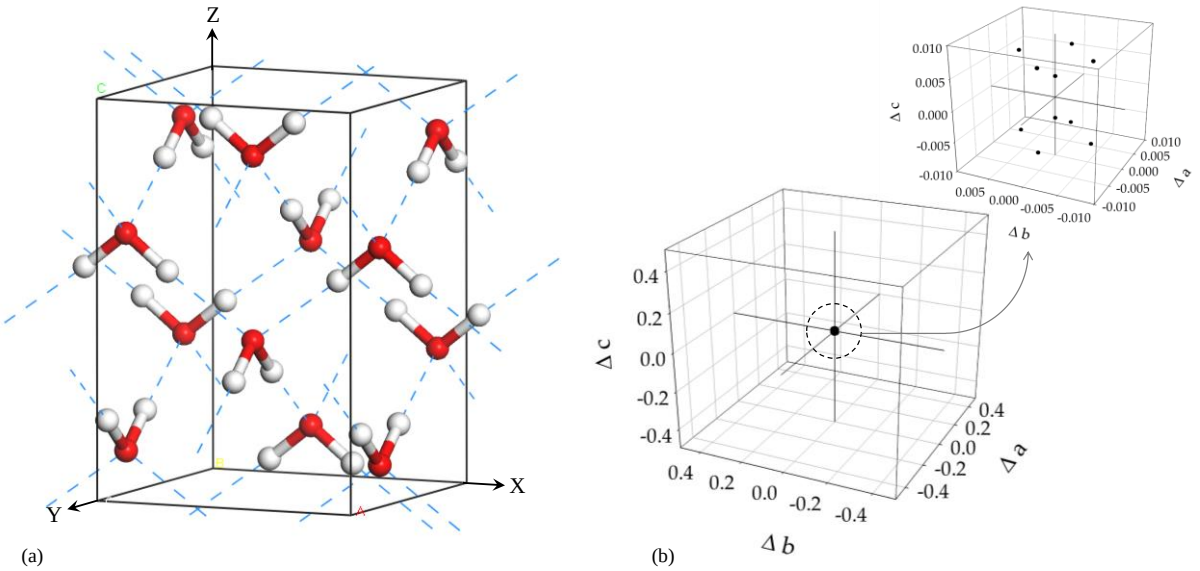

Figure 4.14: (a) The experimental structure of ice VIII including a depiction of the hydrogen bonding illustrated with dashed blue lines. (b) The difference between the fractional coordinates of each atom present in the experimental lattice of ice VIII [16] *and those predicted in this work. The axes of the graph represent the fractional coordinates in the a, b, c directions. Note that in the case of the main graph the scale of these axes is set to illustrate ±50% of the respective lattice length whilst the scale of the inset is set to show ±1% of the respective lattice length.*

In summary, benchmarking the methodology with experimental work has shown that PBE can be used to adequately simulate the structural parameters of ice VIII. Moreover, the results obtained from the benchmarking study indicate that PBE, PBE-TS and PW91 give comparable results. In view of this, and in view of the fact that PBE have been widely used in the literature [127,130,354,404], the rest of the study will mainly be conducted using the PBE functional, with the PBE-TS and PW91 functionals being used in order to confirm the results of the mechanical and vibrational properties obtained (see section 4.3).

4.2.4 Conclusion

In this section a convergence study and benchmarking of the methodology was carried out. It has been shown that an energy cut-off of 1000 eV is appropriate to study ice VIII while the Brillouin zone sampling, carried out using a Monkhorst-Pack grid, was found to be appropriate at a separation of 0.03 $Å^{-1}$. From the benchmarking of the results obtained it was shown that there is adequate agreement between the experimentally derived parameters and the parameters derived through the use of the PBE functional, with the PBE-TS and PW91 functionals also giving comparable results.

4.3 Studying the properties of ice VIII

4.3.1 Introduction

In this section the properties of the ice VIII system in the pressure range of 20 GPa to 40 GPa will be investigated utilising the simulation parameters determined in the previous section. The stability of the ice VIII system in the pressure range of this work will be assessed through the use of lattice dynamics simulations. This will be followed by a study of the mechanical properties of both the polycrystalline aggregate and the single crystal. In particular, the Young's modulus, shear modulus, bulk modulus, Pugh ratio and the Poisson's ratio of the system will be studied. Anomalous mechanical properties will be investigated through the direct measurement of the nanoscale deformation of the ice VIII system. The work on the deformation mechanism of ice VIII will then be consolidated through the use of Raman and infrared spectroscopy.

4.3.2 Methodology

The calculations carried out in this section were performed utilising the parameters determined in the previous section, namely an energy cut-off of 1000 eV and a Monkhorst-Pack k-point grid spacing of 0.03 $Å^{-1}$, employing the PBE functional unless stated otherwise. The methodology employed for studying the properties of ice VIII is described below.

4.3.2.1 Phonon dispersion

The phonon dispersion relations for ice VIII were calculated at 20 GPa and 40 GPa employing the linear response method utilising the interpolation scheme. The q-vector grid spacing for interpolation was set to 0.05 $Å^{-1}$ and the convergence tolerance was set to 1×10^{-5} eV/$Å^2$. In order to assess the convergence for the phonon dispersion relations, the calculations were repeated employing an energy cut-off of 800 eV and a Monkhorst-Pack k-point grid spacing of 0.04 $Å^{-1}$.

4.3.2.2 Mechanical properties

Simulations of the geometry of ice VIII were carried out at different hydrostatic pressures ranging from 20 GPa to 40 GPa in steps of 5 GPa. The elastic constants (c_{ij}) of ice VIII were then determined by employing the constant-strain method which method utilises a series of normal strains and shear strains to determine the respective stress and apply standard transformations to determine the stiffness matrix, [C]. It was made sure that a linear stress-strain relationship was achieved in each case. The stiffness matrix was then utilised to determine the off-axis mechanical properties of ice VIII single crystal, namely Young's modulus, shear modulus and the Poisson's ratio. This was carried out by employing standard transformation techniques[237,397]. This was repeated for all the different hydrostatic pressures considered in this study. The elastic constants obtained were also utilised to determine the

mechanical properties for the polycrystalline aggregate in the pressure range utilised in this study employing equations 3.2 to 3.15 as detailed in section 3.3.2.2. In order to consolidate the work on the mechanical properties of ice VIII, the elastic constants of this system were recalculated employing an energy cut-off of 1200 eV and Monkhorst-Pack k-point grid spacing of 0.02 $Å^{-1}$ and by utilising the functionals PBE-TS and PW91 at 40 GPa and 20 GPa.

4.3.2.3 Deformation mechanism

In order to rationalise the predicted auxetic behaviour of ice VIII single crystal, a number of additional simulations were carried to elucidate the deformation mechanism. The structure was subjected to a series of stresses in the range of ±0.5 % of the Young's modulus in the direction of maximum auxeticity i.e. on-axis in the (001) plane. Bond lengths and bond angles were measured at 20 GPa and 40 GPa in order to determine the deformation mechanism. This was done to study the effect of increasing pressure on the auxetic potential of ice VIII. The orthogonally interconnected rhombi studied in this work are shown in Figure 4.15.

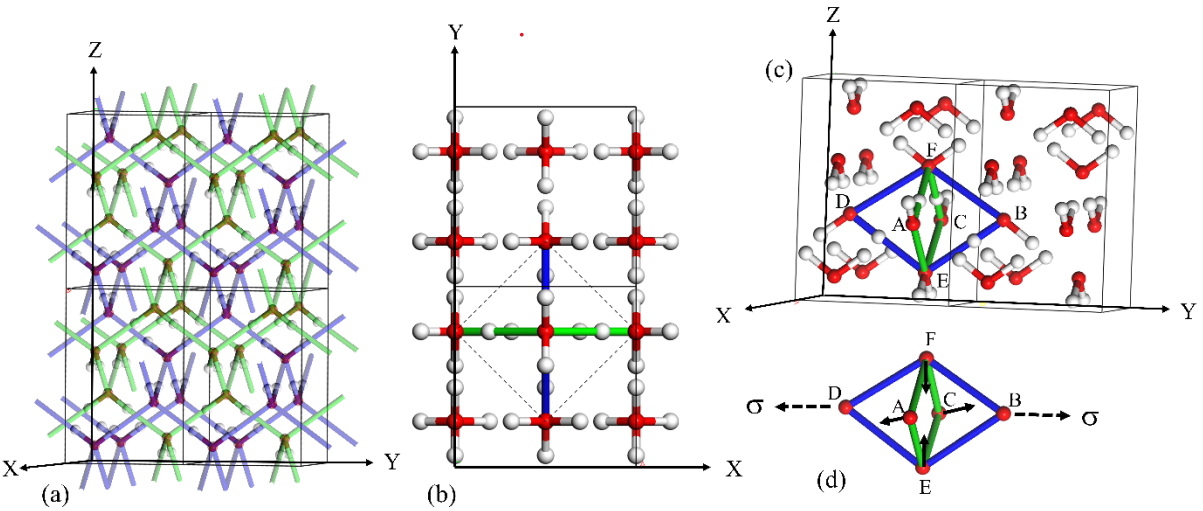

Figure 4.15: (a) Illustration of the two interpenetrating hydrogen bonded systems, one depicted in blue and one depicted in green superimposed on the ice VIII system. (b) Two unit cells of ice VIII in the (001) plane highlighting the body centered arrangement of oxygen atoms the outline of which is shown using dotted black line. (c) An illustration of the two orthogonally interconnected rhombi between two adjacent oxygen body centered sublattices. (d) The two interconnected rhombi responsible for the auxetic potential of ice VIII.

4.3.2.4 Spectroscopy

In order to reinforce the analysis done through the above method (section 4.3.2.3), Raman spectra of ice VIII were calculated at the different pressures namely 20 GPa, 30 GPa and 40 GPa. These Raman spectra were done as implemented in CASTEP, which calculates the Raman tensors by employing a combined DFPT and finite displacement approach. It was also made sure that convergence for the Raman spectra has been achieved.

In order to confirm that the cut-off energy and the spacing for the Monkhorst-Pack grid as selected in section 4.2 were sufficient to for the calculation of the Raman of ice VIII, two simulations were carried out at a pressure of 20 GPa. The first simulation was used to determine the Raman when the cut-off energy was set to 1000 eV and the spacing for the Monkhorst-Pack grid was set at 0.03 $Å^{-1}$ (as selected in section 4.2). In the second simulation, the Raman spectra of ice VIII were determined when the cut-off energy was set to 800 eV and the spacing for the Monkhorst-Pack grid was set at 0.04 $Å^{-1}$. This was then repeated at a pressure of 40 GPa.

The infrared spectra of ice VIII as implemented in CASTEP was also calculated in order to confirm the deformation mechanism suggested. Convergence testing for the infrared spectra was also carried out as described above. The Raman and infrared spectra were also calculated employing the PBE-TS and PW91 functionals in order to confirm the trends obtained.

4.3.3 Results and discussion

In this work it was shown that ice VIII has the potential of exhibiting a negative Poisson's ratio in the (001) plane on application of an on-axis stress. The auxetic behaviour of ice VIII was found to increase with an increase in hydrostatic pressure. This auxetic potential together with its pressure dependence was rationalised through the nanoscale deformation of this system when subjected to a series of stresses as well as through spectroscopic techniques. The simulations carried out suggest that the auxetic behaviour of ice VIII is due to the geometry of the oxygen sublattice in conjunction with an interplay between two deformation mechanisms namely stretching and hinging. As the hydrostatic pressure is increased the stretching mechanism becomes less significant resulting in the hinging mechanism becoming the predominate deformation mechanism. The following is an analysis of the results obtained.

4.3.3.1 Dynamic Lattice calculations

In this study, the structure and mechanical properties of ice VIII in the pressure range of 20 GPa - 40 GPa were investigated, which pressure range is well within the stability field of ice VIII in accordance to the recent phase diagram of dense water ice proposed by Hernandez and Caracas [407]. In order to ensure that the ice VIII system is stable in the pressure range of this study, phonon dispersion relations were calculated at 20 GPa and 40 GPa. Referring to Figure 4.16, the phonon dispersion relations obtained are all positive indicating that the system is stable or metastable at these pressures. To consolidate the results obtained, the phonon dispersion relations were recalculated as described in 4.3.2.1, with the results obtained being shown in Figure 4.16. Varying the simulation parameters had no effect on the dispersion curves obtained suggesting that the results obtained are not an artefact of the simulation parameters employed.

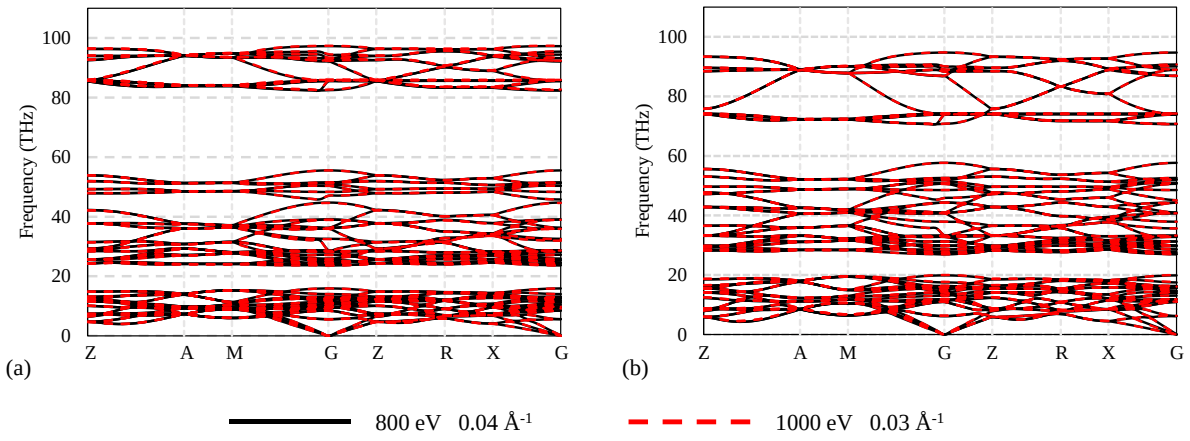

Figure 4.16: The phonon dispersion curves calculated for ice VIII at (a) 20 GPa and (b) 40 GPa utilising an energy cut-off of 800 eV and a Monkhorst-Pack k-point grid spacing of 0.04 Å^{-1} (black solid line) and an energy cut-off of 1000 eV and a Monkhorst-Pack k-point grid spacing of 0.03 Å^{-1} (red dashed line).

4.3.3.2 Elastic constants

The elastic constants (c_{ij}) obtained are of the expected symmetry with $c_{11} = c_{22}$, $c_{31} = c_{32}$, $c_{44} = c_{55}$ while as expected c_{66}, c_{33} and c_{21} are non-zero components of matrix. In order to further validate the methodology employed, and thus consolidate the work done in section 4.2, the calculated elastic constants were compared to the elastic constants present in the literature[130]. Referring to Figure 4.17 it can be seen that the elastic constants calculated at various pressures in this study utilising a first principles approach are in agreement with that of previous work[130], which work also employed a theoretical approach.

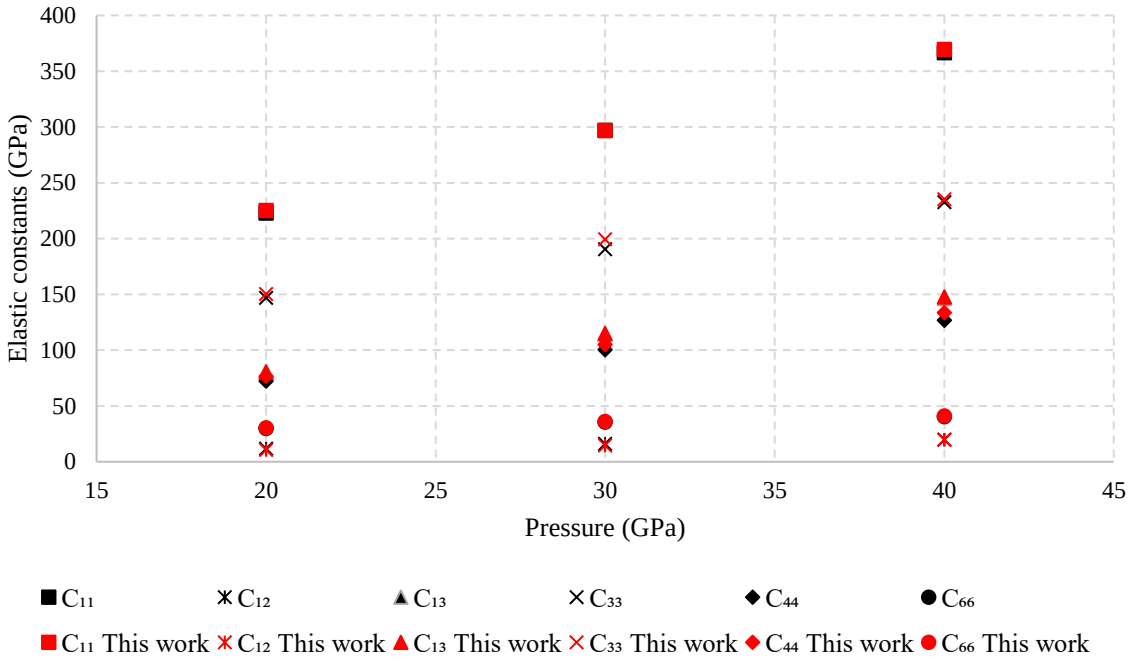

Figure 4.17: Comparison of the calculated elastic constants of ice VIII at various pressures obtained in this work (shown in red) with that present in the literature[130] *(shown in black).*

Following the benchmarking of the methodology the off-axis mechanical properties of ice VIII were determined from its elastic constants. The mechanical properties of ice VIII have been studied at different hydrostatic pressures ranging from 20 GPa to 40 GPa in steps of 5 GPa. The Young's modulus, shear modulus and Poisson's ratio in the (001) and the (010) planes and the variation of these properties with increasing hydrostatic pressure are shown in Figure 4.18. Due to the tetragonal nature of this system, the mechanical properties in the (010) plane are identical to the mechanical properties in the (100) plane and hence only the properties in the (010) plane are shown. Referring to Figure 4.18, the anisotropy of these mechanical properties in both planes is apparent. It can be seen that the mechanical properties obtained are pressure dependent with an increase in hydrostatic pressure resulting in an increase in both the on-axis and off-axis shear modulus in the (001) plane. It should be noted that there is a more pronounced increase in the off-axis shear modulus than that of the on-axis shear modulus, with

the maximum value of the shear modulus being reported at 45° off-axis for all the pressures considered in this study. An increase in shear modulus with pressure is also recorded in the (010) plane with the maximum value of the shear modulus being predicted to be on-axis. Analyses of the variation of the Young's modulus in the (001) plane shows that the maximum Young's modulus is recorded on-axis while the minimum Young's modulus is at 45° off-axis. Moreover, it can also be seen that an increase in hydrostatic pressure results in an increase in the Young's modulus. Such an increase in the Young's modulus is also observed in the (010) plane with the minimum value being recorded on-axis.

Focusing on the Poisson's ratio of the system, one finds that a positive Poisson's ratio is predicted in the (010) plane with the maximum value being predicted to be on-axis while the minimum value is predicted to be at around 45° off-axis. Moreover, an increase in hydrostatic pressure results in a decrease in the minimum value of the Poisson's ratio and a slight increase in the on-axis Poisson's ratio. In the (001) plane the ice VIII system is predicted to exhibit a positive off-axis Poisson's ratio with the maximum value being recorded at 45° off-axis. Most interestingly, the ice VIII system is predicted to exhibit a negative Poisson's ratio on-axis in the (001) plane. Moreover, an increase in hydrostatic pressure results in an increase in the auxetic potential of this system.

In order to confirm that the cut-off energy and the spacing for the Monkhorst-Pack grid as selected in section 4.2.3 were sufficient to for the calculation of the elastic constants of ice VIII, two sets of simulations were carried out at a pressure of 20 GPa. The first set of simulations was used to determine the mechanical properties when the cut-off energy was set to 1000 eV and the spacing for the Monkhorst-Pack grid was set at 0.03 $Å^{-1}$ (as selected in section 4.2.3). In the second set of simulations, the mechanical properties of ice VIII were determined when the cut-off energy was set to 1200 eV and the spacing for the Monkhorst-Pack grid was set at 0.02 $Å^{-1}$. This was then repeated at a pressure of 40 GPa. The off-axis

mechanical properties obtained at 20 GPa and 40 GPa are shown in Figure 4.19 and Figure 4.20 respectively. It can be seen that the properties obtained are not changing with an increase in energy cut-off or a decrease of the spacing used. Hence it can be concluded that in the case of the mechanical properties, convergence has been achieved. Moreover, it can be seen that the mechanical properties predicted is not an artefact of the simulation parameters chosen.

To further consolidate the work done on the auxetic potential of ice VIII, the elastic constants of this system were recalculated utilising PW91 and the dispersion corrected functional PBE-TS at 20 GPa and 40 GPa. The elastic constants obtained were then utilised to calculate the off-axis mechanical properties of ice VIII at 20 GPa and 40 GPa, shown in Figure 4.21 and Figure 4.22 respectively. The plots obtained with these functionals are very similar to the off-axis plot obtained through the use of the PBE functional. It can be seen that the auxetic potential of ice VIII together with the direction of maximum auxeticity is predicted by both functionals in a similar fashion to the results obtained when utilising the PBE functional. This provides evidence that the auxetic potential of ice VIII is an innate property of the system and not an artefact of the functional used.

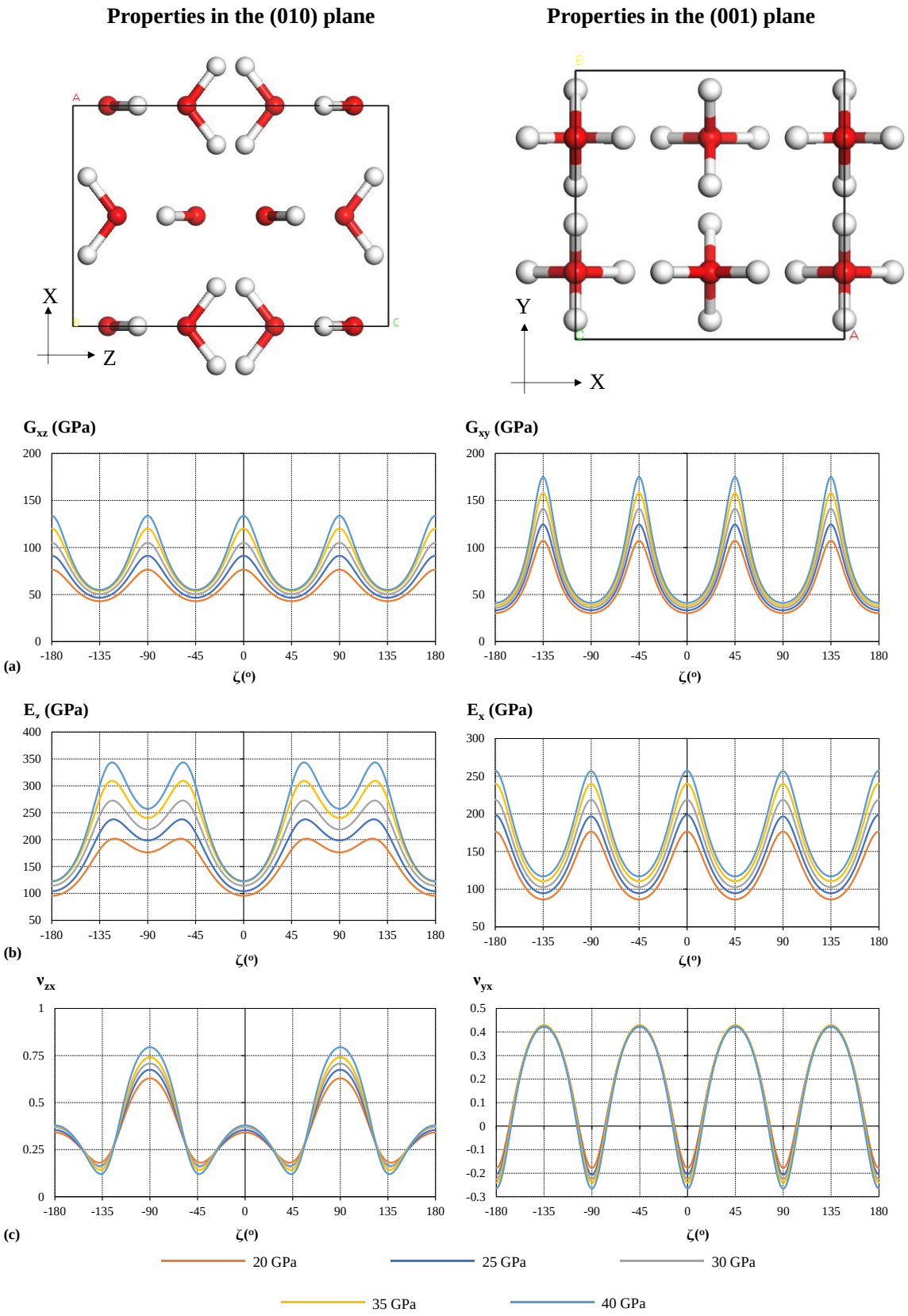

Figure 4.18: The structure of ice VIII together with off-axis plots illustrating the mechanical properties of this system in the (010) and (001) plane at different hydrostatic pressures ranging from 20 GPa to 40 GPa. Shown here are the variation of the (a) shear modulus (in GPa), (b) Young's modulus (in GPa) and (c) Poisson's ratio with angle of rotation, ζ (in °), in these planes.

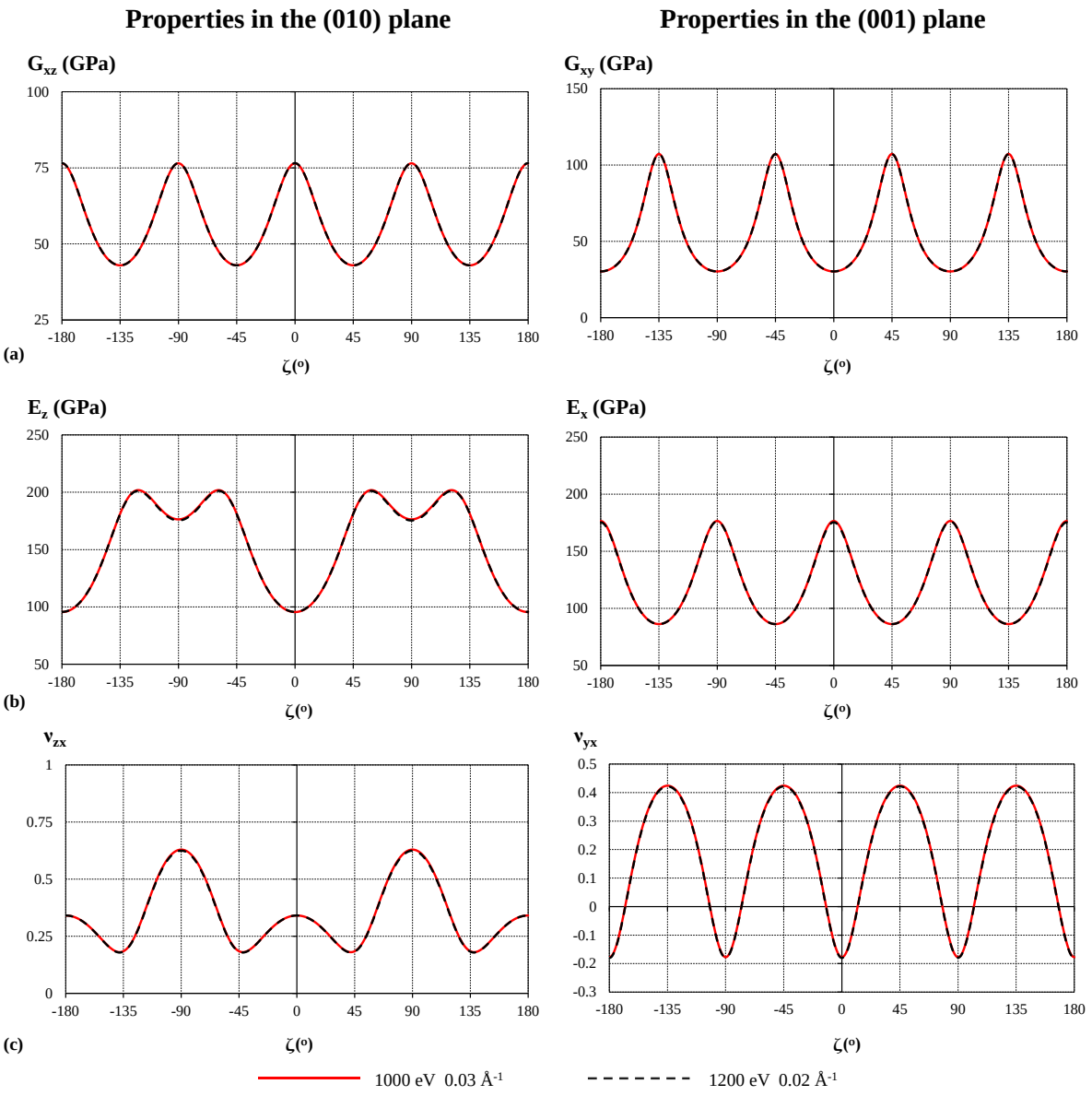

Figure 4.19: The effect of refining simulation parameters on the shear modulus (in GPa) (a), Young's modulus (in GPa) (b) and Poisson's ratio (c) calculated at 20 GPa in the (010) plane and the (001) plane.

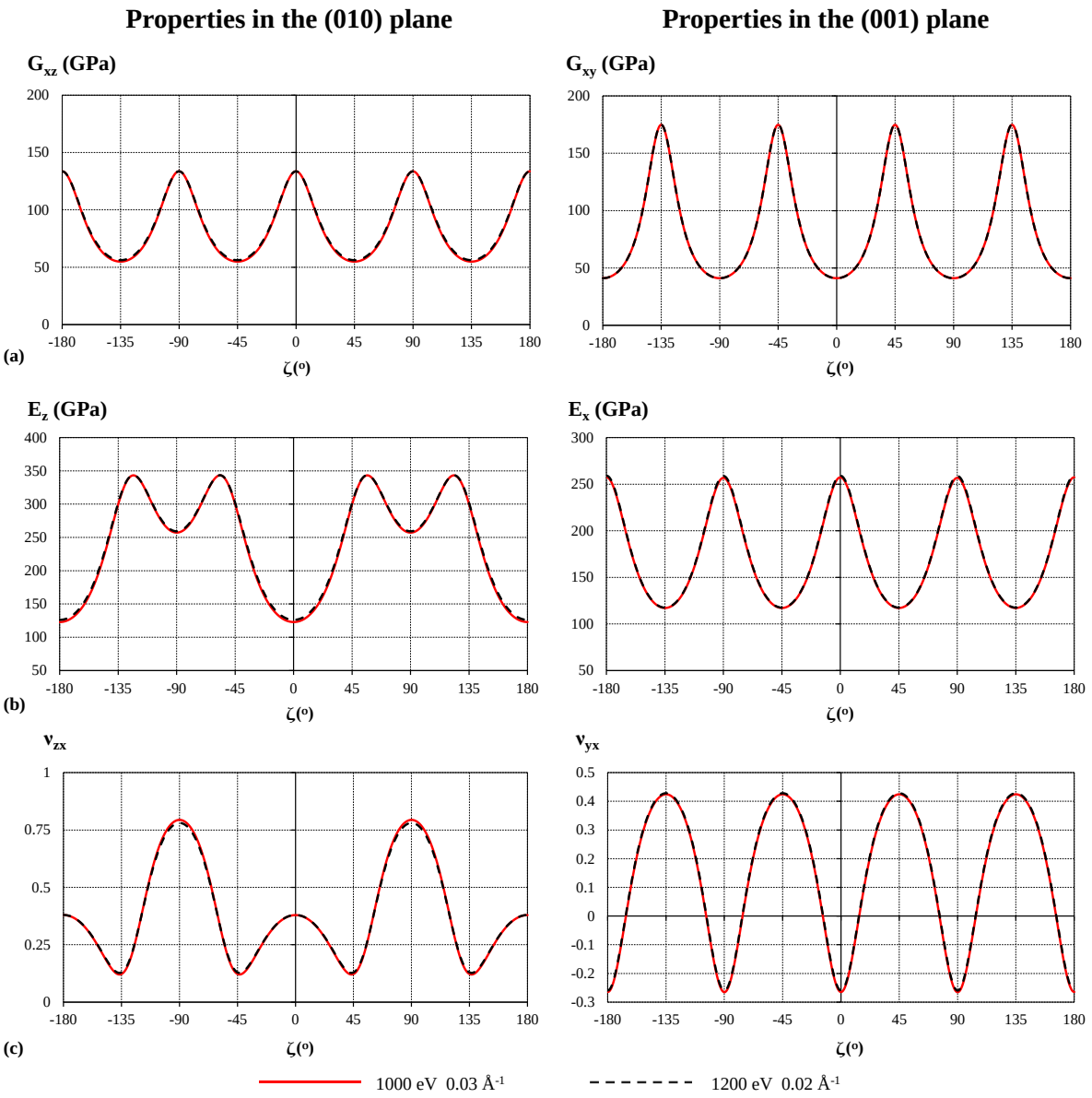

Figure 4.20: The effect of refining simulation parameters on the shear modulus (in GPa) (a), Young's modulus (in GPa) (b) and Poisson's ratio (c) simulated at 40 GPa in the (010) plane and the (001) plane.

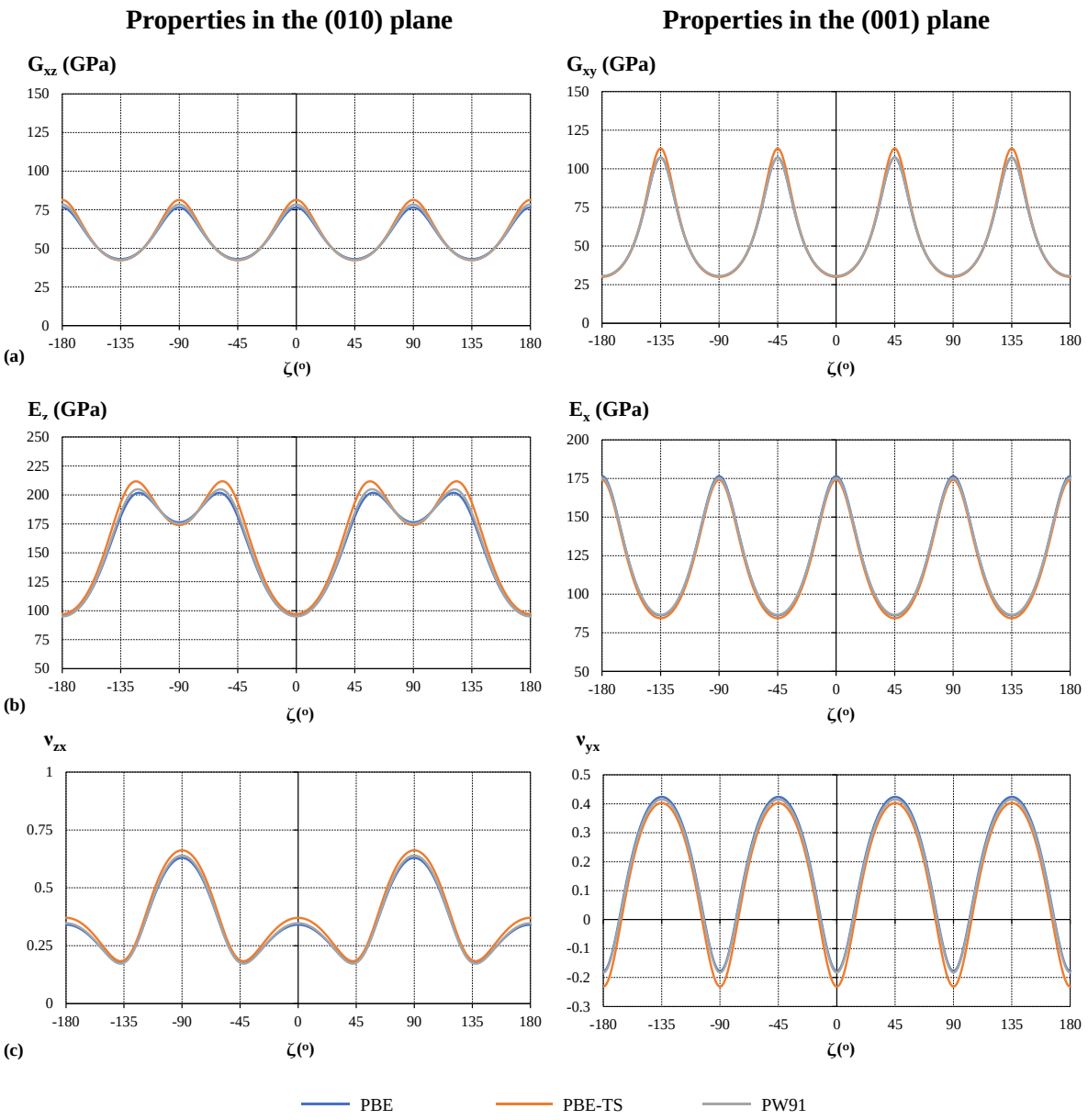

Figure 4.21: The variation of the shear modulus (in GPa) (a), Young's modulus (in GPa) (b) and Poisson's ratio (c) with angle of rotation, ζ (in °) in the (010) plane and the (001) plane at 20 GPa utilising PBE, PBE-TS and PW91. It can be seen that there is good agreement between the mechanical properties calculated with all three functionals. This confirms that mechanical properties predicted are not an artefact of the functional used but an innate property of the system.

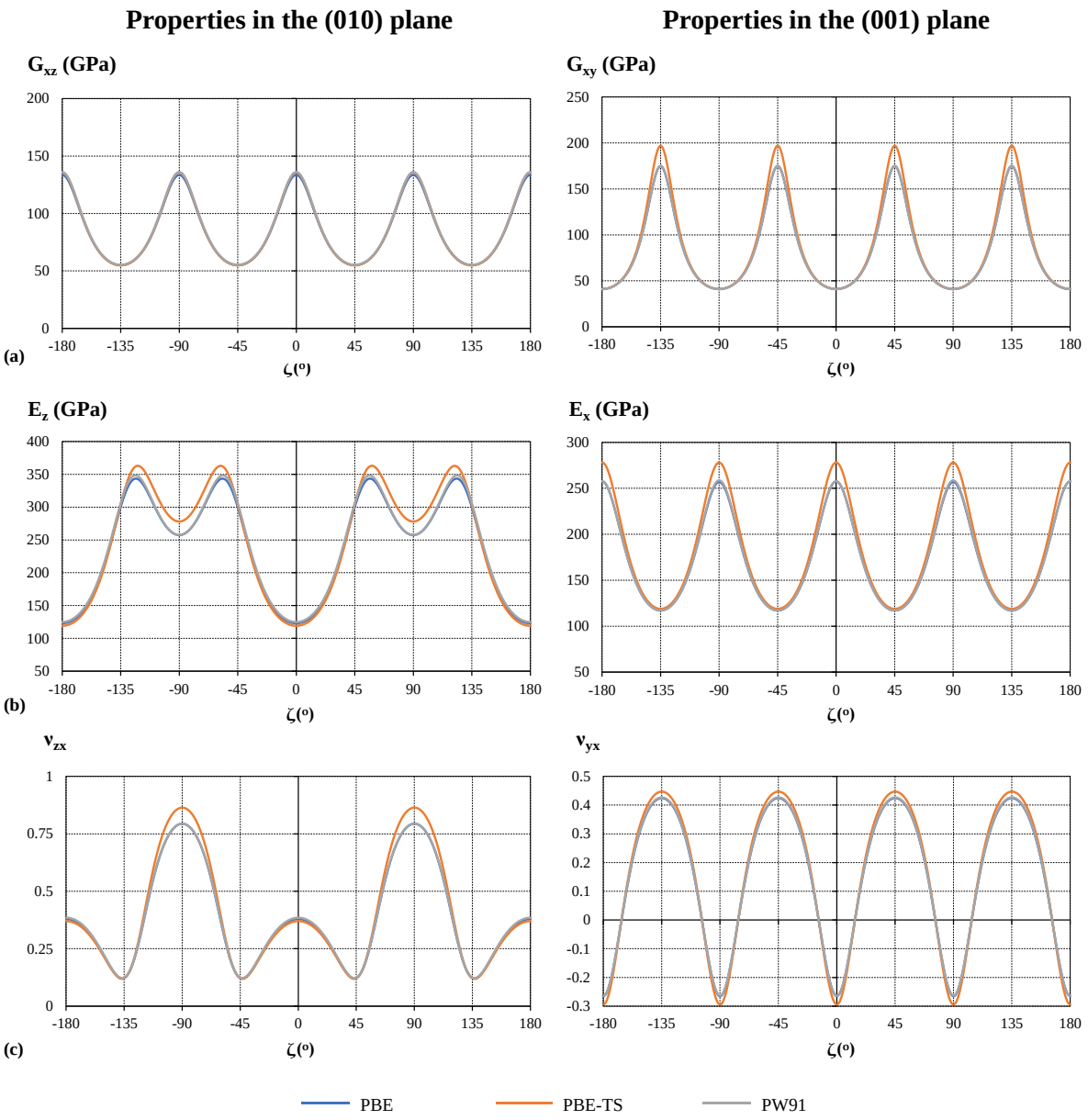

Figure 4.22: The variation of the shear modulus (in GPa) (a), Young's modulus (in GPa) (b) and Poisson's ratio (c) with angle of rotation, ζ (in °) in the (010) plane and the (001) plane at 40 GPa utilising PBE, PBE-TS and PW91. It can be seen that there is good agreement between the mechanical properties calculated with all three functionals. This confirms that mechanical properties predicted are not an artefact of the functional used but an innate property of the system.

4.3.3.3 Polycrystalline properties

The maximum and minimum bounds of the Poisson's ratio for a polycrystalline aggregate can be calculated from the material's elastic constants as shown in Chapter 3 section 3.3.2.2. The calculation assumes that the crystal domains in the sample are arranged in such a way that the material is isotropic. The ice VIII polycrystalline aggregate is predicted to exhibit a positive Poisson's ratio in the pressure range of this study, with the maximum and minimum bounds for the Poisson's ratio both increasing with an increase in hydrostatic pressure as shown in Table 4.4.

Table 4.4: The variation of the maximum and minimum bounds for the Poisson's ratio of ice VIII polycrystalline aggregate with varying hydrostatic pressure.

Pressure (GPa)	ν^{max}	ν^{min}	ν
20	0.288	0.242	0.265
25	0.296	0.244	0.270
30	0.304	0.249	0.277
35	0.311	0.251	0.281
40	0.317	0.253	0.285

The elastic constants can also be utilised to calculate the bulk modulus and shear modulus for the polycrystalline aggregate employing the Voigt-Reus-Hill approximation. The results obtained are reported in Table 4.5, where it can be seen that an increase in pressure results in an increase in both the material's bulk and shear modulus. Moreover, an increase in pressure is associated with an increase in the K/G ratio.

Table 4.5: The pressure dependence of the maximum and minimum bounds for the bulk moduli ($K^{Reuss} = K^{Voigt}$ denoted by K) and shear moduli (G) for ice VIII polycrystalline aggregate together with the K/G ratio (Pugh ratio) of the polycrystalline aggregate.*

Pressure (GPa)	K* (GPa)	G^{Voigt} (GPa)	G^{Reuss} (GPa)	G (GPa)	K/G
20	105	65	52	59	1.79
25	123	76	58	67	1.84
30	143	86	64	75	1.90
35	161	96	70	83	1.94
40	178	106	74	90	1.98

The elastic constants can be utilised in order to predict whether the material is brittle or ductile, where a number of criteria can be analysed. One check for ductility is by studying the Cauchy pressure[408], which for a tetragonal structure can be defined as c_{13}-c_{44} and c_{12}-c_{66}, where a positive value suggests that the material is ductile while a negative value suggests that the material is brittle. In the case of ice VIII, c_{12}-c_{66} (see Figure 4.23) is a negative term suggesting that the material is brittle. Another widely used criterion for ductility is the Frantsevich rule[409], in which the Poisson's ratio is used as a check for ductility/brittleness, where a material with a Poisson's ratio less than 0.33 is brittle while a Poisson's ratio greater than 0.33 is ductile. In the case of ice VIII in the pressure range selected the Poisson's ratio of the polycrystalline aggregate is less than 0.33 (see Table 4.4) suggesting that ice VIII would be brittle.

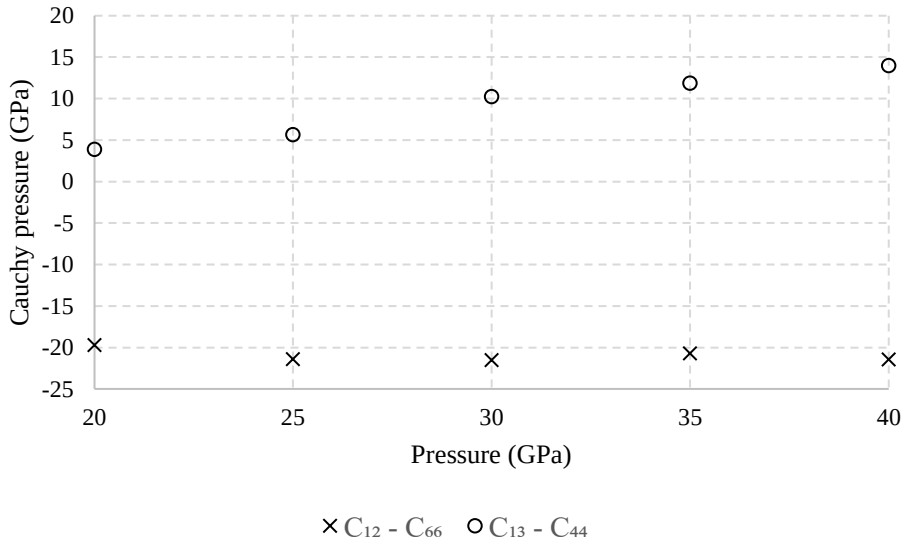

Figure 4.23: The variation of c_{13}-c_{44} and c_{12}-c_{66} with increasing hydrostatic pressure in the pressure range of this study.

The K/G ratio, known as the Pugh ratio[402], gives an indication of the ductility or brittleness of a material with a K/G value exceeding 1.75 indicating that the material is ductile while a K/G value less than 1.75 suggests that the material is brittle. The K/G values obtained (see Table 4.5) in the pressure range under study suggest that ice VIII is ductile leading to an apparent contradiction with the previous predictions employing Cauchy pressure and the Frantsevich rule. Recently[241] it has been argued that Pugh's criterion for the ductile-brittle transition, which employs a K/G value of 1.75 as the benchmark, should be replaced by Christensen's criterion where a K/G value of 2.27 is used to indicate the ductile/brittle transition where a K/G value of less than 2.27 indicates that the material is brittle and a K/G value greater than 2.27 indicating that the material is ductile. Taking the latter criterion ice VIII would be predicted to be brittle in the pressure range of 20 GPa – 40 GPa. All the above suggests that ice VIII would be predicted to be brittle in the pressure range used in this study.

4.3.3.4 Deformation mechanism

Having established the potential for the single crystal of ice VIII to exhibit a negative Poisson's ratio it is interesting to study the reason for such behaviour in detail. It is known that auxetic behaviour is an interplay of the geometry of the material and the way in which the material deforms when a stress is applied. Moreover, it is also possible that a number of deformation mechanisms may be taking place with the overall Poisson's ratio being a result of the interplay between these mechanisms.

Ice VIII structure is composed of two interpenetrating hydrogen bonded systems (see Figure 4.15a), with a body centered oxygen sub-lattice[130] see Figure 4.15b. An analysis of the oxygen atoms present in ice VIII reveals that the O:O interactions can be described as forming two orthogonally interconnected rhombi (see Figure 4.15c), a configuration known to produce a negative Poisson's ratio[304,410]. However, for ice VIII, the O:O interactions making up the interconnected rhombi are not the same, with the O:O interaction between the different interpenetrating hydrogen bonded systems being shorter when compared to the O:O interactions within the same interpenetrating hydrogen bonded system. In the latter case, the interactions between two different water molecules can be more precisely described as a O-H:O interaction. Thus, it is expected that a number of differences will be present when one compares ice VIII to other crystals where the negative Poisson's ratio has been described through this mechanism since in this case the geometry may be more accurately described as interconnected irregular rhombi. In order to confirm if this system is responsible for the predicted auxetic behaviour, nanoscale deformations of the ice VIII system were simulated.

Application of an on-axis stress in the [010] direction results in an increase in the distance BD, as this is on the line of stress, see Figure 4.15d and Figure 4.24. The distance between FE decreases as it is expected since the O:O interactions between oxygen atoms B, F, D and E are forming a rhombus. This is accompanied by an increase in distance AC due to the

deformation of the rhombus formed from the O:O interactions between oxygen atoms A, F, C and E. The increase in distance between BD and AC imparts a negative Poisson's ratio to ice VIII in the (001) plane. Having identified the mechanism which may be responsible for the auxetic potential of this system, it is now interesting to study this system in greater detail.

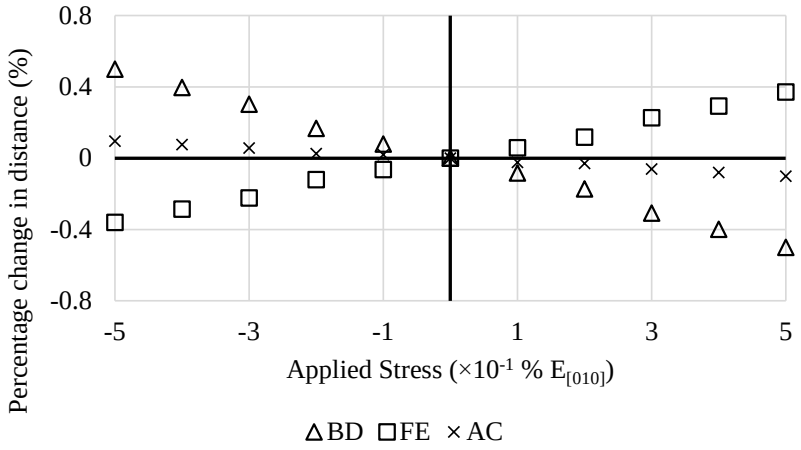

Figure 4.24: The percentage change in distances recorded for various points on the rhombi shown in Figure 4.15, when stress is applied, namely BD, FE and AC. On application of a negative on-axis stress in the [010] direction distance BD increases while FE decreases. This is then accompanied with an increase in distance AC, giving rise to the negative Poisson's ratio in the (001) plane. It should be noted that a negative stress indicates a pulling force while a positive stress indicates a compressive force.

When a tensile stress is applied to the [010] direction, referring to Figure 4.25a, angle FBE, decreases, something which is accompanied with an increase in angle BED. This results in an increase in angle AEC and a subsequent decrease in angle EAF. These changes in angles result in the increase in lengths BD and AC as described above. Also, as expected, the rhombi which have one diagonal in the direction of the stress deform to a greater extent than those which have both diagonals perpendicular to the direction of the stress.

The sides of the rhombi also exhibit a change in length i.e. undergo stretching when a stress is applied in the [010] direction. The rhombus which is parallel to the applied stress exhibits a greater degree of change in sides than the rhombus which is orthogonal to the applied

stress, see Figure 4.25b. In both cases the sides of the rhombi stretch to different extent and hence there is a distortion of the rhombi. The sides made up from the O:O interactions within the same interpenetrating system (O-H:O interactions) are stiffer than the sides made up of the O:O interactions from the different interpenetrating systems, and hence the former deform less than the latter. This is in agreement with work of Chen et al. [403] where it has been shown that the O-H:O interaction is stiffer than the O:O non-bond interaction.

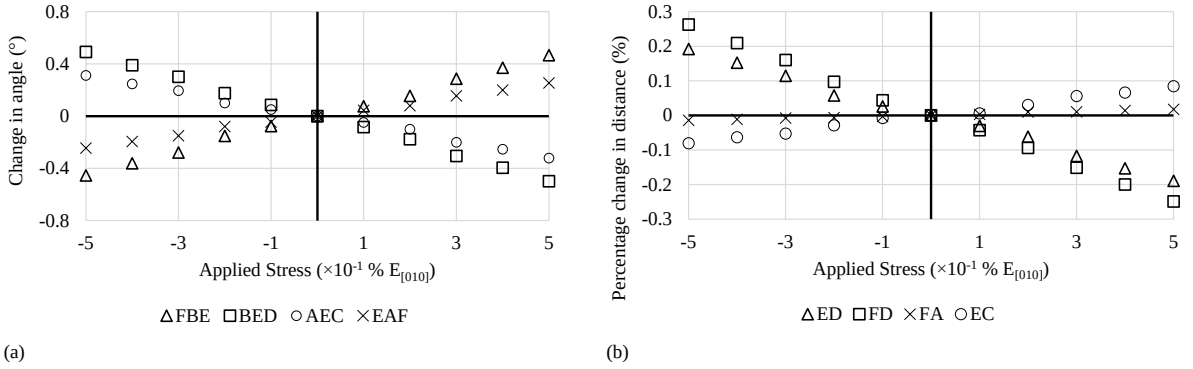

Figure 4.25: (a) Results for hinging mechanism for ice VIII at 20 GPa. Considering rhombus BEDF, application of a negative on-axis stress in the [010] direction results in a decrease in angle FBE and an increase in angle BED. This is accompanied by a decrease in angles EAF and an increase in angle AEC in rhombus AFCE. (b) Results for stretching of the rhombi in ice VIII at 20 GPa. Considering rhombus BEDF, application of a negative on-axis stress in the [010] direction results in an increase in length for sides FD and ED, as expected since these are on the line of stress. Sides FA and EC in rhombus AFCE show a decrease in length. In both rhombi the side made up of the O-H:O interaction (ED and FA) shows a change in length which is smaller than the side made up of the O:O non-bond interaction (FD and EC).

Thus, in view of all the above the auxetic potential of ice VIII at 20 GPa may be explained as an interplay between stretching and hinging of two interconnected rhombi. At this point, it is interesting to highlight that another high-pressure polymorph of ice, ice X, was also found to be auxetic in Chapter 3. At higher pressures, ice VIII undergoes a phase transformation to form ice X [46,47,120,142,145,148,149]. In the case of ice X, a similar mechanism made up interconnected rhombi was used to explain its auxetic behaviour. As discussed above, ice VIII is auxetic in the (001) plane whilst ice X is auxetic in the three major planes at 45° off-axis. It

was recently shown[130] that for the (001) plane the elastic constants between body centered tetragonal and cubic systems is derived by a rotation of 45° around the *c* axis of the stress and strain tensor. This gives more confidence that a variation of the same mechanism is responsible for the observed negative Poisson's ratio in ice VIII and ice X. It also explains why using a similar mechanism, VIII is predicted to be auxetic on-axis in the (001) plane while ice X is predicted to exhibit auxetic behaviour at 45° off-axis in the same plane.

Having established the deformation mechanism of ice VIII at 20 GPa, it would be interesting to study this deformation mechanism at higher pressures. It is known that as the hydrostatic pressure is increased the O-H covalent bond of ice VIII increases in length while the hydrogen bond decreases in length resulting in an overall decrease in the O-H:O distance [127,143,383,403]. In the case of simulations carried out in this work, as the pressure increases, the initial dimensions of the O:O and O-H:O interactions become slightly more similar, with the length ratio O:O / O-H:O changing from 0.971 at 20 GPa to 0.977 at 40 GPa. This means that the interconnected rhombi identified earlier are becoming more regular. Furthermore, when a stress in the [010] direction is applied at a pressure of 40 GPa, the O-H:O and O:O interactions change to a smaller degree when compared to the same loading at a pressure of 20 GPa. This indicates that these interactions become stiffer at higher pressures. From the simulations carried out, it can also be shown that the change in the stiffness of the O:O interactions is smaller when compared to the change in stiffness of the O-H:O interactions. Referring to Figure 4.26, it can be seen that side ED, which is made up of O-H:O interaction, stretches less at 40 GPa than at 20 GPa. This is also true for side FD which is made up of O:O non-bond interaction. Furthermore, the percentage change in length for side FD is greater at 20 GPa than at 40 GPa. All this implies that the sides of the rhombi are getting stiffer with pressure. It can also be noted that at both pressures the O:O non-bond interaction (side FD) exhibits a greater percentage change in length than the O-H:O interaction (side ED) showing that the O-H:O interaction is

stiffer than the O:O non-bond interaction. Moreover, it can also be seen that an increase in pressure is associated with a smaller percentage change in length for the O-H:O than for the O:O interaction. This shows that with an increase in pressure the O-H:O interaction increases in stiffness more than the O:O interaction. This is in accordance with the work of Chen and co-workers [403] where it was shown that the O:O interactions are stronger between hydrogen bonded water molecules than non-hydrogen bonded water molecules.

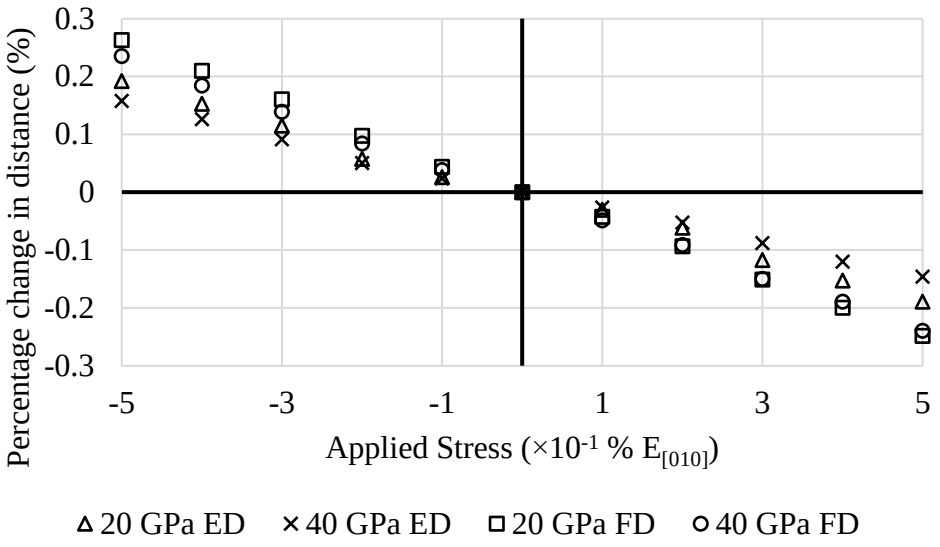

Figure 4.26: Results for stretching of sides ED which is made up of O-H:O interaction and FD which is made up O:O non-bond interaction in ice VIII at 20 GPa and 40 GPa.

Analysing the changes in angles BED and FBE at 20 GPa and 40 GPa, one notes that an increase in hydrostatic pressure is associated with a very slight increase in the changes of these angles. Referring to Figure 4.27, it may be noticed that angles BED and FBE deform slightly more at 40 GPa than at 20 GPa. Thus, it may be argued that an increase in hydrostatic pressure from 20 GPa to 40 GPa does not considerably affect the hinging of the interconnected rhombi, albeit a very slight increase in hinging can be noted. This, together with the decrease in stretching, shows that the hinging is becoming more significant as the pressure is increasing.

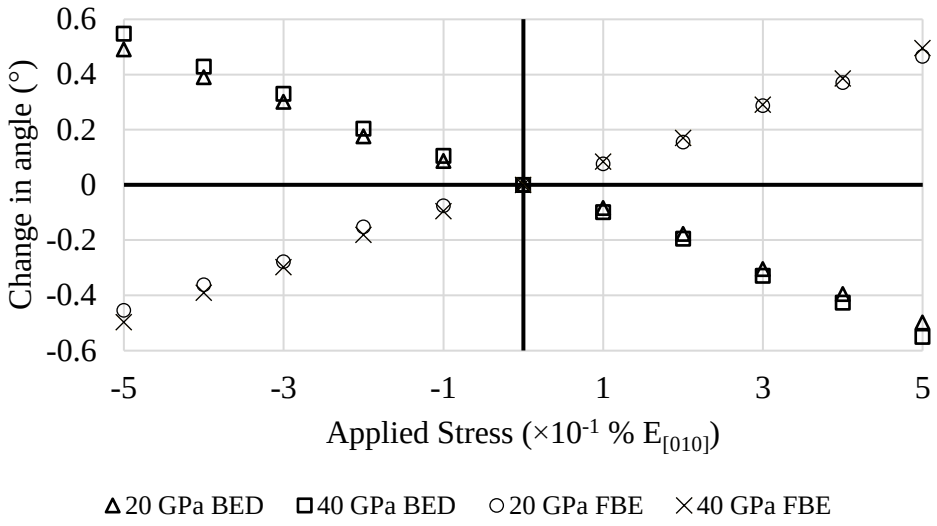

Figure 4.27: Results for the change in angles BED and FBE at 20 GPa and 40 GPa.

All of the above indicates that the increase in auxeticity of ice VIII with increasing pressure may be explained by two factors; (1) the formation of a more regular initial geometry of the interconnected rhombi and (2) an increase in the stiffness of the O:O and O-H:O interactions. In fact, as the hydrostatic pressure is increased the hinging of the rhombi becomes more prominent when compared to the stretching of the same rhombi. Taking into consideration the changes in angle FBE, one notes that the ratios O:O / FBE and O-H:O / FBE change from -0.0142 Å/ ° and -0.0107 Å/ ° at 20 GPa to -0.0117 Å/ ° and -0.0076 Å/ ° at 40 GPa.

4.3.3.5 Consolidating deformation through spectroscopy

At this point, it is interesting to investigate if the same conclusions may be reached from spectroscopic techniques, more specifically infrared and Raman spectroscopy. To this effect, the vibrational spectra of ice VIII have been simulated at various pressures as explained in the methodology section. As expected from literature [117,411], the infrared spectrum of ice VIII obtained from the simulations carried out (see Figure 4.28) shows a number of infrared active modes, including the stretching modes v_1 (A_{2u}) and v_3 (E_u), the bending intramolecular mode

v_2 (A_{2u}), librational mode v_R (E_u) and the lattice translational modes v_T (E_u). The most intense peaks are due to the O—H stretching and these dominate the spectrum of ice VIII. An increase in hydrostatic pressure is accompanied by a shift to lower wavenumbers of the O—H stretching modes, v_1 (A_{2u}) and v_3 (E_u), indicating that the O—H bond becomes less stiff as pressure increases. This trend is in accordance with both bond length measurements carried out in this work in section 4.3.3.4 and previous studies [127,383,403] where it has been shown that the O—H covalent bond increases in length and decreases in stiffness with an increase in pressure. From Figure 4.28, it can also be noted that the v_T (E_u) mode which is associated with antisymmetric hydrogen-bond stretching[411] shifts to higher wavenumbers with increasing pressure. This indicates that the hydrogen bond increases in stiffness with increasing pressure as expected from our measurements and from literature [127,383,403]. Taking into consideration the bending intramolecular mode v_2 (A_{2u}), one notes a slight decrease in wavenumber with an increase in pressure, illustrating that the O—H—O hinge, shown as FBE in Figure 4.15 c and d, is slightly decreasing in stiffness with pressure. In fact, this mode is the least sensitive to changes in pressure with a change from 1526 cm^{-1} at 20 GPa to 1504 cm^{-1} at 40 GPa compared to changes from about 2754 cm^{-1} at 20 GPa to 2356 cm^{-1} at 40 GPa for the O—H stretching mode.

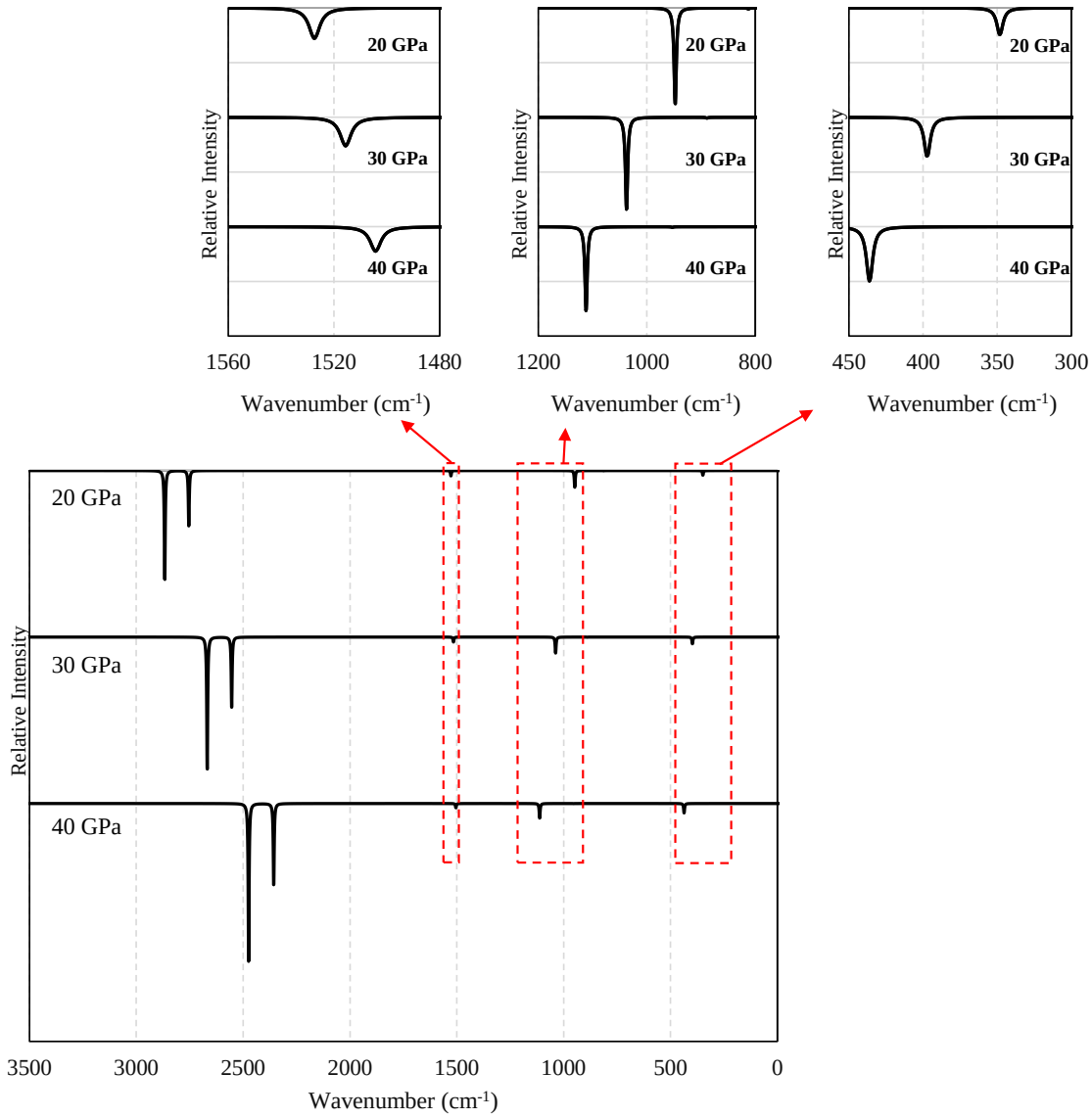

Figure 4.28: The calculated infrared spectrum of ice VIII at 20 GPa, 30 GPa and 40 GPa. Inset: the peaks at lower wavenumbers zoomed 10 times with respect to intensity.

The Raman spectrum, similar to the infrared spectrum is dominated by the O—H stretching modes, with the ν_1 (B_{1g}), ν_3 (E_g) and ν_1 (A_{1g}) modes which are associated with the Raman-active O—H stretching modes shifting to lower wavenumbers with increasing pressure. This indicates that the O—H bond is becoming weaker in accordance with the infrared spectrum and literature [127,383,403]. The ν_{Tz} (B_{1g}) and ν_{TxTy} (Eg) modes, which are associated with

the stiffness of the O:O interaction[124,354,412,413] shift to higher wavenumbers with increasing pressure (see Figure 4.29) indicating an increase in stiffness off the O:O mode.

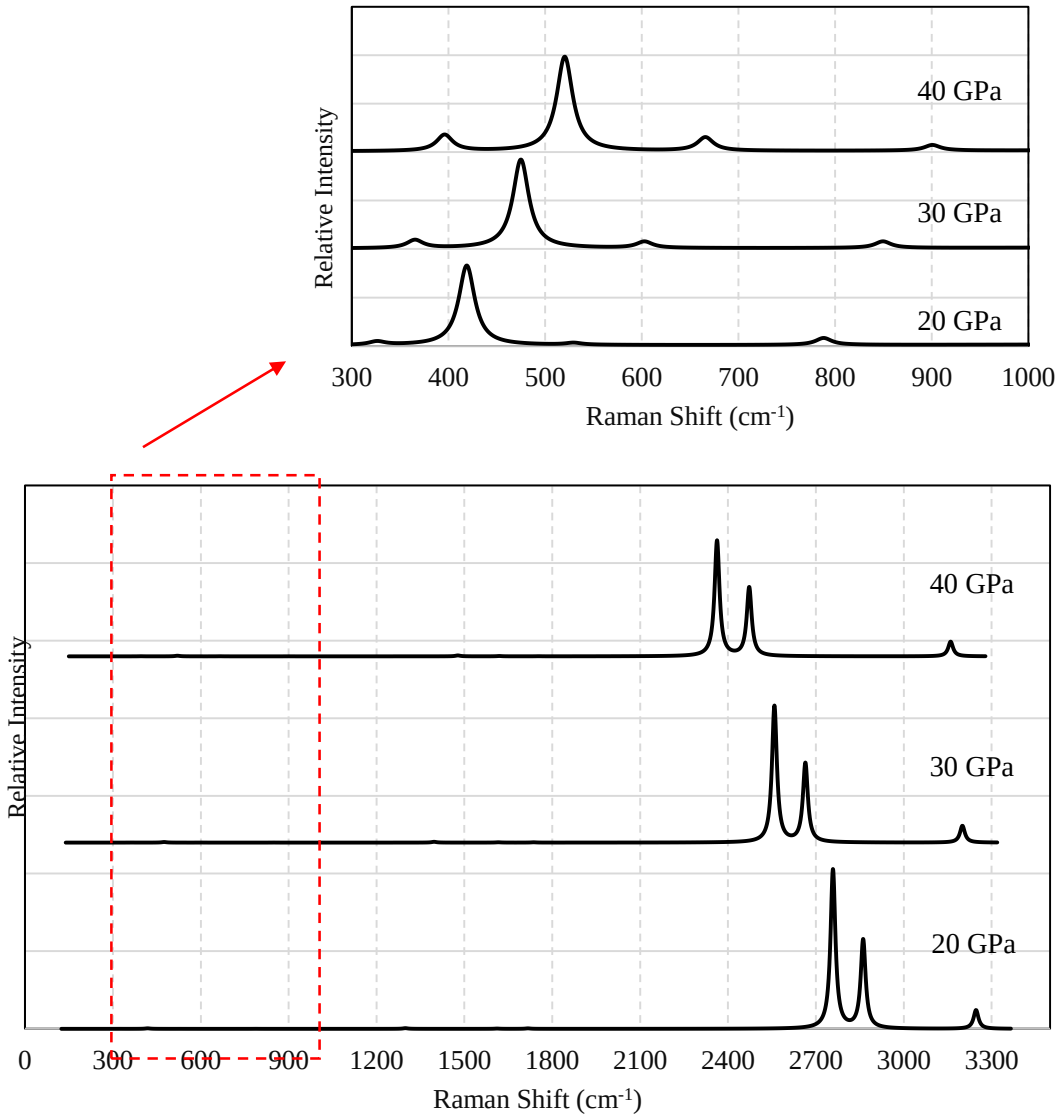

Figure 4.29: The calculated Raman spectrum of ice VIII at 20 GPa, 30 GPa and 40 GPa. Inset: the peaks at lower wavenumbers zoomed 250 times with respect to intensity.

Taking the observations from the IR and Raman spectra one may confirm that the proposed deformation mechanism where an increase in pressure is associated with an increase in stiffness of the O:O interaction (confirmed from the Raman spectrum), and a slight increase in the hinging mechanism. Thus, as the hydrostatic pressure is increased the distortion and

stretching of the orthogonally interconnected rhombi decreases as the structure is becoming more rigid, with the hinging mechanism becoming a more predominate mechanism. The interplay between these two deformation mechanisms for the proposed interconnected rhombi geometry of ice VIII is thus possibly responsible for the predicted auxetic potential of this system.

In order to confirm that the Raman and infrared spectra obtained are not an artefact of the cut-off energy and the spacing for the Monkhorst-Pack grid chosen, the spectra were recalculated employing an energy cut-off of 800 eV and a Monkhorst-Pack grid spacing of 0.04 $Å^{-1}$ at 20 GPa and 40 GPa. Referring to Figure 4.30 and Figure 4.31 it can be seen that an increase in energy cut off and a decrease in the spacing of the Monkhorst-Pack grid at both pressures does not alter the spectra obtained illustrating that the convergence has been achieved. It can be seen that the peaks obtained and the effect of increasing pressure on the position of the peaks is not altered by refining the simulation parameters.

To further consolidate the work carried out in this study utilising the PBE functional, the infrared and Raman spectra of ice VIII were recalculated employing the functional PW91 and the dispersion corrected functional PBE-TS at 20 GPa and 40 GPa. The spectra obtained are shown in Figure 4.32 and Figure 4.33. All functionals used reproduced the expected peaks, albeit some slight shift in the position of the peaks is noted. Furthermore, all functionals used are in agreement with respect to the shift in peak positions with increasing hydrostatic pressure, indicating that that the mechanism for the observed negative Poisson's ratio described above is not an artefact of the functional used.

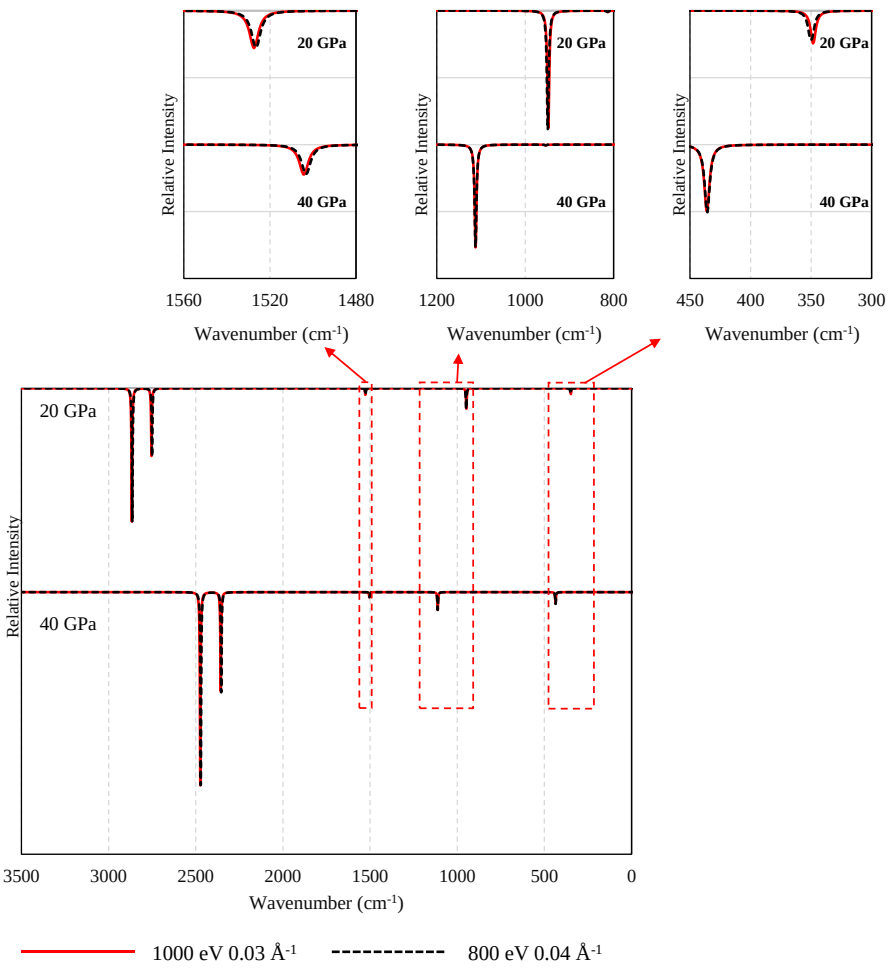

Figure 4.30: Comparison of the infrared spectrum obtained when employing a cut-off energy of 800 eV and a Monkhorst-Pack grid spacing of 0.04 Å^{-1} with the spectrum obtained utilising a cut-off energy of 1000 eV and a spacing of 0.03 Å^{-1} at 20 GPa and at 40 GPa. Inset: the peaks at lower wavenumbers zoomed 10 times with respect to intensity.

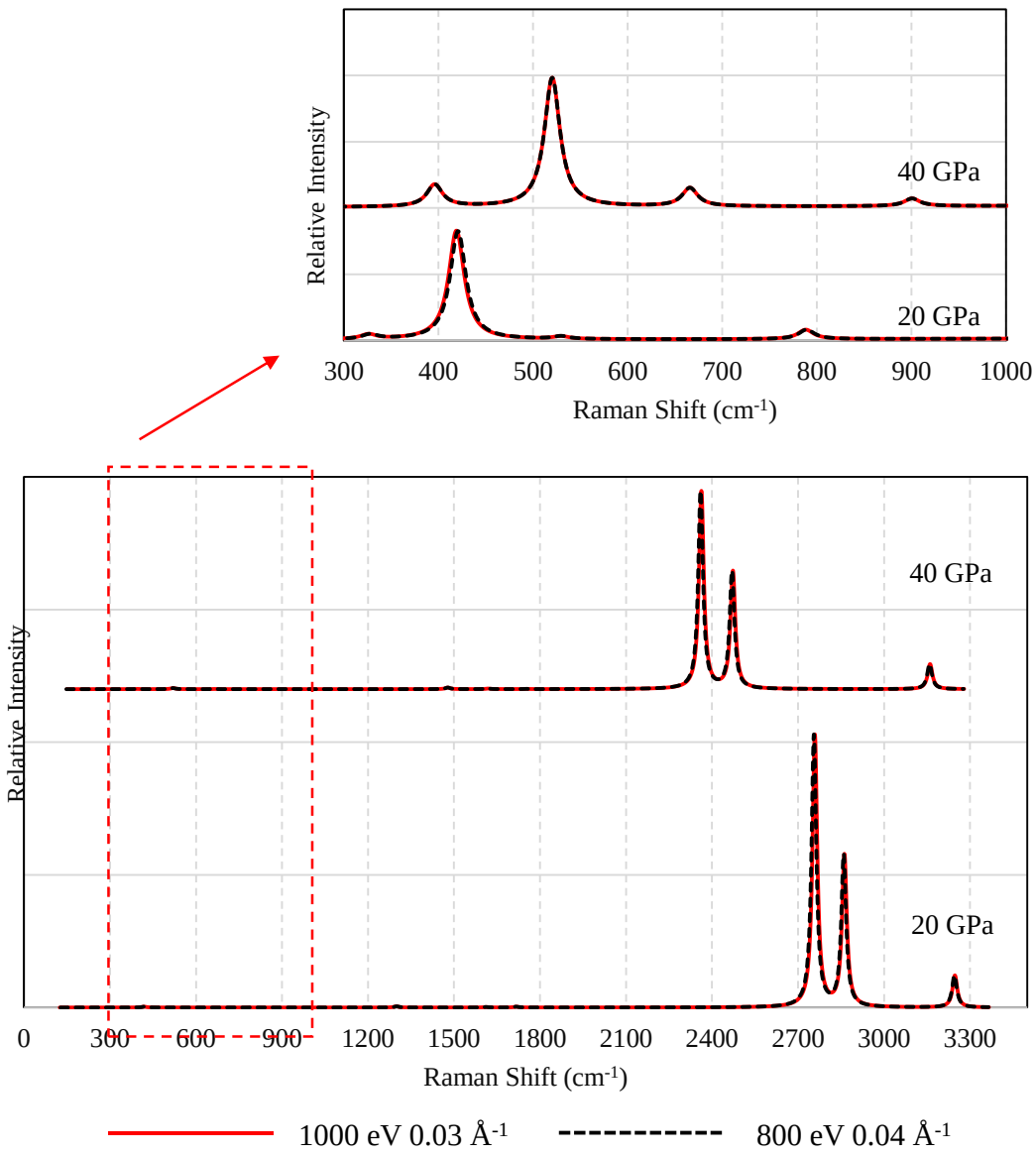

Figure 4.31: Comparison of the Raman spectrum obtained when employing a cut-off energy of 800 eV and a Monkhorst-Pack grid spacing of 0.04 Å^{-1} with the spectrum obtained utilising a cut-off energy of 1000 eV and a spacing of 0.03 Å^{-1} at 20 GPa and at 40 GPa. Inset: the peaks at lower wavenumbers zoomed 250 times with respect to intensity.

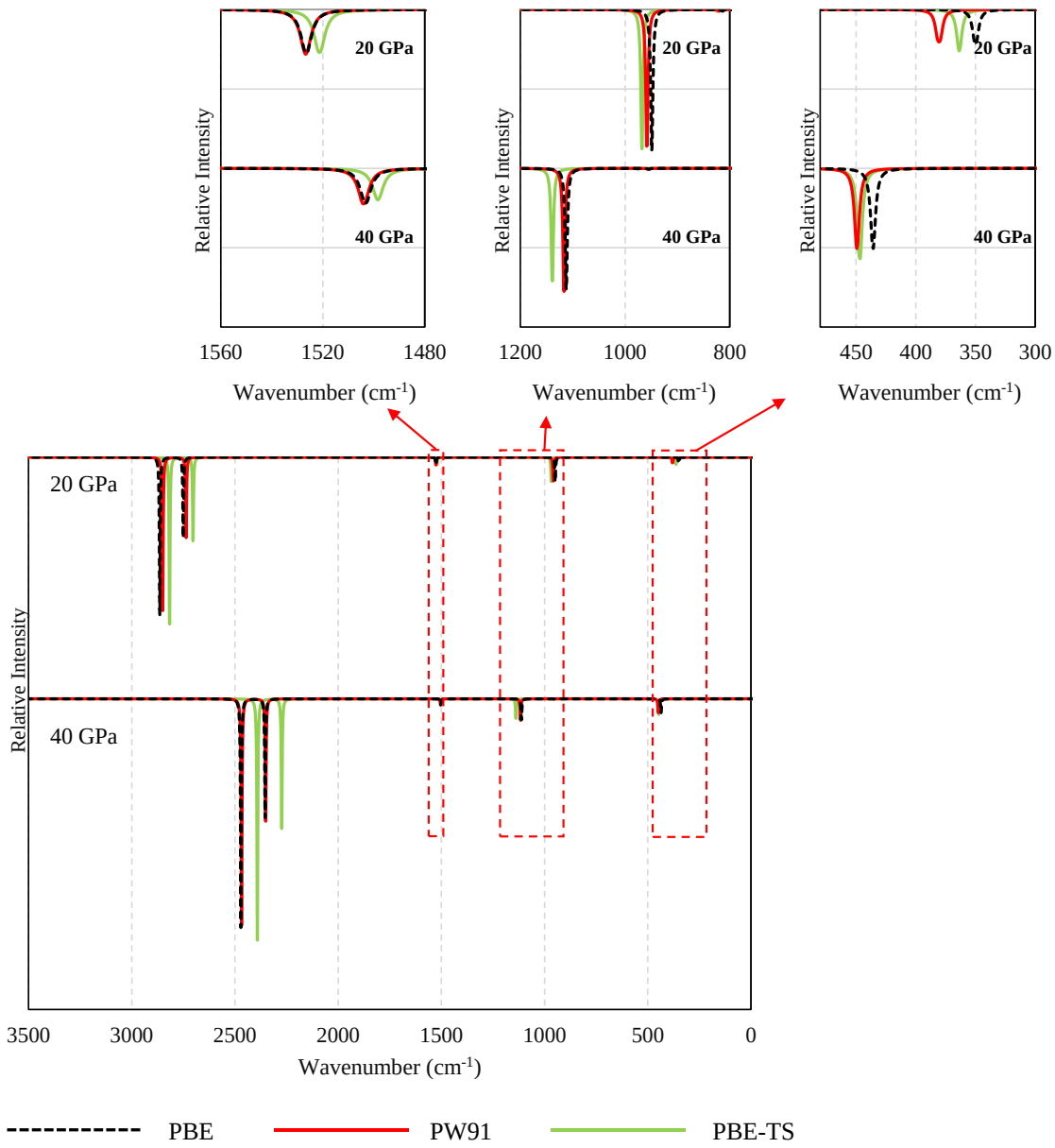

Figure 4.32: Comparison of the infrared spectrum calculated using PBE, PW91 and PBE-TS at 20 GPa and 40 GPa. Inset: the peaks at lower wavenumbers zoomed 10 times with respect to intensity.

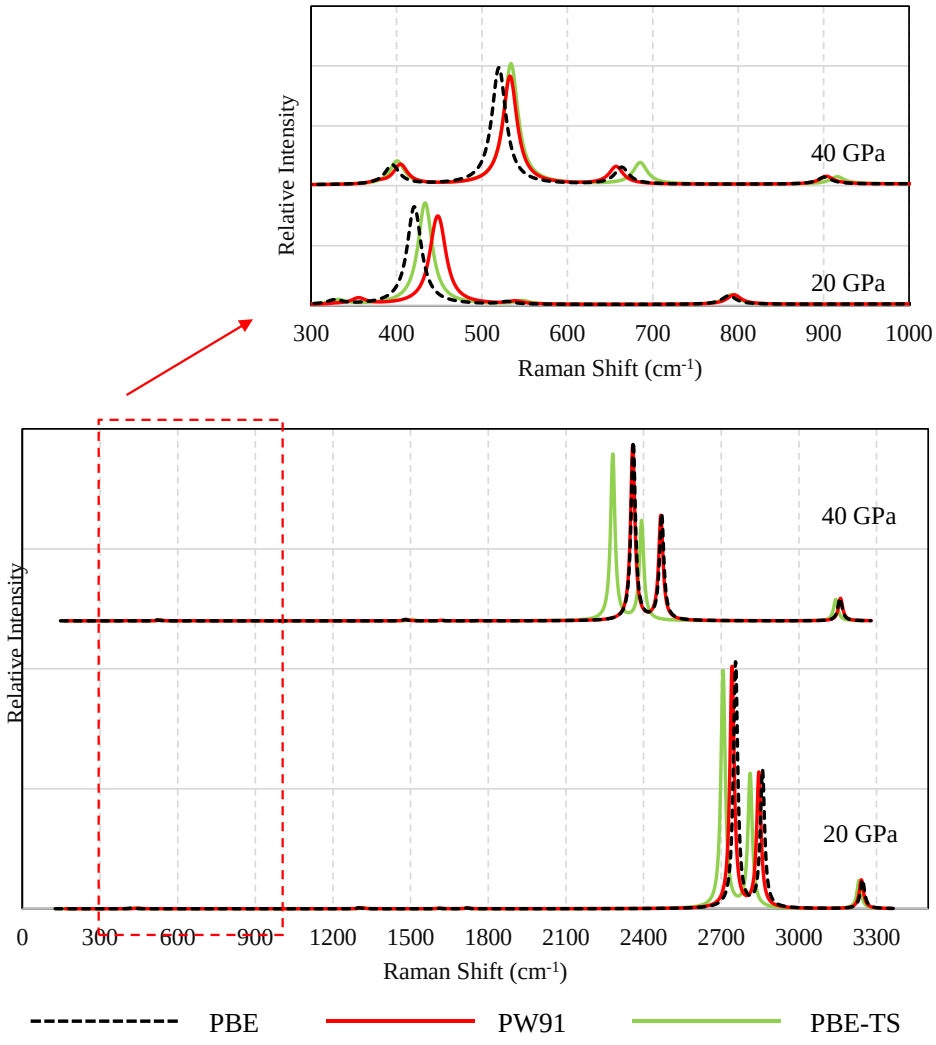

Figure 4.33: Comparison of the Raman spectrum calculated using PBE, PW91 and PBE-TS at 20 GPa and 40 GPa. Inset: the peaks at lower wavenumbers zoomed 250 times with respect to intensity.

In view of the work carried out in this study, it would be interesting to carry out further work on the auxetic potential of other ice systems, particularly those that have a body centred arrangement of oxygen atoms such as ice VII and ice I_c. Ice VII is the hydrogen disordered counterpart of ice VIII, having the same oxygen sublattice as ice VIII. Thus, ice VII may also have the potential to exhibit auxetic behaviour though the extent of the auxeticity may vary since the O:O and O-H:O interactions would be different than those in ice VIII due to the

hydrogen disorder of the ice VII system. Therefore, the deformation mechanism rationalising the auxetic potential of ice VIII described in this work could be used as a blueprint for further study of such systems.

4.3.4 Conclusion

In this work the mechanical properties of ice VIII have been studied by utilising first principles DFT simulations to calculate the elastic constants of this system. The variation of the Young's modulus, shear modulus and Poisson's ratio with pressure in the pressure range of 20 GPa – 40 GPa of both the bulk and single crystal was analysed. Moreover, it has been shown that this system has the potential of exhibiting auxetic behaviour in the (001) plane when subjected to an on-axis stress, with an increase in hydrostatic pressure resulting in an increase in the auxetic potential for this system. The results obtained suggest that this negative Poisson's ratio is a result of an interplay between stretching and hinging of the bonds in ice VIII. An increase in pressure resulted in a decrease in the stretching mechanism and hence the hinging mechanism became the predominate deformation mechanism.

Chapter 5: [*]An investigation of the mechanical properties of CO_2-V

5.1 Introduction

In Chapters 3 and 4, the mechanical properties of the high-pressure polymorphs of H_2O ice were investigated, where it was shown that ice X and ice VIII have the potential to exhibit auxetic behaviour. It would now be interesting to investigate the mechanical properties of the high-pressure polymorphs of other compounds employing the methodology developed in the previous Chapters. Another compound of interest to various fields such as geophysics and planetary science is carbon dioxide [1,2,164], a simple covalent molecule at ambient conditions, which has an extremely rich phase diagram as discussed in Chapter 2. A high-pressure macromolecular phase of CO_2 that has attracted particular attention is phase V. As discussed in more detail in Chapter 2, CO_2-V has been synthesised from CO_2-III through laser heating above 40 GPa and 1800 K in a diamond anvil cell (DAC)[48,166]. The structure of CO_2-V has been shown to be that of partially collapsed tetragonal β-cristobalite with $I\bar{4}2d$ space group composed of corner sharing CO_4 tetrahedra with the carbon atoms forming a diamond network [26,162]. Despite the numerous studies on the structure and properties of CO_2-V, research on the Poisson's ratio of this system is lacking, contrary to SiO_2 polymorphs which have been studied extensively vis-à-vis their Poisson's ratio and auxetic behaviour[60–65,250,252,253].

In view of the above, this work will study the structural and mechanical properties of CO_2-V in the pressure range of 40 GPa – 60 GPa employing first principle DFT simulations.

[*] The contents of this chapter have been submitted for publication in the peer-reviewed Journal of Physics and Chemistry of Solids: Gambin, D., Grima, J. N. & Gatt, R. Unusual mechanical properties of CO_2-V: auxetic potential in a high-pressure polymorph of carbon dioxide

Moreover, the Poisson's ratio of this system will be studied in detail, and the geometries/deformation mechanisms responsible for the observed behaviour (both a 2D and 3D approach) will be elucidated by studying the behaviour of the system when a series of stresses are applied. The results obtained from such measurements will then be supplemented through spectroscopic techniques. To achieve this, this chapter will be subdivided into two sections. In the first section, convergence and benchmarking studies will be carried out to validate the DFT methodology used. In the second part, the mechanical properties of this system will be elucidated and studied in detail.

5.2 Convergence and Benchmarking study of CO_2-V

5.2.1 Introduction

CO_2-V, a macromolecular phase of carbon dioxide known to be stable at high pressures, has been the subject of a number of theoretical studies involving DFT where the structure[185], stability[176], vibrational properties[162] and mechanical properties[56] have been studied. The DFT studies carried out on CO_2-V[56,162,168,174,176,185] have used different simulation parameters and therefore, a convergence and benchmarking study will be carried out in order to ascertain that the results obtained are not an artefact of the simulation parameters employed.

5.2.2 Methodology

The structure of CO_2-V was constructed within the CASTEP[382] modelling platform as implemented in Materials Studio utilising experimentally determined fractional coordinates obtained from the literature[162]. The crystal lattice was aligned within the global coordinate system in accordance to the convention adopted by the Institute of Radio Engineers (IRE)[414] i.e. in such a way that the *c* crystal direction was parallel to the global *z*-axis while the *b* crystal direction was aligned in the global *yz*-plane and no constraints were imposed on the *a* crystal

direction. All simulations were carried out employing density functional theory[405,406] utilising full periodic boundary conditions on a 1 × 1 × 1 unit cell. In order to carry out geometry optimisation of the CO_2-V structure the $I\bar{4}2d$ symmetry of this system was set to P1, thus removing symmetry constraints apart from those imposed by the unit cell itself. As stated in Chapter 3, this increases the simulation time but has the benefit of allowing all elements within the cell to act independently.

The suitable simulation parameters for CO_2-V, when employing different GGA functionals namely PBE[384], PBE-TS[385] and PBE-Grimme[386] were then investigated. All convergence tests were carried out at two pressures i.e. 43 GPa and 60 GPa by carrying out geometry optimisation while systematically increasing the energy cut-off from 400 eV to 1200 eV in steps of 200 eV and systematically decreasing the Monkhorst-Pack k-point grid [390] spacing from 0.08 $Å^{-1}$ to 0.02 $Å^{-1}$. The DFT calculations were carried out employing norm conserving pseudopotentials and an SCF tolerance of 5 $x10^{-7}$ eV/atom. Geometry optimisation was carried out employing the Broyden-Fletcher-Goldfarb-Shanno (BFGS) algorithm utilising the line search method. Stringent convergence criteria were utilised including a maximum force of 0.01 eV/Å, an energy cut-off of 5.0 $\times 10^{-6}$ eV/atom, a maximum stress of 0.02 GPa and maximum displacement of 5.0 $\times 10^{-4}$ Å. Convergence testing was carried out by comparing various structural parameters obtained using different combinations of energy cut-off and spacing of the Monkhorst-Pack grid with the structural parameters obtained using the most refined simulation parameters, namely an energy cut-off of 1200 eV and a spacing of the Monkhorst-Pack grid of 0.02 $Å^{-1}$. The structural parameters assessed were the lattice parameters, the C-O bond length, the C-O-C angle and the O-C-O angle.

The performance of the aforementioned functionals was also assessed by comparing the experimentally determined structural parameters[162] with those calculated employing the different functionals. The structural parameters which were used for the benchmarking of the

methodology were also the lattice parameters, C-O bond length, C-O-C and O-C-O angles. Benchmarking was carried out at a pressure of 43 GPa, the pressure at which experimental data was available[162].

5.2.3 Results and discussion

Convergence tests were carried out at 43 GPa and 60 GPa utilising different GGA functionals namely PBE[384], PBE-TS[385] and PBE-Grimme[386]**.** All three functionals considered in this study, correctly predicted the $I\bar{4}2d$ symmetry of this system, which symmetry is reported in the literature [162]. In all tests performed, a tetragonal crystal system was obtained and therefore the *a*-lattice parameter was equal to the *b*-lattice parameter, see Figure 5.1. The *a*-lattice parameter and c-lattice parameter obtained from each combination of the energy cut-off and the Monkhorst-Pack k-point grid tested were compared to those obtained using an energy cut-off of 1200 eV and a Monkhorst-Pack k-point grid spacing of 0.02 $Å^{-1}$. The results obtained (see Figure 5.2 and Figure 5.3) indicate that an energy cut-off of 800 eV and a Monkhorst-Pack k-point grid spacing of 0.06 $Å^{-1}$ is adequate in simulating the lattice parameters of CO_2-V as further refinements in simulation parameters did not significantly change the lattice parameters obtained. In order to further confirm the appropriate simulation parameters for the structure of CO_2-V, convergence testing was carried as described above for the C-O bond length, the C-O-C angle and the O-C-O angle with the results obtained being shown in Figure 5.4, Figure 5.5 and Figure 5.6 respectively. From these figures, it can be inferred that an energy cut-off of 400 eV is not adequate in simulating the aforementioned bonds and angles irrespective of the spacing of the Monkhorst-Pack grid being utilised. It can also be noted that an energy cut-off of 800 eV and a Monkhorst-Pack grid spacing of 0.06 $Å^{-1}$ is appropriate for studying the structural parameters of CO_2-V with a further refinement of the simulation parameters not significantly changing the results obtained.

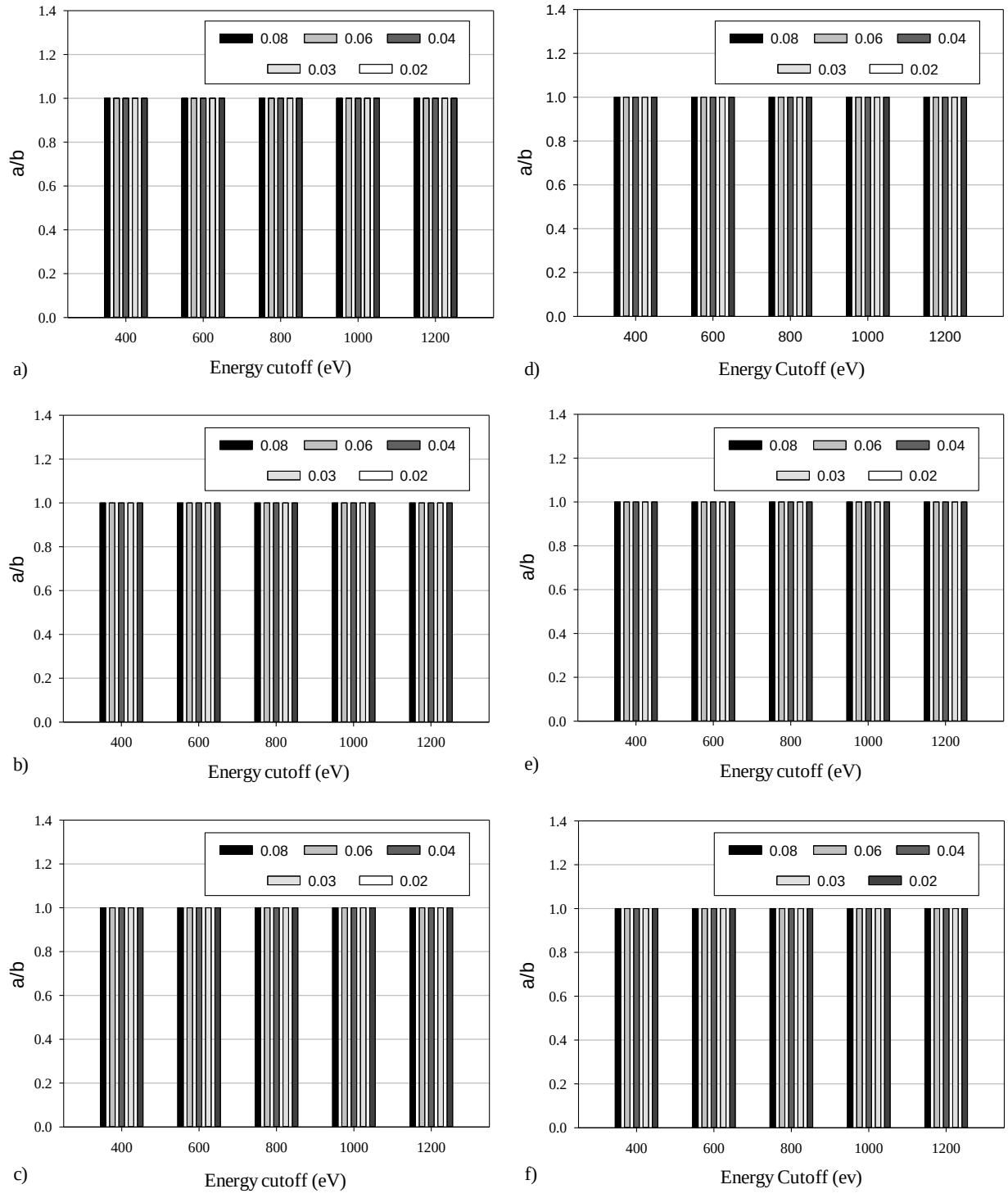

Figure 5.1: The convergence test carried out on CO_2-V for the ratio of a/b lattice parameters, using (a) GGA-PBE, (b) GGA-PBE-TS, (c) GGA-PBE-Grimme when subjected to a hydrostatic pressure of 43 GPa and using (d) GGA-PBE, (e) GGA-PBE-TS and (f) GGA-PBE-Grimme when subjected to a hydrostatic pressure of 60 GPa. Since CO_2-V is a tetragonal system, a=b and hence the a/b ratio should be equal to 1. The legend indicates the spacing used (in $Å^{-1}$) for the Monkhorst-Pack grid.

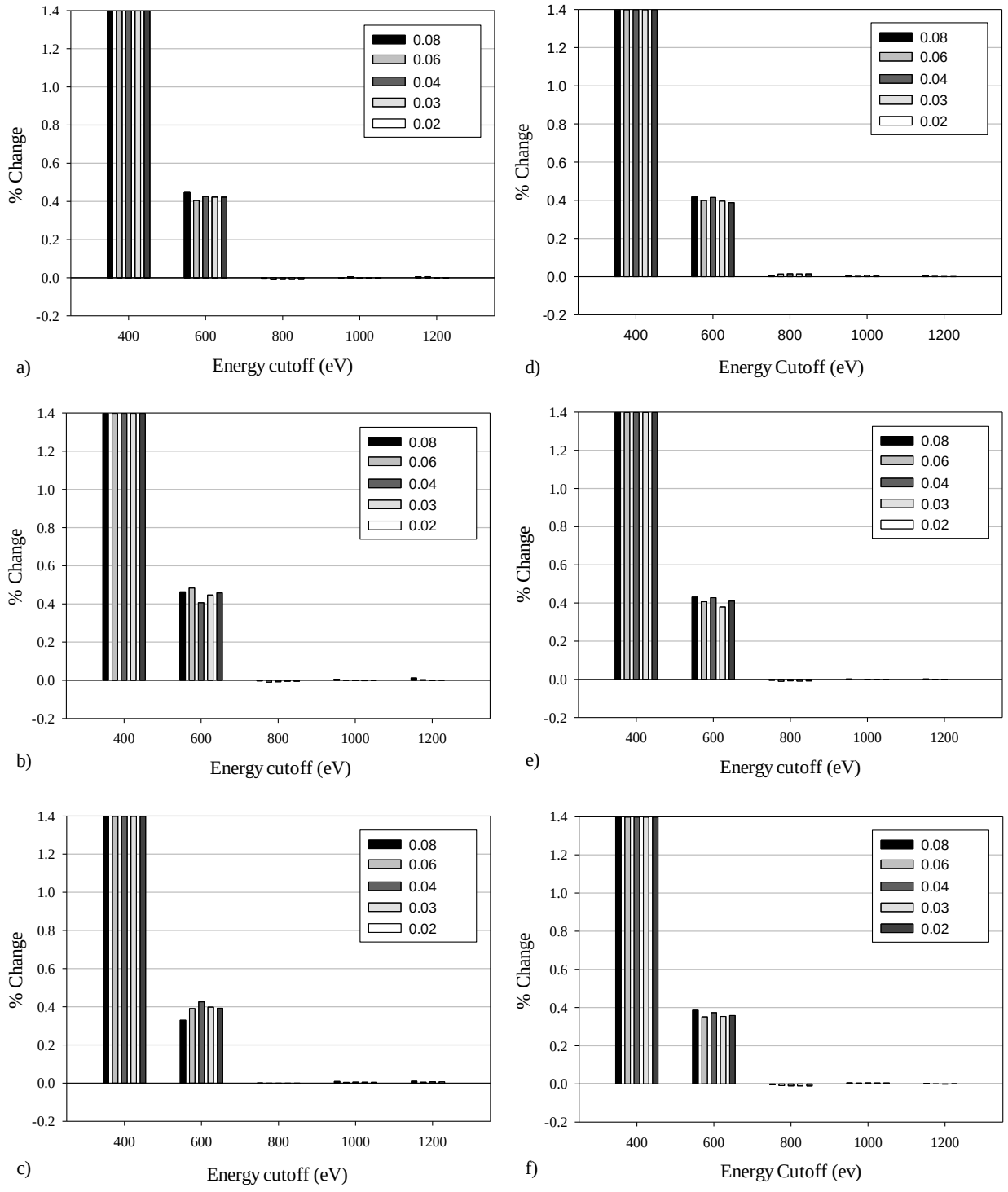

Figure 5.2: The convergence test carried out on CO2-V for the a-lattice parameter, using (a) GGA-PBE, (b) GGA-PBE-TS, (c) GGA-PBE-Grimme when subjected to a hydrostatic pressure of 43 GPa and using (d) GGA-PBE, (e) GGA-PBE-TS and (f) GGA-PBE-Grimme when subjected to a hydrostatic pressure of 60 GPa. Note that the Y axis give the percentage deviation for the a-lattice parameter when compared to the a-parameter obtained when the simulation is carried out using a cut-off energy of 1200 eV and a spacing of 0.02 Å-1 for the Monkhorst-Pack grid, whilst the legend indicates the spacing used (in Å-1) for the Monkhorst-Pack grid. The scale of the graph is truncated to 1.4 and -0.2.

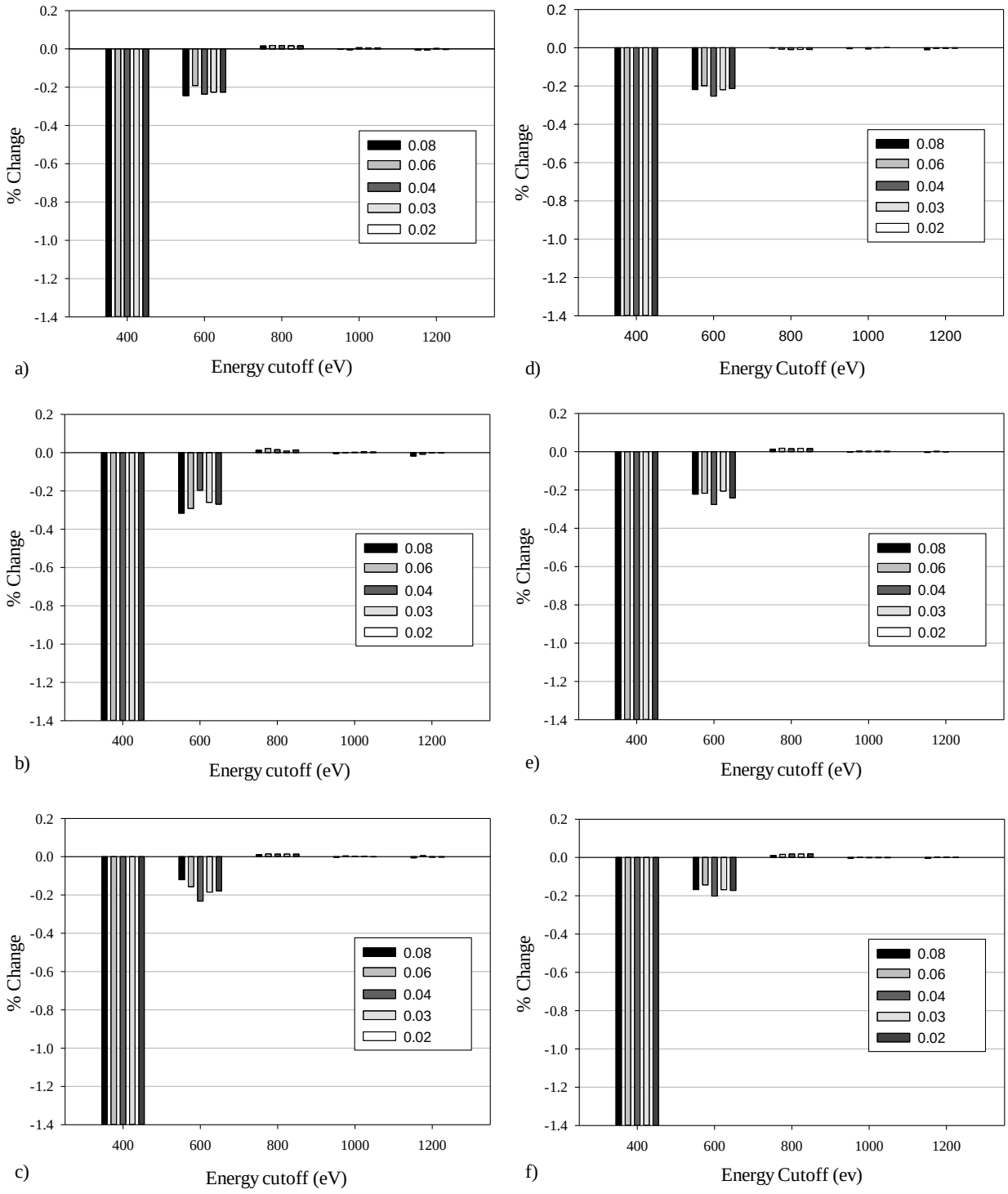

Figure 5.3: The convergence test carried out on CO_2-V for the c-lattice parameter, using (a) GGA-PBE, (b) GGA-PBE-TS, (c) GGA-PBE-Grimme when subjected to a hydrostatic pressure of 43 GPa and using (d) GGA-PBE, (e) GGA-PBE-TS and (f) GGA-PBE-Grimme when subjected to a hydrostatic pressure of 60 GPa. Note that the Y axis give the percentage deviation for the a-lattice parameter when compared to the a-parameter obtained when the simulation is carried out using a cut-off energy of 1200 eV and a spacing of 0.02 $Å^{-1}$ for the Monkhorst-Pack grid, whilst the legend indicates the spacing used (in $Å^{-1}$) for the Monkhorst-Pack grid. The scale of the graph is truncated to 0.2 and -1.4.

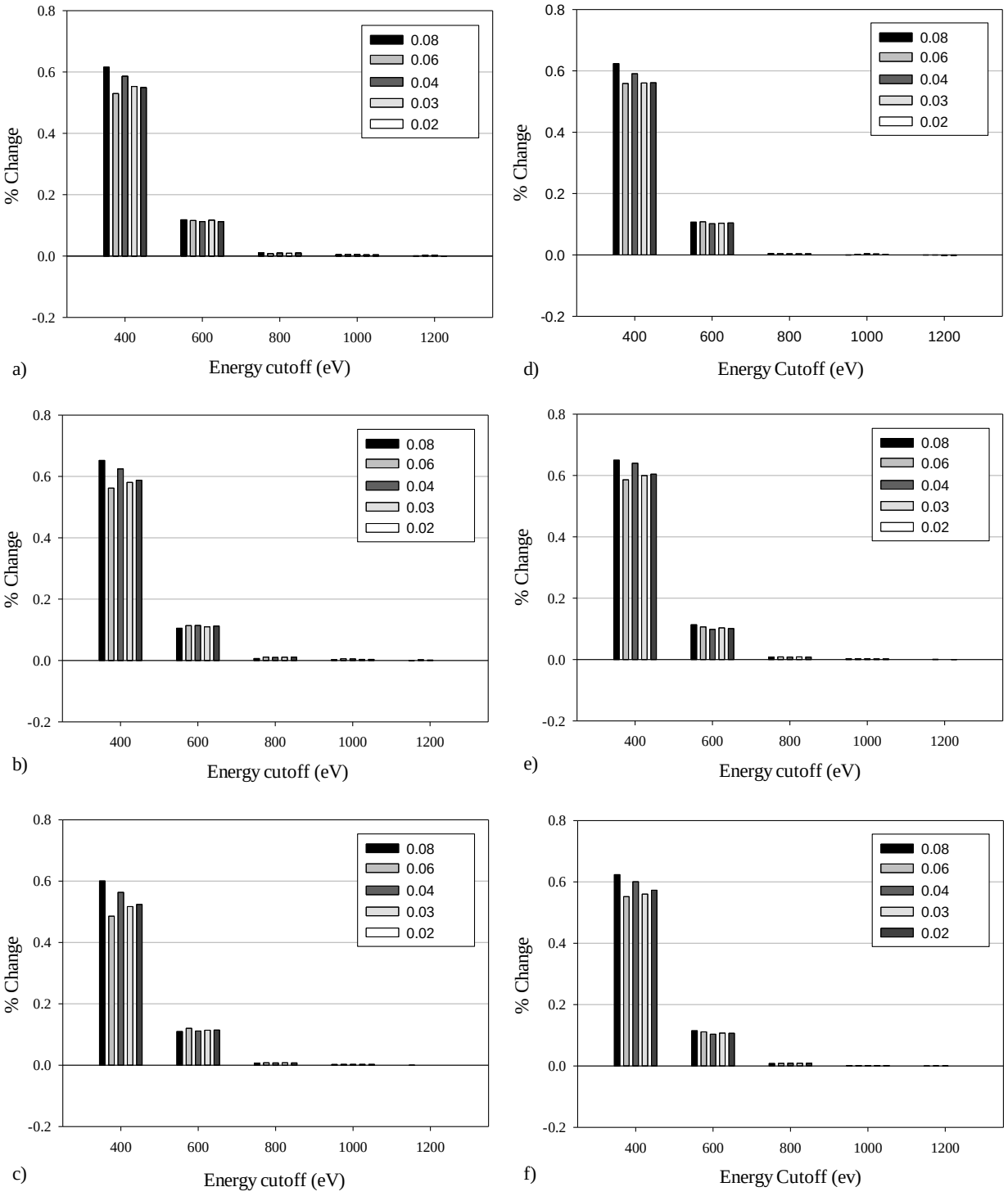

Figure 5.4: The convergence test carried out on CO_2-V for the C-O bond length, using (a) GGA-PBE, (b) GGA-PBE-TS, (c) GGA-PBE-Grimme when subjected to a hydrostatic pressure of 43 GPa and using (d) GGA-PBE, (e) GGA-PBE-TS and (f) GGA-PBE-Grimme when subjected to a hydrostatic pressure of 60 GPa. Note that the Y axis give the percentage deviation for the C-O bond length when compared to the C-O bond length obtained when the simulation is carried out using a cut-off energy of 1200 eV and a spacing of 0.02 $Å^{-1}$ for the Monkhorst-Pack grid, whilst the legend indicates the spacing used (in $Å^{-1}$) for the Monkhorst-Pack grid.

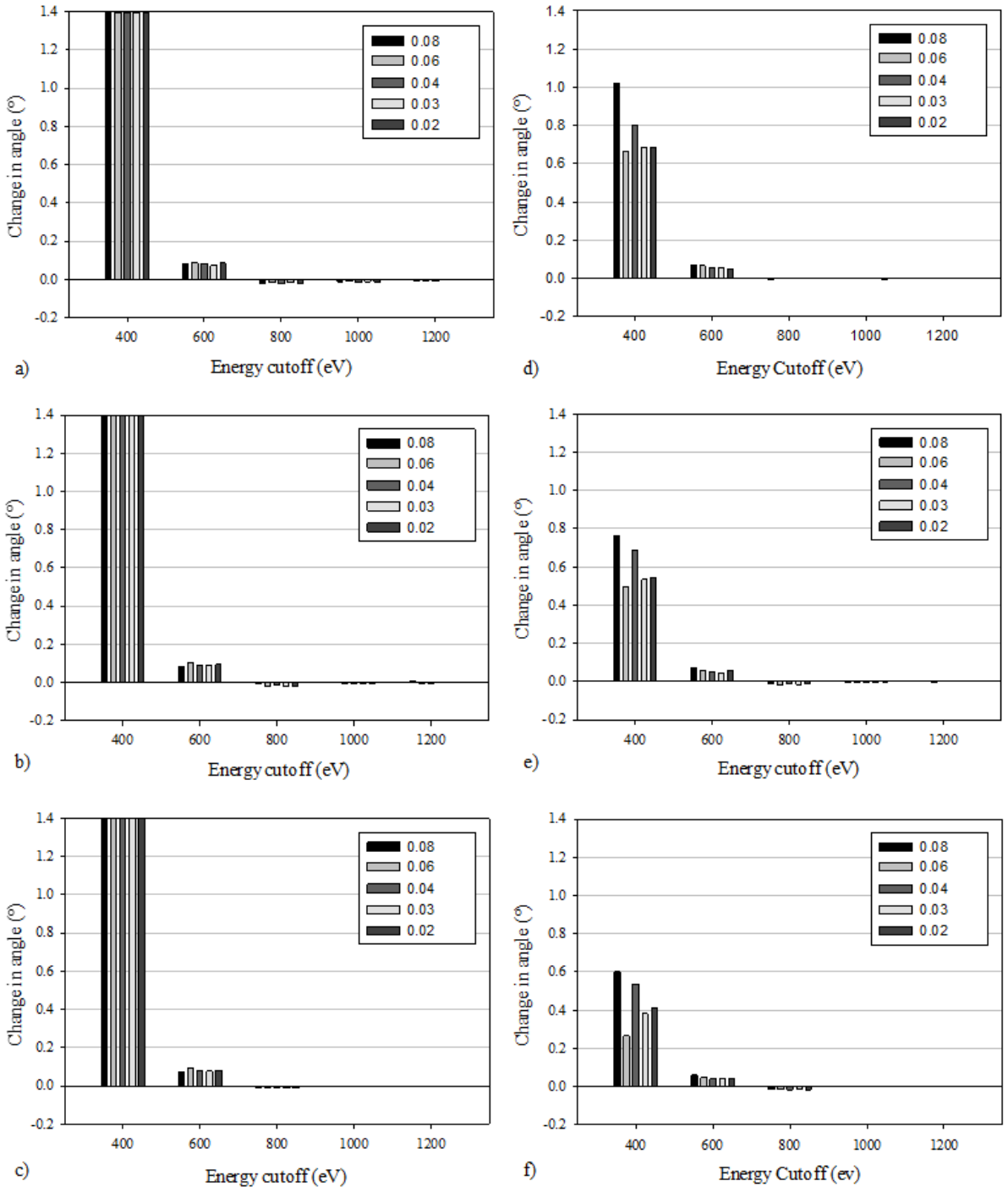

Figure 5.5: The convergence test carried out on CO_2-V for the C-O-C angle, using (a) GGA-PBE, (b) GGA-PBE-TS, (c) GGA-PBE-Grimme when subjected to a hydrostatic pressure of 43 GPa and using (d) GGA-PBE, (e) GGA-PBE-TS and (f) GGA-PBE-Grimme when subjected to a hydrostatic pressure of 60 GPa. Note that the Y axis give the change in angle (°) for the C-O-C angle when compared to the C-O-C angle obtained when the simulation is carried out using a cut-off energy of 1200 eV and a spacing of 0.02 $Å^{-1}$ for the Monkhorst-Pack grid, whilst the legend indicates the spacing used (in $Å^{-1}$) for the Monkhorst-Pack grid. The scale of the graph is truncated to 1.4 and -0.2.

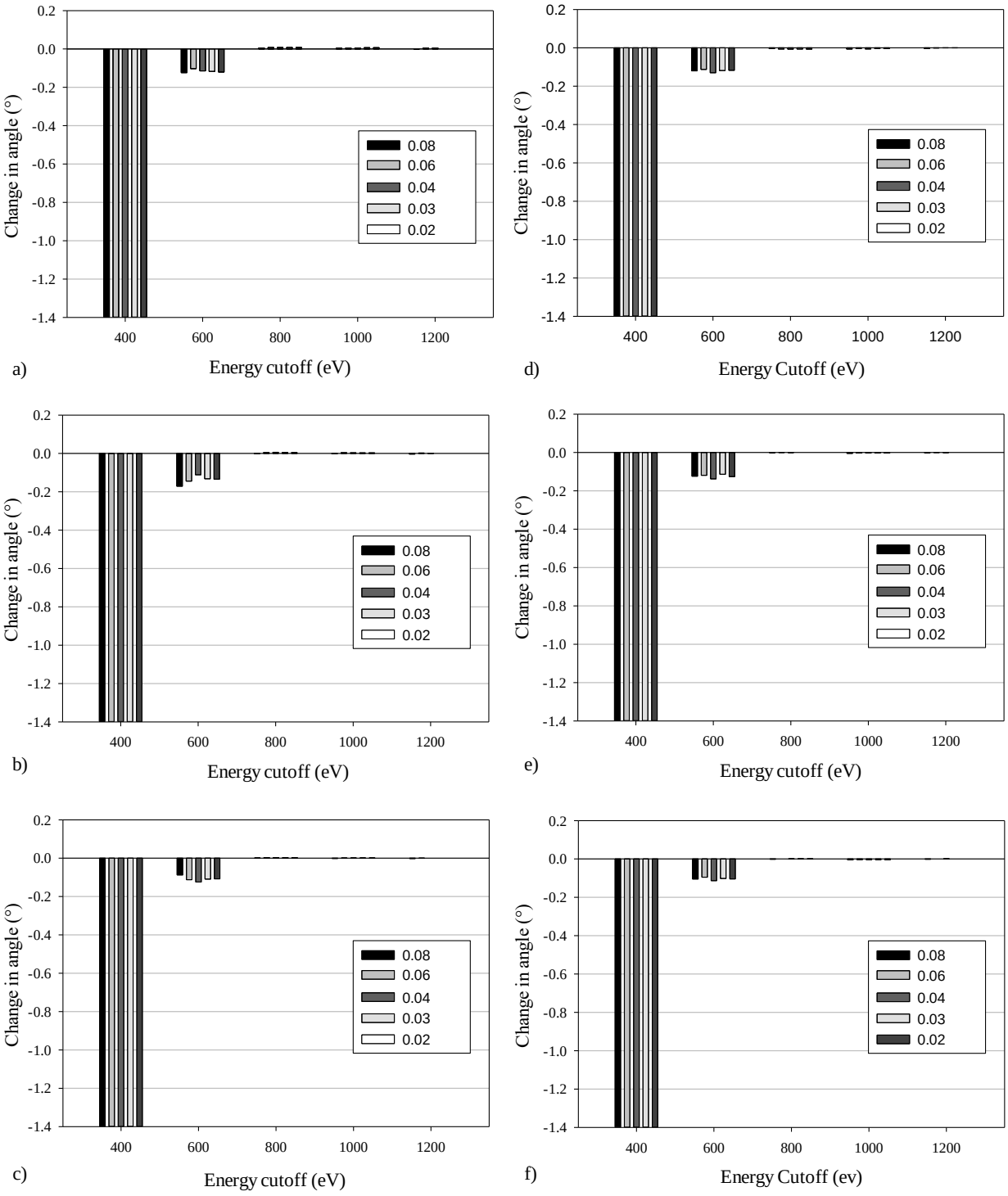

Figure 5.6: The convergence test carried out on CO_2-V for the O-C-O angle, using (a) GGA-PBE, (b) GGA-PBE-TS, (c) GGA-PBE-Grimme when subjected to a hydrostatic pressure of 43 GPa and using (d) GGA-PBE, (e) GGA-PBE-TS and (f) GGA-PBE-Grimme when subjected to a hydrostatic pressure of 60 GPa. Note that the Y axis give the change in angle (°) for the O-C-O angle when compared to the O-C-O angle obtained when the simulation is carried out using a cut-off energy of 1200 eV and a spacing of 0.02 $Å^{-1}$ for the Monkhorst-Pack grid, whilst the legend indicates the spacing used (in $Å^{-1}$) for the Monkhorst-Pack grid. The scale of the graph is truncated to 0.2 and -1.4.

In order to benchmark the methodology employed and choose an appropriate functional for the rest of the study, structural parameters as calculated utilising the different functionals namely PBE, PBE-TS and PBE-Grimme, were compared to experimentally determined values[162] with both the experimental work and calculations being conducted at a hydrostatic pressure of 43 GPa. Comparing the calculated lattice parameters to the experimentally determined values, (see Table 5.1), one can note that all three functionals give good agreement with the experimental work with all three functionals giving a percentage deviation of less than 0.5 % for the *a*-lattice parameter and *b*-lattice parameter and a maximum deviation of 1 % for the *c*-lattice parameter. In particular for the *a*-lattice parameter and *b*-lattice parameter percentage deviations of 0.47 %, 0.10 % and -0.20 % were recorded when utilising PBE, PBE-TS and PBE-Grimme respectively while for the *c*-lattice parameter percentage deviations of 0.64 %, 0.35 % and 1.01 % was recorded when utilising PBE, PBE-TS and PBE-Grimme respectively.

Table 5.1: Comparison of the calculated lattice parameters for CO_2-V at 43 GPa employing PBE, PBE-TS and PBE-Grimme and the experimentally determined data[162] obtained at the same pressure.

		This work		
Lattice parameter	Experimental[162]	PBE	PBE-TS	PBE-Grimme
a (Å)	3.5601	3.5768	3.5636	3.5529
b (Å)	3.5601	3.5768	3.5635	3.5529
c (Å)	5.8931	5.9305	5.9137	5.9525

Following the benchmarking of the lattice parameter, bond lengths and bond angles obtained utilising DFT calculations were also benchmarked by comparing to experimentally determined values [162] as shown in Table 5.2. It can be seen that all three functionals adequately simulate the structure of CO_2-V with a maximum deviation of less than 1 % being recorded for the C-O bond length, a maximum deviation of about 1° for the C-O-C angle and a maximum deviation of less than 0.15° for the O-C-O angle. In particular for the C-O bond length a percentage difference of 0.91 %, 0.72 % and 0.79 % was recorded for PBE, PBE-TS and PBE-Grimme respectively, while for the C-O-C angle a difference of -0.72°, -0.99° and -0.95° was recorded for PBE, PBE-TS and PBE-Grimme respectively. For the O-C-O angle a difference of -0.05°, -0.09° and 0.12° was recorded for PBE, PBE-TS and PBE-Grimme respectively.

Table 5.2: Comparison of the calculated bond lengths and angles for CO_2-V at 43 GPa employing PBE, PBE-TS and PBE-Grimme and the experimentally determined[162] data obtained at that the same pressure.

		This work		
Bond length or angle	Experimental[162]	Distance (Å) or angle (°) PBE	Distance (Å) or angle (°) PBE-TS	Distance (Å) or angle (°) PBE-Grimme
C-O	1.353	1.365	1.363	1.364
C-O-C	117.3	116.6	116.3	116.4
O-C-O	107.2	107.2	107.1	107.3

Given that all three functionals give good agreement with the experimental work with PBE providing a slightly more accurate representation of the angles, PBE will be used for the rest of the study with PBE-TS and PBE-Grimme being used to consolidate the work carried out. In addition, using the PBE functional, the simulated fractional coordinates of the atoms in

the CO_2-V unit cell had a maximum deviation of 2.65×10^{-3} in any direction when compared with experimental data[162], see Figure 5.7. In view of all this and in accordance with other studies carried out on CO_2-V in the literature[26,56,174,176], in this work PBE was used to study the mechanical properties of CO_2-V with the dispersion corrected functionals PBE-Grimme and PBE-TS being utilised to consolidate the work done.

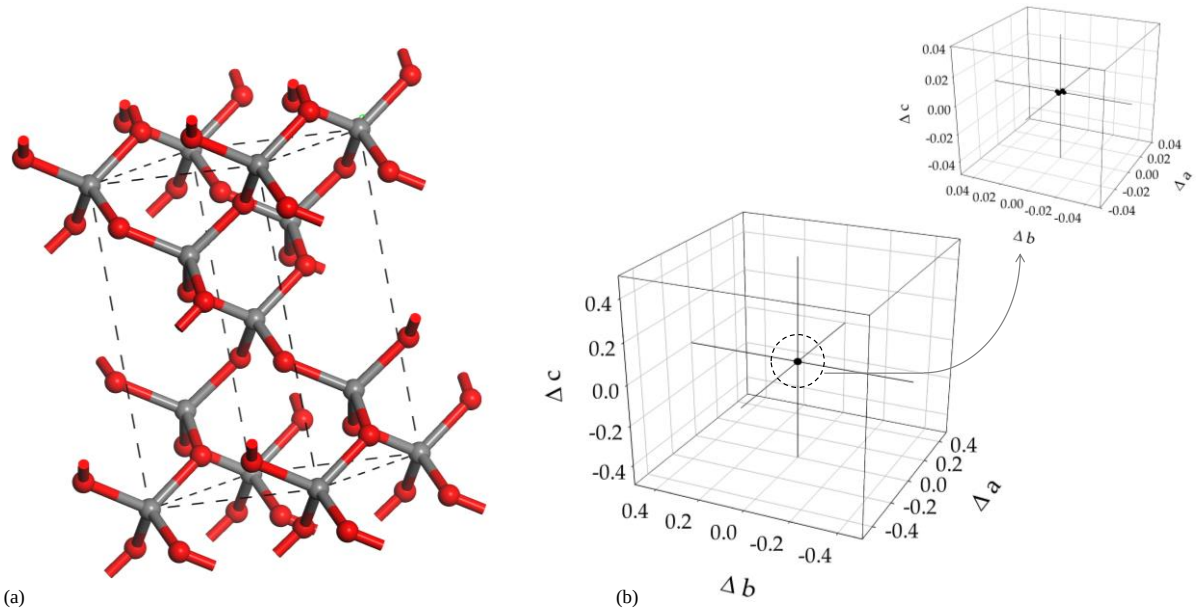

Figure 5.7: (a) The experimental structure of CO_2-V where grey spheres represent carbon atoms while red spheres represent oxygen atoms. (b) The difference between fractional coordinates of each atom present in the experimental lattice of CO_2-V [162] and those predicted in this work. The axes of the graph represent the change in fractional coordinates in the a, b, c directions. Note that in the case of the main graph the scale of these axes is set to illustrate ±50% of the respective lattice length whilst the scale of the inset is set to show ±1% of the respective lattice length.

5.2.4 Conclusion

The work in this section served to validate and benchmark the methodology employed. In brief, this section has shown that an energy cut-off of 800 eV and a Monkhorst-Pack grid spacing of 0.06 $Å^{-1}$ are appropriate to study the properties of the CO_2-V crystal. Moreover, it has also been shown that even though the PBE, PBE-TS and PBE-Grimme all give appropriate representation of this system, the PBE functional gives a slightly better representation and thus,

will be used for the rest of the study with the PBE-TS and PBE-Grimme being used to consolidate the results obtained where appropriate.

5.3 Studying the properties of CO_2-V

5.3.1 Introduction

Following the convergence study and benchmarking of the methodology, the mechanical and vibrational properties of CO_2-V will be assessed. First the stability of CO_2-V will be assessed through the use of lattice dynamics simulations in the pressure range of 40 GPa to 60 GPa. This will be followed by an investigation of the mechanical properties of the single crystal and the polycrystalline aggregate. The Young's modulus, shear modulus, bulk modulus, Pugh ratio and the Poisson's ratio of the system will be investigated. Anomalous mechanical properties of this system will be rationalised by studying the deformation mechanism of the system through measurements of the nanoscale deformation of the system and the use of infrared and Raman spectroscopy.

5.3.2 Methodology

Unless otherwise stated, simulations were performed using the PBE functional, an energy cut-off of 800 eV and a Monkhorst-Pack k-point grid spacing of 0.06 $Å^{-1}$, as determined in the previous section. As stated in Section 5.3.1, various properties were simulated in this section, with each methodology described in detail below.

5.3.2.1 Phonon dispersion

Phonon dispersion curves were calculated at 40 GPa and 60 GPa employing the linear response method utilising the interpolation scheme, as shown in Chapter 4 section 4.3.2.1. Convergence for the phonon dispersion relations was also tested by repeating the simulation using an energy cut-off of 1000 eV and a Monkhorst-Pack k-point grid spacing of 0.04 $Å^{-1}$.

5.3.2.2 Mechanical Properties

Geometry optimisation of the structure of CO_2-V was carried out in the pressure range of 40 GPa to 60 GPa in steps of 5 GPa. For each structure generated, the stiffness matrix, [C] was calculated using the constant-strain method, making sure that a linear stress-strain relationship was achieved in each case. Stringent convergence criteria were employed including a maximum force of 0.002 eV/Å, a maximum displacement of 1×10^{-4} Å and an energy cut-off of 1×10^{-6} eV/atom. The maximum strain amplitude was set to 0.003 with 4 steps for each strain.

Employing standard transformation techniques[397], each stiffness matrix was utilised to determine the off-axis mechanical properties for the CO_2-V single crystal namely the Young's modulus, the shear modulus and the Poisson's ratio. To ensure that the mechanical properties generated were not an artefact of the simulation parameters chosen or the functional employed, the mechanical properties at 40 and 60 GPa were recalculated using an energy cut-off of 1000 eV and a Monkhorst-Pack k-point grid spacing of 0.04 $Å^{-1}$and different functionals (PBE-TS and PBE-Grimme). The elastic constants calculated employing the PBE functional were then utilised to calculate the mechanical properties of the polycrystalline aggregate in the pressure range of this study, as described in Chapter 3 section 3.3.2.2. The bulk modulus, shear modulus and the Pugh ratio for the polycrystalline aggregate were determined as explained in detail in Chapter 3 section 3.3.2.2.

5.3.2.3 Deformation mechanism

In order to rationalise the measured Poisson's ratio of the CO_2-V single crystal, the deformation of this system was studied by applying a series of stresses, σ, in the range of ±0.5% of the Young's modulus in the two different directions, namely in the [100] direction and at 45° to this direction i.e. in the [110] direction. This was carried out at 40 GPa and 60 GPa. The stresses applied were in the form of:

$$\begin{pmatrix} \cos(\zeta) & \sin(\zeta) & 0 \\ -\sin(\zeta) & \cos(\zeta) & 0 \\ 0 & 0 & 1 \end{pmatrix} \begin{pmatrix} \sigma & 0 & 0 \\ 0 & 0 & 0 \\ 0 & 0 & 0 \end{pmatrix} \begin{pmatrix} \cos(\zeta) & -\sin(\zeta) & 0 \\ \sin(\zeta) & \cos(\zeta) & 0 \\ 0 & 0 & 1 \end{pmatrix}$$

where ζ is the in-plane rotation angle. Measurements of lengths and angles were then carried out for the 3D CO_4 tetrahedra and for projected distances of these tetrahedra in the (001) plane as shown in Figure 5.8 at 40 GPa and 60 GPa in order to elucidate the deformation mechanism.

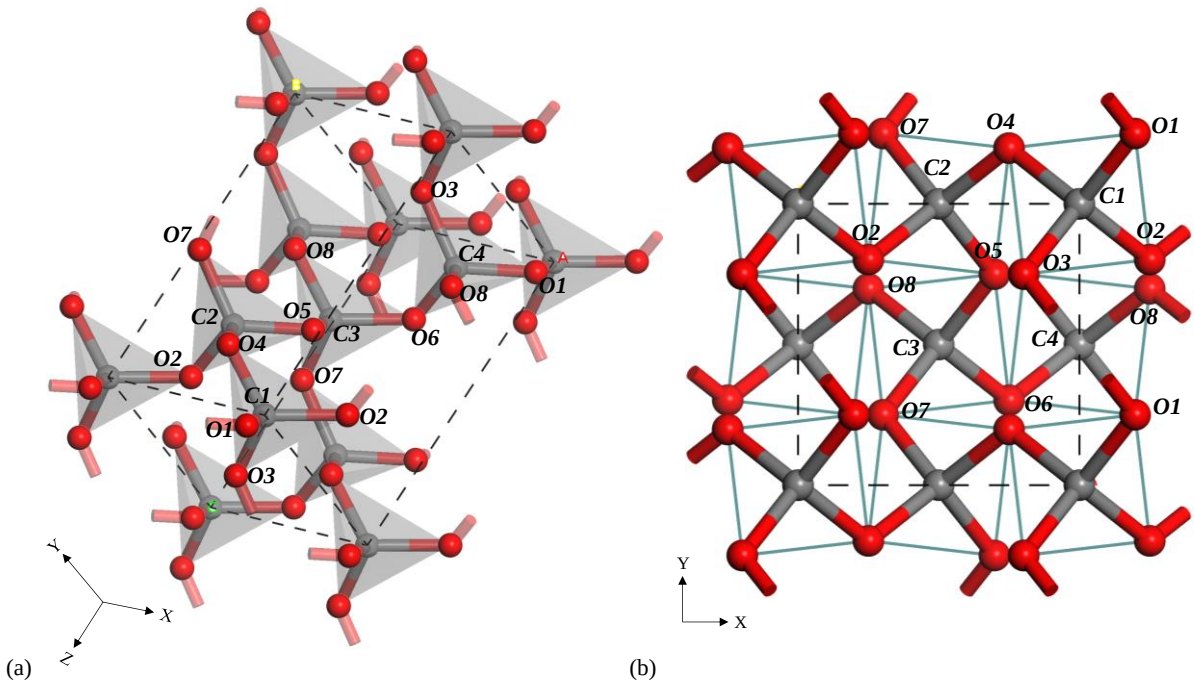

Figure 5.8: (a) The structure of CO_2-V with the CO_4 tetrahedra highlighted. (b) The (001) plane of CO_2-V with the projected 'rotating' squares highlighted.

5.3.2.4 IR and Raman spectroscopy

Raman and IR spectra of CO_2-V were also calculated at 40 GPa and 60 GPa to further substantiate the proposed deformation mechanism. These simulations were carried out as explained in Chapter 3 section 3.3.2.4 and Chapter 4 section 4.3.2.4. To confirm that the Raman and infrared spectra obtained were not an artefact of the simulation parameters or functional employed, the spectra were recalculated using an energy cut-off of 1000 eV and a Monkhorst-Pack k-point grid spacing of 0.04 $Å^{-1}$ whilst also using the PBE-TS and PBE-Grimme functionals at 40 GPa and 60 GPa.

5.3.3 Results and discussion

The results obtained shows that CO_2-V is predicted to exhibit auxetic behaviour over a wide range of pressures, with auxeticity becoming more pronounced with increasing pressure. This negative Poisson's ratio, exhibited in the (001) plane for loading in any direction within this plane, is rationalised through the use of the rotating squares mechanism, which squares are a projection of three-dimensional CO_4 tetrahedra. A detailed discussion on the results obtained is given below.

5.3.3.1 Lattice Dynamics calculations

Several studies have shown that of CO_2-V is stable within this pressure range of 40 GPa to 60 GPa[37,176,182]. This was also confirmed in this study through the use of lattice dynamics calculations. The results obtained, see Figure 5.9, show that the phonon dispersion relations obtained at 40 GPa and 60 GPa were all in the positive region indicating that CO_2-V is indeed stable or metastable at these pressures. To ensure that the simulation parameters used are indeed suitable to calculate the phonon dispersion curves for CO_2-V, the simulation was repeated using a higher energy cut-off and a smaller Monkhorst-Pack grid spacing as described in Section 5.3.2.1. Referring to Figure 5.9 refining the simulation parameters had no significant effect on

the dispersion curve obtained, ensuring that the result obtained i.e. CO_2-V is stable or metastable at the pressures ranges studied, is not an artefact of the simulation parameters utilised.

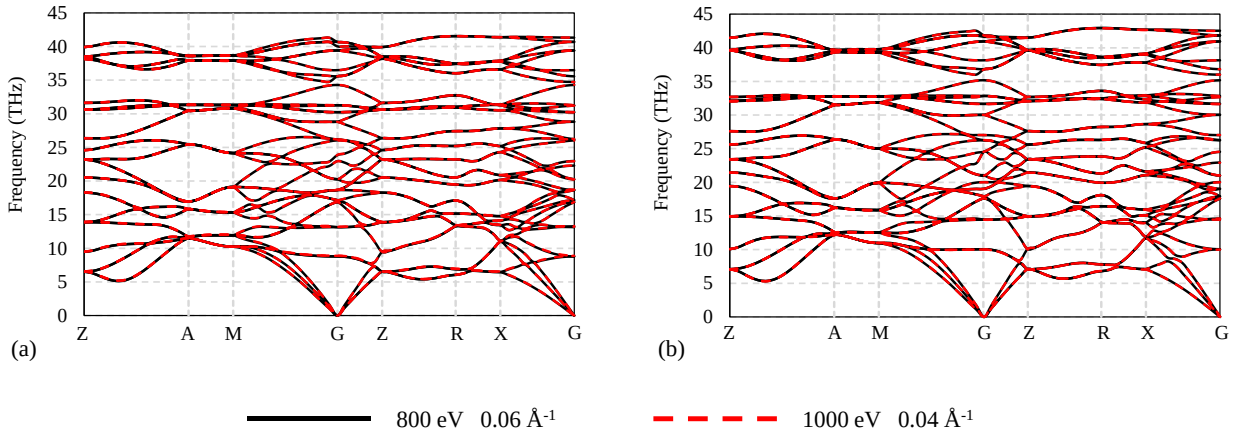

Figure 5.9: The phonon dispersion curves calculated for CO_2-V at (a) 40 GPa and (b) 60 GPa employing an energy cut-off of 800 eV and a Monkhorst-Pack k-point grid spacing of 0.06 $Å^{-1}$ (black solid line) and an energy cut-off of 1000 eV and a Monkhorst-Pack k-point grid spacing of 0.04 $Å^{-1}$ (red dashed line).

5.3.3.2 Elastic constants

The elastic constants obtained for CO_2-V had the expected symmetry for a tetragonal system [397] with crystal class $\bar{4}2m$ where $c_{11} = c_{22}$, $c_{31} = c_{32}$, $c_{44} = c_{55}$ while as expected c_{66}, c_{33} and c_{21} are non-zero components of matrix for all the pressures considered. The elastic stiffness constants obtained for each pressure computed in this study are shown in Table 5.3. The calculated elastic constants were then utilised to determine the off-axis mechanical properties for the CO_2-V single crystal. Due to the tetragonal nature of the CO_2-V system, the mechanical properties in the (010) plane are identical to the mechanical properties in the (100) plane and thus only the mechanical properties in the (010) plane are shown. The results obtained, see Figure 5.10, indicate that CO_2-V is anisotropic and exhibits a negative Poisson's ratio. For all

pressures considered in this study, auxetic behaviour was found in the (001) plane, with the maximum auxeticity measured when loading in the [100] direction.

Table 5.3: The computed elastic constants for CO_2-V in the pressure range of 40 GPa to 60 GPa.

Pressure (GPa)	**c_{11} (GPa)**	**c_{33} (GPa)**	**c_{21} (GPa)**	**c_{31} (GPa)**	**c_{44} (GPa)**	**c_{66} (GPa)**
40	495.03	497.46	77.20	290.07	295.43	135.36
45	515.51	525.51	86.52	311.69	310.27	140.90
50	533.27	552.18	96.09	330.79	324.57	146.74
55	553.30	580.47	108.28	350.88	338.75	153.32
60	570.96	609.48	120.98	370.91	352.67	160.40

Figure 5.10 also shows how the mechanical properties of CO_2-V change as a function of pressure, with the auxetic potential of CO_2-V in the (001) plane increasing with an increase in hydrostatic pressure. Considering the (001) plane, an increase in the hydrostatic pressure results in a larger change for the Poisson's ratio obtained when loading in the [110] direction when compared to the Poisson's ratio obtained when loading in the [100] direction. In fact, the ratio $\nu_{yx}^{\zeta=0^\circ}/\nu_{yx}^{\zeta=45^\circ}$ changes from 3.89 at 40 GPa to 2.12 at 60 GPa. The Young's modulus in the [100] direction and shear modulus in the (001) plane also increase with increasing pressure. Similarly, to the Poisson's ratio, the on-axis and off-axis E_x and G_{xy} change to a different extent with increasing hydrostatic pressure. The ratio $E_x^{\zeta=0^\circ}/E_x^{\zeta=45^\circ}$ changes from 1.19 at 40 GPa to 1.14 at 60 GPa while the ratio $G_{xy}^{\zeta=0^\circ}/G_{xy}^{\zeta=45^\circ}$ changes from 0.65 at 40 GPa to 0.71 at 60 GPa.

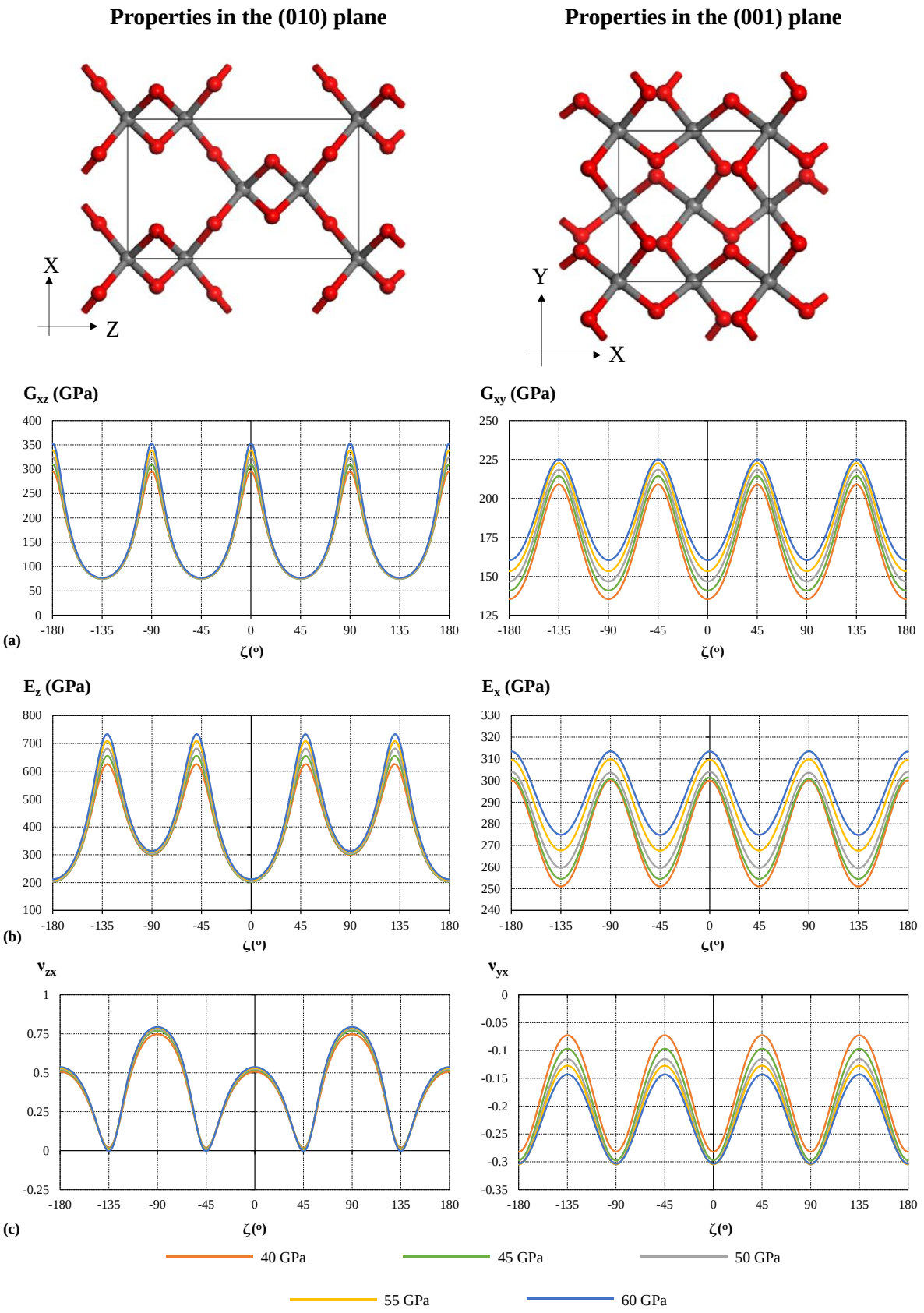

Figure 5.10: The structure of CO_2-V together with off-axis plots illustrating the mechanical properties of this system in the (010) and (001) plane with varying pressure from 40 GPa to 60 GPa in steps of 5 GPa. Shown here are the variation of the shear modulus (in GPa) (a), Young's modulus (in GPa) (b) and Poisson's ratio (c) with angle of rotation, ζ (in °), in these planes.

This result was confirmed with the use of more stringent simulation parameters as described in Section 5.3.2.2. The off-axis shear modulus, Young's modulus and Poisson's ratio obtained at 40 GPa and 60 GPa are shown in Figure 5.11 and Figure 5.12. The results obtained show that a refinement in the energy cut-off and the spacing of the Monkhorst-Pack grid had no significant effect on the off-axis mechanical properties obtained and hence the parameters used are adequate to simulate the mechanical properties.

In order to consolidate the work done in section above, the elastic constants of CO_2-V were recalculated employing PBE-TS and PBE-Grimme at 40 GPa and 60 GPa. The elastic constants obtained were then utilised to calculate the off-axis mechanical properties of CO_2-V at 40 GPa and 60 GPa, as shown in Figure 5.13 and Figure 5.14 respectively. It can be seen that the trends for mechanical properties obtained utilising the different functionals are similar. Of particular interest to this study is the fact that the negative Poisson's ratio of CO_2-V in the (001) plane is reported with all functionals utilised. This suggests that the auxetic potential of CO_2-V is not an artefact of the functional used but rather an innate property of the system.

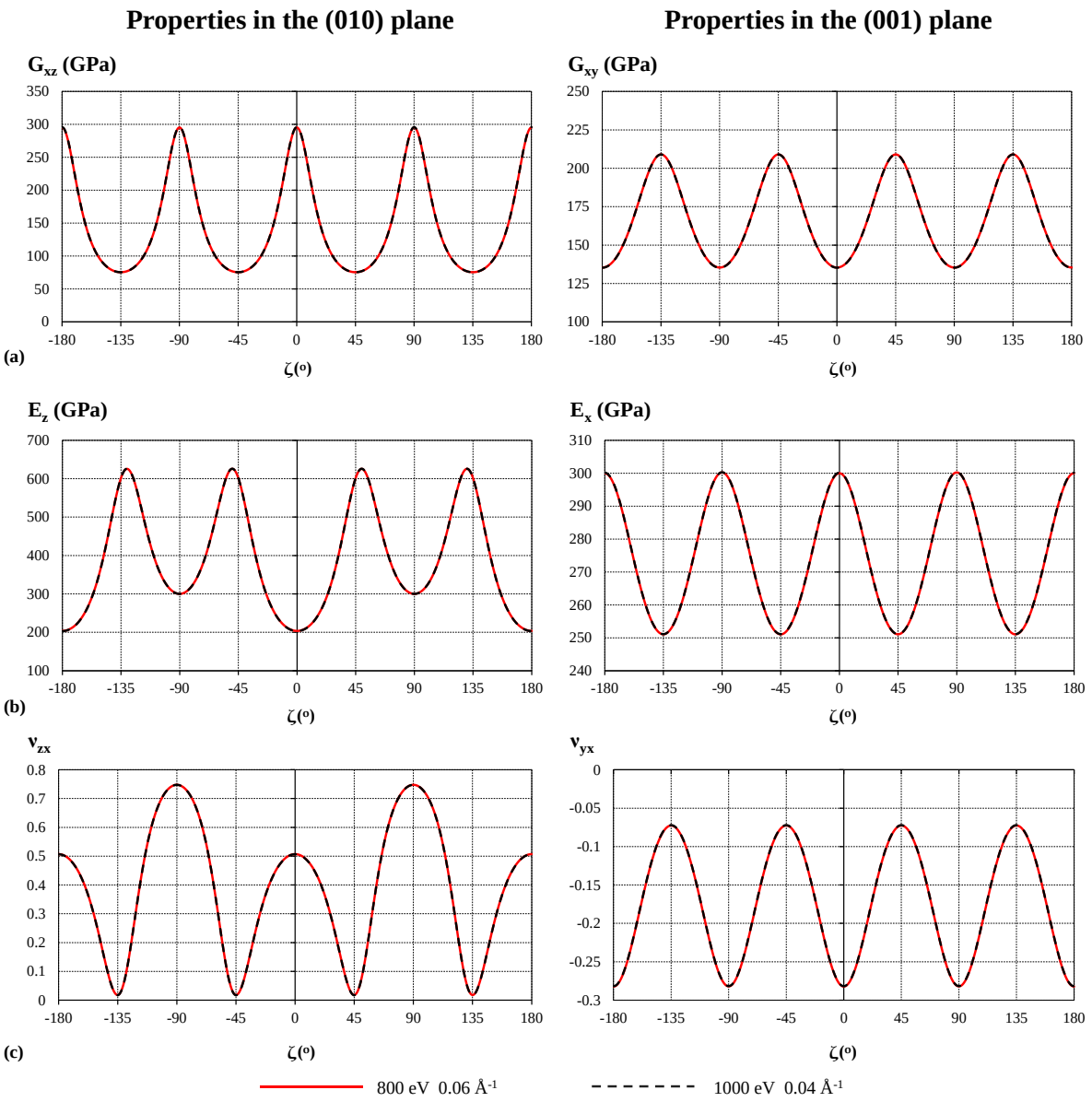

Figure 5.11: The effect of refining simulation parameters from an energy cut-off of 800 eV and a Monkhorst-Pack grid spacing of 0.06 Å^{-1} to 1000 eV and 0.04 Å^{-1} respectively on the shear modulus (in GPa) (a), Young's modulus (in GPa) (b) and Poisson's ratio (c) calculated at 40 GPa in the (010) plane and the (001) plane.

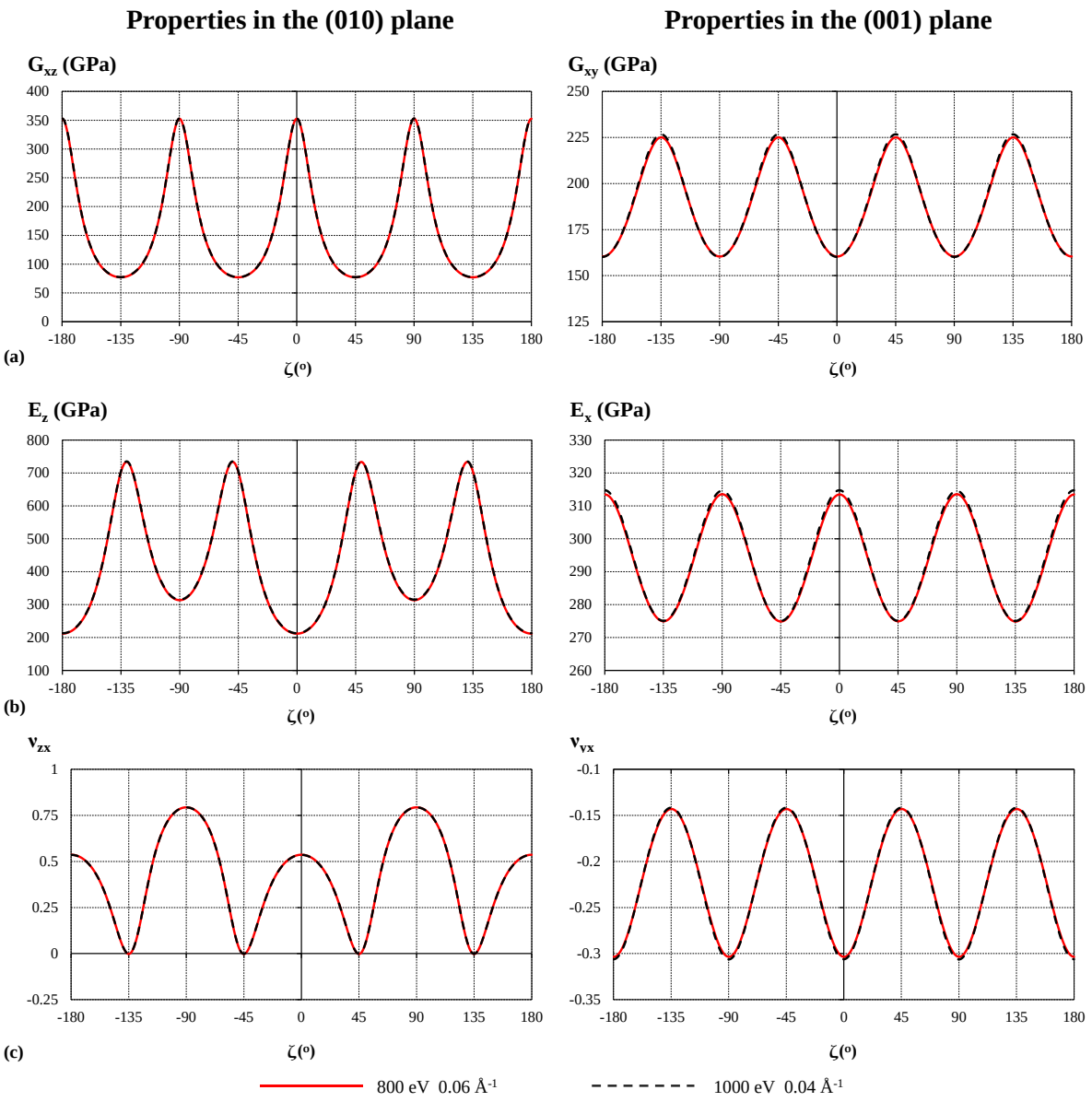

Figure 5.12: The effect of refining simulation parameters from an energy cut-off of 800 eV and a Monkhorst-Pack grid spacing of 0.06 Å^{-1} to 1000 eV and 0.04 Å^{-1} respectively on the shear modulus (in GPa) (a), Young's modulus (in GPa) (b) and Poisson's ratio (c) calculated at 60 GPa in the (010) plane and the (001) plane.

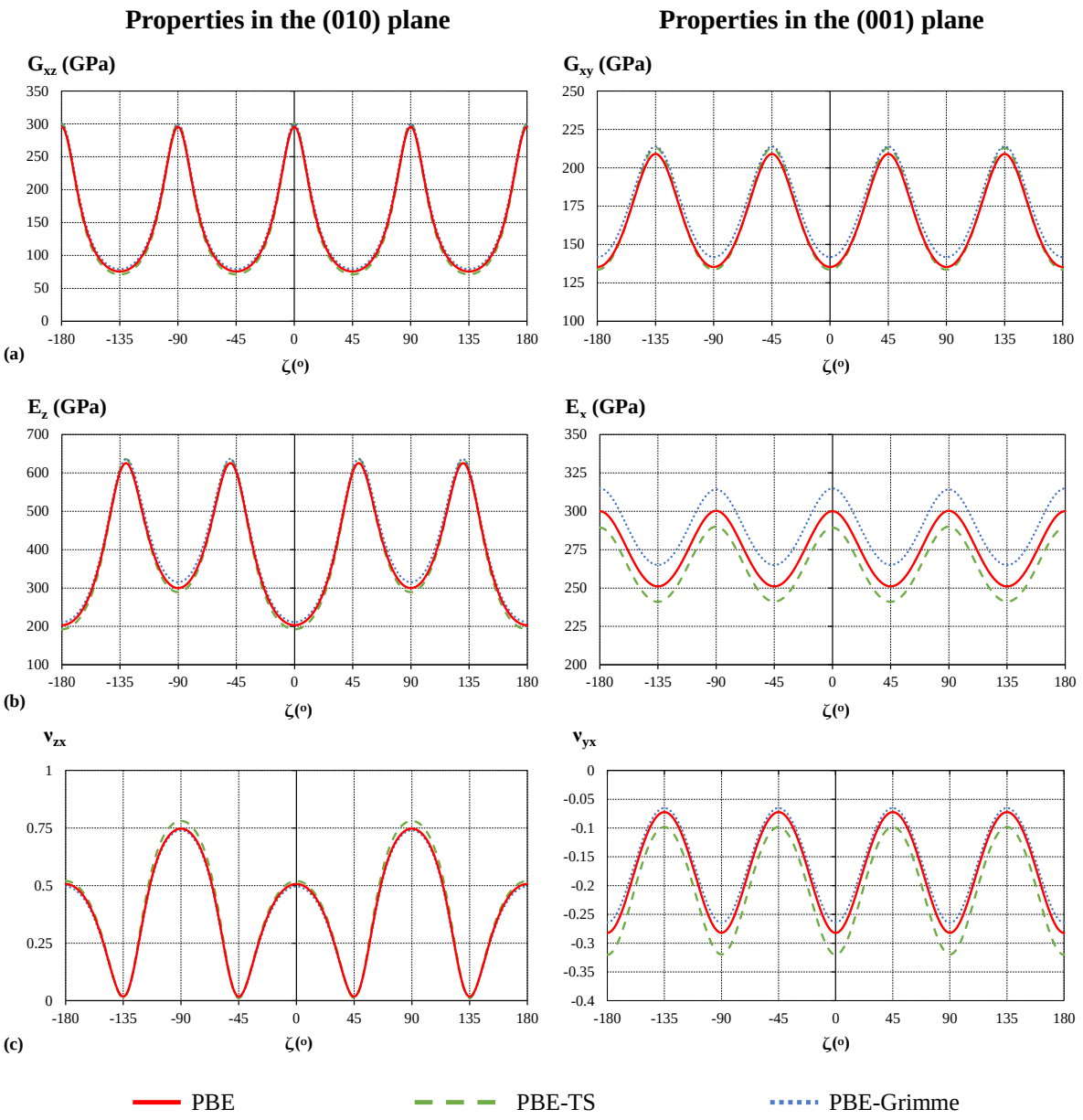

Figure 5.13: The variation of the shear modulus (in GPa) (a), Young's modulus (in GPa) (b) and Poisson's ratio (c) with angle of rotation, ζ (in °) in the (010) plane and the (001) plane at 40 GPa as calculated utilising PBE, PBE-TS and PBE-Grimme. It can be seen that there is good agreement between the mechanical properties calculated with all three functionals. This confirms that mechanical properties predicted are not an artefact of the functional used but an innate property of the system.

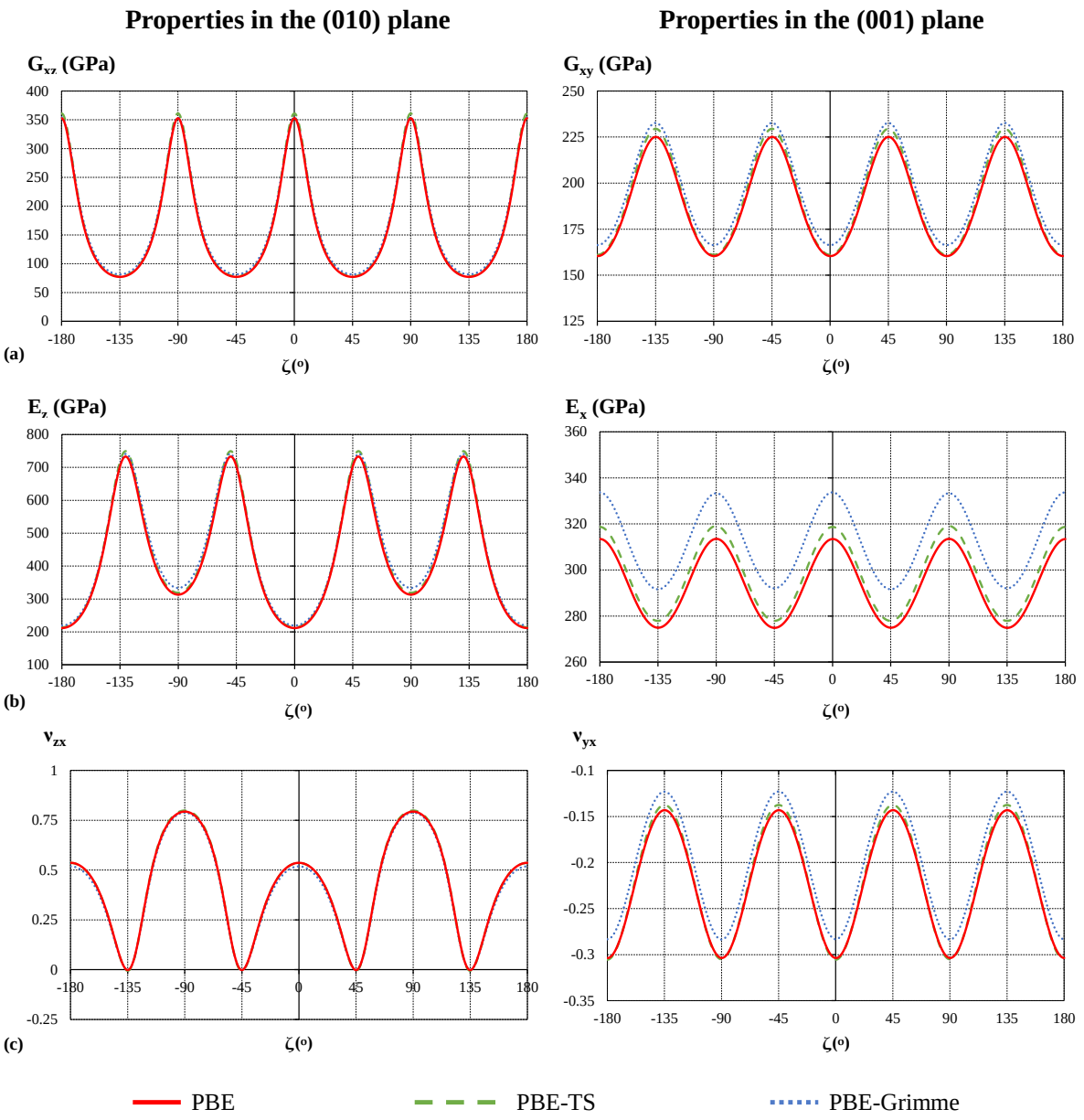

Figure 5.14: The variation of the shear modulus (in GPa) (a), Young's modulus (in GPa) (b) and Poisson's ratio (c) with angle of rotation, ζ (in °) in the (010) plane and the (001) plane at 60 GPa as calculated utilising PBE, PBE-TS and PBE-Grimme. It can be seen that there is good agreement between the mechanical properties calculated with all three functionals. This confirms that mechanical properties predicted are not an artefact of the functional used but an innate property of the system.

5.3.3.3 Polycrystalline properties

Although a negative Poisson's ratio was measured in the (001) plane, the Poisson's ratio for the polycrystalline aggregate of CO_2-V was always computed to be positive at all pressures considered in this study. The elastic constants of CO_2-V can be utilised to determine the mechanical properties for the polycrystalline aggregate as described in previous work[400], employing an approach which assumes that the crystal domains in the sample are arranged in such a way that the material is isotropic. In particular, the maximum and minimum bounds of the Poisson's ratio for the CO_2-V polycrystalline aggregate can be calculated from the material's elastic constants, which results are shown in Table 5.4. It can be noted that the polycrystalline aggregate is predicted to exhibit a positive Poisson's ratio in the pressure range of this study, in contrast to the single crystal which is predicted to exhibit a negative Poisson's ratio in the (001) plane. In addition to this, it can be noted that an increase in hydrostatic pressure is associated with an increase in both the maximum and minimum bounds for the Poisson's ratio.

Table 5.4: The variation of the maximum and minimum bounds for the Poisson's ratio of CO_2-V polycrystalline aggregate with varying hydrostatic pressure in the pressure range of 40 GPa to 60 GPa.

Pressure (GPa)	ν^{max}	ν^{min}	ν
40	0.301	0.216	0.258
45	0.309	0.218	0.263
50	0.314	0.219	0.266
55	0.318	0.222	0.270
60	0.323	0.224	0.273

The elastic constants of CO_2-V may also be employed to determine the bulk modulus and shear modulus of the polycrystalline aggregate employing the Voigt-Reus-Hill approximation[399–401], which properties, together with the Pugh ratio (K/G ratio), are shown in Table 5.5 . It can be noted that an increase in hydrostatic pressure is associated with an increase in both the bulk modulus and the shear modulus.

Table 5.5: The pressure dependence of the maximum and minimum bounds for the bulk modulus K^{Voigt} and K^{Reuss}, and shear modulus G^{Voigt} and G^{Reuss} for CO_2-V polycrystalline aggregate together with the K/G ratio (Pugh ratio) of the polycrystalline aggregate.

Pressure (GPa)	**K^{Voigt} (GPa)**	**K^{Reuss} (GPa)**	**K* (GPa)**	**G^{Voigt} (GPa)**	**G^{Reuss} (GPa)**	**G (GPa)**	**K/G**
40	311	286	299	201	143	172	1.74
45	331	300	315	209	145	177	1.78
50	348	313	331	217	148	182	1.81
55	368	329	348	225	152	188	1.85
60	386	343	365	232	155	194	1.88

The calculated elastic constants may also be utilised to predicted whether CO_2-V is expected to be brittle or ductile in the pressure range of this study. A number of different criteria may be considered such as the Cauchy pressure, the Poisson's ratio and the K/G ratio. The Cauchy pressure[408], for a tetragonal system can be defined as c_{13}-c_{44} and c_{12}-c_{66}, where a positive value suggests that the material is ductile while a negative value suggests that the material is brittle. The results obtained, shown in Figure 5.15, suggest that CO_2-V is expected to be brittle in the pressure range under consideration with the term c_{13}-c_{44} being a negative term over the whole pressure range.

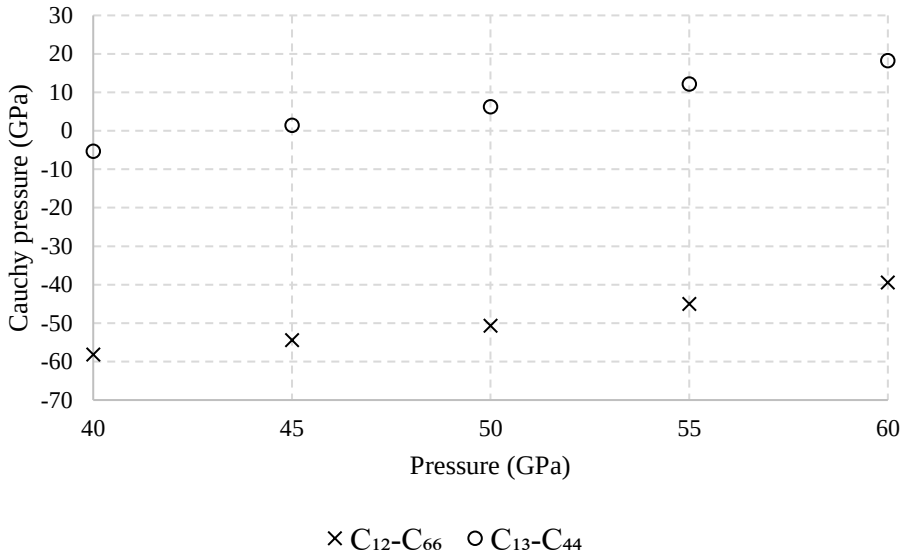

Figure 5.15: The variation of c_{13}-c_{44} and c_{12}-c_{66} with increasing hydrostatic pressure in the pressure range of this study.

The Poisson's ratio may also be utilised to predicted whether a material is expected to be brittle or ductile by employing what is known as Frantsevich rule[409] where a Poisson's ratio less than 0.33 indicates that a material is brittle while a Poisson's ratio greater than 0.33 indicates that the material is ductile. In the case of CO_2-V, the Poisson's ratio for the polycrystalline aggregate is less than 0.33 as shown in Table 5.1, suggesting that CO_2-V is brittle in the pressure range of 40 GPa – 60 GPa, which is in accordance to the work done when analysing the Cauchy pressure.

Another check for the brittle or ductile nature of the material is by studying the K/G ratio which is known as the Pugh ratio [402]. It was suggested that a K/G value exceeding 1.75 indicates that the material is ductile while a K/G value less than 1.75 suggests that the material is brittle. Referring to Table 5.5, it can be noted that the K/G ratio is above 1.75 in most of the pressure range under study with the exception of 40 GPa where a value of 1.74 is reported. The K/G values above 1.75 indicate that the material is ductile which is in contradiction to the previous predictions made employing the Cauchy pressure and the Frantsevich rule.

Recently[241] it has been argued that Pugh's criterion for the ductile-brittle transition, which employs a K/G value of 1.75 as the benchmark, should be replaced by Christensen's criterion where a K/G value of 2.27 is used to indicate the ductile/brittle transition where a K/G value of less than 2.27 indicates that the material is brittle and a K/G value greater than 2.27 indicating that the material is ductile. Utilising Christensen's criterion, CO_2-V would be predicted to be brittle as the K/G ratio is less than 2.27 in the pressure range under study. All the above considerations suggest that CO_2-V is expected to be brittle in the pressure range of 40 GPa to 60 GPa.

5.3.3.4 Deformation mechanism

At this stage it would be interesting to rationalise the simulated auxetic potential of the CO_2-V system in the (001) plane. An analysis of the projections of the atoms in this plane reveals a 'connected squares' motif, see Figure 5.8. These 'connected squares' are the two-dimensional projection of three-dimensional CO_4 tetrahedra with each square having a carbon atom at its centre and four oxygen atoms at its corners. The projected squares have internal angles of 90.00° (st. dev. 0.000°) and side lengths of 1.63 Å (st. dev. 0.000 Å) at 40 GPa while at 60 GPa, the projected squares have side lengths of 1.60 Å (st. dev. 0.000 Å) and internal angles of 90.00° (st. dev. 0.001°). It is known that such 'connected squares motif' can result in a negative Poisson's ratio of -1 if the system deforms solely through the relative rotations of the squares upon loading[215]. As explained in the methodology, a series of stresses were applied in the [100] direction of CO_2-V (the direction of maximum auxeticity), in order to assess how these projected squares deform.

At a pressure of 40 GPa, application of a stress in the [100] direction results in the relative rotation and distortion of the projected squares. More specifically, referring to Figure

5.16, upon the application of a tensile stress, the projected squares rotate relative to each other such that they open up, with angle O5-O4-O3 increasing in size and angle O4-O3-O6 decreasing in size. Concurrently, the application of the tensile stress in this direction also results in an 'asymmetric stretching' of the projected squares with the sides of the projected squares oriented in the direction of side O3-O2 (see Figure 5.8 and Figure 5.16) stretching to a higher degree than the sides of the projected squares oriented in the direction of side O2-O1, with the ratio $\Delta O3-O2/\Delta O2-O1$ having a value of 4.71. The 'asymmetric stretching' of the projected squares is also accompanied by a change in internal angles. This change in internal angles of the projected squares is also quite large when compared to the change in angle between the projected squares, with the ratio $\Delta O3-O4-O5/\Delta O3-O4-O1$ having a value of -3.36 (the negative value is due to the fact that angle O3-O4-O1 is becoming smaller while O3-O4-O5 is becoming larger when the system is stretched in the [100] direction). All this means that when a load in the [100] direction is applied to CO_2-V, the projected squares rotate relative to each other whilst distorting to form parallelograms, rationalising the deviation of the Poisson's ratio from the theoretical value of -1 expected from the rotating rigid units mechanism.

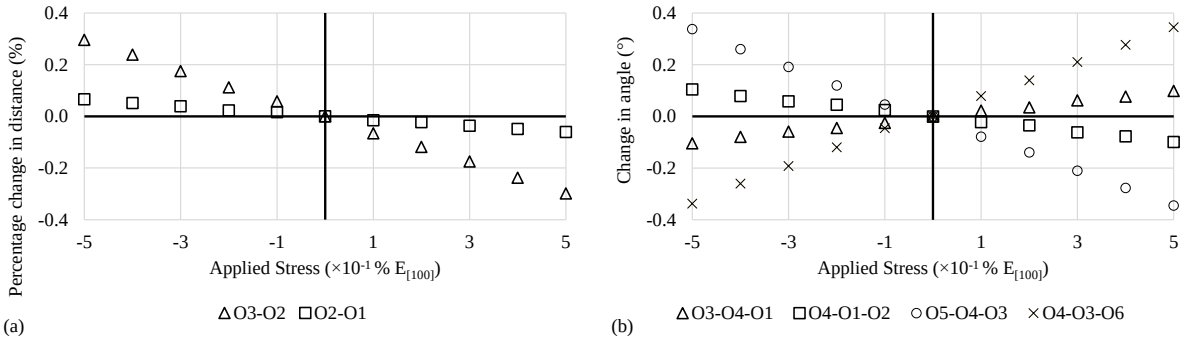

Figure 5.16: (a) Percentage change in distances (%) and (b) change in angles (°) recorded for various points shown in Figure 5.8 at 40 GPa on application of a stress in the [100] direction. It should be noted that a negative stress indicates a pulling force while a positive stress indicates a compressive force.

Considering CO_2-V at 60 GPa, one finds that the application of a stress in the [100] direction results in a similar mechanism described above, where the projected squares are acting as semi-rigid rotating squares (see Figure 5.17). Also, the on-axis auxetic potential of CO_2-V increases slightly with an increase in hydrostatic pressure, a phenomenon that may be attributed to a slight increase in the rigidity of the projected squares. In fact, when a load is applied in the [100] direction, the sides of the projected squares oriented in the direction of side O3-O2 change by -3.21×10^{-3} Å/GPa at 40 GPa whilst at 60 GPa they change by -2.95×10^{-3} Å/GPa. On the other hand, the sides of the projected squares oriented in the direction of side O2-O1 change by -6.80×10^{-4} Å/GPa at 40 GPa while at 60 GPa they change by -5.83×10^{-4} Å/GPa. Furthermore, the changes in the angles inside the projected squares vary from 0.0668 °/GPa at 40 GPa to 0.0546 °/GPa at 60 GPa. The changes in the angles between the projected squares also become smaller as the hydrostatic pressure increases, however these decrease at a lower rate than the angles inside the projected squares. For example, the quantity ΔO5-O4-O3/ΔO3-O4-O1 changes from -3.36 at 40 GPa to -3.48 at 60 GPa indicating that the internal angles of the projected squares are becoming stiffer than the angles between the projected squares. Thus, as hydrostatic pressure increases, even though the hinge between the projected squares becomes stiffer, the projected squares deform to a smaller extent, resulting in a small increase in the auxetic potential.

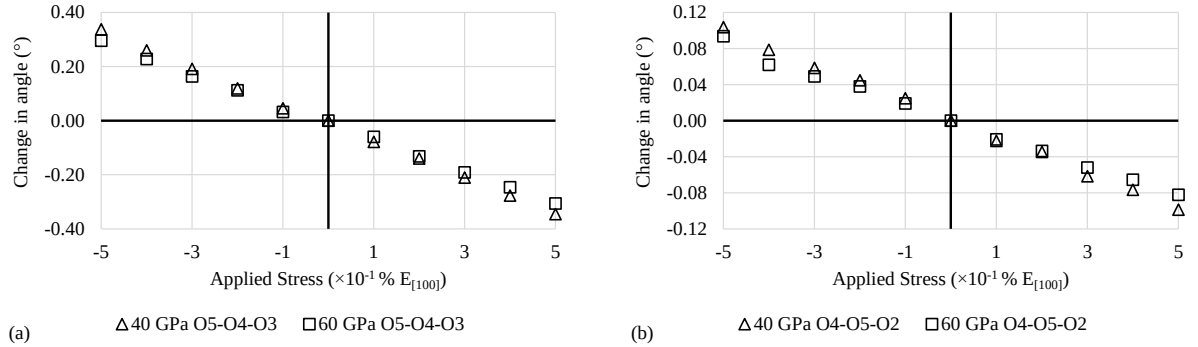

Figure 5.17: (a) Comparison of change in angle O5-O4-O3 at 40 GPa and 60 GPa. (b) Comparison of change in angle O4-O5-O2 at 40 GPa and 60 GPa.

As discussed above, CO_2-V is also predicted to exhibit auxetic behaviour when loaded in the [110] direction. This auxetic behaviour may be rationalised by studying the nanoscale deformation on application of a stress as detailed in the methodology section. Similarly, to the on-axis auxetic behaviour in the (001) plane, the auxetic behaviour when loading in the [110] direction may be explained through the rotation of the semi-rigid projected squares where the squares rotate relative to each other and concurrently deform. Referring to Figure 5.18 application of a stress in the [110] direction results in a change in angle O5-O4-O3 and angle O4-O3-O6 which angles are the angles between the projected 'squares' indicating that the squares are rotating relative to each other. It can also be noticed that the angles within the squares, O3-O4-O1 and O4-O1-O2, are also changing albeit at a lower rate than the angles between the squares. The change in interior angles of the squares denote that the squares are in fact distorting on application of a stress. In addition to this, referring to Figure 5.18, application of a stress in the [110] direction results in change in sides O3-O2 and O2-O1 of the projected 'squares'. It can be noted that the percentage change in length of the sides is not the same, with side O2-O1 changing length at a higher rate resulting in the distortion of the projected square. This distortion explains why the obtained Poisson's ratio deviates from -1[215], which is the expected value for the rotating squares mechanism which mechanism assumes that the squares rotate relative to each other without the deformation of the squares.

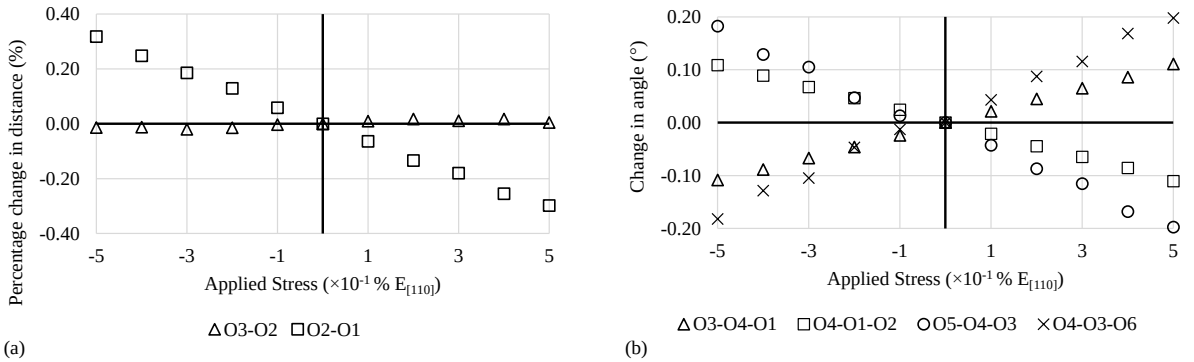

Figure 5.18: (a) Percentage change in distances (%) and (b) change in angles (°) recorded for various points shown in the main paper at 40 GPa on application of a stress in the [110] direction

Also, as discussed above, the Poisson's ratio obtained when loading in the [110] direction is less negative when compared to that obtained when loading in the [100] direction. This can be explained by the ratio of the projected squares' 'rigidity' to their relative rotation of the projected squares. For instance, at a hydrostatic pressure of 40 GPa loading in the [110] direction results in a smaller relative rotation of the projected squares with angle O5-O4-O3 changing by -0.147 °/GPa when loading in this direction, compared with a change of -0.225 °/GPa when loading in the [100] direction. Furthermore, a load in the [100] direction results in a change of 3.21×10^{-3} Å/GPa and -6.80×10^{-4} Å/GPa for side lengths O3-O2 and O4-O3 of the projected squares respectively. On the other hand, a load in the [110] direction at the same hydrostatic pressure results in a change of 2.23×10^{-4} Å/GPa and -4.03×10^{-3} Å/GPa for side lengths O3-O2 and O4-O3 of the projected squares respectively. Additionally, the quantity ΔO3-O4-O5/ΔO3-O4-O1 changes from -3.36 when loading in the [100] direction to -1.69 when loading in the [110] direction indicating that the internal angles of the projected squares are less stiff when loading in the [110] direction.

As in the case of loading in the [100] direction, a load in the [110] direction at higher ambient pressures, results in a more negative Poisson's ratio. As discussed above, the change

in the Poisson's ratio when loading in the [110] direction is larger than that obtained when loading in the [100] direction. At higher ambient pressures, the 'rigidity' of the projected squares becomes larger when loading in the [110] direction compared to loading in the [100] direction for the same relative rotation of the projected squares.

For example, the ratio ΔO3-O2/ΔO4-O3 changes from 4.71 to 5.06 when loading in the [100] direction as the pressure changes from 40 GPa to 60 GPa whilst when loading in the [110] direction, the same ratio changes from -0.0555 to 0.0175 as the pressure changes from 40 GPa to 60 GPa. This indicates that when loading in the [110] direction the projected squares are retaining their square geometry more when compared to loading in the [100] direction. Moreover, the quantity ΔO3-O4-O5/ΔO3-O4-O1 changes from -3.36 to -3.48 when loading in the [100] direction whilst when loading in the [110] direction, the same ratio changes from -1.69 to -1.67 as the pressure changes from 40 GPa to 60 GPa indicating that the internal angles of the projected squares are relatively stiffer when loading in the [110] direction.

This two-dimensional approach is the result of the deformation of the CO_4 tetrahedra. In fact, as discussed above, each 2D square is the projection of a single CO_4 tetrahedron in the (001) plane, see Figure 5.8. Thus, the relative rotations and distortions of the projected squares are a direct result of the distortions and rotations of the CO_4 tetrahedra. In fact, referring to Figure 5.19, application of a stress in the [100] direction results in the concurrent rotation and distortion of the CO_4 tetrahedra. Application of a stress in the [100] direction results in an increase in C-O bond lengths, with the C-O bonds in the CO_4 tetrahedra stretching to different extents, contributing to the distortion of the tetrahedra. Moreover, the stress also results in a change in intertetrahedra angle (C-O-C), similarly as above, the C-O-C angles within a tetrahedron change to different extents contributing to distortion. Referring to Figure 5.19, it can be noted that O8-C3-O6 changes at a larger rate than C3-O6-C4. In addition to this,

application of a stress results in an increase in the angle C3-O6-C4 which is on the line of stress. This is then coupled with a very slight increase in C2-O5-C3. It can be noted that the change in intertetrahedral angles (O-C-O) are more significant than the change in intratetrahedral angle (C-O-C). This suggests that the auxetic potential of CO_2-V is a result of an interplay between stretching of C-O bonds, distortion of CO_4 tetrahedra and hinging between tetrahedra which is consistent with the 2D mechanism where it was shown that distortion and hinging of the 2D units played a role in explaining the auxetic potential of this system.

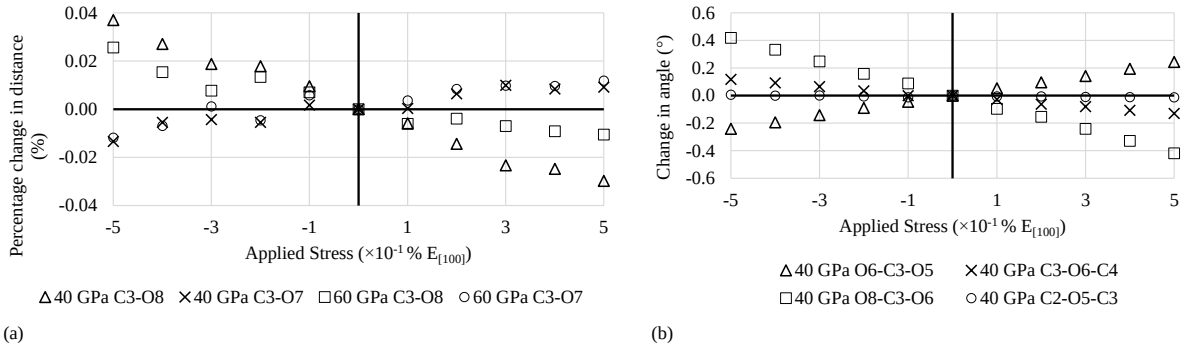

Figure 5.19: (a) Percentage change in C-O bond length with stress at 40 GPa and 60 GPa. (b) Change in C-O-C and O-C-O angles at 40 GPa.

Studying the effect of increase in hydrostatic pressure on the deformation mechanism, it can be noted an increase in hydrostatic pressure is associated with an increase in stiffness of the C-O covalent bond, with lengths C3-O8 showing a smaller percentage change in length at 60 GPa than 40 GPa (see Figure 5.19). It can also be noted that the C-O bonds within the CO_4 unit change length in a more similar manner leading to less distortion of the system. At 40 GPa C-O bond lengths, denoted by C3-O7 and C3-O8 change at a rate of 9.66×10^{-5} Å/GPa and -3.10×10^{-4} Å/GPa on application of a stress in the [100] direction while at 60 GPa C3-O7 and C3-O8 change at a rate of 9.23×10^{-5} Å/GPa and -1.46×10^{-4} Å/GPa respectively.

An increase in pressure is also associated with a decrease in the change of the O-C-O angles which also contribute to a decrease in distortion. At 40 GPa, application of a stress results in O8-C3-O6 and O6-C3-O5 changing at a rate of -0.276 °/GPa and 0.160 °/GPa respectively while at 60 GPa O8-C3-O6 and O6-C3-O5 change at a rate of -0.256 °/GPa and 0.153 °/GPa respectively. The C-O-C angle also changes albeit to a smaller degree, with C3-O6-C2 changing at a rate of -0.0816 °/GPa and C2-O5-C3 changing at a rate of -4.99×10^{-3} °/GPa at 40 GPa while C3-O6-C4 changes at a rate of -0.0591 °/GPa and C2-O5-C3 changes at a rate of 0.0137 °/GPa. Thus, as the hydrostatic pressure is increasing the CO_4 units distort to a smaller extent. The decrease in hinging is compensated by the fact the CO_4 units are acting in a more regular manner as the hydrostatic pressure is increased.

The above mechanism can also be utilised to rationalise the off-axis auxetic potential of CO_2-V, where application of a stress at 45° off-axis results in relative rotation of the semi-rigid CO_4 units. It has been shown that there is a more pronounced increase in auxetic potential off-axis than on-axis. Studying the effect of increasing pressure on the ratio of the rate of change of the intertetrahedral angles O7-C3-O5 and O8-C3-O6 shows that the larger the ratio the lower the auxetic potential of the system. The larger the ratio implies that the angles are changing at different rates from each other leading to distortion of the CO_4 unit. On-axis values of this ratio at 40 GPa and 60 GPa are 2.27 and 2.12 respectively while off-axis values at 40 GPa and 60 GPa are 3.24 and 2.71 respectively. On-axis values of this ratio are smaller than off-axis values which is consistent with the calculated Poisson's ratio, where CO_2-V exhibits greater auxetic potential on-axis than off-axis. It can also be noted that off-axis there is a larger decrease in this ratio with pressure than on-axis, which is associated with a more pronounced increase in auxetic behaviour off-axis than on-axis. Off-axis this ratio varies by 0.523 while on-axis this ratio varies by 0.154 on going from 40 GPa to 60 GPa.

5.3.3.5 Consolidating deformation through spectroscopy

In order to consolidate the work done on the three-dimensional deformation mechanism of CO_2-V, the Raman and infra-red spectrum of CO_2-V were calculated in the pressure range of 40 GPa – 60 GPa. The Raman spectrum of CO_2-V at 40 GPa, shown in Figure 5.20, is dominated by a strong A_1 peak at circa 765 cm^{-1} which shifts to circa 820 cm^{-1} at 60 GPa. This peak is due to the symmetric intertetrahedral C-O-C mode which involves stretching of the two C-O bonds and bending of the C-O-C angle[162,415]. The positive shift of this mode with increasing pressure shows that the intertetrahedral C-O-C is increasing in rigidity with an increase in hydrostatic pressure, which is consistent with the proposed three-dimensional deformation mechanism. The positive shift of the mode with pressure has also been reported in other studies[162,415]. The infra-red active modes for CO_2-V are B_2 and E which are split into a longitudinal and a transverse optical component[162]. These modes involve simultaneous stretching and bending which give an indication of the strength of the C-O bond and the O-C-O intratetrahedral angle. Referring to Figure 5.21, it can be seen that all the peaks in the infra-red spectrum shift to higher wavenumbers with an increase in hydrostatic pressure indicating an increase in the stiffness of the C-O bond and the C-O-C angle which is consistent with the proposed deformation mechanism.

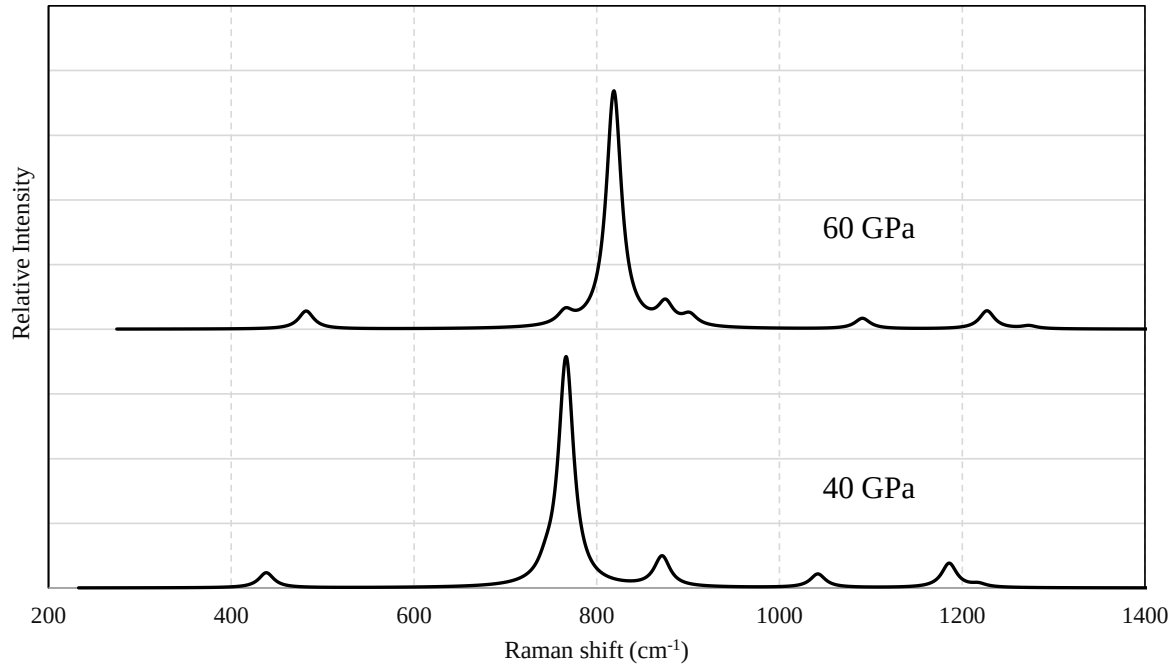

Figure 5.20: The Raman spectrum of CO_2-V at 40 GPa and 60 GPa as calculated utilising the PBE functional.

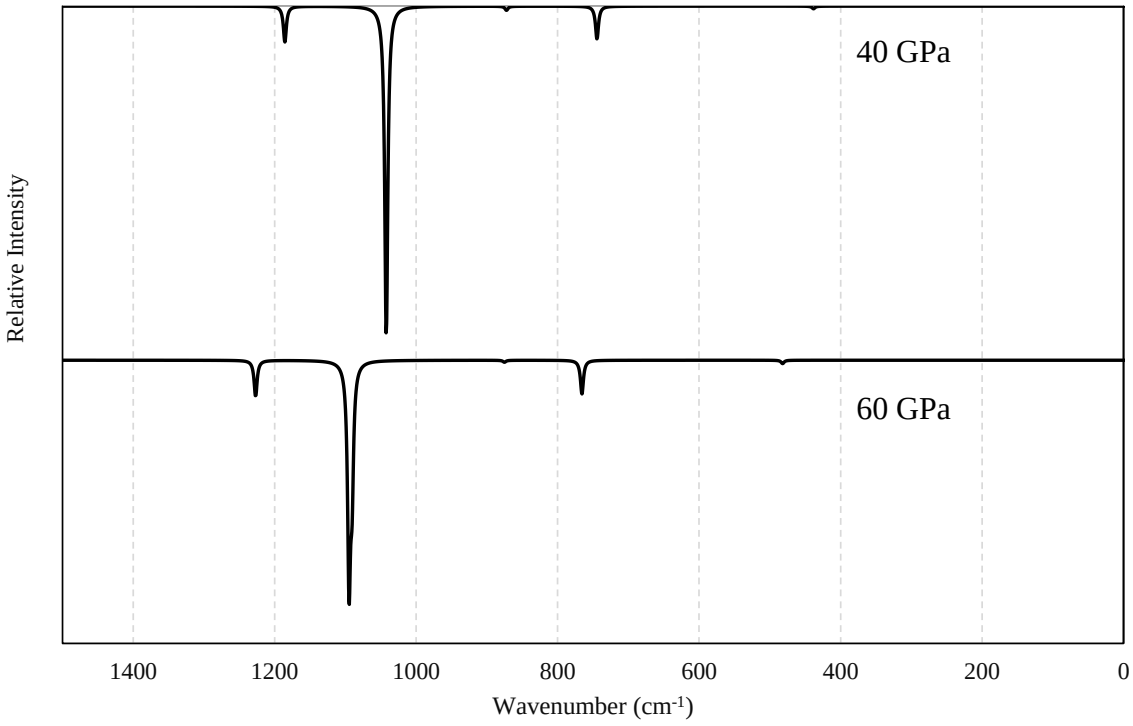

Figure 5.21: The infra-red spectrum of CO_2-V at 40 GPa and 60 GPa as calculated utilising the PBE functional.

To confirm that the cut-off energy and the spacing for the Monkhorst-Pack grid chosen are sufficient to adequately determine the Raman and infrared spectra of CO_2-V when using the PBE functional at 40 and 60 GPa, the simulations were repeated using an energy cut-off of 1000 eV and a Monkhorst-Pack grid spacing of 0.04 $Å^{-1}$ as explained in the methodology section. The results obtained, see Figure 5.22 and Figure 5.23, show that the refining the simulation parameters had no significant effect on the spectra obtained at both 40 GPa and 60 GPa. In particular, the same number of peaks are obtained and the effect of increasing hydrostatic pressure on the position of the peaks is the same irrespective of the simulation parameters employed. Furthermore, recalculating the spectra employing the dispersion corrected functionals PBE-TS and PBE-Grimme at 40 GPa and 60 GPa, see Figure 5.24 and Figure 5.25 also give very similar results. In fact, these spectra show that the same number of peaks are obtained, albeit with some slight shift in peak position depending on the functional used. Moreover, the shift in peak position with increasing hydrostatic pressure is the same irrespective of the functional used. This shows that the description of the deformation mechanism rationalising the auxetic potential of CO_2-V employing these spectra described above is not an artefact of the functional employed.

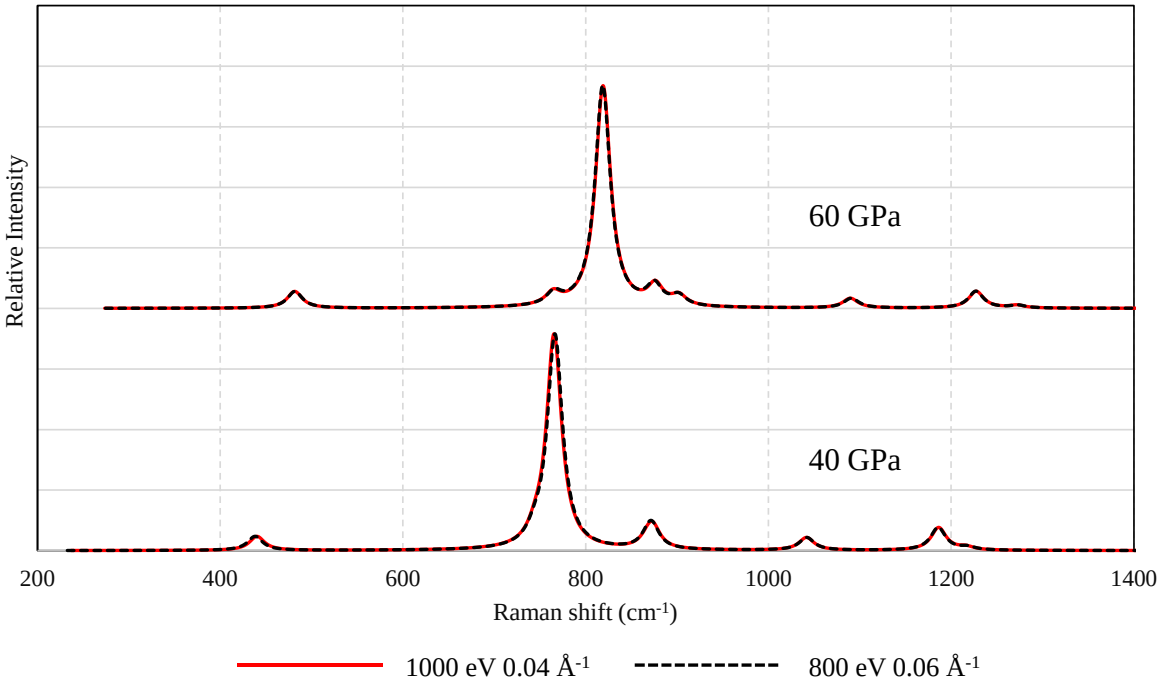

Figure 5.22: Comparison of the Raman spectrum obtained for CO_2-V when employing a cut-off energy of 800 eV and a Monkhorst-Pack grid spacing of 0.06 $Å^{-1}$ with the spectrum obtained utilising a cut-off energy of 1000 eV and a spacing of 0.04 $Å^{-1}$ at 40 GPa and at 60 GPa.

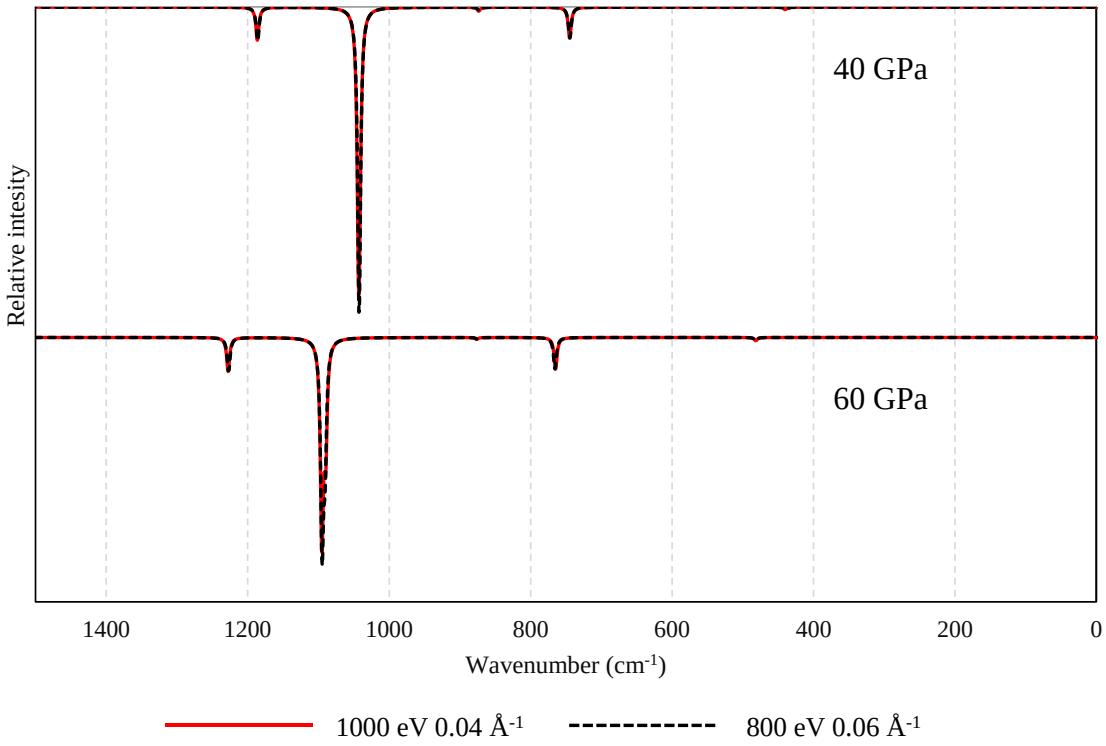

Figure 5.23: Comparison of the infrared spectrum obtained for CO_2-V when employing a cut-off energy of 800 eV and a Monkhorst-Pack grid spacing of 0.06 $Å^{-1}$ with the spectrum obtained utilising a cut-off energy of 1000 eV and a spacing of 0.04 $Å^{-1}$ at 40 GPa and at 60 GPa.

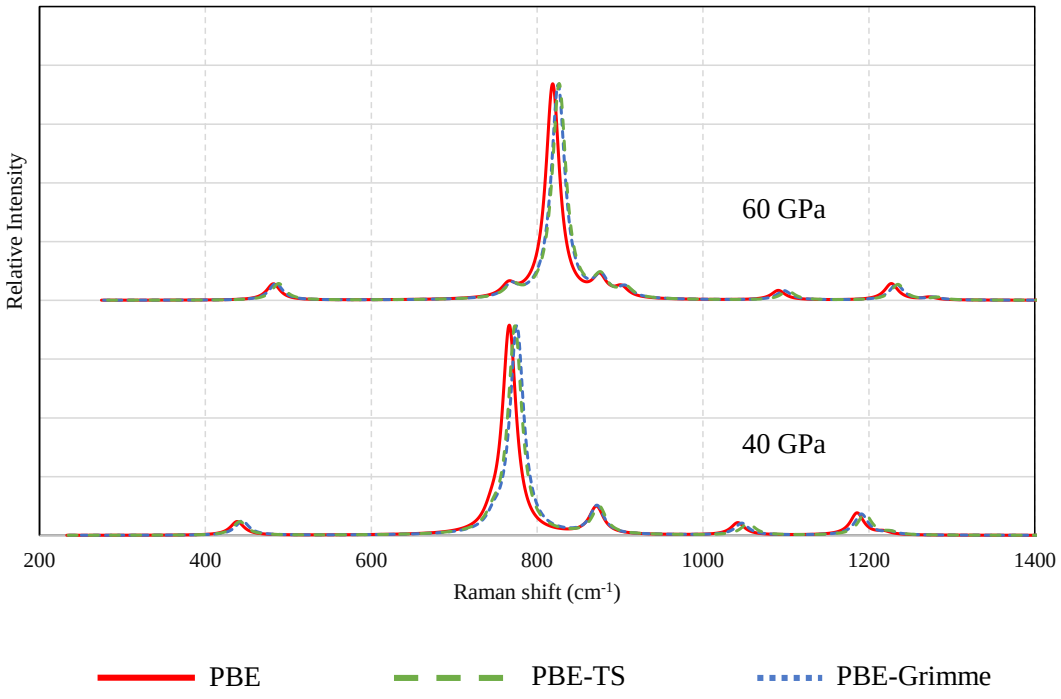

Figure 5.24: Comparison of the Raman spectrum calculated for CO_2-V using PBE, PBE-Grimme and PBE-TS at 40 GPa and 60 GPa.

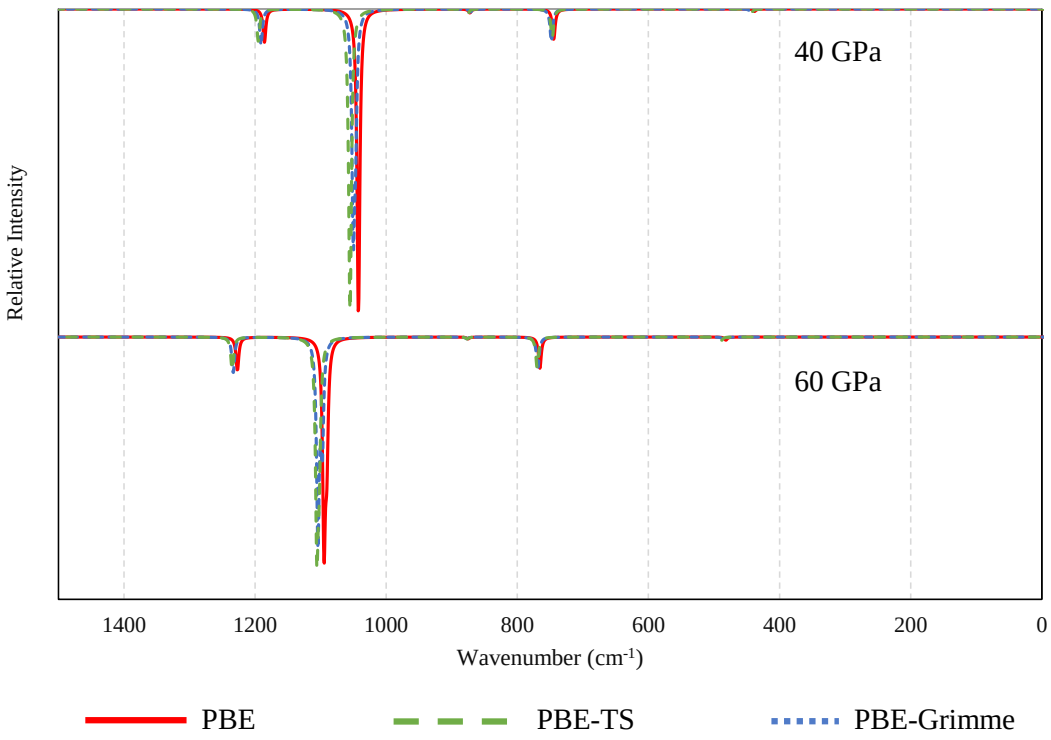

Figure 5.25: Comparison of the infrared spectrum calculated for CO_2-V using PBE, PBE-Grimme and PBE-TS at 40 GPa and 60 GPa.

All this is very significant as it increases the corpus of knowledge on the mechanical properties of CO_2-V, a substance which plays a vital role in planetary science. In particular, it has been shown that CO_2-V has the potential to exhibit a negative Poisson's ratio in the pressure range of this study which auxetic behaviour will have significant consequences on other physical properties of this material. This work also highlights the importance of the rotating squares geometry in the generation of auxetic behaviour and thus, this geometry may be used as a blueprint by experimentalists to synthesis materials with auxetic behaviour.

5.3.4 Conclusions

In this work, first principles calculations have been used to determine the structural, vibrational and mechanical properties of CO_2-V. It has been shown that CO_2-V has the potential of exhibiting a negative Poisson's ratio in the (001) plane with the auxetic potential varying depending on the direction of loading with the highest auxetic potential being reported for loading on-axis. It has also been shown that the Poisson's ratio of this system is pressure dependent with an increase in pressure resulting in an increase in auxetic potential both on-axis and off-axis with a more pronounced increase in auxetic potential being reported at 45° off-axis. The auxetic potential of this system has been studied by analysing the nanoscale deformation of this system on the application of a stress. The Poisson's ratio of CO_2-V was explained through the rotating squares mechanism where the squares are projections of the CO_4 tetrahedra in the (001) plane and were found to behave as semi-rigid units. Thus, the auxetic potential of CO_2-V may be explained by an interplay between the relative rotation of the units and deformation of the projected squares. As hydrostatic pressure is increased the rigidity of the units increases resulting in a decrease in the deformation of the projected squares. The decrease in deformation of the projected squares could explain the increase in auxetic potential of this system. The behaviour of the projected squares was shown to be a direct result of the rotation and distortion of the CO_4 tetrahedra.

Chapter 6: [*]An investigation of the mechanical properties of CO_2-II

6.1 Introduction

Following the work on the mechanical properties of CO_2-V carried out in Chapter 5, it would be now interesting to study another high-pressure polymorph of carbon dioxide. CO_2-V can be formed from CO_2-II by the application of pressure with a recent theoretical study showing that CO_2-II should undergo a phase transition to the macromolecular CO_2-V at 21.5 GPa at 0 K[176]. As detailed in Chapter 2, CO_2-II is a rather controversial substance with debates on the stability and structure of this high-pressure polymorph. In fact, some studies suggest that CO_2-II is more stable than CO_2-III at lower temperatures and high pressures[176,178] while others suggest that CO_2-III is the more stable phase at these conditions[15]. Moreover, some studies suggest that CO_2-II is an intermediate form between molecular and nonmolecular solids[179], while other studies did not find evidence of this intermediate state and instead it was argued that CO_2-II is a molecular system[15,57,171].

Despite efforts over the past years to fully characterise CO_2-II, work studying the Poisson's ratio of this system are lacking. Work involving the mechanical properties of CO_2-II is mostly limited to experimental[57,179] or theoretical[56,167,171] determination of the bulk modulus, with some theoretical studies also determining the elastic constants[56,57] of this system. Nevertheless, a detailed study on the Poisson's ratio and auxetic behaviour of CO_2-II is lacking. In order to fully characterise a material, knowledge of its mechanical properties is essential.

[*] The contents of this chapter have been submitted for publication in the peer-reviewed journal Physica Status Solidi B: Gambin, D., Dudek, K. K., Dudek, M. R., Grima, J. N. & Gatt, R. On the mechanical properties of CO_2-II with particular emphasis on its auxetic potential

In view of the above, this work will employ *ab initio* DFT calculations in order to study the mechanical properties of CO_2-II and the variation of these properties with increasing hydrostatic pressure. In particular, this work will aim to provide the first detailed study of the Poisson's ratio of CO_2-II together with the pressure dependence of this property. The calculated Poisson's ratio of the CO_2-II single crystal will be rationalised through the use of spectroscopic techniques. In order to achieve this, this chapter will be subdivided into two sections with the first section being devoted to the convergence and benchmarking studies. This will be followed by a detailed study of the mechanical properties of CO_2-II in the second part of the chapter.

6.2 Convergence and Benchmarking study for CO_2-II

6.2.1 Introduction

CO_2-II is a high pressure phase of carbon dioxide which has attracted the attention of a number of researchers, with this system being the subject of a number of theoretical studies involving DFT[56,57,167,171,176]. Theoretical studies have investigated the structure[56,57,167,171], vibrational properties[57,171], stability[176] and mechanical properties[56,57] of this system. The studies carried out employed different simulation parameters and thus, to ensure that adequate parameters are employed in this work, a convergence and benchmarking study will be carried out. This will ensure that the results obtained in this work are indeed adequate representations of the properties of phase II and not an artefact of the simulation parameters employed. To this end, convergence testing and benchmarking was carried out for the GGA functionals PBE[384], PBE-TS[385] and PBE-Grimme[386]. Previous work[176] has shown that CO_2-II is predicted to undergo a phase change to CO_2-V at 21.5 GPa at 0 K, thus in order to ensure that the work carried out is well within the stability field of CO_2-II, this study was conducted in the pressure range of 15 GPa to 20 GPa.

6.2.2 Methodology

The experimental crystal structure of CO_2-II was constructed within the CASTEP [382] modelling platform as implemented in Materials Studio employing experimentally determined fractional coordinates and lattice parameters as obtained from the literature [57]. The crystal lattice was aligned within the global coordinate system in accordance to the convention adopted by the Institute of Radio Engineers (IRE)[414] i.e. in such a way that the *c* crystal direction was parallel to the global *z*-axis while the *b* crystal direction was aligned in the global *yz*-plane and no constraints were imposed on the *a* crystal direction. All simulations were carried out employing DFT[405,406] utilising full periodic boundary conditions on a 1 × 1 × 1 unit cell. The $P4_2/mnm$ symmetry of this system was set to P1 when carrying out geometry optimisation in order to remove symmetry constraints on the system, apart from those imposed by the unit cell itself, during the minimisation process. This allows all the elements within the cell to act independently albeit increasing simulation time.

In order to determine the simulation parameters suitable for studying CO_2-II the convergence study was carried out employing different GGA functionals namely PBE[384], PBE-Grimme[386] and PBE-TS[385]. Extensive convergence testing was carried out, which in particular includes checking the effect of increasing the energy cut-off and decreasing the spacing of the Monkhorst-Pack k-point grid. The convergence study was carried out at two pressures namely 15 GPa and 20 GPa, by carrying out geometry optimisation of the structure of CO_2-II while systematically increasing the energy cut-off employed from 400 eV to 1200 eV in steps of 200 eV and systematically decreasing the spacing of the Monkhorst-Pack k-point grid [390] from 0.08 $Å^{-1}$ to 0.02 $Å^{-1}$.

The DFT calculations were carried out employing norm conserving pseudopotentials and an SCF tolerance of 5 $x10^{-7}$ eV/atom. Geometry optimisation was carried out employing

the Broyden-Fletcher-Goldfarb-Shanno (BFGS) algorithm employing the line search method. This algorithm allows for relaxation of both the cell parameters and the internal degrees of freedom. Stringent convergence criteria were utilised including a maximum force of 0.01 eV/Å, an energy cut-off of 5.0 $\times 10^{-6}$ eV/atom, a maximum stress of 0.02 GPa and maximum displacement of 5.0 $\times 10^{-4}$ Å.

Following the approach taken in previous chapters, convergence testing was carried out by comparing various structural parameters obtained using different combinations of energy cut-off and spacing of the Monkhorst-Pack grid with the structural parameters obtained using the most refined simulation parameters, namely an energy cut-off of 1200 eV and a spacing of the Monkhorst-Pack grid of 0.02 $Å^{-1}$. The structural parameters assessed were the lattice parameters, the C=O intramolecular bond length, the C:O non-bond length, the O=C=O intramolecular bond angle, the C-O-C and the O-C-O angles (see Figure 6.1), at 15 GPa and 20 GPa employing PBE, PBE-TS and PBE-Grimme.

In order to assess the suitability of the different functionals for calculating the properties of CO_2-II, the results obtained through the use of different functionals were benchmarked to other work present in the literature in the pressure range of this study, namely 15 GPa to 20 GPa. To this end, the experimentally derived lattice parameters available in the literature[57], were compared to those calculated employing the PBE functional and the dispersion corrected functionals PBE-Grimme and PBE-TS at 15.5 GPa and 19.9 GPa.

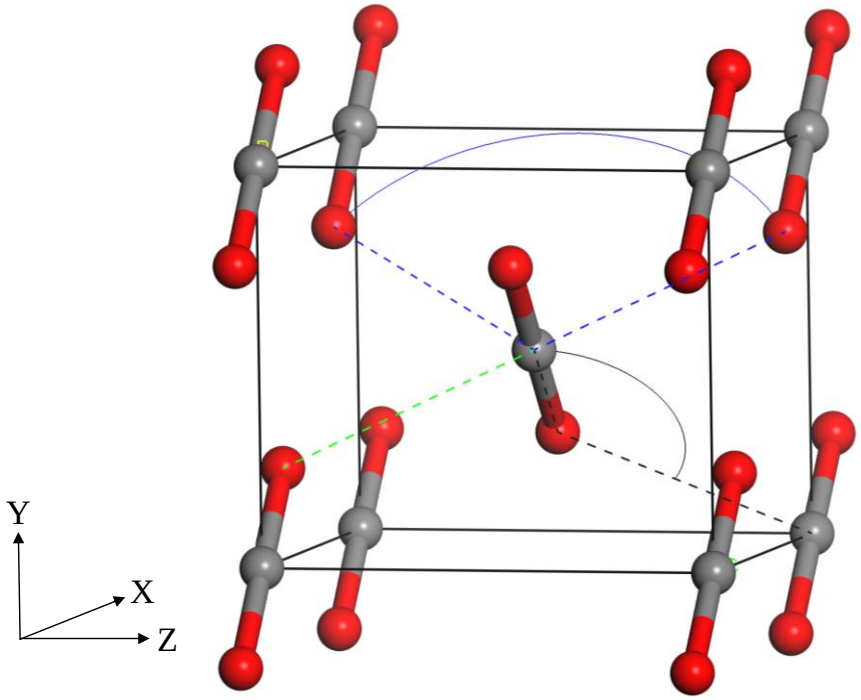

Figure 6.1: CO_2-II structure where grey spheres represent carbon and red spheres represent oxygen. Examples of different structural parameters are indicated namely, the C:O non-bond length (shown with dotted green lines), the C-O-C angle (shown in black) and the O-C-O angle (shown in blue).

6.2.3 Results and discussion

A convergence study of the different GGA functionals employed in this work was carried out to ensure that the results obtained are not an artefact of the simulation parameters utilised. Firstly, convergence testing of the lattice parameters was carried out at 15 GPa and 20 GPa. The tetragonal crystal system of CO_2-II was reproduced for all calculations carried out, with the *a*-lattice parameter being equal to the *b*-lattice parameter. Referring to Figure 6.2, it can be seen that an a/b ratio of 1 is obtained for all calculations carried out. The *a*-lattice parameter and *c*-lattice parameter obtained from each combination of the energy cut-off and the spacing of the Monkhorst-Pack k-point grid tested were compared to those obtained using an energy cut-off of 1200 eV and a Monkhorst-Pack k-point grid of 0.02 $Å^{-1}$. From the results obtained, see Figure 6.3 and Figure 6.4, it can be inferred that an energy cut-off of 800 eV and

Monkhorst-Pack k-point grid spacing of 0.04 $Å^{-1}$ is adequate for calculating the lattice parameters of CO_2-II as further refinement in simulation parameters did not significantly change the lattice parameters obtained.

In order to consolidate the work done, convergence testing was also carried out on a number of lengths and angles, namely the C=O intramolecular bond length, the C:O non-bond length, the O=C=O intramolecular bond angle, the C-O-C and the O-C-O angles (see Figure 6.1), at 15 GPa and 20 GPa employing PBE, PBE-TS and PBE-Grimme. The results obtained, see Figure 6.5 to Figure 6.9, confirm that an energy cut-off of 800 eV and a Monkhorst-Pack k-point grid spacing of 0.04 $Å^{-1}$ are adequate to calculate the structural parameters of CO_2-II. In fact, an increase in the energy cut-off and a decrease in the spacing of the Monkhorst-Pack k-point grid does not significantly change the lengths and angles calculated, showing that convergence has been achieved.

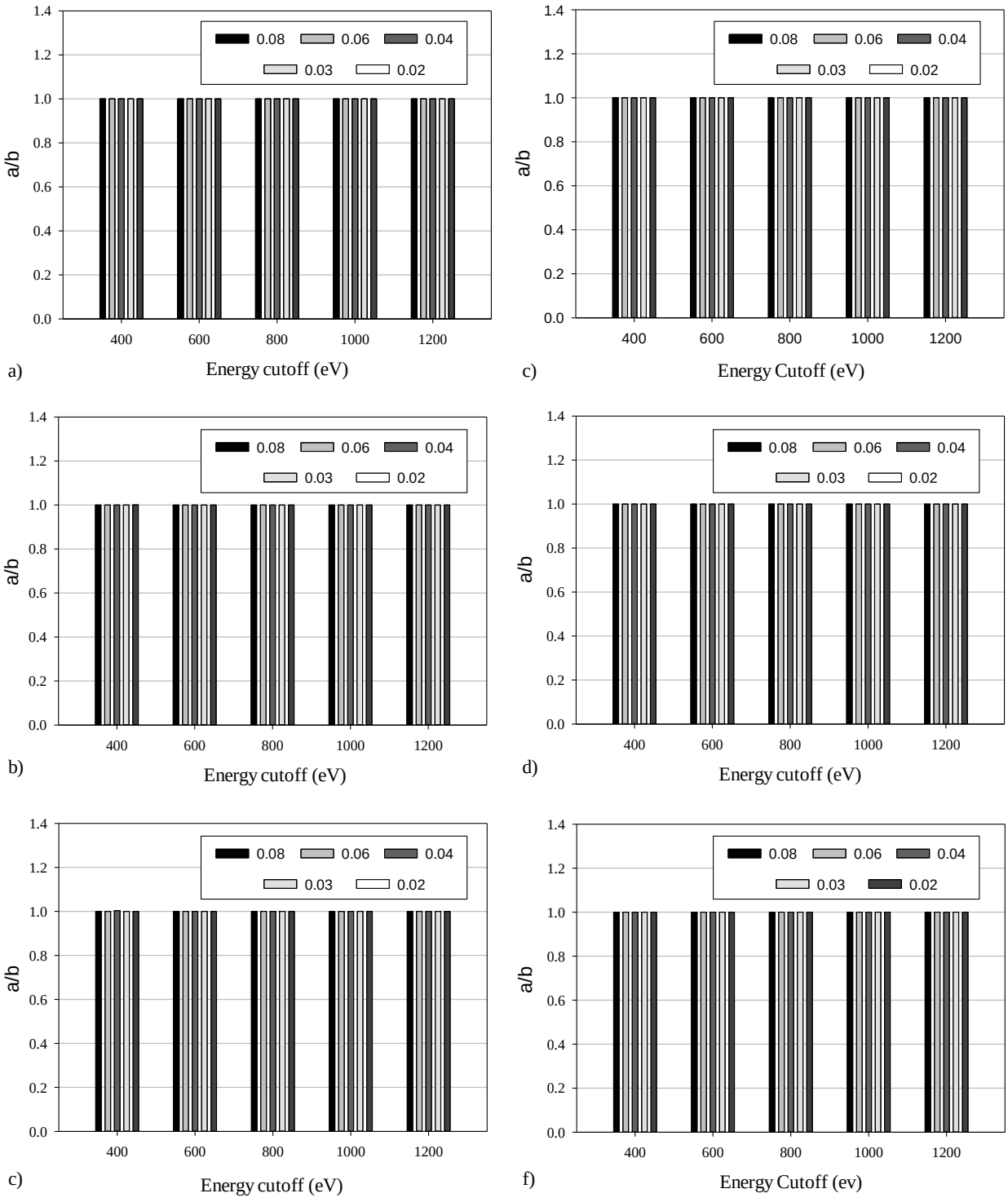

Figure 6.2: The convergence test carried out on CO_2-II for the ratio of a/b lattice parameters, using (a) GGA-PBE, (b) GGA-PBE-TS, (c) GGA-PBE-Grimme when subjected to a hydrostatic pressure of 15 GPa and using (d) GGA-PBE, (e) GGA-PBE-TS and (f) GGA-PBE-Grimme when subjected to a hydrostatic pressure of 20 GPa. Since CO2-II is a tetragonal system, a=b and hence the a/b ratio should be equal to 1. The legend indicates the spacing used (in Å-1) for the Monkhorst-Pack grid.

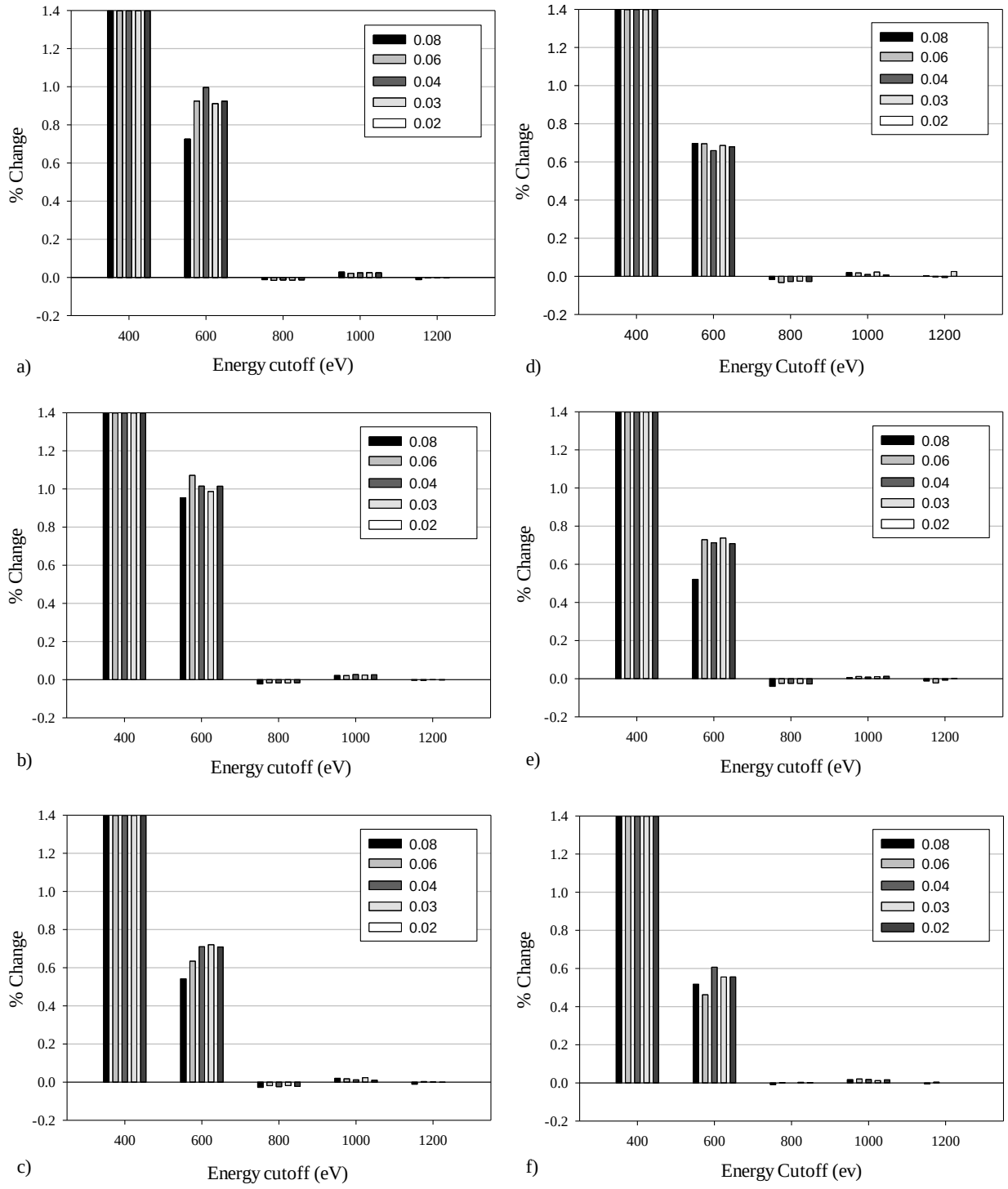

Figure 6.3: The convergence test carried out on CO_2-II for the a-lattice parameter, using (a) GGA-PBE, (b) GGA-PBE-TS, (c) GGA-PBE-Grimme when subjected to a hydrostatic pressure of 15 GPa and using (d) GGA-PBE, (e) GGA-PBE-TS and (f) GGA-PBE-Grimme when subjected to a hydrostatic pressure of 20 GPa. Note that the Y axis give the percentage deviation for the a-lattice parameter when compared to the a-parameter obtained when the simulation is carried out using a cut-off energy of 1200 eV and a spacing of 0.02 $Å^{-1}$ for the Monkhorst-Pack grid, whilst the legend indicates the spacing used (in $Å^{-1}$) for the Monkhorst-Pack grid. The scale of the graphs is truncated to 1.4 and -0.2.

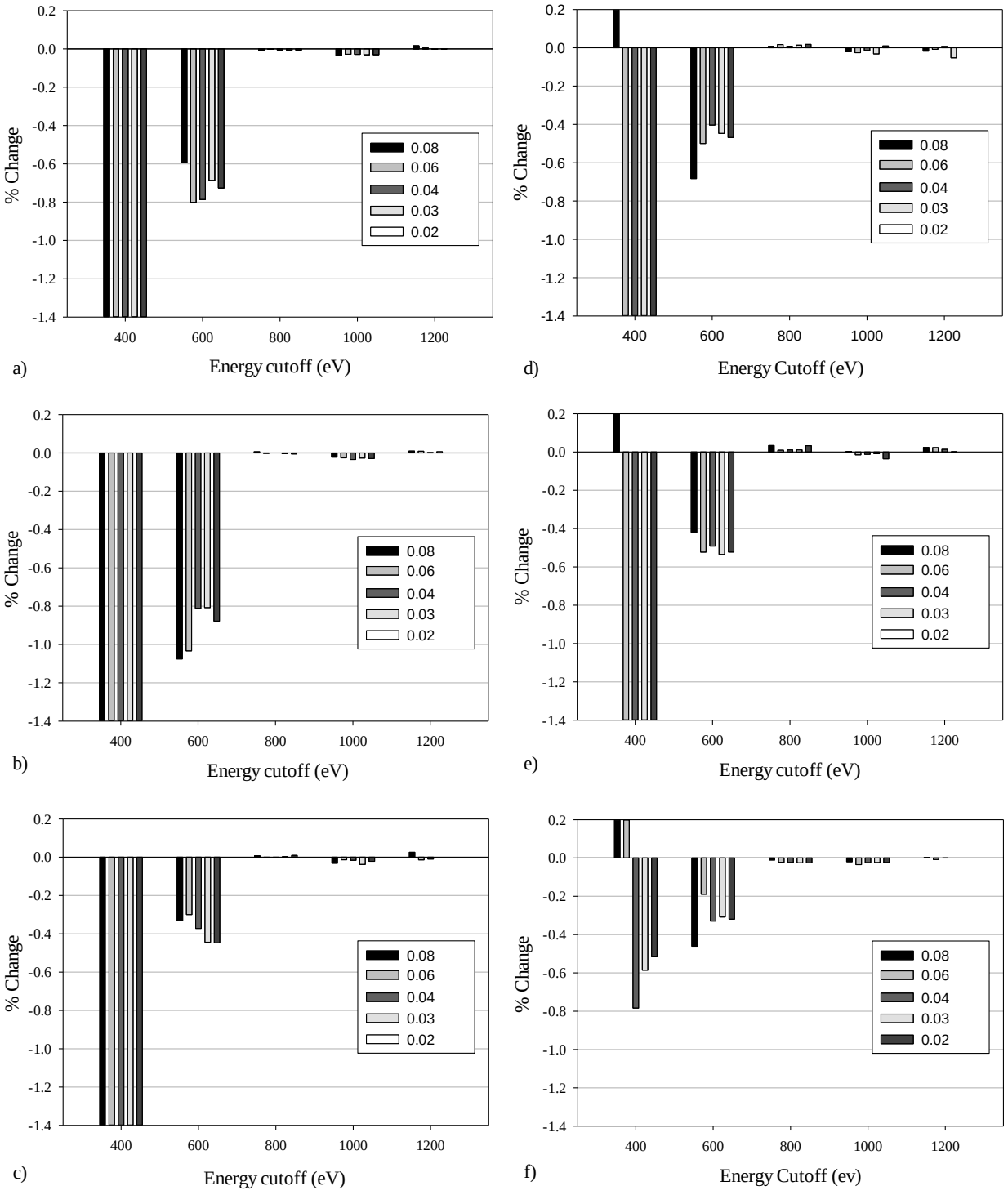

Figure 6.4: The convergence test carried out on CO_2-II for the c-lattice parameter, using (a) GGA-PBE, (b) GGA-PBE-TS, (c) GGA-PBE-Grimme when subjected to a hydrostatic pressure of 15 GPa and using (d) GGA-PBE, (e) GGA-PBE-TS and (f) GGA-PBE-Grimme when subjected to a hydrostatic pressure of 20 GPa. Note that the Y axis give the percentage deviation for the a-lattice parameter when compared to the a-parameter obtained when the simulation is carried out using a cut-off energy of 1200 eV and a spacing of 0.02 $Å^{-1}$ for the Monkhorst-Pack grid, whilst the legend indicates the spacing used (in $Å^{-1}$) for the Monkhorst-Pack grid. The scale of the graphs is truncated to 0.2 and -1.4.

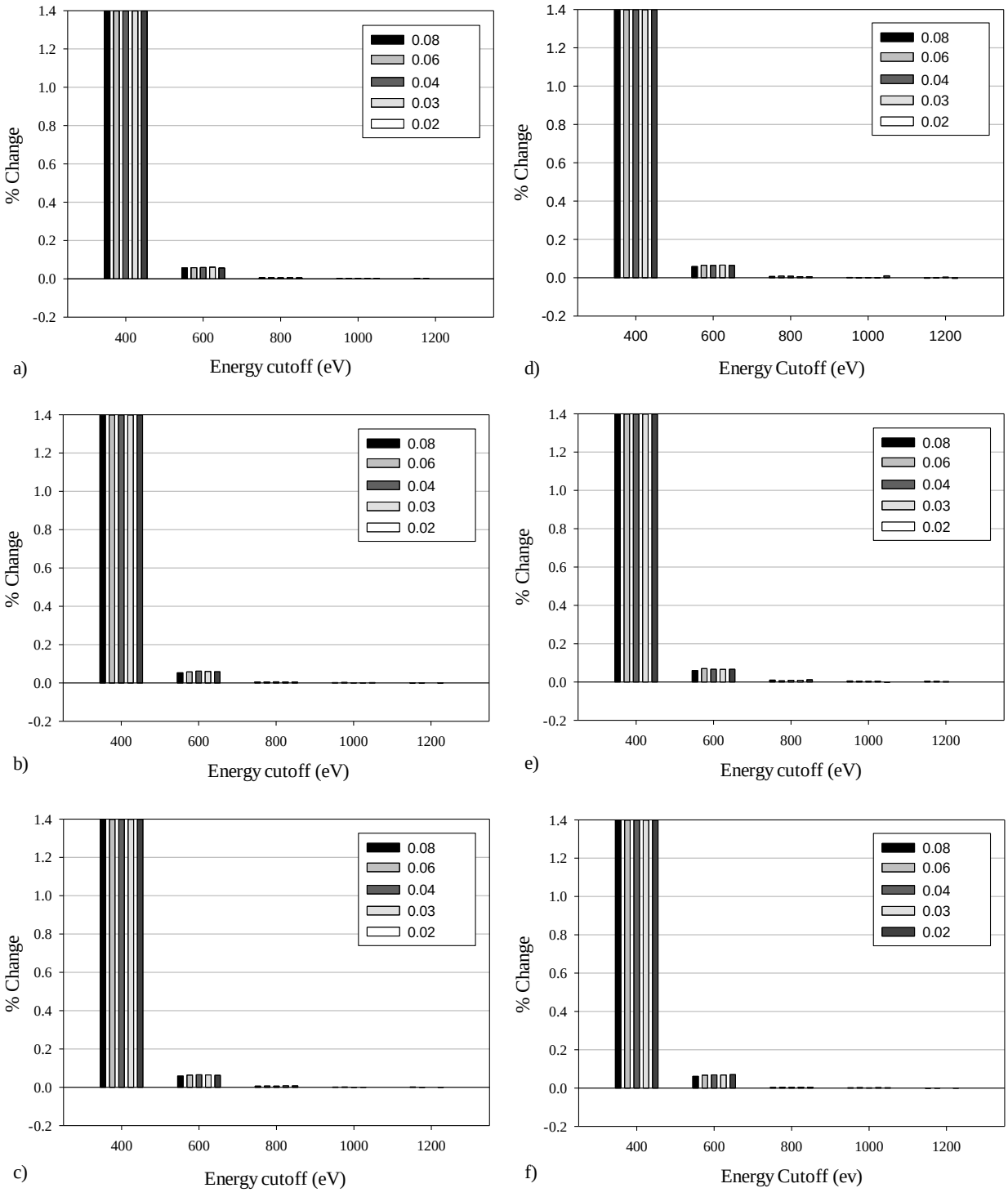

Figure 6.5: The convergence test carried out on CO_2-II for the C=O bond length, using (a) GGA-PBE, (b) GGA-PBE-TS, (c) GGA-PBE-Grimme when subjected to a hydrostatic pressure of 15 GPa and using (d) GGA-PBE, (e) GGA-PBE-TS and (f) GGA-PBE-Grimme when subjected to a hydrostatic pressure of 20 GPa. Note that the Y axis give the percentage deviation for the C=O bond length when compared to the C=O bond length obtained when the simulation is carried out using a cut-off energy of 1200 eV and a spacing of 0.02 $Å^{-1}$ for the Monkhorst-Pack grid, whilst the legend indicates the spacing used (in $Å^{-1}$) for the Monkhorst-Pack grid. The scale of the graphs is truncated to 1.4 and -0.2.

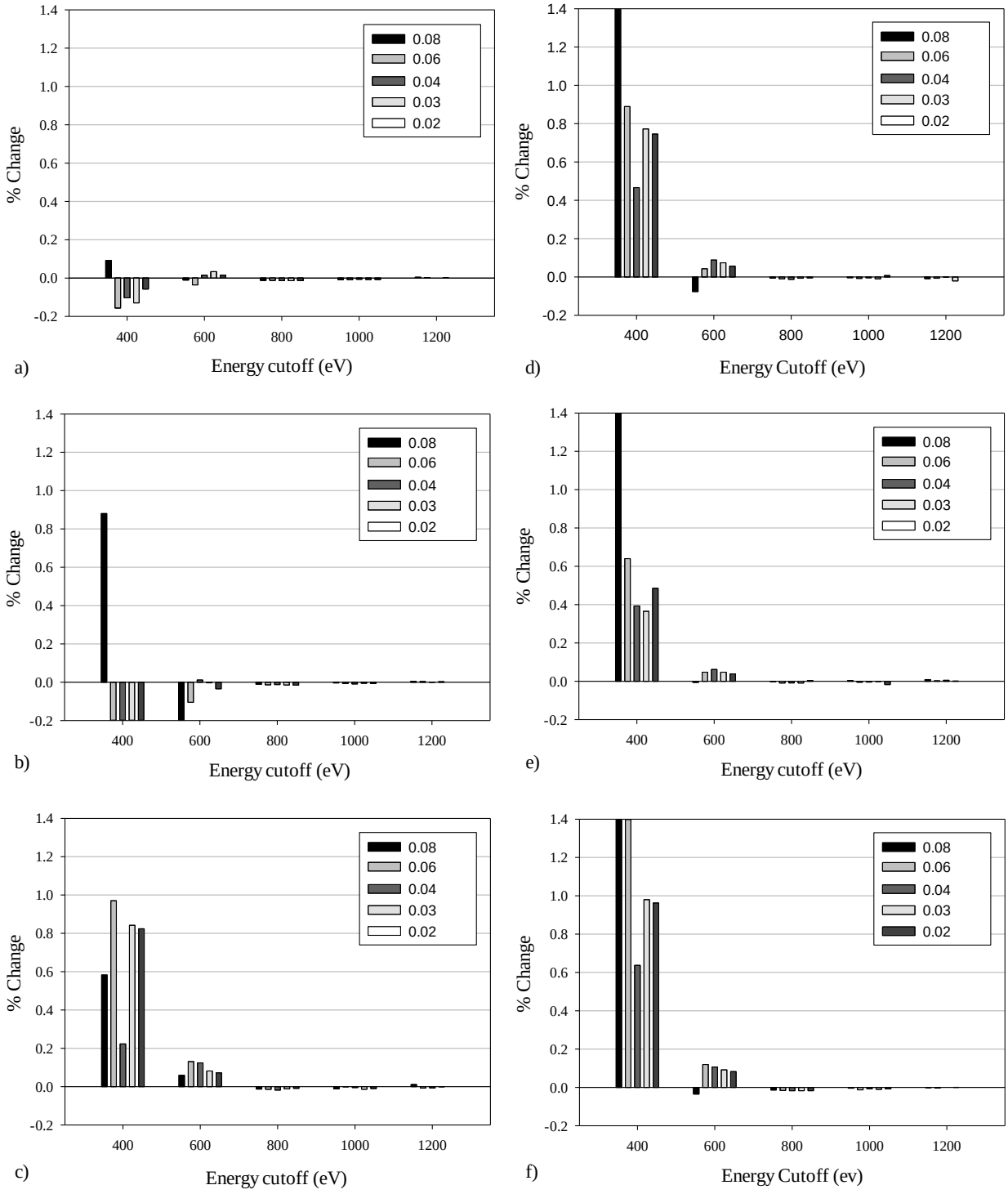

Figure 6.6: The convergence test carried out on CO_2-II for the C:O non-bond length, using (a) GGA-PBE, (b) GGA-PBE-TS, (c) GGA-PBE-Grimme when subjected to a hydrostatic pressure of 15 GPa and using (d) GGA-PBE, (e) GGA-PBE-TS and (f) GGA-PBE-Grimme when subjected to a hydrostatic pressure of 20 GPa. Note that the Y axis give the percentage deviation for the C:O non-bond length when compared to the C:O non-bond length obtained when the simulation is carried out using a cut-off energy of 1200 eV and a spacing of 0.02 $Å^{-1}$ for the Monkhorst-Pack grid, whilst the legend indicates the spacing used (in $Å^{-1}$) for the Monkhorst-Pack grid. The scale of the graphs is truncated to 1.4 and -0.2.

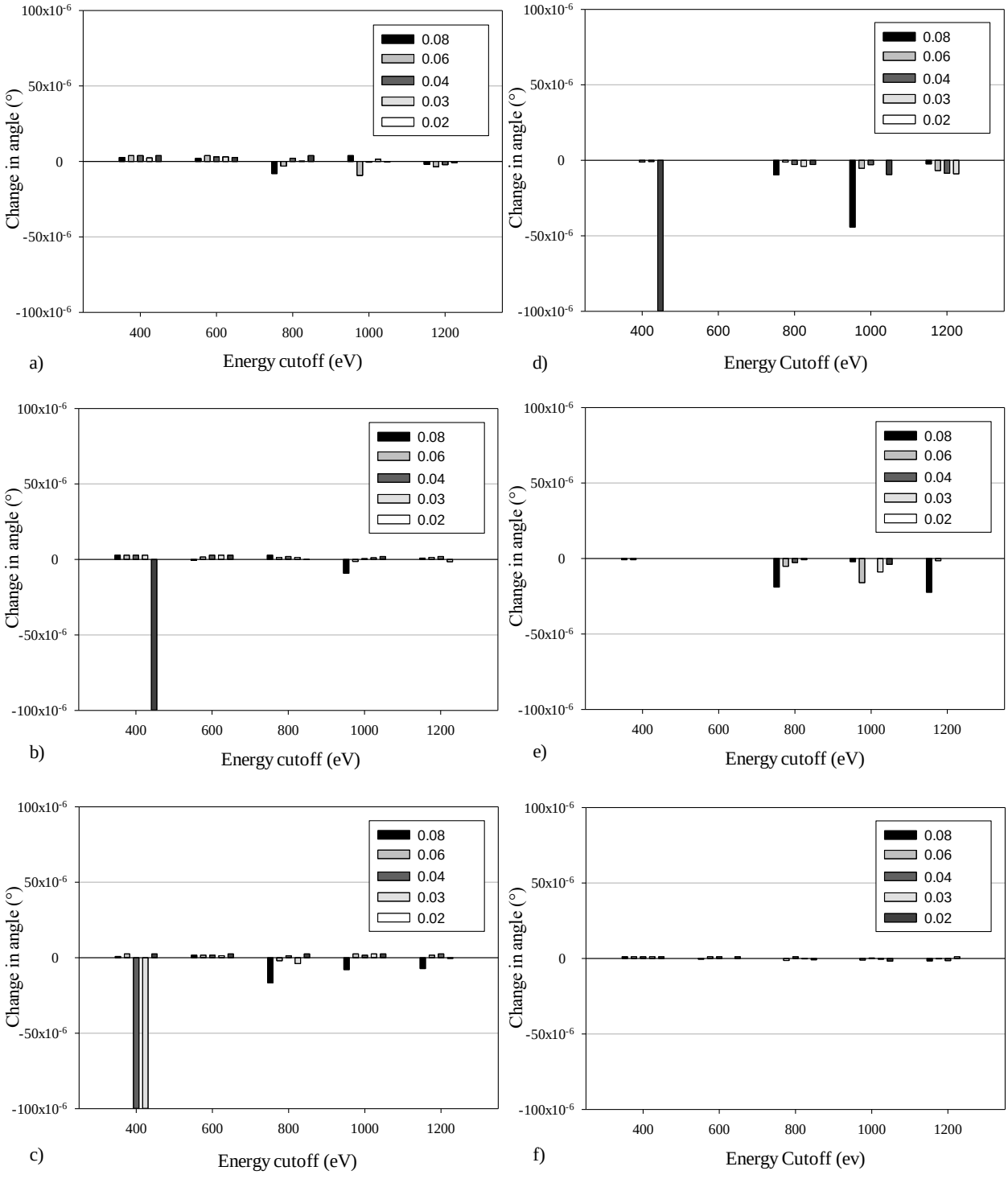

Figure 6.7: The convergence test carried out on CO_2-II for the O=C=O angle, using (a) GGA-PBE, (b) GGA-PBE-TS, (c) GGA-PBE-Grimme when subjected to a hydrostatic pressure of 15 GPa and using (d) GGA-PBE, (e) GGA-PBE-TS and (f) GGA-PBE-Grimme when subjected to a hydrostatic pressure of 20 GPa. Note that the Y axis give the change in angle (°) for the O=C=O angle when compared to the O=C=O angle obtained when the simulation is carried out using a cut-off energy of 1200 eV and a spacing of 0.02 $Å^{-1}$ for the Monkhorst-Pack grid, whilst the legend indicates the spacing used (in $Å^{-1}$) for the Monkhorst-Pack grid. The scale of the graph is truncated to -100×10^{-6}.

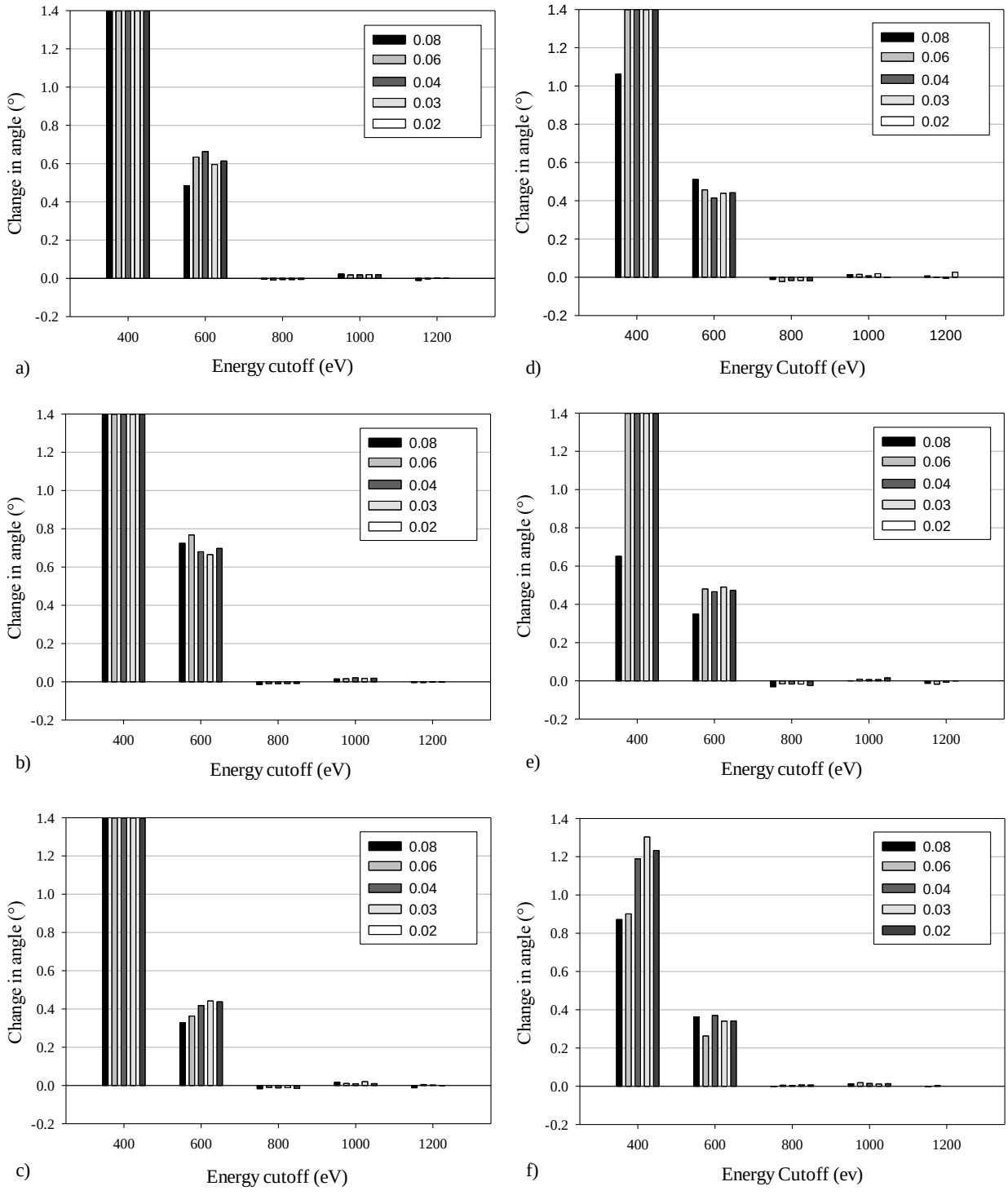

Figure 6.8: The convergence test carried out on CO_2-II for the C-O-C angle, using (a) GGA-PBE, (b) GGA-PBE-TS, (c) GGA-PBE-Grimme when subjected to a hydrostatic pressure of 15 GPa and using (d) GGA-PBE, (e) GGA-PBE-TS and (f) GGA-PBE-Grimme when subjected to a hydrostatic pressure of 20 GPa. Note that the Y axis give the change in angle (°) for the O-C-O angle when compared to the O-C-O angle obtained when the simulation is carried out using a cut-off energy of 1200 eV and a spacing of 0.02 $Å^{-1}$ for the Monkhorst-Pack grid, whilst the legend indicates the spacing used (in $Å^{-1}$) for the Monkhorst-Pack grid. The scale of the graph is truncated to 0.2 and -1.4.

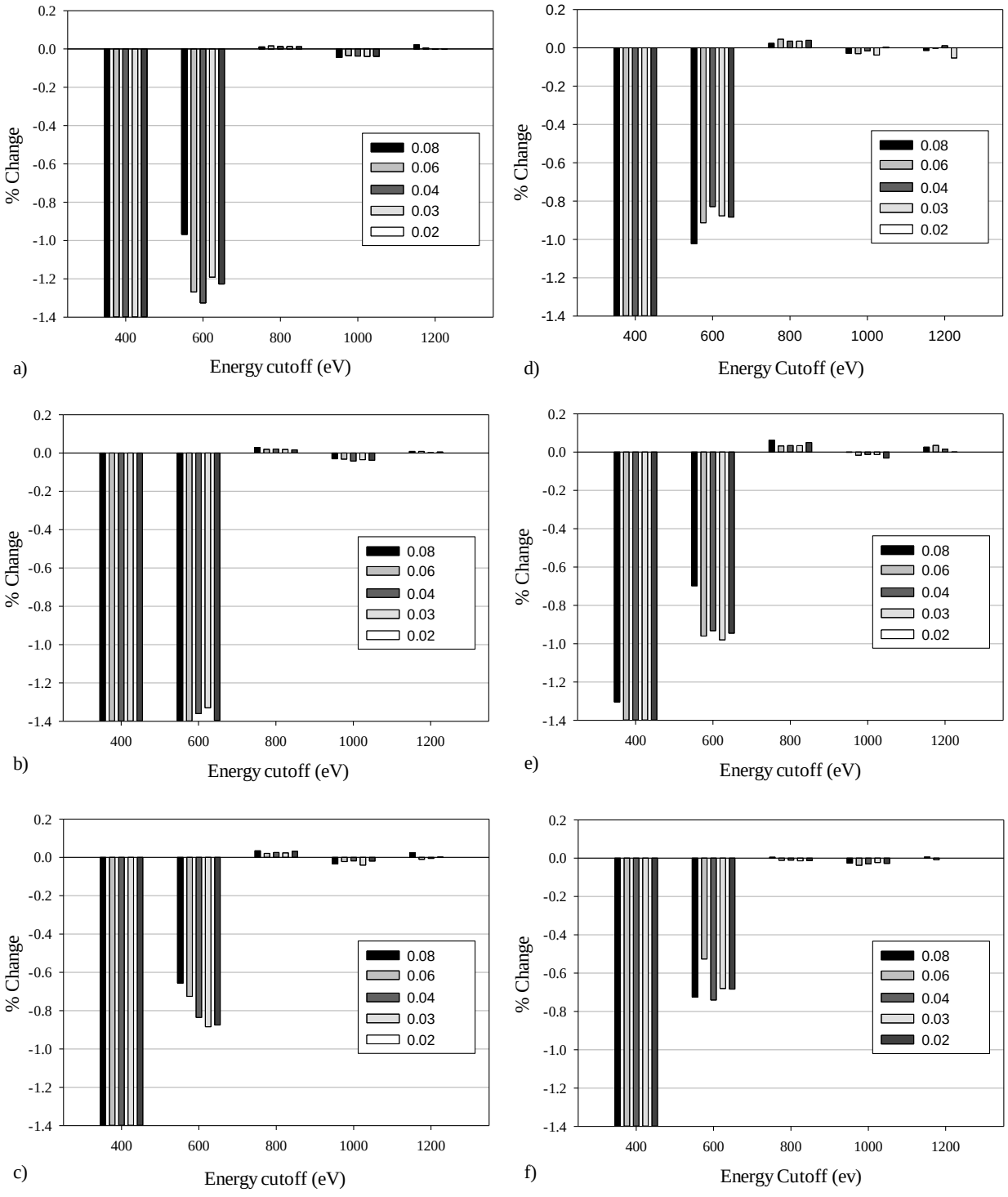

Figure 6.9: The convergence test carried out on CO_2-II for the O-C-O angle, using (a) GGA-PBE, (b) GGA-PBE-TS, (c) GGA-PBE-Grimme when subjected to a hydrostatic pressure of 15 GPa and using (d) GGA-PBE, (e) GGA-PBE-TS and (f) GGA-PBE-Grimme when subjected to a hydrostatic pressure of 20 GPa. Note that the Y axis give the change in angle (°) for the O-C-O angle when compared to the O-C-O angle obtained when the simulation is carried out using a cut-off energy of 1200 eV and a spacing of 0.02 $Å^{-1}$ for the Monkhorst-Pack grid, whilst the legend indicates the spacing used (in $Å^{-1}$) for the Monkhorst-Pack grid. The scale of the graph is truncated to 0.2 and -1.4.

In order to benchmark the methodology, theoretically derived parameters determined in this study were compared to work present in the literature in the pressure range of this study, namely 15 GPa to 20 GPa. All three functionals correctly predict the $P4_2/mnm$ symmetry of the system[57]. Moreover, the results obtained, see Table 6.1 and Table 6.2, show that all three functionals utilised in this work give adequate agreement with experimentally derived lattice parameters with a maximum deviation of 1.419 % for the *a*-lattice parameter and a maximum deviation of 0.572 % for the *c*-lattice parameter at 15.5 GPa while at 19.9 GPa, the maximum deviation for the *a*-lattice parameter was of 1.264 % and the maximum deviation for the *c*-lattice parameter was of 0.724 %. In particular, when utilising the PBE, PBE-TS and PBE-Grimme functionals at 15.5 GPa, the percentage deviations in the *a* and *b*-lattice parameters were of 1.419 %, 1.202 % and 0.553 % respectively while for the *c*-lattice parameter the percentage deviations were of -0.197 %, -0.572 % and -0.213 % when utilising PBE, PBE-TS and PBE-Grimme respectively. Referring to the results obtained at 19.9 GPa, the percentage deviations of the *a* and *b*-lattice parameters were recorded to be 1.264 %, 1.042 % and 0.724 % when utilising PBE, PBE-TS and PBE-Grimme respectively while the percentage deviations for the *c*-lattice parameter was recorded to be -0.511 %, -0.882 % and -0.691 % when utilising PBE, PBE-TS and PBE-Grimme respectively.

Table 6.1: Comparison of the calculated lattice parameters for CO_2-II at 15.5 GPa employing PBE, PBE-TS and PBE-Grimme and the experimentally determined data[57] obtained at the same pressure.

		This work		
Lattice parameter	**Experimental[57]**	**PBE**	**PBE-TS**	**PBE-Grimme**
a (Å)	3.639	3.691	3.683	3.659
b (Å)	3.639	3.691	3.683	3.659
c (Å)	4.248	4.240	4.224	4.239

Table 6.2: Comparison of the calculated lattice parameters for CO_2-II at 19.9 GPa employing PBE, PBE-TS and PBE-Grimme and the experimentally determined data[57] obtained at the same pressure.

		This work		
Lattice parameter	**Experimental[57]**	**PBE**	**PBE-TS**	**PBE-Grimme**
a (Å)	3.579	3.624	3.616	3.605
b (Å)	3.579	3.624	3.616	3.605
c (Å)	4.188	4.167	4.151	4.159

The results obtained show that all three functionals tested give adequate representation of the CO_2-II system with the dispersion corrected functional PBE-Grimme giving a slightly better representation. The comparison of the experimentally determined lattice parameters[57] with those calculated in this work, shows that all three functionals are, in general, in agreement with the experimentally determined values, with PBE-Grimme being slightly better at representing the lattice parameters. In view of this, and in accordance with previous work[56,167] the rest of the study will be carried out utilising the PBE-Grimme functional with PBE and PBE-TS being employed to consolidate the mechanical and spectroscopic results obtained.

6.2.4 Conclusion

The convergence study has shown that an energy cut-off of 800 eV and a Monkhorst-Pack k-point grid[390] spacing of 0.04 $Å^{-1}$ is adequate to simulate the structure of CO_2-II in the pressure range of this study. These parameters will be used for the rest of the study. All three functionals investigated give adequate agreement with the experimental work available in the pressure range of this study, with PBE-Grimme giving an overall slightly better agreement with experimentally derived lattice parameters. In view of this, PBE-Grimme will be used for this work with PBE and PBE-TS being utilised to consolidate the work done when calculating the mechanical properties, Raman and IR spectra of CO_2-II.

6.3 Studying the properties of CO_2-II

6.3.1 Introduction

In this section the mechanical and vibrational properties of CO_2-II will be studied by utilising the simulation parameters determined in the previous section. The stability of this system in the pressure range of this study will be assessed by employing lattice dynamics calculations. This will be followed by a study of the mechanical properties of the polycrystalline aggregate and of the single crystal. Anomalous mechanical properties for the CO_2-II system will be rationalised through the use of Raman and infrared spectroscopy.

6.3.2 Methodology

Unless otherwise stated, simulations were performed using the PBE-Grimme functional, an energy cut-off of 800 eV and a Monkhorst-Pack k-point grid spacing of 0.04 $Å^{-1}$, as determined in the previous section. As stated in Section 6.3.1, various properties were simulated in this section, with each methodology described below.

6.3.2.1 Phonon dispersion

Phonon dispersion curves for CO_2-II were computed at 15 GPa and 20 GPa utilising the linear response method employing the interpolation scheme, as carried out in Chapter 4 section 4.3.2.1. Convergence for the phonon dispersion relations was subsequently assessed by repeating the calculation employing an energy cut-off of 1000 eV and a Monkhorst-Pack k-point grid spacing of 0.02 $Å^{-1}$.

6.3.2.2 Mechanical properties

Geometry optimisation of the CO_2-II structure was carried out in the pressure range of 15 GPa to 20 GPa in steps of 1 GPa. For each structure generated, the stiffness matrix, [C] was calculated utilising the constant-strain method, ensuring that a linear stress-strain relationship was achieved in each case. Following the approach taken in previous chapters, stringent

convergence criteria were employed including a maximum force of 0.002 eV/Å, a maximum displacement of 1 $\times 10^{-4}$ Å and an energy cut-off of 1×10^{-6} eV/atom. The maximum strain amplitude was set to 0.003 with 4 steps for each strain.

Employing standard transformation techniques[397], each stiffness matrix was utilised to determine the off-axis mechanical properties for the CO_2-II single crystal. In particular the off-axis Young's modulus, shear modulus and Poisson's ratio for the CO_2-II single crystal were determined. In order to ensure that the results obtained were not an artefact of the functional employed or simulation parameters utilised, the off-axis mechanical properties at 15 GPa and 20 GPa were recalculated utilising different functionals, namely PBE and PBE-TS, and more refined simulation parameters, namely an energy cut-off of 1000 eV and a Monkhorst-Pack k-point grid spacing of 0.02 $Å^{-1}$.

The elastic constants calculated employing PBE-Grimme were also used to determine the mechanical properties of the polycrystalline aggregate as described in Chapter 3 section 3.3.2.2. In particular, the Poisson's ratio, bulk modulus, shear modulus and Pugh ratio for the polycrystalline aggregate were computed.

6.3.2.3 IR and Raman spectroscopy

In order to rationalise the auxetic potential of the CO_2-II single crystal, the Raman and infra-red spectra of CO_2-II in the pressure range of 15 GPa to 20 GPa were determined in steps of 1 GPa. Convergence for the vibrational properties obtained was also assessed by recalculating these spectra at 15 GPa and 20 GPa employing an energy cut-off of 1000 eV and a Monkhorst-Pack k-point grid spacing of 0.02 $Å^{-1}$. In order to consolidate the work done with PBE-Grimme, the spectra were recalculated utilising PBE and PBE-TS at 15 GPa and 20 GPa.

6.3.3 Results and discussion

The results obtained in this work show that within the pressure range considered (15 GPa – 20 GPa), CO_2-II single crystal has the potential to exhibit an off-axis negative Poisson's ratio in the (100) and (010) planes. The auxetic potential of this system is also shown to be pressure dependent whereby an increase in pressure results in the Poisson's ratio of CO_2-II becoming slightly more negative in the direction of maximum auxeticity. This negative Poisson's ratio is rationalised by studying changes in the IR and Raman spectra of CO_2-II with pressure. A detailed discussion of the results obtained is given in this section.

6.3.3.1 Lattice dynamic calculations

As discussed in the introduction section, there is a debate on the stability window of CO_2-II, with a recent theoretical study[176] on the phase diagram of CO_2 suggesting that CO_2-II undergoes a phase transition to CO_2-V at 21.5 GPa at 0 K. In order to confirm the dynamic stability of CO_2-II in the pressure range used in this study, phonon dispersion calculations were carried out. The results obtained, see Figure 6.10, show no imaginary frequencies suggesting that CO_2-II is indeed stable or metastable in the pressure range of 15 GPa to 20 GPa which is consistent with previous work[57,176].

Convergence testing was carried out in order to ensure that the simulation parameters determined in section 6.2 may be used to calculate the phonon dispersion curves of CO_2-II at 15 GPa and 20 GPa. To achieve this the phonon dispersion curves were recalculated employing more stringent parameters, namely an energy cut-off of 1000 eV and a Monkhorst-Pack k-point grid spacing of 0.02 $Å^{-1}$. The results obtained, see Figure 6.10, show that the dispersion relations obtained are not a function of the simulation parameters employed at both 15 GPa and 20 GPa, providing greater confidence in the results obtained.

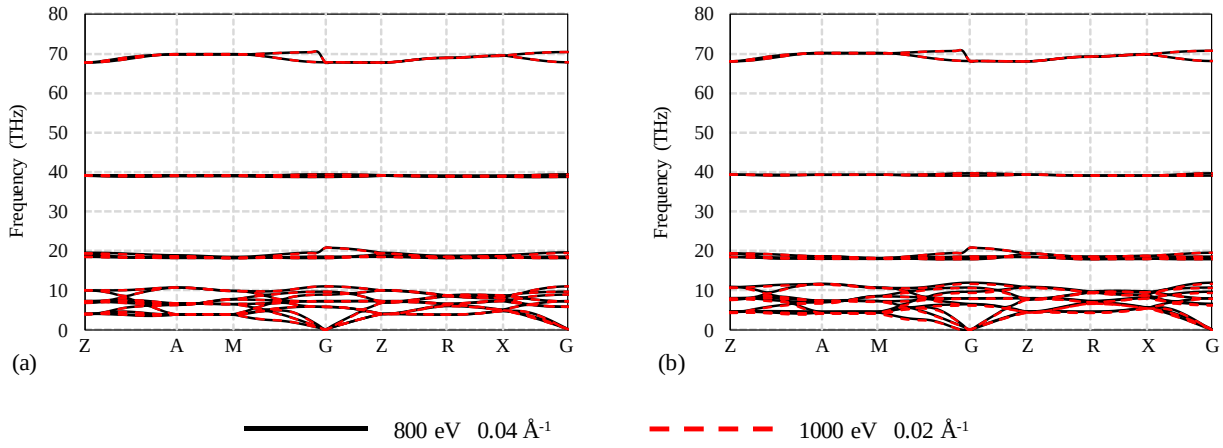

Figure 6.10: The phonon dispersion curves calculated for CO_2-II at (a) 15 GPa and (b) 20 GPa employing an energy cut-off of 800 eV and a Monkhorst-Pack k-point grid spacing of 0.04 $Å^{-1}$ (black solid line) and an energy cut-off of 1000 eV and a Monkhorst-Pack k-point grid spacing of 0.02 $Å^{-1}$ (red dashed line).

6.3.3.2 Elastic constants

Following the determination of the dynamic stability, the elastic constants of CO_2-II in the pressure range of 15 GPa – 20 GPa were calculated employing the dispersion corrected functional PBE-Grimme. The elastic stiffness constant obtained from the stiffness matrix for each pressure computed in this study are shown in Table 6.3.

Table 6.3: The computed elastic constants for CO_2-II in the pressure range of 15 GPa to 20 GPa.

Pressure (GPa)	**c_{11} (GPa)**	**c_{33} (GPa)**	**c_{21} (GPa)**	**c_{31} (GPa)**	**c_{44} (GPa)**	**c_{66} (GPa)**
15	96.54	108.35	78.12	52.91	36.45	51.46
16	102.02	113.46	82.80	55.72	38.35	54.73
17	107.39	119.54	87.48	58.90	40.10	58.06
18	112.62	123.62	92.04	64.72	41.77	61.20
19	119.02	129.51	98.00	67.84	43.58	64.46
20	123.52	135.01	101.86	71.37	45.23	67.35

For all pressures considered, the elastic constants obtained for CO_2-II had the expected symmetry for a tetragonal system [397] with crystal class *4/mmm* where $c_{11} = c_{22}$, $c_{31} = c_{32}$, $c_{44} = c_{55}$ and c_{66}, c_{33} and c_{21} are non-zero components. The elastic constants calculated were then employed to determine the off-axis mechanical properties of the CO_2-II single crystal. In particular, the variation of the Young's modulus, shear modulus and Poisson's ratio with angle of rotation for the CO_2-II single crystal were determined at 15 GPa, 17.5 GPa and 20 GPa. Referring to Figure 6.11, the anisotropy for the mechanical properties of CO_2-II is immediately apparent. It can also be noted that the Young's modulus, shear modulus and Poisson's ratio for the CO_2-II single crystal are pressure dependent.

As expected from the tetragonal nature of CO_2-II, the mechanical properties in the (010) plane are identical to the mechanical properties in the (100) plane and thus only the mechanical properties in the (010) plane are shown. CO_2-II exhibits a negative Poisson's ratio in the (100) and (010) planes with the maximum auxetic behaviour being recorded at circa 48° to the y-axis in the (100) plane and similarly in the (010) plane. For loading in the direction of maximum auxeticity, an increase in pressure is accompanied by an increase in the auxetic potential of the system, albeit to a small degree. This result was confirmed with the use of more stringent simulation parameters and through the use of the functionals PBE and PBE-TS suggesting that the predicted auxetic behaviour is not an artefact of the simulation parameters or functional employed.

In order to cement the work done in section 6.2, convergence testing was carried out on the mechanical properties of CO_2-II single crystal at 15 GPa and 20 GPa. To assess the suitability of the parameters chosen in section 6.2 vis-à-vis the calculation of the mechanical properties of CO_2-II, the elastic constants of this system were recalculated employing more refined simulation parameters namely an energy cut-off of 1000 eV and a Monkhorst-Pack k-point grid spacing of 0.02 $Å^{-1}$. The results obtained in Figure 6.12 and Figure 6.13 show that

varying the simulation parameters had no significant effect on the results obtained suggesting that the simulation parameters determined in section 6.2 can indeed be utilised to study the mechanical properties of CO_2-II.

The elastic constants of CO_2-II were recalculated utilising the functionals PBE and PBE-TS at 15 GPa and 20 GPa in order to confirm that the mechanical properties obtained are not an artefact of the functional employed. The results obtained, see Figure 6.14 and Figure 6.15, show that there is qualitative agreement between off-axis mechanical properties obtained when employing different functionals. Focusing on the main scope of this work, namely the auxetic potential of CO_2-II, the results obtained show that the CO_2-II single crystal is expected to exhibit a negative Poisson's ratio in the pressure range of this study irrespective of the functional employed. Moreover, the direction of maximum auxeticity is the same irrespective of the functional employed. This suggests that the auxetic behaviour of CO_2-II is an innate mechanical property of the system and not an artefact of the functional employed.

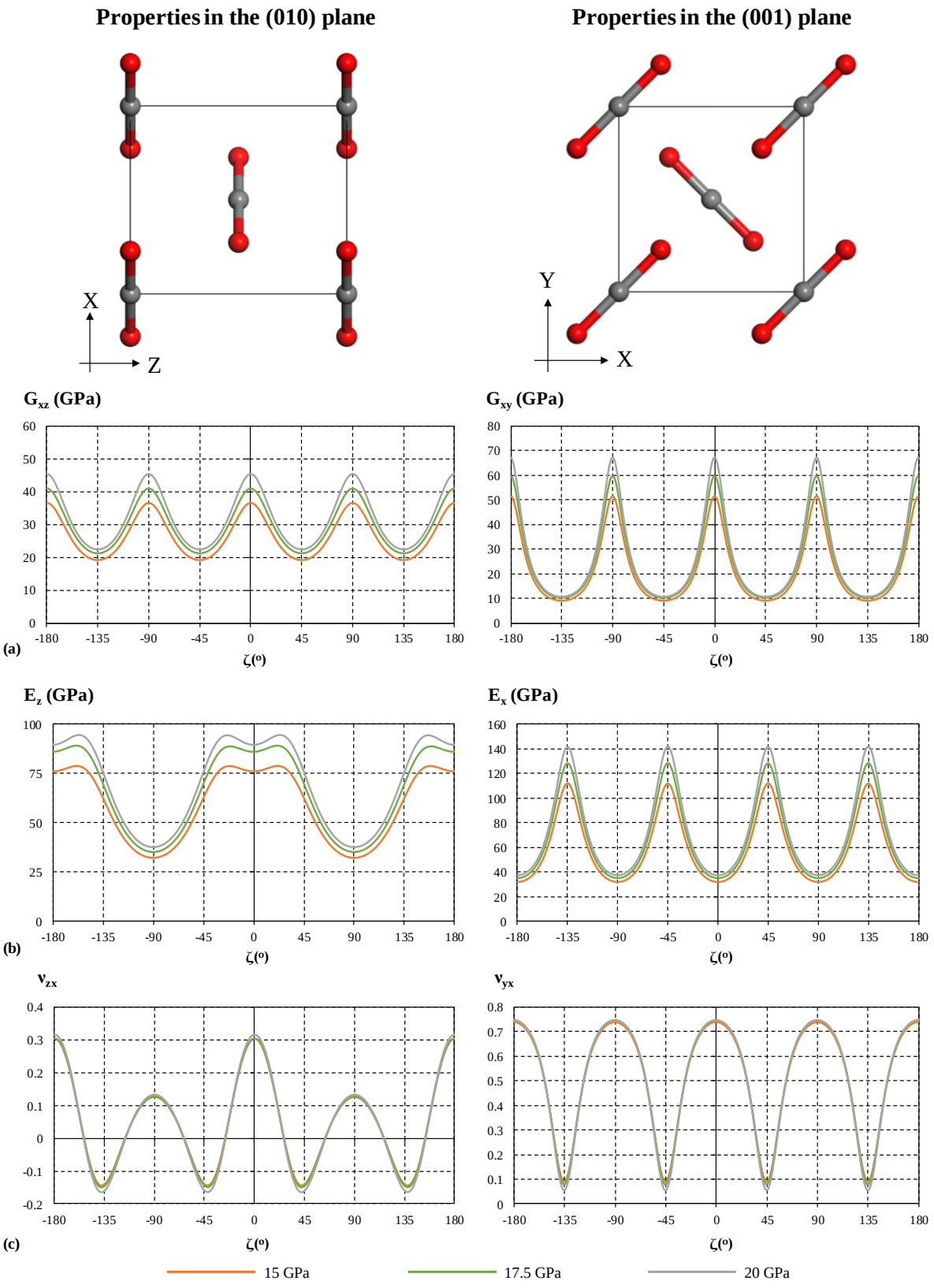

Figure 6.11: The structure of CO_2-II together with off-axis plots illustrating the mechanical properties of this system in the (010) and (001) plane with varying pressure from 15 GPa to 20 GPa in steps of 2.5 GPa. Shown here are the variation of the shear modulus (in GPa) (a), Young's modulus (in GPa) (b) and Poisson's ratio (c) with angle of rotation, ζ (in °), in these planes.

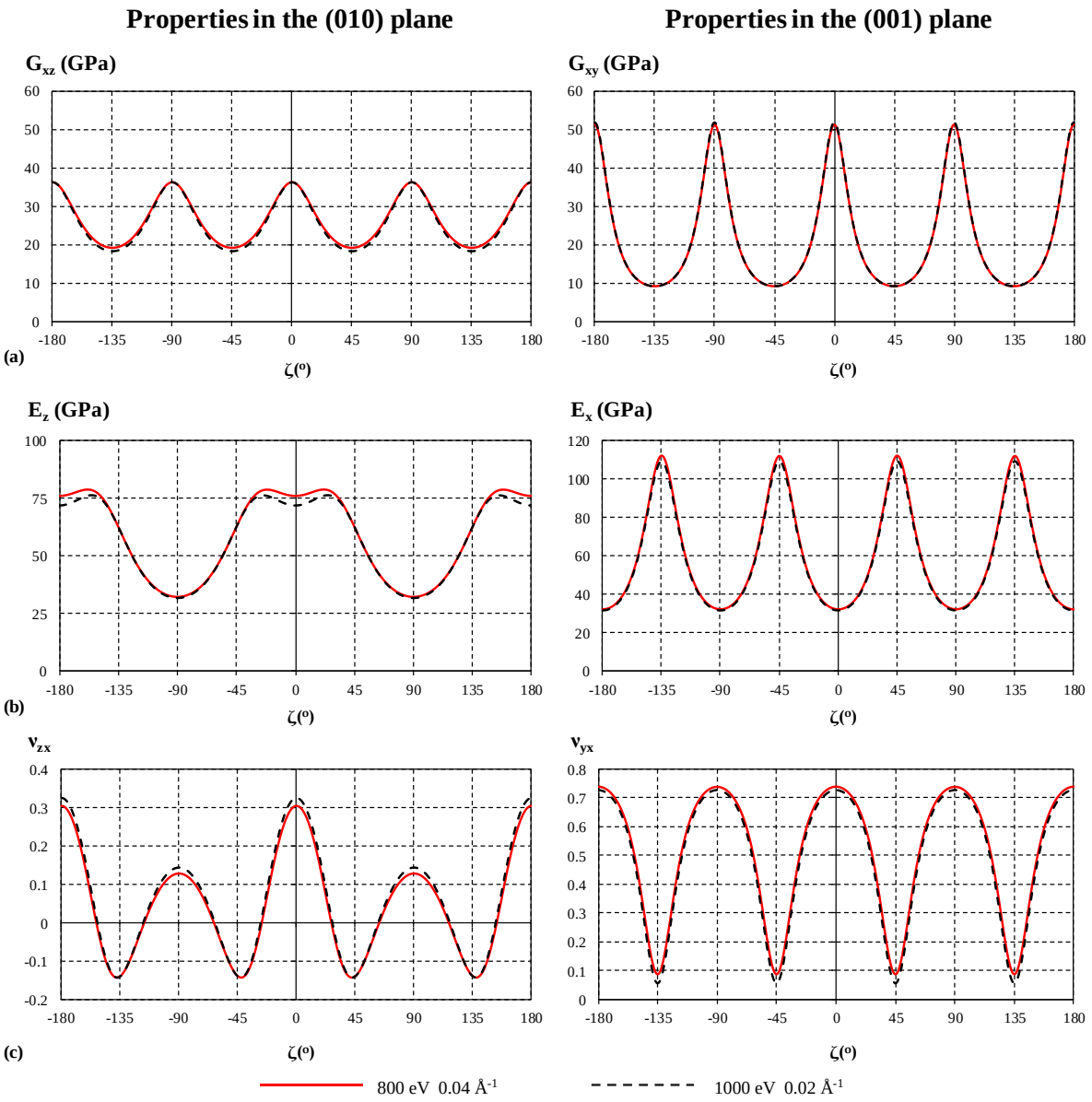

Figure 6.12: The effect of refining simulation parameters from an energy cut-off of 800 eV and a Monkhorst-Pack grid spacing of 0.04 Å^{-1} to 1000 eV and 0.02 Å^{-1} respectively on the shear modulus (in GPa) (a), Young's modulus (in GPa) (b) and Poisson's ratio (c) calculated at 15 GPa in the (010) plane and the (001) plane.

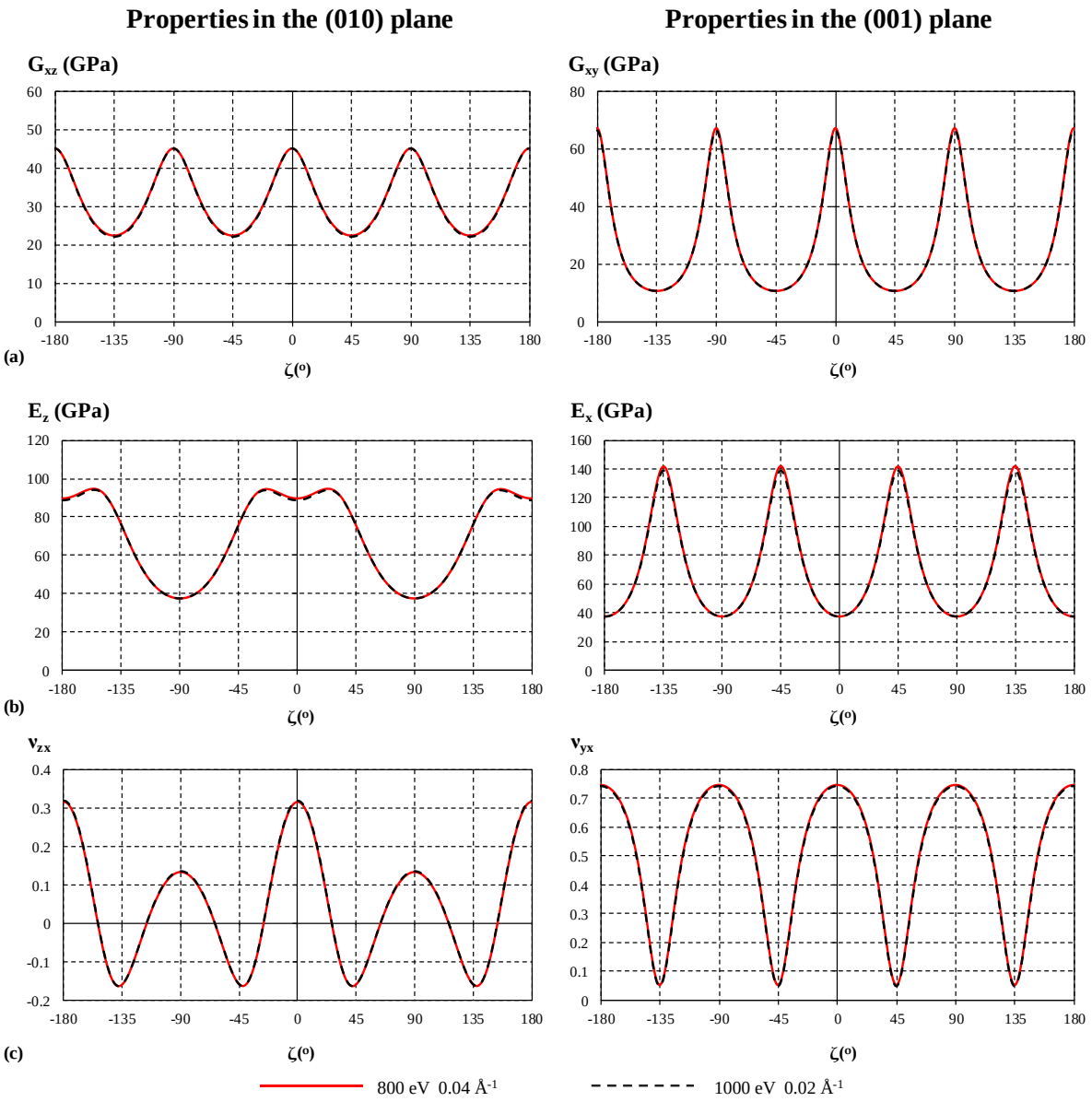

Figure 6.13: The effect of refining simulation parameters from an energy cut-off of 800 eV and a Monkhorst-Pack grid spacing of 0.04 Å^{-1} to 1000 eV and 0.02 Å^{-1} respectively on the shear modulus (in GPa) (a), Young's modulus (in GPa) (b) and Poisson's ratio (c) calculated at 20 GPa in the (010) plane and the (001) plane.

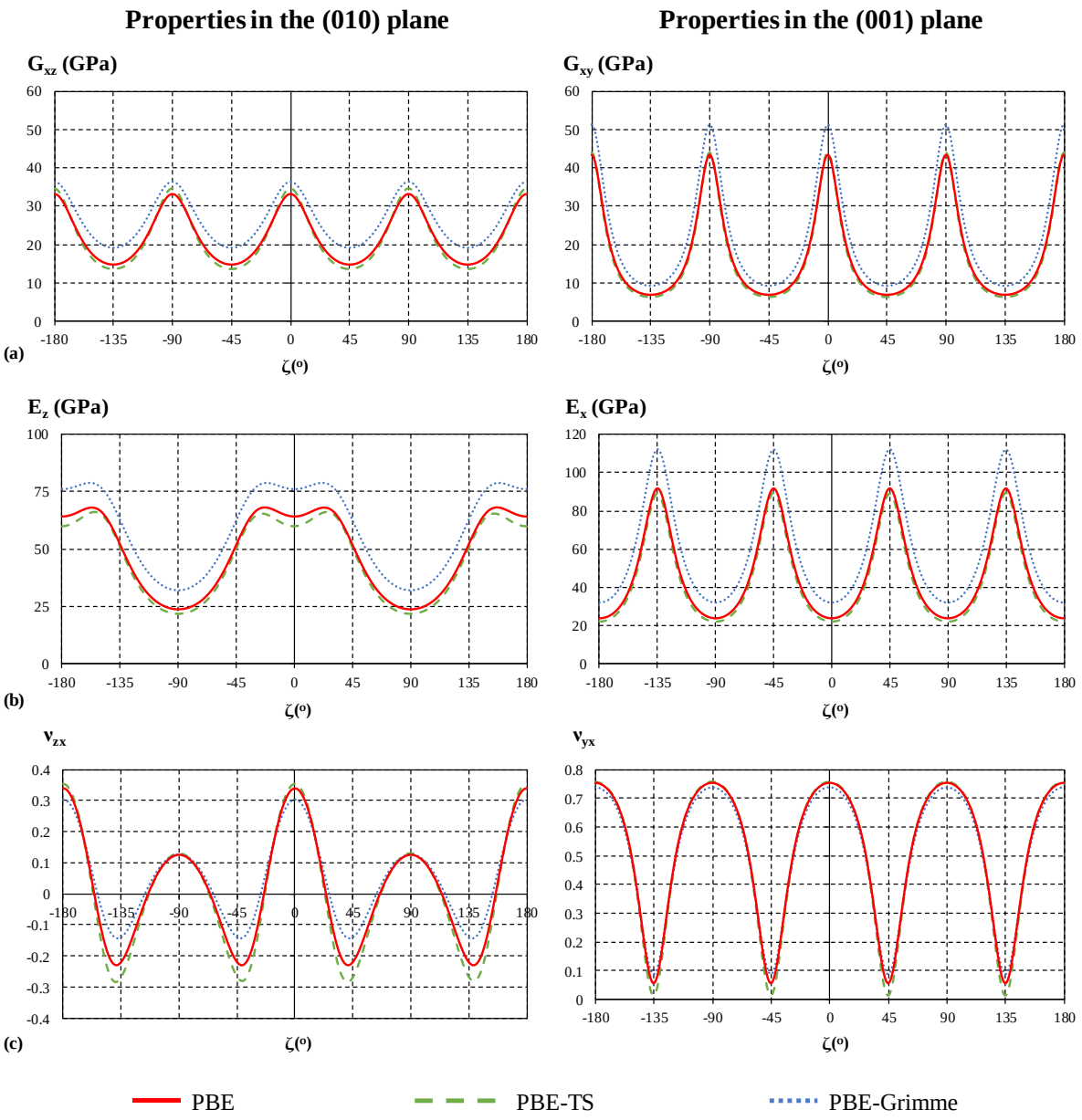

Figure 6.14: The variation of the shear modulus (in GPa) (a), Young's modulus (in GPa) (b) and Poisson's ratio (c) with angle of rotation, ζ (in °) in the (010) plane and the (001) plane at 15 GPa as calculated utilising PBE, PBE-TS and PBE-Grimme. It can be seen that there is good agreement between the mechanical properties calculated with all three functionals. This confirms that mechanical properties predicted are not an artefact of the functional used but an innate property of the system.

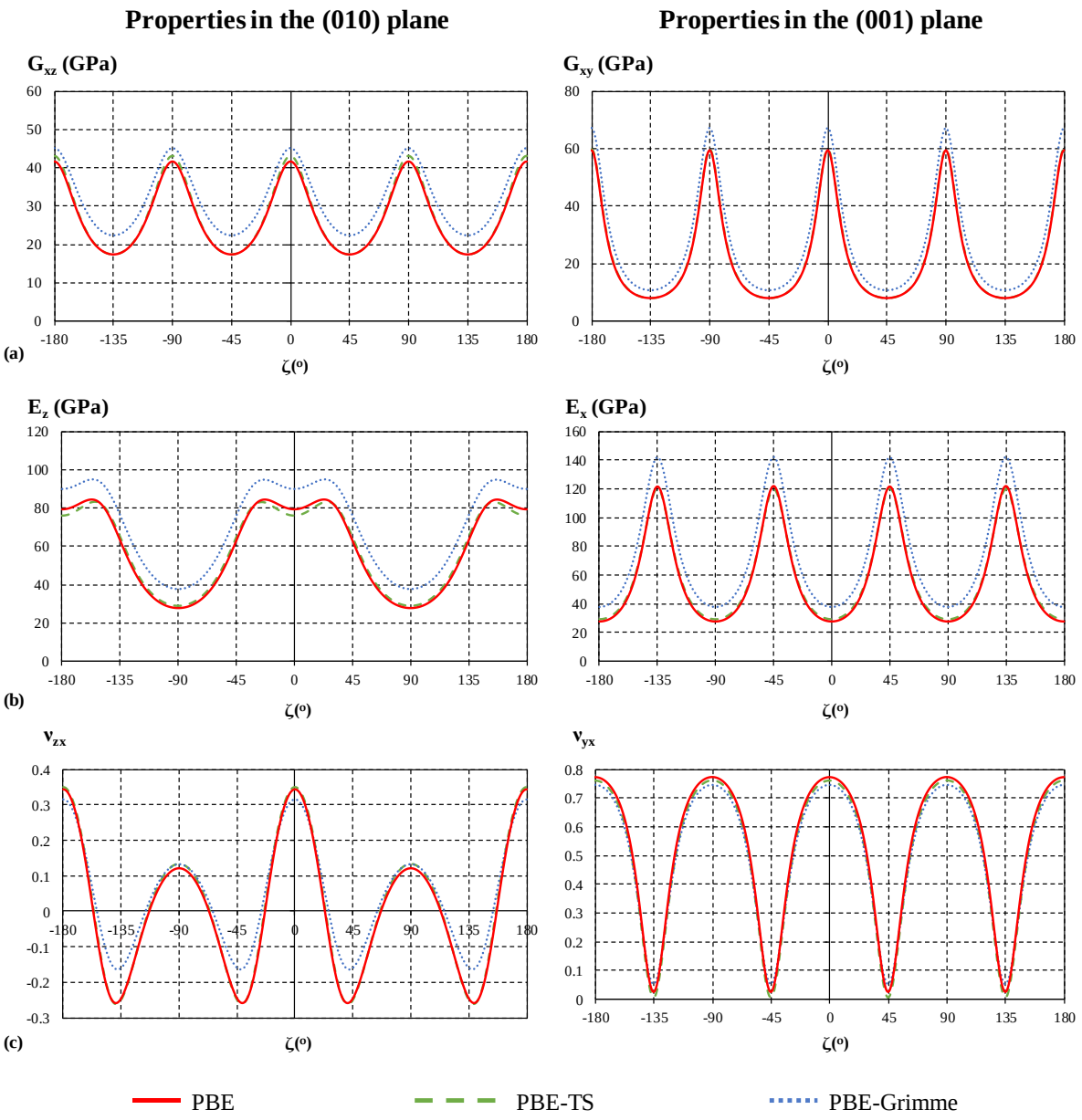

Figure 6.15: The variation of the shear modulus (in GPa) (a), Young's modulus (in GPa) (b) and Poisson's ratio (c) with angle of rotation, ζ (in °) in the (010) plane and the (001) plane at 20 GPa as calculated utilising PBE, PBE-TS and PBE-Grimme. It can be seen that there is good agreement between the mechanical properties calculated with all three functionals. This confirms that mechanical properties predicted are not an artefact of the functional used but an innate property of the system.

6.3.3.3 Polycrystalline properties

The mechanical properties of the CO_2-II polycrystalline aggregate can be computed from the elastic constants of this system as discussed in previous work[400] and in Chapter 3, assuming that the crystal domains in the sample are arranged in such a way that the material is isotropic. Focusing on the Poisson's ratio of the polycrystalline aggregate, see Table 6.4, it can be noted that the CO_2-II system is expected to have a positive Poisson's ratio in the pressure range of this study with an increase in pressure resulting in an increase in the Poisson's ratio. This is in sharp contrast to the single crystal which is predicted to exhibit a negative Poisson's ratio off-axis in the (100) and (010) planes and an increase in hydrostatic pressure is associated with an increase in auxetic behaviour. It can also be noted that an increase in pressure is associated with an increase in both the maximum and minimum bounds for the Poisson's ratio of CO_2-II polycrystalline aggregate.

Table 6.4: The variation of the maximum and minimum bounds for the Poisson's ratio of CO_2-II polycrystalline aggregate with varying hydrostatic pressure in the pressure range of 15 GPa to 20 GPa.

Pressure (GPa)	ν^{max}	ν^{min}	ν
15	0.359	0.308	0.333
16	0.360	0.308	0.334
17	0.361	0.308	0.335
18	0.366	0.313	0.339
19	0.368	0.314	0.341
20	0.369	0.315	0.342

In addition to the Poisson's ratio, the elastic constants of CO_2-II can also be utilised to calculate other mechanical properties of the polycrystalline aggregate, such as the bulk modulus and the shear modulus utilising the Voigt-Reus-Hill approximation[399–401].

Referring to Table 6.5, it can be noted that an increase in hydrostatic pressure is associated with an increase the bulk modulus and shear modulus of the polycrystalline aggregate in the pressure range of this study. In addition to this, an increase in hydrostatic pressure is also associated with an increase in the K/G ratio (Pugh ratio).

Table 6.5: The pressure dependence of the maximum and minimum bounds for the bulk modulus K^{Voigt} and K^{Reuss}, and shear modulus G^{Voigt} and G^{Reuss} for CO_2-II polycrystalline aggregate together with the K/G ratio (Pugh ratio) of the polycrystalline aggregate.

Pressure (GPa)	**K^{Voigt} (GPa)**	**K^{Reuss} (GPa)**	**K (GPa)**	**G^{Voigt} (GPa)**	**G^{Reuss} (GPa)**	**G (GPa)**	**K/G**
15	74	74	74	33	23	28	2.66
16	78	78	78	35	24	29	2.67
17	83	82	83	36	25	31	2.69
18	88	88	88	37	26	32	2.77
19	93	92	93	39	27	33	2.80
20	97	96	97	41	28	34	2.82

The computed elastic constants may also be employed to determine whether the material is expected to be brittle or ductile. A number of different criteria can be employed to this effect namely the Cauchy pressure, Frantsevich rule, Pugh's criterion and Christensen's criterion. The Frantsevich rule[409] employs the Poisson's ratio to determine whether the material is ductile or brittle with a Poisson's ratio less than 0.33 indicating that the material is brittle and a Poisson's ratio greater than 0.33 indicating that the material is ductile. Referring to Table 6.4, it can be noted that the expected Poisson's ratio is greater than 0.33 at the higher pressures of this study and close to 0.33 at the lower end suggesting that the material is ductile. Given that the values of the Poisson's ratio are close to the benchmark utilised by the Frantsevich rule, it would be opportune to utilise the other criteria to consolidate the work done.

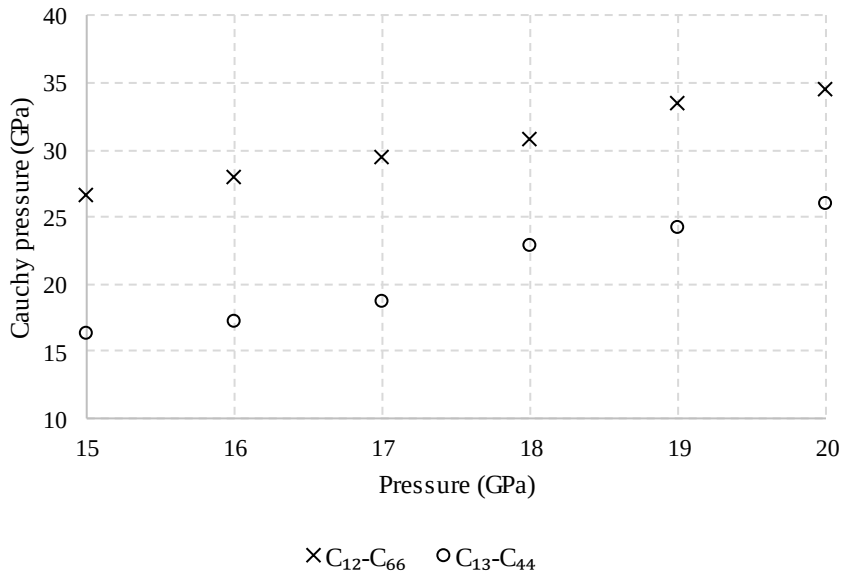

Figure 6.16 Figure S15: The variation of c_{13}-c_{44} and c_{12}-c_{66} with increasing hydrostatic pressure in the pressure range of this study.

The Cauchy pressure[408] for a tetragonal system can be defined as c_{13}-c_{44} and c_{12}-c_{66}, where a positive value suggests that the material is ductile and a negative value suggests that the material is brittle. Figure 6.16 shows the variation of the Cauchy pressure for the CO_2-II in the pressure range of this work. The results obtained suggest that CO_2-II is expected to be ductile with positive values being recorded for both c_{13}-c_{44} and c_{12}-c_{66}, with an increase in pressure resulting in an increase in both these values. The K/G ratio[402] may also be utilised to determine whether a material is ductile or brittle by employing the Pugh criterion where a K/G value exceeding 1.75 indicates that the material is ductile while a K/G value less than 1.75 suggests that the material is brittle. Recent work[241] suggests that this criterion could be replaced with the Christensen's criterion which employs a K/G ratio of 2.27 as the benchmark where a K/G value greater than 2.27 indicates that the material is ductile. The results in Table 6.5 show that the K/G ratio is above both 1.75 and 2.27 in the pressure range of this study suggesting that the material is expected to be ductile. Thus, taking together all the above-mentioned criteria, CO_2-II is expected to be ductile in the pressure range of this study.

6.3.3.4 Rationalising the auxetic potential of CO_2-II

At this stage it would be interesting to study the deformation mechanism giving rise to the predicted auxetic behaviour in CO_2-II. It is known that auxetic behaviour is a result of the interplay between the geometry of the system and the way in which the system deforms on application of a stress. Moreover, the auxetic behaviour may be the result of one or more deformation mechanisms and the interplay between these mechanisms. Stretching or compressing the crystal of CO_2-II in the direction of maximum auxeticity, to study the nanoscale deformation of the system as done in studies for other molecular auxetics[67,68,256,364] and in Chapters 3 to 5, results in a discontinuous trend in the measured parameters, even when using very small stresses (maximum of ±0.5% of the Youngs modulus, see Figure 6.17b). Using smaller maximum stresses to try and avoid this discontinuity would inevitably increase the errors due to computational noise. This behaviour could be an indication that a stress induced phase transition is taking place. Thus, in the case of this study, the auxetic behaviour of CO_2-II was rationalised by studying the changes in the Raman and infra-red spectra under different pressure conditions. A similar approach was taken in Chapters 3 to 5, where spectroscopic measurements were utilised to consolidate the proposed deformation mechanism determined through the nanoscale deformation of the system.

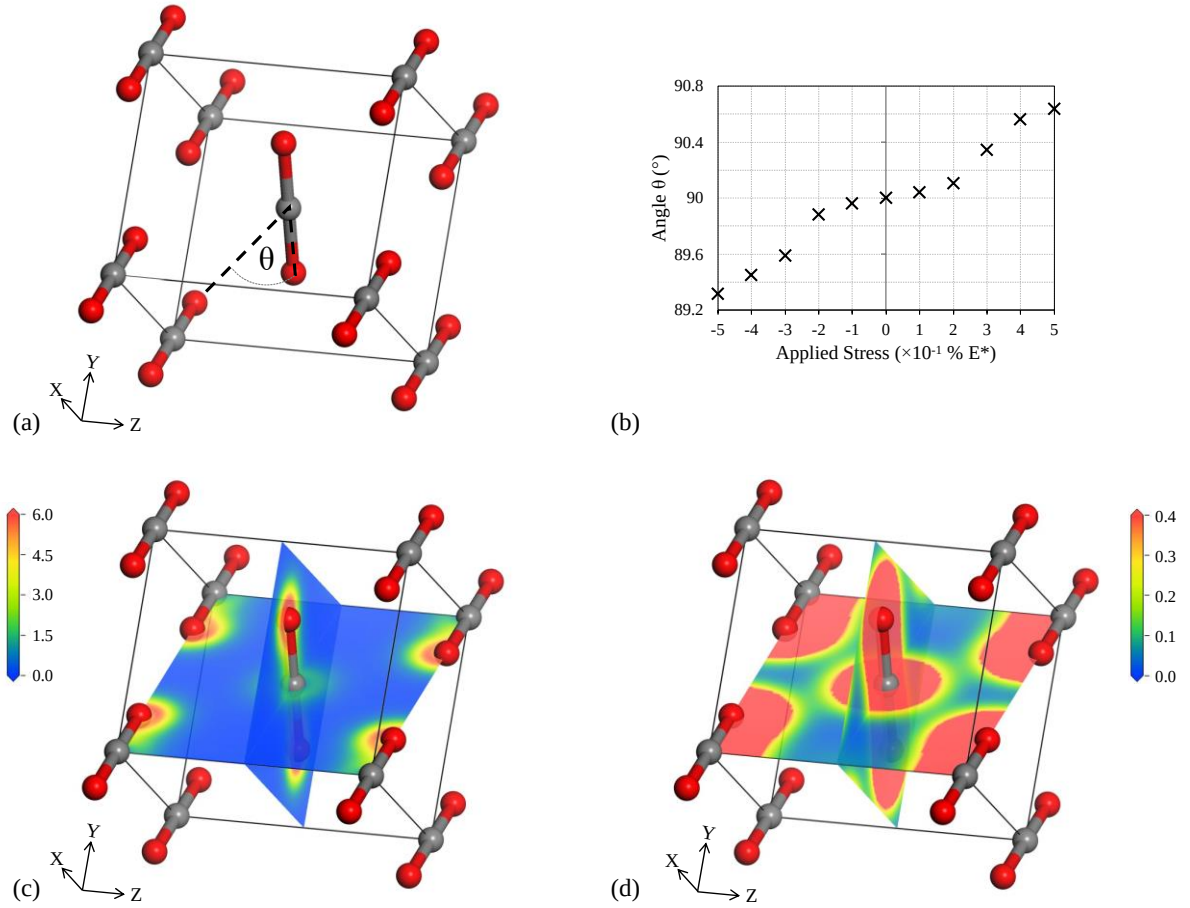

Figure 6.17: (a) The CO_2-II structure with an example of a structural parameter, angle θ, which could be studied to determine the deformation mechanism. (b) An example of the discontinuous trend obtained in the measured parameter on application of a stress. (c) The electron density map of CO_2-II at 15 GPa which is zoomed in by a factor of 15 in (d).

Before analysing the spectra obtained from CO_2-II at different pressures, it is important to first describe the geometry of this crystal system. The space group of CO_2-II is the same as that of rutile type structures. Rutile structures may be described as crystals having a tetragonal unit cell with $P4_2/mnm$ symmetry and which are composed of a central species bonded to six oxygen (or fluorine) atoms based on the TiO_2 prototype[416–418]. Even though CO_2-II is a molecular system, a similar geometry can be identified when taking into consideration the C:O non-bond interactions. As shown in Figure 6.17c and d these weak interactions are oriented in the same direction as expected for the rutile type systems. When taking the bonding and non-bonding interactions together 'octahedral units', as in the case of other rutile systems, may be

identified. Such ‘octahedral units’ will henceforth be referred to as octahedral configurations. It should be highlighted that a typical rutile system would have identical distances in the octahedral configuration. In the case of the octahedral configuration identified in CO_2-II, the carbon to oxygen distances are not all identical. In fact, the equatorial C:O distances are different for the axial C:O distances. Nevertheless, such a configuration is commonly referred as being a rutile-type structure such as in the case of stishovite, and will thus, be referred to as a rutile-type structure in this work.

The Raman spectrum of CO_2-II is dominated by a peak at circa 1300 cm^{-1} (see Figure 6.18). This peak which corresponds to the A_{1g} mode is due to the in-phase stretching vibration of the C=O bonds[57,179]. With increasing hydrostatic pressure, this mode shifts to a higher wavenumber, indicating that the C=O bonds are becoming stiffer with increasing pressure. The Raman spectrum has an additional two modes, namely the E_g mode which corresponds to a rocking motion along the c axis and the B_{1g} mode which corresponds to a shear type libration in the ab plane (see Figure 6.18). At 15 GPa, the E_g mode can be found at a wavenumber of 242 cm^{-1}, while the B_{1g} mode was found at 296 cm^{-1}. Both the B_{1g} and E_g mode shift to higher wavenumbers with an increase in hydrostatic pressure.

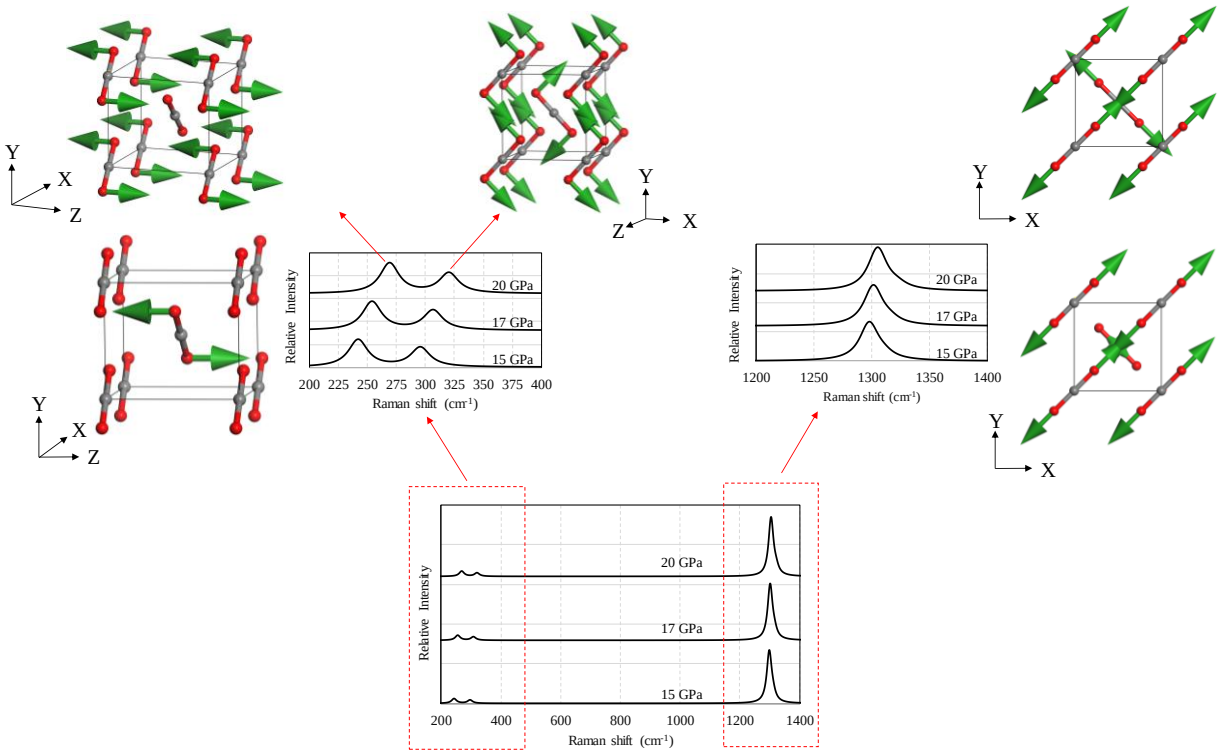

Figure 6.18: The Raman spectrum of CO_2-II at 15 GPa and 20 GPa as calculated utilising the PBE-Grimme functional. Inset: spectrum at lower Raman shift zoomed 10 times with respect to intensity and spectrum at higher Raman shift zoomed 1.25 times with respect to intensity. The vibration modes associated with each peak are shown next to each zoomed inset.

Referring to Figure 6.18, the E_g mode may be associated with internal distortions (these are unequal changes in C=O lengths, C:O non-bond interactions and angles of the octahedral configuration) of the octahedral configuration. On the other hand, the B1g mode may be associated with the relative rotation of the octahedral configuration. As stated above, an increase in pressure is accompanied by an increase in wavenumber of both modes, however, referring to Figure 6.19, the E_g mode increases to a higher extent than the B_{1g} mode. This may indicate that as the ambient pressure increases, upon the application of a uniaxial stress, the rotation : distortion ratio of the octahedral configurations identified for CO_2-II would possibly increase. This would indicate an increase in rotation of the octahedral configuration relative to the distortion of the octahedral configuration. Taking into consideration that an increase in ambient pressure is also accompanied with an increase in auxetic behaviour (in the direction of

maximum auxeticity) one may conjecture that the octahedral configuration rotations are important for the observed negative Poisson's ratio of CO_2-II. This is in accordance with results obtained for the rutile type silicate Stishovite which was also shown to have a negative Poisson's ratio in the (010) and (100) planes where octahedral rotations were also deemed to be important for the observed negative Poisson's ratio[364]. In the case of stishovite, the B_{1g} mode which represents the rotation of the SiO_6 unit was found to become softer with pressure[419], whilst the E_g mode representing the antiphase stretching of Si-O bond[419], was found to shift to higher wave numbers with an increase in pressure.

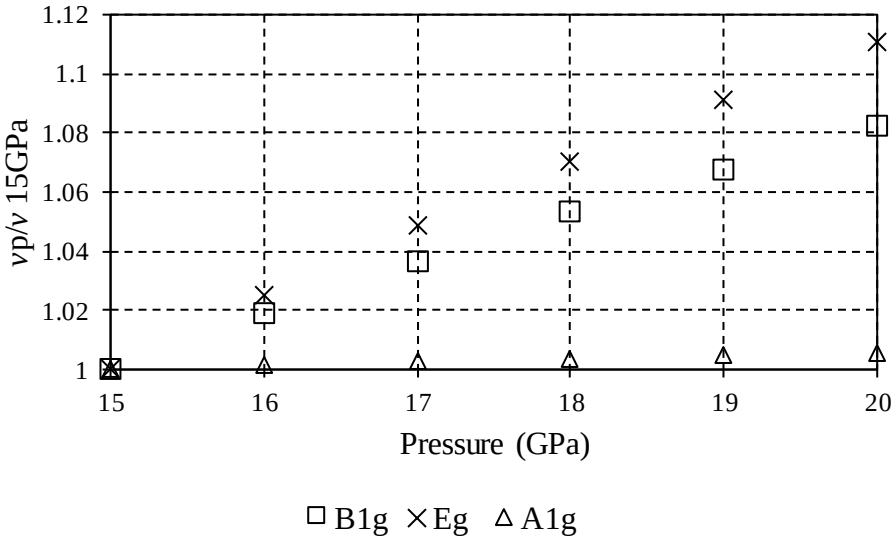

Figure 6.19:Variation of v_p/v_{15GPa} where P is pressure, with pressure (in GPa) for the Raman active modes B_{1g}, E_g and A_{1g}.

The IR spectrum of CO_2-II, see Figure 6.20, is dominated by the A_{2u} mode peak which is found at circa 2260 cm^{-1} at 15 GPa. This mode corresponds to the asymmetric stretch of the C=O bond in the CO_2 molecule. The A_{2u} mode shifts to a higher wavenumber with an increase in hydrostatic pressure, indicating that the C=O bond is becoming stiffer with increasing pressure. This is consistent with the shift to higher wavenumbers of the Raman active A_{1g} mode, as explained above. The IR spectrum of CO_2-II has an additional mode, namely the E_u

mode, located at circa 622 cm^{-1} at 15 GPa and corresponds to the bending motion of the CO_2 molecule, see Figure 6.20.

The E_u mode shifts to a lower wavenumber with an increase in hydrostatic pressure, indicating that the CO_2 bending becomes easier with increasing pressure. This is not unexpected as previous work on CO_2 polymorphs has also reported softening of the bending modes with increasing pressure[420]. The softening of the E_u mode correlates with an increase in auxetic behaviour of the system, when loaded in the direction of maximum auxeticity. This suggests that the softening of this mode would also have important implications on the deformation mechanism of CO_2-II. In fact, these results can be linked with another part of the deformation mechanism which was proposed for the silicate stishovite. In the case of this high-pressure silicate, certain distortions of the SiO_6 octahedra, mainly the equatorial scissoring of the Si-O bonds was found to be an important factor for the observed negative Poisson's ratio of stishovite when loaded in the direction of maximum auxeticity. Such octahedral distortions of stishovite were also attributed to possible electronics effects[364].

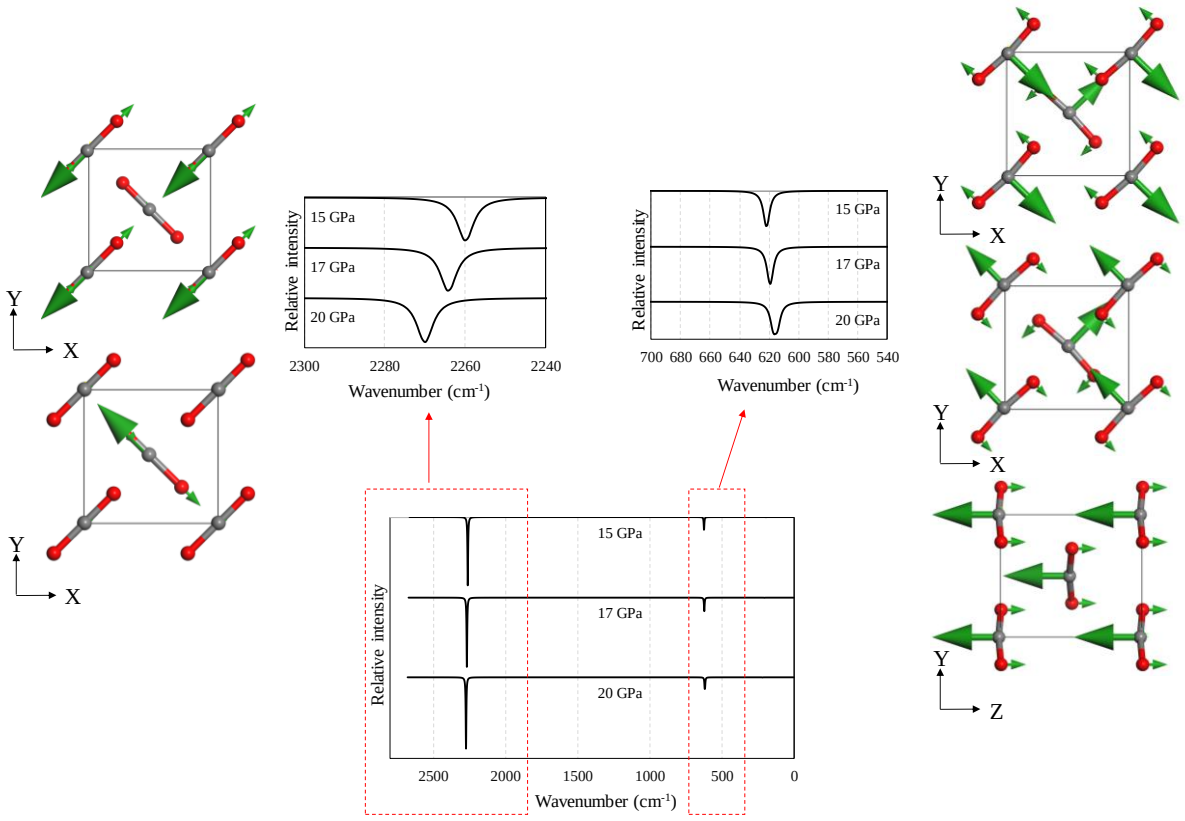

Figure 6.20: The infra-red spectrum of CO_2-II at 15 GPa and 20 GPa as calculated utilising the PBE-Grimme functional. Inset: spectrum at lower wavenumber zoomed circa 4.5 times with respect to intensity. The vibration modes associated with each peak are shown next to each zoomed inset.

To consolidate the work done in section 6.2, convergence testing was also carried out when calculating the Raman and infrared spectra of CO_2-II. The results obtained, see Figure 6.21 and Figure 6.22, show that the refinement in the simulation parameters had no significant effect on the spectra computed at both 15 GPa and 20 GPa ensuring that convergence has been achieved and that the vibrational properties computed are not an artefact of the simulation parameters employed. In fact, refining the simulation parameters had no effect the number of peaks obtained and no effect on the shift direction of these peaks with a change in hydrostatic pressure.

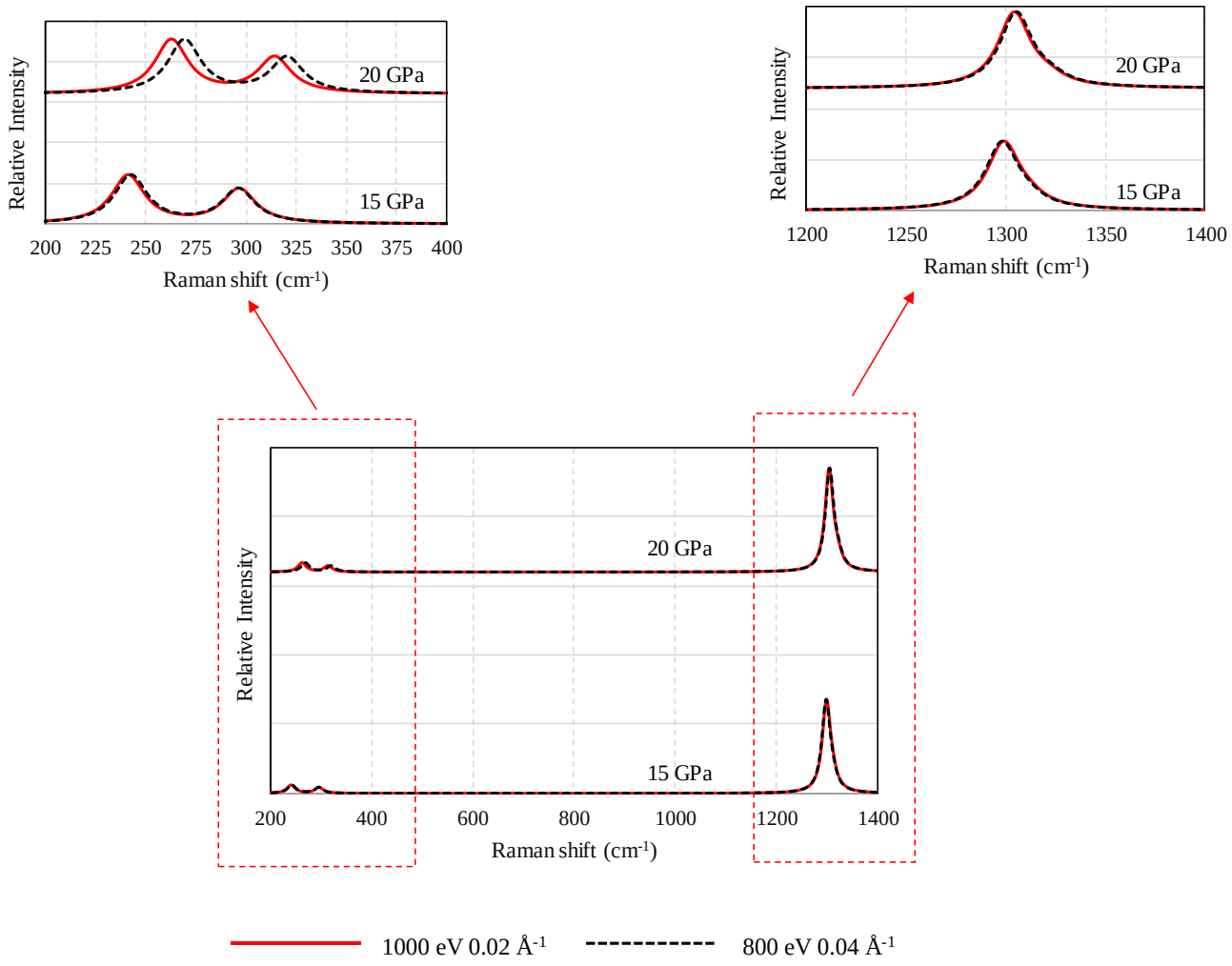

Figure 6.21: Comparison of the Raman spectrum obtained for CO_2-II when employing a cut-off energy of 800 eV and a Monkhorst-Pack grid spacing of 0.04 $Å^{-1}$ with the spectrum obtained utilising a cut-off energy of 1000 eV and a spacing of 0.02 $Å^{-1}$ at 15 GPa and at 20 GPa. Inset: spectrum at lower Raman shift zoomed 10 times with respect to intensity and spectrum at higher Raman shift zoomed 1.25 times with respect to intensity.

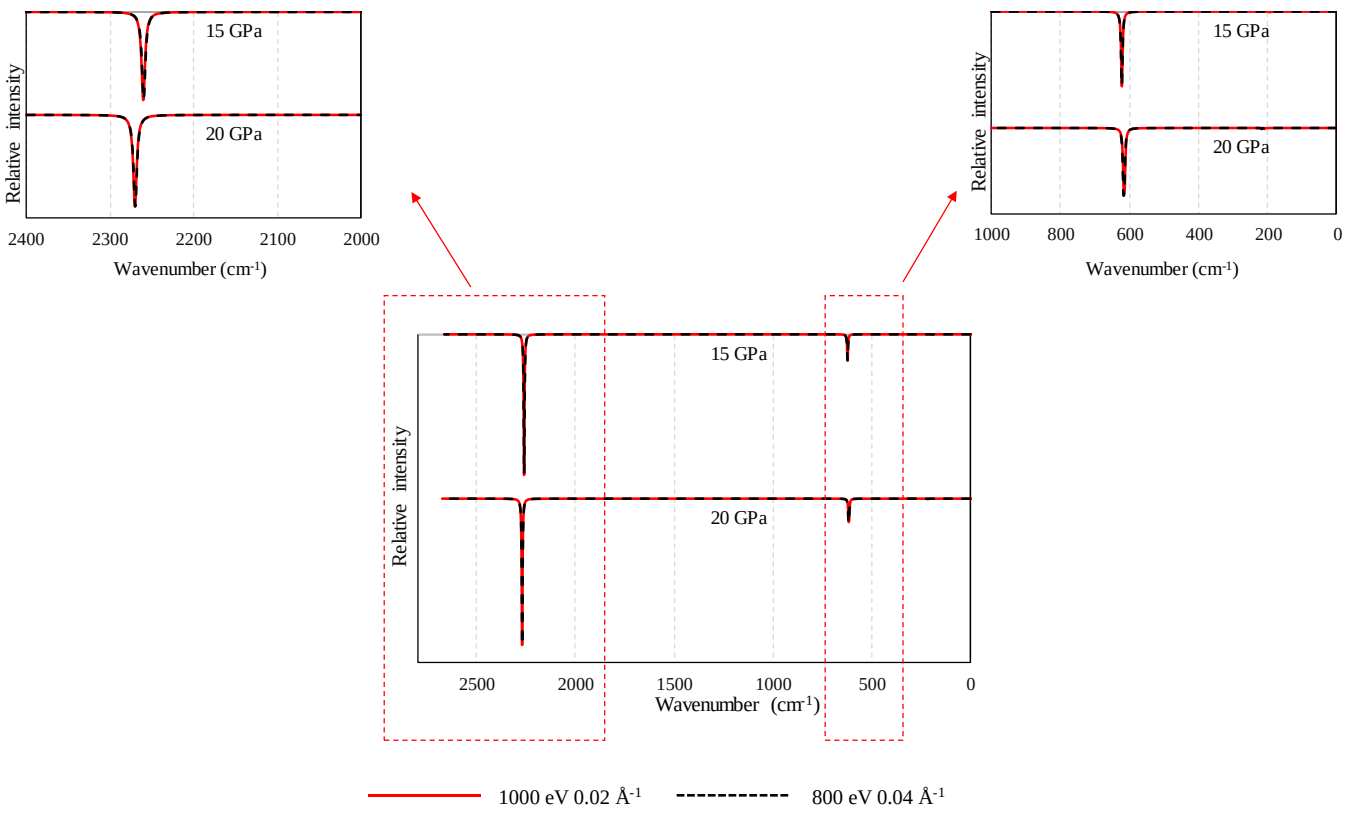

Figure 6.22: Comparison of the infrared spectrum obtained for CO_2-II when employing a cut-off energy of 800 eV and a Monkhorst-Pack grid spacing of 0.04 $Å^{-1}$ with the spectrum obtained utilising a cut-off energy of 1000 eV and a spacing of 0.02 $Å^{-1}$ at 15 GPa and at 20 GPa. Inset: spectrum at lower wavenumber zoomed circa 5 times with respect to intensity.

To cement the work done on the deformation mechanism of CO_2-II, the infra-red and Raman spectra of CO_2-II were recalculated employing PBE and PBE-TS at 15 GPa and 20 GPa. The vibrational properties computed were then compared to those calculated when employing the PBE-Grimme functional at the same hydrostatic pressures. The results obtained, see Figure 6.23 and Figure 6.24, show there is qualitative agreement between the spectra obtained when utilising different functionals albeit with some slight shift in peak position depending on the functional used. In particular, the functionals all calculate the same number of peaks and the pressure dependence of the shift in position of these peaks. This ensures that the description rationalising the negative Poisson's ratio of CO_2-II utilising these vibrational properties is not an artefact of the functional employed.

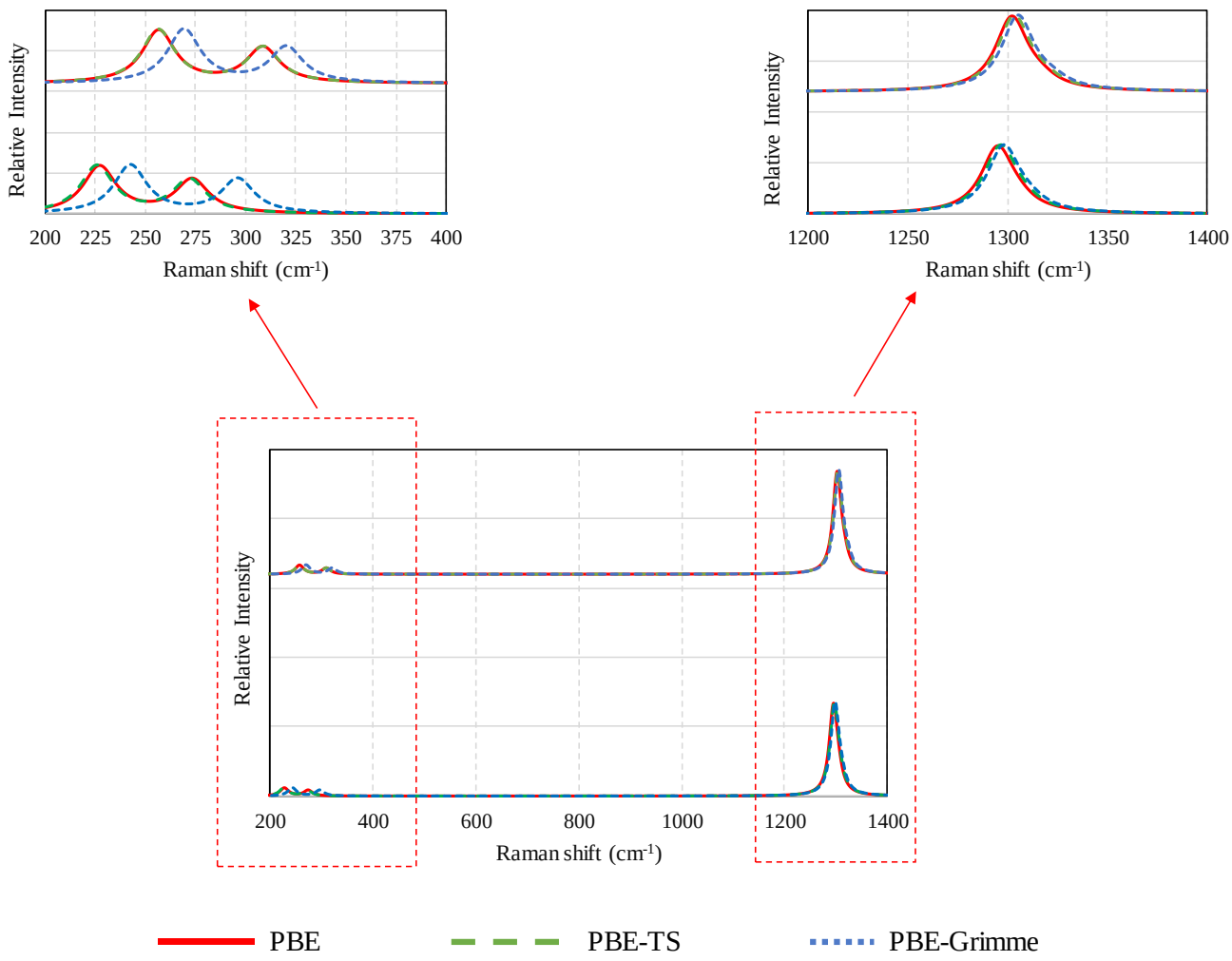

Figure 6.23: Comparison of the Raman spectrum calculated for CO_2-II using PBE, PBE-Grimme and PBE-TS at 15 GPa and 20 GPa. Inset: spectrum at lower Raman shift zoomed 10 times with respect to intensity and spectrum at higher Raman shift zoomed 1.25 times with respect to intensity.

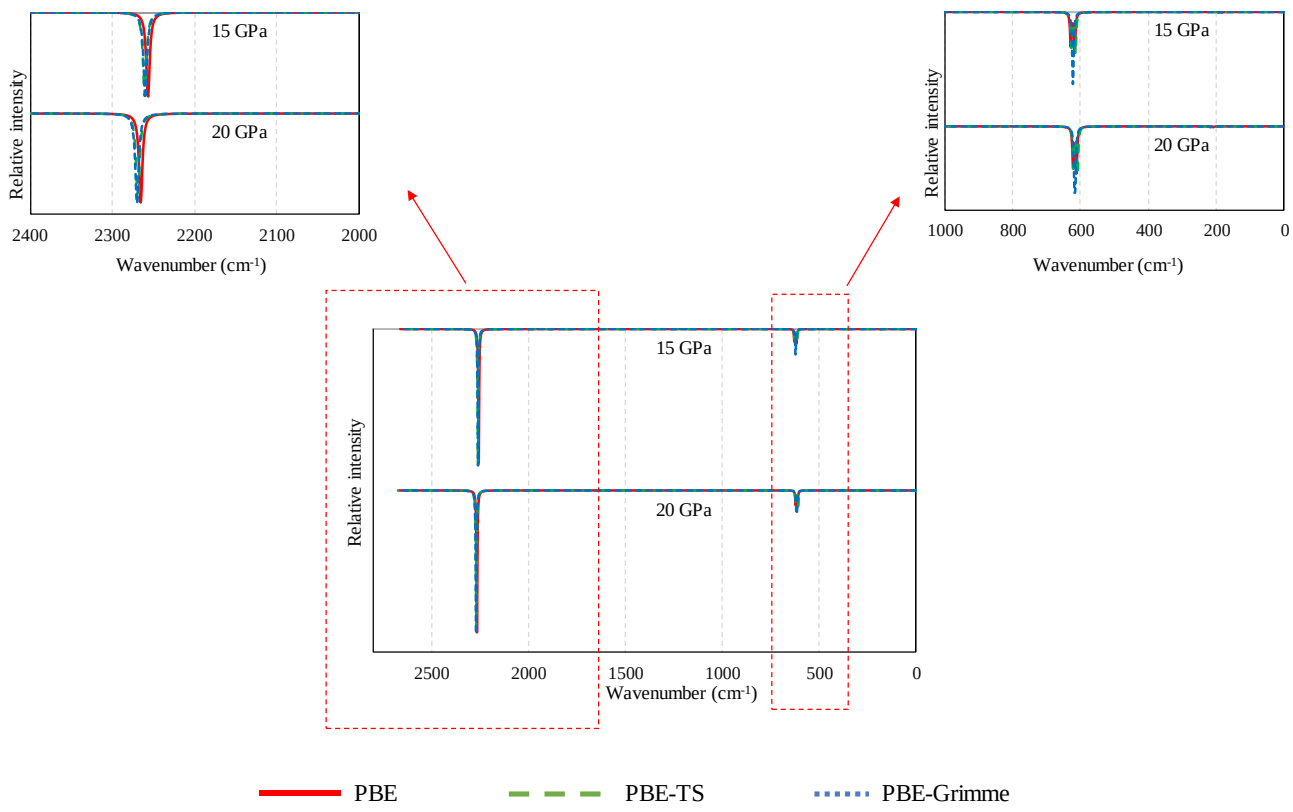

Figure 6.24: Comparison of the infrared spectrum calculated for CO_2-II using PBE, PBE-Grimme and PBE-TS at 15 GPa and 20 GPa. Inset: spectrum at lower wavenumber zoomed circa 5 times with respect to intensity.

Before concluding, it is important to highlight the importance of the use of Raman and IR spectroscopy, even in theoretical studies, when elucidating possible deformation mechanisms of auxetic systems. Such spectra could also be consolidated through experimental work on the system, albeit not a simple task given the pressures required for systems like CO_2-II. This work also paves the way for further studies on this system and other systems with $P4_2/mnm$ symmetry such as gamma nitrogen (γ-nitrogen), a solid phase of nitrogen.

6.3.4 Conclusions

In this work, first principles DFT calculations have been employed to study the structural, mechanical and vibrational properties of CO_2-II in the pressure range of 15 GPa to 20 GPa. In particular, the Young's modulus, shear modulus and Poisson's ratio for both the single crystal and the polycrystalline aggregate were determined. Moreover, it has been shown that CO_2-II is dynamically stable in the pressure range of this work. The CO_2-II single crystal has been shown to exhibit a negative Poisson's ratio for loading at circa 48° to the y-axis in the (100) plane and similarly in the (010) plane. The negative Poisson's ratio of this system is pressure dependent with an increase in pressure resulting in an increase in the auxetic behaviour in the direction of maximum auxeticity. Through the use of Raman and IR spectroscopy the auxetic behaviour in this system was rationalised. It was shown that that as hydrostatic pressure increases the A_{1g}, B_{1g} and E_g modes shift to higher wavenumbers while the E_u mode shifts to lower wavenumbers. These shifts in vibration modes with increasing pressure correlate with an increase in auxetic potential of the system. These shifts suggest that rotations and certain distortions of the intermolecular and intramolecular interactions may be used to rationalise the predicted auxetic behaviour.

Chapter 7: General Discussion, Conclusions and Future Perspective

Researchers have always been intrigued by the idea of studying materials at extreme conditions such as very high pressures. On a fundamental level, studies of materials at high pressures shape our understanding of electrons and bonding[39,40,44,45]. For example, at pressures nearing 250 GPa a polymeric nitrogen phase has recently been synthesized[421], illustrating the formation of a macromolecular species at high pressures from substances which are molecular systems at ambient conditions. Moreover, advances in high pressure research are also of interest from a geoscience point of view, where such developments can improve our understanding of planet dynamics. For instance, CO_2-V was shown to be stable in the thermodynamic conditions of the deep lower mantle and as a result, studies on this system could aid in the understanding of carbon distribution in the layers of Earth[37]. In addition to this, advances in high pressure research could also possibly lead to the formation of substances with novel and useful properties which may be metastable at ambient conditions[42]. For example, stishovite is a high pressure SiO_2 polymorph and one of the hardest oxides known to exist[422] and may be found as a metastable crystal at ambient conditions[422] even though it is formed at high pressures and temperatures.

In this thesis, high pressure polymorphs of low mass oxides (i.e. low-Z oxides[39]) were studied through the use of density functional theory calculations. This work focused on the properties of substances which are ubiquitous and known to all at ambient conditions. Nevertheless, when subjected to high external pressures, H_2O and CO_2 form substances with

unexpected and interesting properties. The formation of numerous solid polymorphs at various conditions of pressure and temperature is in itself an interesting phenomenon, where these simple triatomic molecules can form such a vast array of polymorphs, some of which have been the subject of studies for over a hundred years[50,51]. Nevertheless, studies on the polymorphs of these simple systems are still attracting the attention of researchers[9,423–425].

The main aim of this work was to study the mechanical properties of high-pressure polymorphs of CO_2 and H_2O paying particular attention to the Poisson's ratio (see Chapter 2, Section 2.4). The work in Chapter 3 and Chapter 4 **reported for the first time that high pressure polymorphs of H_2O ice have the potential to exhibit a negative Poisson's ratio** signifying a substantial advancement in the field of high-pressure ice research and in the field of auxetics. In Chapter 3, the mechanical properties of ice X, a macromolecular phase of ice where the H_2O molecules are no longer distinct but are bonded through covalent bonds, were studied. The ice X system can be formed from ice VIII through a pressure induced phase transition[120,145,149,152]. The mechanical properties of ice VIII were studied in Chapter 4. Following the work on high pressure H_2O systems, the behaviour of CO_2, another common triatomic molecule found in everyday life at ambient conditions, was investigated. The work in Chapter 5 and Chapter 6 reported for the first time that **high pressure polymorphs of CO_2 also have the potential to exhibit a negative Poisson's ratio**. In Chapter 5, the mechanical properties of CO_2-V were studied. Similar to ice X, CO_2-V is a macromolecular polymorph which is also reported to be found at high pressures. CO_2-V can be formed when the hydrostatic pressure of CO_2-II is increased at certain temperatures[167,176,426]. The mechanical properties of CO_2-II were discussed in Chapter 6.

In this thesis, different aspects of the chemistry of these high-pressure polymorphs were assessed through the use of DFT calculations. When carrying out DFT simulations, the choice of cut-off energy and spacing of the Monkhorst-Pack k-point grid is essential to ensure an

adequate representation of the system. Thus, to ensure that the properties determined are not an artefact of the simulation parameters employed, but an innate property of the system, detailed convergence studies were carried out for all systems studied. In particular, the effect of increasing the cut-off energy and decreasing the spacing of the Monkhorst-Pack k-point grid was studied in order to assess the suitability of the simulation parameters employed for the different pressure ranges used. An energy cut-off of 800 eV was found to be sufficient in the case of ice X (150 GPa to 300 GPa), CO_2-V(40 GPa to 60 GPa) and CO_2-II(15 GPa to 20 GPa). On the other hand, in the case of ice VIII (20 GPa to 40 GPa) an energy cut-off of 1000 eV was employed. From these results there seems to be no apparent relationship between the energy cut-off employed and the pressure ranges used for the different polymorphs. However, a less refined Monkhorst-Pack k-point grid was needed when studying the different H_2O and CO_2 polymorphs at increasing pressure windows. In fact, in the case of ice X a mesh spacing of 0.07 $Å^{-1}$ was needed while in the case of ice VIII a mesh spacing of 0.03 $Å^{-1}$ was needed. Similarly in the case of CO_2-V a mesh spacing of 0.06 $Å^{-1}$ was needed, while in the case of CO_2-II a mesh spacing of 0.04 $Å^{-1}$ was required.

In addition to carrying out convergence studies, the methodology employed was benchmarked by comparing the properties obtained through the DFT calculations with results present in the literature. This ensures that the simulation parameters employed can adequately represent the system. It is interesting to note that overall, there was a reasonably good agreement between the theoretical results obtained in this work and the data present in the literature. For example, a comparison of the calculated lattice parameters with those obtained experimentally at the same pressure showed a maximum deviation of circa 1% when comparing the results obtained for all four high-pressure systems investigated in this thesis. It should be noted that this value refers to the results obtained utilising the best performing functional in each study. Indeed, some functionals did not perform as well, with for example PW91-OBS

showing a deviation of circa 11 % when benchmarking the lattice parameters of the ice VIII system. Thus, another factor which is essential to the success of the DFT calculations is the choice of functional. In this work the suitability of numerous functionals were assessed. The results obtained suggest that PBE can be used to study ice X, ice VIII and CO_2-V while PBE-Grimme can be used to study CO_2-II suggesting the need for dispersion corrected functionals at lower pressures, albeit all functionals giving fairly similar results when studying the CO_2-II system. Nevertheless, the properties determined for the polymorphs was confirmed by using other functionals. This provides confidence that the properties obtained are indeed an adequate representation of the system being studied and not an artefact of the calculation parameters utilised. The detailed convergence study together with the benchmarking of the methodology carried out in this thesis provides confidence in the simulations carried out.

A problem which was encountered in Chapters 3 to 6 was the choice of the pressure range where a particular polymorph was studied. This is because in the literature there are several debates on the pressure stability fields of particular polymorphs. For example, as highlighted in Chapter 2 Section 2.1.6, there is a debate on the stability field of ice X with the pressure at which ice VIII undergoes a phase change to ice X being a source of controversy[145,146,154]. Another example is the controversial nature of the stability field of CO_2-II and the pressure at which CO_2-II is expected to undergo a phase change to CO_2-V[15,57,171,176,178,180]. Thus, to ensure that the polymorphs studied in this thesis are stable within the selected pressure range, phonon dispersion relations were calculated. The phonon dispersions obtained had no imaginary frequencies, which suggests that the systems considered in this thesis are indeed stable or metastable within the selected pressure ranges.

In Chapters 3 to 6, the mechanical properties of different polymorphs of H_2O and CO_2 have also been investigated. For example, the variation of the Young's modulus, shear modulus, bulk modulus and Pugh ratio (K/G ratio) for the polycrystalline aggregate have been

studied. It was found that the Young's modulus tends to increase with increasing pressure. Furthermore, the shear moduli for the systems investigated increases with increasing hydrostatic pressure. Moreover, for all the polymorphs considered in this thesis, an increase in pressure was associated with an increase in the Pugh ratio (K/G). When considering the Pugh ratio, which gives an indication of the ductility or brittle nature of the material, it was found that ice X and CO_2-II are expected to be ductile while ice VIII and CO_2-V are expected to be brittle in the pressure range of the study. In addition to the Pugh ratio, the Cauchy pressure and the Poisson's ratio may also be used to assess the ductility or brittle nature of the material. The results obtained when utilising the Cauchy pressure and the Poisson's ratio were consistent with the results obtained when employing the Pugh ratio. Through the use of different approaches, one may have greater confidence in the conclusions derived regarding the material property of the system.

As discussed above, ice X, ice VIII, CO_2-II and CO_2-V single crystals have been found to exhibit a negative Poisson's ratio. Cubic ice X was found to exhibit a negative Poisson's ratio at 45° off-axis in the (100), (010) and (001) planes. DFT simulations performed on tetragonal ice VIII also showed that this polymorph of ice, which was studied in Chapter 4, exhibits a negative Poisson's ratio. Contrary to ice X, it was shown that ice VIII exhibits an auxetic behaviour when loaded on-axis in the (001) plane. In Chapter 5, it was shown that CO_2-V exhibits a negative Poisson's ratio for loading in all directions in the (001) plane. In Chapter 6 it was shown that CO_2-II has the potential to exhibit off-axis auxetic behaviour for loading at circa 48° to the y-axis in the (100) plane and similarly in the (010) plane. In the case of all four polymorphs, it was shown that the Poisson's ratio is pressure dependent, with an increase in pressure resulting in an increase in auxetic behaviour in the direction of maximum auxeticity. In sharp contrast, studying the Poisson's ratio for the polycrystalline aggregate showed that all

four polymorphs are expected to exhibit a positive Poisson's ratio which increases with increasing hydrostatic pressure.

The deformation mechanisms responsible for the observed negative Poisson's ratios were also investigated. When studying the deformation mechanism of crystalline systems using molecular modelling, it is typical to apply a stress in the direction of maximum auxeticity and study the nanoscale deformation of the system when subjected to this stress[67,68,256,364]. In this thesis, this method was successfully employed to study ice X, ice VIII and CO_2-V. However, it was not possible to use such a method to study the deformation mechanism of the CO_2-II. This was because the application of a stress resulted in a non-continuous change in the structural parameters studied, which may be an indication of a stress induced phase transition. Thus, the auxetic potential of the CO_2-II, was rationalised through a novel methodology developed in this thesis which employed a comparison of changes in spectroscopic data and auxetic behaviour as the system is subjected to different pressures. This method was also used to consolidate the deformation mechanisms of ice X, ice VIII and CO_2-V.

The work carried out suggests that the auxetic behaviour of cubic ice X is a result of the geometry of the oxygen lattice system, wherein two orthogonally interconnected rhombi were identified. It was shown that on application of a stress these rhombi concurrently undergo hinging and distortion, whereby the hinging deformations contribute to a negative Poisson's ratio whilst the distortions of these interconnected rhombi contribute to a positive Poisson's ratio. It is interesting to note that in his seminal work, Baughman[304] had shown that 69% of a sample of cubic metals studied had the potential to exhibit auxetic behaviour and used a similar geometry/deformation mechanism to rationalise their auxetic behaviour. This shows the importance of considering existing deformation mechanisms in rationalising newly predicted auxetic behaviour. As discussed above, an increase in hydrostatic pressure resulted in a more negative Poisson's ratio in the direction of maximum auxeticity. The increase in hydrostatic

pressure was also accompanied by an increase in the stiffness and hinging of the rhombi. Thus, with an increase in hydrostatic pressure deformation through distortion of the interconnected rhombi became less prominent whilst the hinging of the interconnected rhombi became more important, explaining the increase in auxeticity. Also as stated above, this deformation mechanism was confirmed through the use of Raman spectroscopy. In the case of ice X, the increase in rigidity of the rhombi was inferred from the shift to higher wavenumbers of the T_{2g} Raman active mode with increasing pressure, which implies increase in strength of the O-O interaction with increasing pressure.

A similar deformation mechanism was also found to operate in ice VIII. The Ice VIII structure is composed of two interpenetrating hydrogen bonded systems with a body centred oxygen sub-lattice [130]. The O:O interactions in these body centred oxygen sub-lattices may be described as forming two orthogonally interconnected rhombi. In the case of ice VIII, the O:O interactions which make up the interconnected rhombi are not the same and thus, may be more accurately described as orthogonally interconnected irregular rhombi. Through direct measurement of the identified geometry, it was shown that the auxetic behaviour of ice VIII is due to interplay between two deformation mechanisms namely stretching and hinging of the two interconnected rhombi. As the pressure increased, these rhombi become more regular. It was also shown that as the hydrostatic pressure increases, the sides of the rhombi become stiffer and thus, the stretching mechanism and distortion becomes less significant, with the hinging of the rhombi becoming more prominent, changes that are accompanied with an increase in auxeticity. The deformation mechanism of the ice VIII system was consolidated through the use of spectroscopic techniques, specifically Raman and infrared spectroscopy. Taking into consideration the IR active bending intramolecular mode v_2 (A_{2u}), a slight decrease in wavenumber was noted with an increase in pressure, illustrating that the O—H—O hinge is slightly decreasing in stiffness with pressure. On the other hand, the Raman

active ν_{Tz} (B_{1g}) and ν_{TxTy} (Eg) modes, which are associated with the stiffness of the O:O interaction[124,354,412,413] shift to higher wavenumbers with increasing pressure indicating an increase in stiffness off the O:O mode.

In the case of CO_2-V, a two dimensional and three-dimensional approach were used to study the deformation mechanism of this system. An analysis of the projections of the atoms of the CO_2-V system in the (001) plane reveals a 'connected squares' motif, where these 'connected squares' are the two-dimensional projections of the three-dimensional CO_4 tetrahedra, with each square having a central carbon atom and four oxygen atoms at its conners. On application of a stress, it was shown that the squares rotate relative to each other and simultaneously distort, indicating that the 'connected squares' are behaving as semi-rigid rotating units. As discussed above and in Chapter 5, an increase in pressure was found to result in a more negative Poisson's ratio in the (001) plane of CO_2-V. This increase in auxetic potential was accompanied with an increased rotation of the projected squares relative to the distortion of the squares. This indicates that as the projected squares distort less, they approach the theoretical Poisson's ratio of -1 expected from the rotating rigid units mechanism[215]. An investigation of the deformation of the three-dimensional CO_4 tetrahedra, rather than their projection in the (001) plane, suggested that three principle events are taking place, (1) stretching of some of the C-O bonds, and (2) distortion of the CO_4 tetrahedra, which together account for the observed distortion of the projected squares and (3) relative rotation of the tetrahedra which accounted for relative rotation of the projected squares. The same conclusions were also derived from Raman and infrared spectra of CO_2-V conducted in the pressure range of 40 GPa to 60 GPa, where it was found that C-O bonds, C-O-C and O-C-O angles increase in stiffness with increasing pressure albeit to different extents indicating that one mechanism is being favoured over the others.

Studying the variation of the Raman active and infrared active modes of CO_2-II with pressure it was shown that an increase in hydrostatic pressure was associated with a shift of the A_{1g}, B_{1g} and E_g modes to higher wavenumbers while the E_u mode shifts to lower wavenumbers. These shifts suggested that rotations and distortions of the system may be utilised to explain the predicted auxetic behaviour of CO_2-II, which explanation is consistent with the deformation mechanism of stishovite, a rutile type silicate which was also shown to have a negative Poisson's ratio in the (010) and (100) planes where octahedral rotations and distortions were also shown to be important to rationalise the observed auxetic behaviour[364].

All this highlights the importance of DFT as a tool for the study of high-pressure systems. Studying such systems at extreme conditions experimentally is challenging[44,45] and it requires highly specialised equipment which may be expensive to acquire and maintain. Moreover, there is also difficulty associated with experimentally achieving the extremely high pressure conditions required to study certain systems[44]. Carrying out DFT calculations and then confirming the results obtained through experimental data or using DFT calculations to understand experimentally measured properties of high-pressure materials would provide an ideal situation to maximise the knowledge of high-pressure systems.

The work carried out in this thesis paves the way for further research on the properties of high-pressure systems. For example, the properties of other high-pressure polymorphs of H_2O and CO_2 can be investigated. For instance, it is thought that ice X may undergo pressure induced phase transitions on increasing pressure with structures belonging to the *Pbcm*, *Pbca* and *Cmcm* space group being predicted to form, as outlined in the literature review (Chapter 2). It would thus, be interesting to investigate the properties of these systems. For example, dynamic stability of these phases can be assessed. Moreover, the Poisson's ratio of these systems may be investigated to assess whether these systems have the potential to exhibit auxetic behaviour and subsequently study the mechanism/s behind this behaviour.

Furthermore, other phases of ice which have a body centred arrangement of oxygen atoms such as ice VII and ice I_c can be studied, as in the case of both ice phases investigated in this thesis the orthogonally interpenetrating rhombi geometry was found to operate when oxygens are found in a body centred arrangement. This geometry may be used as a blueprint for synthetic chemists when trying to synthesis materials which exhibit a negative Poisson's ratio. Similarly, in the case of CO_2 polymorphs, other phases such as CO_2-III and CO_2-IV can also be studied to investigate if such phases can also exhibit a negative Poisson's ratio.

It would also be interesting to investigate the possible phases which may form on application of a non-hydrostatic pressure. It may be possible that a stress induced phase transition takes place on application of a sufficiently high non-hydrostatic pressure. This is a very important area of study as it would enable planetary geologists to further understand the mantle dynamics of ice giant planets such as Neptune and Uranus as well as geologists working on high-pressure phases of H_2O and CO_2 ice found on Earth. The new phases formed can then be investigated for their dynamic stability and their mechanical properties studied. For example, the auxetic potential of these systems can then be assessed and studied through nanoscale deformation of the system and through the use of spectroscopic techniques as carried out in this thesis.

It would also be interesting to study the effect of inclusions such as ions on the mechanical properties of the high-pressure systems with the effect of inclusions being the subject of a number of recent studies[358,427,428]. For example, a recent study on KCl bearing ice VII found that impurities had an effect on the density of the ice with the sample being 6-8% denser than ice VII formed from pure water[6]. Thus, it would be interesting to examine the effect of the presence of ions on the mechanical properties of the high-pressure ice polymorphs studied in this work. For example, study the effect of the presence of salts such as NaCl or KCl

or other inclusions on the auxetic behaviour of the system and how this would vary with increasing hydrostatic pressure.

In addition, in analogy to H_2O and CO_2, research can focus on the properties of H_2S[429] and CS_2[430] where, amongst other research interests, the Poisson's ratio of the high pressure polymorphs of these systems can be assessed. Moreover, the dynamic stability together with the Raman and infrared spectra of these systems can be assessed. Another example would be studying the properties of other typically molecular systems at ambient conditions, by subjecting them to high pressures such as high pressure oxygen[431], nitrogen[432], hydrogen[433], methane[434] or ammonia[435].

In summary, this work has shown, for the first time, that the high-pressure polymorphs ice X, ice VIII, CO_2-V and CO_2-II have the potential to exhibit a negative Poisson's ratio. This thesis provided the first detailed study of the auxetic potential of these systems together with the development of deformation mechanisms which can rationalise the predicted auxetic behaviour. This work also determined the vibrational properties and the dynamic stability of these systems. Infrared and Raman spectroscopy have been used to consolidate the deformation mechanism of these systems, an approach used for the first time in this thesis, thus providing a novel approach to study the auxetic behaviour of a system. This work may inspire and pave the way for future studies in the fields of high-pressure research and auxetic materials.

References

1. Sun, J. *et al.* High-pressure polymeric phases of carbon dioxide. *Proc. Natl. Acad. Sci.* **106**, 6077–6081 (2009).

2. Litasov, K. D., Goncharov, A. F. & Hemley, R. J. Crossover from melting to dissociation of CO2 under pressure: Implications for the lower mantle. *Earth Planet. Sci. Lett.* **309**, 318–323 (2011).

3. Shieh, S. R. *et al.* Electronic structure of carbon dioxide under pressure and insights into the molecular-to-nonmolecular transition. *Proc. Natl. Acad. Sci. U. S. A.* **110**, 18402–18406 (2013).

4. Bina, C. R. & Navrotsky, A. Possible presence of high-pressure ice in cold subducting slabs. *Nature* **408**, 844–847 (2000).

5. Men, Z., Fang, W., Li, D., Li, Z. & Sun, C. Raman spectra from symmetric hydrogen bonds in water by high-intensity laser-induced breakdown. *Sci. Rep.* **4**, 1–5 (2014).

6. Frank, M. R., Scott, H. P., Aarestad, E. & Prakapenka, V. B. Potassium chloride-bearing ice VII and ice planet dynamics. *Geochim. Cosmochim. Acta* **174**, 156–166 (2016).

7. Schmidt, B. E. *et al.* Geomorphological evidence for ground ice on dwarf planet Ceres. *Nat. Geosci.* **10**, 338–343 (2017).

8. Cavazzoni, C. *et al.* Superionic and metallic states of water and ammonia at giant planet conditions. *Science* **283**, 44–46 (1999).

9. Shieh, S. R., Hsieh, W. P., Tsao, Y. C., Crisostomo, C. & Hsu, H. Low Thermal Conductivity of Carbon Dioxide at High Pressure: Implications for Icy Planetary Interiors. *J. Geophys. Res. Planets* **127**, (2022).

10. Li, J., Sode, O., Voth, G. A. & Hirata, S. A solid-solid phase transition in carbon dioxide at high pressures and intermediate temperatures. *Nat. Commun.* **4**, 1–8 (2013).

11. Loerting, T., Fuentes-Landete, V., Tonauer, C. M. & Gasser, T. M. Open questions on the structures of crystalline water ices. *Commun. Chem.* **3**, 1–4 (2020).

12. Hansen, T. C. The everlasting hunt for new ice phases. *Nat. Commun.* **12**, 10–12 (2021).

13. Salzmann, C. G. Advances in the experimental exploration of water's phase diagram. *J. Chem. Phys.* **150**, (2019).

14. Hirata, S., Gilliard, K., He, X., Li, J. & Sode, O. Ab initio molecular crystal structures, spectra, and phase diagrams. *Acc. Chem. Res.* **47**, 2721–2730 (2014).

15. Han, Y., Liu, J., Huang, L., He, X. & Li, J. Predicting the phase diagram of solid carbon dioxide at high pressure from first principles. *npj Quantum Mater.* **4**, (2019).

16. Kuhs, W. F., Finney, J. L., Vettier, C. & Bliss, D. V. Structure and hydrogen ordering in ices VI, VII, and VIII by neutron powder diffraction. *J. Chem. Phys.* **81**, 3612–3623 (1984).

17. Besson, J. M. *et al.* Variation of interatomic distances in ice VIII to 10 GPa. *Phys. Rev. B* **49**, 12540–12550 (1994).

18. Yoshimura, Y., Stewart, S. T., Somayazulu, M., Mao, H. K. & Hemley, R. J. High-pressure x-ray diffraction and Raman spectroscopy of ice VIII. *J. Chem. Phys.* **124**, 1–7 (2006).

19. Salzmann, C. G., Loveday, J. S., Rosu-Finsen, A. & Bull, C. L. Structure and nature of ice XIX. *Nat. Commun.* **12**, 1–7 (2021).

20. Salzmann, C. G., Radaelli, P. G., Mayer, E. & Finney, J. L. Ice XV: A new

thermodynamically stable phase of ice. *Phys. Rev. Lett.* **103**, 105701 (2009).

21. Yoo, C. S. Physical and chemical transformations of highly compressed carbon dioxide at bond energies. *Phys. Chem. Chem. Phys.* **15**, 7949–7966 (2013).

22. Giordano, V. M. & Datchi, F. Molecular carbon dioxide at high pressure and high temperature. *EPL (Europhysics Lett.* **77**, 46002 (2007).

23. Yoo, C. S., Sengupta, A. & Kim, M. Phase diagram of carbon dioxide: Update and challenges. *High Press. Res.* **31**, 68–74 (2011).

24. Kim, M., Ryu, Y. J., Lim, J. & Yoo, C. S. Transformation of molecular CO2-III in low-density carbon to extended CO2-V in porous diamond at high pressures and temperatures. *J. Phys. Condens. Matter* **30**, (2018).

25. Iota, V. *et al.* Six-fold coordinated carbon dioxide VI. *Nat. Mater.* **6**, 34–38 (2007).

26. Datchi, F., Mallick, B., Salamat, A. & Ninet, S. Structure of Polymeric Carbon Dioxide CO2-V. *Phys. Rev. Lett.* **108**, 125701 (2012).

27. Teweldeberhan, A. M., Boates, B. & Bonev, S. A. CO2 in the mantle: Melting and solid-solid phase boundaries. *Earth Planet. Sci. Lett.* **373**, 228–232 (2013).

28. Moog, M., Pietrucci, F. & Saitta, A. M. Carbon Dioxide under Earth Mantle Conditions: From a Molecular Liquid through a Reactive Fluid to Polymeric Regimes. *J. Phys. Chem. A* **125**, 5863–5869 (2021).

29. Vance, S. D., Journaux, B., Hesse, M. & Steinbrügge, G. The Salty Secrets of Icy Ocean Worlds. *J. Geophys. Res. Planets* **126**, (2021).

30. Zeng, L. & Sasselov, D. The effect of temperature evolution on the interior structure of H 2O-rich planets. *Astrophys. J.* **784**, 96 (2014).

31. Noack, L. *et al.* Water-rich planets: How habitable is a water layer deeper than on Earth? *Icarus* **277**, 215–236 (2016).

32. Poirier, J. P. Rheology of ices: A key to the tectonics of the ice moons of Jupiter and Saturn. *Nature* **299**, 683–688 (1982).

33. Ahrens, C., Meraviglia, H. & Bennett, C. A Geoscientific Review on CO and CO2 Ices in the Outer Solar System. *Geosciences* **12**, 51 (2022).

34. Redmer, R., Mattsson, T. R., Nettelmann, N. & French, M. The phase diagram of water and the magnetic fields of Uranus and Neptune. *Icarus* **211**, 798–803 (2011).

35. Helled, R. & Fortney, J. J. The interiors of Uranus and Neptune: Current understanding and open questions. *Philos. Trans. R. Soc. A Math. Phys. Eng. Sci.* **378**, (2020).

36. Helled, R., Nettelmann, N. & Guillot, T. Uranus and Neptune: Origin, Evolution and Internal Structure. *Space Sci. Rev.* **216**, 1–26 (2020).

37. Dziubek, K. F. *et al.* Crystalline polymeric carbon dioxide stable at megabar pressures. *Nat. Commun.* **9**, 3148 (2018).

38. McMillan, P. F. New materials from high-pressure experiments. *Nat. Mater.* **1**, 19–25 (2002).

39. Yoo, C. S. New states of matter and chemistry at extreme pressures: Low-Z extended solid. *MRS Bull.* **42**, 724–728 (2017).

40. Grochala, W., Hoffmann, R., Feng, J. & Ashcroft, N. W. The chemical imagination at work in very tight places. *Angew. Chemie - Int. Ed.* **46**, 3620–3642 (2007).

41. Winkler, B. & Milman, V. Density functional theory based calculations for high pressure research. *Zeitschrift fur Krist.* **229**, 112–122 (2014).

42. Zhang, L., Wang, Y., Lv, J. & Ma, Y. Materials discovery at high pressures. *Nat. Rev. Mater.* **2**, (2017).

43. Mc Millan, P. F. Chemistry at high pressure. *Chem. Soc. Rev.* **35**, 855–857 (2006).

44. Yoo, C. S. Chemistry under extreme conditions: Pressure evolution of chemical bonding and structure in dense solids. *Matter Radiat. Extrem.* **5**, (2020).

45. Miao, M., Sun, Y., Zurek, E. & Lin, H. Chemistry under high pressure. *Nat. Rev. Chem.* **4**, 508–527 (2020).

46. Aoki, K., Yamawaki, H., Sakashita, M. & Fujihisa, H. Infrared absorption study of the hydrogen-bond symmetrization in ice to 110 GPa. *Phys. Rev. B - Condens. Matter Mater. Phys.* **54**, 15673–15677 (1996).

47. Polian, A. & Grimsditch, M. New high-pressure phase of H2O: Ice X. *Phys. Rev. Lett.* **52**, 1312–1314 (1984).

48. Iota, V. Quartzlike Carbon Dioxide: An Optically Nonlinear Extended Solid at High Pressures and Temperatures. *Science* **283**, 1510–1513 (1999).

49. Serra, S. Pressure-Induced Solid Carbonates from Molecular CO2 by Computer Simulation. *Science* **284**, 788–790 (1999).

50. Tammann, G. Ueber die Grenzen des festen Zustandes IV. *Ann. Phys.* **307**, 1–31 (1900).

51. Bridgman, P. W. Water, in the Liquid and Five Solid Forms, under Pressure. *Proc. Am. Acad. Arts Sci.* **47**, 441–558 (1912).

52. Gagnon, R. E., Kiefte, H., Clouter, M. J. & Whalley, E. Acoustic velocities and densities of polycrystalline ice Ih, II, III, V, and VI by Brillouin spectroscopy. *J. Chem. Phys.* **92**, 1909–1914 (1990).

53. Shaw, G. H. Elastic properties and equation of state of high pressure ice. *J. Chem. Phys.* **84**, 5862–5868 (1986).

54. Journaux, B. *et al.* Elasticity and dislocations in ice X under pressure. *Phys. Earth Planet. Inter.* **236**, 10–15 (2014).

55. Tsuchiya, Jun, Tsuchiya, T. First principles investigation of the elasticity of ice VIII and ice X. in 3188 (2016).

56. Parq, J. H., Lee, S. K., Lee, S. M. & Yu, J. Ab Initio Study of Elastic Properties of High-Pressure Polymorphs of CO2 Phases II and V. *J. Phys. Chem. C* **120**, 23152–23164 (2016).

57. Datchi, F. *et al.* Structure and compressibility of the high-pressure molecular phase II of carbon dioxide. *Phys. Rev. B - Condens. Matter Mater. Phys.* **89**, 144101 (2014).

58. Lakes, R. Foam structures with a negative Poisson's ratio. *Science* **235**, 1038–1040 (1987).

59. Evans, K. E., Nkansah, M. A., Hutcherson, I. J. & Rogers, S. C. Molecular network design. *Nature* **353**, 124 (1991).

60. Yeganeh-Haeri, A., Weidner, D. J. & Parise, J. B. Elasticity of α-cristobalite: A silicon dioxide with a negative poisson's ratio. *Science* **257**, 650–652 (1992).

61. Alderson, A. *et al.* Molecular Modelling of the Deformation Mechanisms Acting in Auxetic Silica. *Comput. Methods Sci. Technoloin Sci. Technol.* **10**, 117–126 (2004).

62. Grima, J. N., Gatt, R., Alderson, A. & Evans, K. E. An alternative explanation for the negative Poisson's ratios in α-cristobalite. *Mater. Sci. Eng. A* **423**, 219–224 (2006).

63. Alderson, A., Alderson, K. L., Evans, K. E., Grima, J. N. & Williams, M. Modelling of

negative poisson's ratio nanomaterials: Deformation mechanisms, structure-property relationships and applications. *J. Metastable Nanocrystalline Mater.* **23**, 55–58 (2005).

64. Kimizuka, H., Kaburaki, H. & Kogure, Y. Mechanism for negative poisson ratios over the alpha-beta transition of cristobalite, SiO2: a molecular-dynamics study. *Phys. Rev. Lett.* **84**, 5548–5551 (2000).

65. Kimizuka, H., Ogata, S. & Shibutani, Y. High-Pressure Elasticity and Auxetic Property of α-Cristobalite. *Mater. Trans.* **46**, 1161–1166 (2005).

66. Grima, J. N., Jackson, R., Alderson, A. & Evans, K. E. Do zeolites have negative Poisson's ratios? *Adv. Mater.* **12**, 1912–1918 (2000).

67. Grima, J. N. *et al.* Natrolite: A zeolite with negative Poisson's ratios. *J. Appl. Phys.* **101**, (2007).

68. Gatt, R., Zammit, V., Caruana, C. & Grima, J. N. On the atomic level deformations in the auxetic zeolite natrolite. *Phys. Status Solidi* **245**, (2008).

69. Siddorn, M., Coudert, F.-X., Evans, K. E. & Marmier, A. A systematic typology for negative Poisson's ratio materials and the prediction of complete auxeticity in pure silica zeolite JST. *Phys. Chem. Chem. Phys.* **17**, 17927–17933 (2015).

70. O'Neill, P. *Environmental Chemistry*. (CRC Press, 1998).

71. Kwok, S. *Physics and chemistry of the interstellar medium*. (University Science Books, 2007).

72. Ball, P. Water- an enduring mystery. *Nature* **452**, 291–292 (2008).

73. Stiopkin, I. V. *et al.* Hydrogen bonding at the water surface revealed by isotopic dilution spectroscopy. *Nature* **474**, 192–195 (2011).

74. Marx, D., Tuckerman, M. E., Hutter, J. & Parrinello, M. The nature of the hydrated excess proton in water. *Nature* **397**, 601–604 (1999).

75. Kang, D., Dai, J., Hou, Y. & Yuan, J. Structure and vibrational spectra of small water clusters from first principles simulations. *J. Chem. Phys.* **133**, 014302 (2010).

76. Lu, Q., Ali, I. & Li, J. Prediction of properties from first principles with quantitative accuracy: Six representative ice phases. *New J. Chem.* **44**, 21012–21020 (2020).

77. Prakapenka, V. B., Holtgrewe, N., Lobanov, S. S. & Goncharov, A. F. Structure and properties of two superionic ice phases. *Nat. Phys.* **17**, 1233–1238 (2021).

78. Reinhardt, A. *et al.* Thermodynamics of high-pressure ice phases explored with atomistic simulations. *Nat. Commun.* **13**, 1–10 (2022).

79. Hobbs, P. V. *Ice Physics*. (Oxford University Press, 1974).

80. Mishima, O., Calvert, L. D. & Whalley, E. 'Melting ice' I at 77 K and 10 kbar: a new method of making amorphous solids. *Nature* **310**, 393–395 (1984).

81. Mishima, O., Calvert, L. D. & Whalley, E. An apparently first-order transition between two amorphous phases of ice induced by pressure. *Nature* **314**, 76–78 (1985).

82. Salim, M. A., Willow, S. Y. & Hirata, S. Ice Ih anomalies: Thermal contraction, anomalous volume isotope effect, and pressure-induced amorphization. *J. Chem. Phys.* **144**, (2016).

83. Salzmann, C. G., Radaelli, P. G., Slater, B. & Finney, J. L. The polymorphism of ice: Five unresolved questions. *Phys. Chem. Chem. Phys.* **13**, 18468–18480 (2011).

84. Fuentes-Landete, V. *et al.* Crystalline and amorphous ices. in *Proceedings of the International School of Physics "Enrico Fermi". Water: Fundamentals as the Basis for*

Understanding the Environment and Promoting Technology **187**, 173–208 (IOS Press, 2015).

85. Fortes, A. D. Structural manifestation of partial proton ordering and defect mobility in ice Ih. *Phys. Chem. Chem. Phys.* **21**, 8264–8274 (2019).

86. Röttger, K., Endriss, A., Ihringer, J., Doyle, S. & Kuhs, W. F. Lattice constants and thermal expansion of H2O and D2O ice Ih between 10 and 265 K. *Acta Crystallogr. Sect. B Struct. Sci.* **50**, 644–648 (1994).

87. Liu, Z. K., Wang, Y. & Shang, S. L. Thermal expansion anomaly regulated by entropy. *Sci. Rep.* **4**, 7043 (2014).

88. Buckingham, D. T. W., Neumeier, J. J., Masunaga, S. H. & Yu, Y. K. Thermal Expansion of Single-Crystal H2 O and D2 O Ice Ih. *Phys. Rev. Lett.* **121**, 185505 (2018).

89. Fortes, A. D. Accurate and precise lattice parameters of H2O and D2O ice Ih between 1.6 and 270 K from high-resolution time-of-flight neutron powder diffraction data. *Acta Crystallogr. Sect. B Struct. Sci. Cryst. Eng. Mater.* **74**, 196–216 (2018).

90. Yamane, R. *et al.* Experimental evidence for the existence of a second partially-ordered phase of ice VI. *Nat. Commun.* **12**, (2021).

91. Gasser, T. M., Thoeny, A. V., Fortes, A. D. & Loerting, T. Structural characterization of ice XIX as the second polymorph related to ice VI. *Nat. Commun.* **12**, (2021).

92. Monserrat, B., Brandenburg, J. G., Engel, E. A. & Cheng, B. Liquid water contains the building blocks of diverse ice phases. *Nat. Commun.* **11**, 5757 (2020).

93. Petrenko, Victor, F. & Whitworth, Robert, V. *Physics of Ice*. *Physics of ice* (OUP, 1999).

94. Bernal, J. D. & Fowler, R. H. A theory of water and ionic solution, with particular

reference to hydrogen and hydroxyl ions. *J. Chem. Phys.* **1**, 515–548 (1933).

95. Piaggi, P. M. & Car, R. Enhancing the formation of ionic defects to study the ice Ih/XI transition with molecular dynamics simulations. *Mol. Phys.* **119**, (2021).

96. Knight, C. *et al.* Hydrogen bond topology and the ice VII/VIII and Ih/XI proton ordering phase transitions. *Phys. Rev. E - Stat. Nonlinear, Soft Matter Phys.* **73**, 1–14 (2006).

97. Singer, S. J. *et al.* Hydrogen-Bond Topology and the Ice VII/VIII and Ice Ih/XI Proton-Ordering Phase Transitions. *Phys. Rev. Lett.* **94**, 135701 (2005).

98. Fan, X., Bing, D., Zhang, J., Shen, Z. & Kuo, J. L. Predicting the hydrogen bond ordered structures of ice Ih, II, III, VI and ice VII: DFT methods with localized based set. *Comput. Mater. Sci.* **49**, S170–S175 (2010).

99. Whalley, E., Heath, J. B. R. & Davidson, D. W. Ice IX: An antiferroelectric phase related to ice III. *J. Chem. Phys.* **48**, 2362–2370 (1968).

100. Knight, C. & Singer, S. J. A reexamination of the ice III/IX hydrogen bond ordering phase transition. *J. Chem. Phys.* **125**, 064506 (2006).

101. Ning, S. Y. *et al.* Computational Analysis of Hydrogen Bond Vibrations of Ice III in the Far-Infrared Band. *Crystals* **12**, 910 (2022).

102. Sharif, Z. *et al.* Effect of ammonium fluoride doping on the ice III to ice IX phase transition. *J. Chem. Phys.* **154**, 114502 (2021).

103. Salzmann, C. G., Rosu-Finsen, A., Sharif, Z., Radaelli, P. G. & Finney, J. L. Detailed crystallographic analysis of the ice V to ice XIII hydrogen-ordering phase transition. *J. Chem. Phys.* **154**, 134504 (2021).

104. Rosu-Finsen, A. & Salzmann, C. G. Benchmarking acid and base dopants with respect

to enabling the ice V to XIII and ice VI to XV hydrogen-ordering phase transitions. *J. Chem. Phys.* **148**, 244507 (2018).

105. Knight, C. & Singer, S. J. Hydrogen bond ordering in ice V and the transition to ice XIII. *J. Chem. Phys.* **129**, 164513 (2008).

106. Shephard, J. J. & Salzmann, C. G. The complex kinetics of the ice VI to ice XV hydrogen ordering phase transition. *Chem. Phys. Lett.* **637**, 63–66 (2015).

107. Whalley, E., Davidson, D. W. & Heath, J. B. R. Dielectric properties of ice VII. Ice VIII: A new phase of ice. *J. Chem. Phys.* **45**, 3976–3982 (1966).

108. Komatsu, K. *et al.* Anomalous hydrogen dynamics of the ice VII – VIII transition revealed by high-pressure neutron diffraction. *Proc. Natl. Acad. Sci.* **117**, 6356–6361 (2020).

109. Köster, K. W. *et al.* Dynamics enhanced by HCl doping triggers full Pauling entropy release at the ice XII-XIV transition. *Nat. Commun.* **6**, (2015).

110. Fuentes-Landete, V., Köster, K. W., Böhmer, R. & Loerting, T. Thermodynamic and kinetic isotope effects on the order-disorder transition of ice XIV to ice XII. *Phys. Chem. Chem. Phys.* **20**, 21607–21616 (2018).

111. Salzmann, C. G., Radaelli, P. G., Hallbrucker, A., Mayer, E. & Finney, J. L. The preparation and structures of hydrogen ordered phases of ice. *Science* **311**, 1758–1761 (2006).

112. Gasser, T. M., Thoeny, A. V., Greussing, V. & Loerting, T. Calorimetric investigation of hydrogen-atom sublattice transitions in the ice VI/XV/XIX Trio. *J. Phys. Chem. B* **125**, 11777–11783 (2021).

113. Jorgensen, J. D., Beyerlein, R. A., Watanabe, N. & Worlton, T. G. Structure of D2O ice VIII from in situ powder neutron diffraction. *J. Chem. Phys.* **81**, 3211–3214 (1984).

114. Londono, J. D., Kuhs, W. F. & Finney, J. L. Neutron diffraction studies of ices III and IX on under-pressure and recovered samples. *J. Chem. Phys.* **98**, 4878–4888 (1993).

115. La Placa, S. J., Hamilton, W. C., Kamb, B. & Prakash, A. On a nearly proton-ordered structure for ice IX. *J. Chem. Phys.* **58**, 567–580 (1973).

116. Chaplin, M. Water Phase Diagram. (2020). Available at: http://www1.lsbu.ac.uk/water/water_phase_diagram.html.

117. Pruzan, P. *et al.* Phase diagram of ice in the VII-VIII-X domain. Vibrational and structural data for strongly compressed ice VIII. *J. Raman Spectrosc.* **34**, 591–610 (2003).

118. Song, M., Yamawaki, H., Fujihisa, H., Sakashita, M., Aoki, K. Infrared investigation on ice VIII and the phase diagram of dense ices. *Phys. Rev. B - Condens. Matter Mater. Phys.* **68**, 1–10 (2003).

119. Benoit, M., Bernasconi, M., Focher, P. & Parrinello, M. New High-Pressure Phase of Ice. *Phys. Rev. Lett.* **76**, 2934–2936 (1996).

120. Caracas, R. Dynamical instabilities of ice X. *Phys. Rev. Lett.* **101**, 1–4 (2008).

121. Kuo, J. L. & Klein, M. L. Structure of Ice-VII and Ice-VIII: A quantum mechanical study. *J. Phys. Chem. B* **108**, 19634–19639 (2004).

122. Umemoto, K. & Wentzcovitch, R. M. First principles study of volume isotope effects in ices VIII and X. *Jpn. J. Appl. Phys.* **56**, (2017).

123. Pham, C. H., Reddy, S. K., Chen, K., Knight, C. & Paesani, F. Many-Body Interactions

in Ice. *J. Chem. Theory Comput.* **13**, 1778–1784 (2017).

124. Yao, S. K. *et al.* Computing analysis of lattice vibrations of ice VIII. *RSC Adv.* **7**, 31789–31794 (2017).

125. Caracas, R. & Hemley, R. J. Ferroelectricity in high-density H2O ice. *J. Chem. Phys.* **142**, 0–6 (2015).

126. Tse, J. S., Shpakov, V. P. & Belosludov, V. R. Vibrational spectrum, elastic moduli and mechanical stability in ice VIII. *J. Chem. Phys.* **111**, 11111 (1999).

127. Umemoto, K. & Wentzcovitch, R. M. Amorphization in quenched ice VIII: A first-principles study. *Phys. Rev. B - Condens. Matter Mater. Phys.* **69**, 1–4 (2004).

128. Dong, S., Kolesnikov, A. I. & Li, J.-C. Lattice Dynamical Calculations of Ice VIII. *J. Phys. Chem. B* **101**, 6087–6089 (1997).

129. Ojamae, L., Hermansson, K., Dovesi, R., Roetti, C. & Saunders, V. R. Mechanical and molecular properties of ice VIII from crystal-orbital ab initio calculations. *J. Chem. Phys.* **100**, 2128–2138 (1994).

130. Tsuchiya, J. & Tsuchiya, T. First principles calculation of the elasticity of ice VIII and X. *J. Chem. Phys.* **146**, 014501 (2017).

131. Ikeda, T. First Principles Isothermal-Isobaric Centroid Molecular Dynamics Simulation of High Pressure Ices. **934**, 3275 (2018).

132. Moberg, D. R., Sharp, P. J. & Paesani, F. Molecular-Level Interpretation of Vibrational Spectra of Ordered Ice Phases. *J. Phys. Chem. B* **122**, 10572–10581 (2018).

133. Nelmes, R. J. *et al.* Neutron diffraction study of the structure of deuterated ice VIII to 10 GPa. *Phys. Rev. Lett.* **71**, 1192–1195 (1993).

134. Klotz, S. *et al.* Bulk moduli and equations of state of ice VII and ice VIII. *Phys. Rev. B* **95**, (2017).

135. Pruzan, P., Chervin, J. C. & Canny, B. Stability domain of the ice VIII proton-ordered phase at very high pressure and low temperature. *J. Chem. Phys.* **99**, 9842–9846 (1993).

136. Pruzan, P. Pressure effects on the hydrogen bond in ice up to 80 GPa. *J. Mol. Struct.* **322**, 279–286 (1994).

137. Pruzan, P., Chervin, J. C. & Canny, B. Determination of the D2O ice VII-VIII transition line by Raman scattering up to 51 GPa. *J. Chem. Phys.* **97**, 718–721 (1992).

138. Yamane, R. *et al.* Search for a ferroelectrically ordered form of ice VII by neutron diffraction under high pressure and high electric field. *Phys. Rev. B* **99**, 174201 (2019).

139. Sugimura, E. *et al.* Compression of H2O ice to 126 GPa and implications for hydrogen-bond symmetrization: Synchrotron x-ray diffraction measurements and density-functional calculations. *Phys. Rev. B - Condens. Matter Mater. Phys.* **77**, 1–6 (2008).

140. Umemoto, K., Wentzcovitch, R. M., De Gironcoli, S. & Baroni, S. Order-disorder phase boundary between ice VII and VIII obtained by first principles. *Chem. Phys. Lett.* **499**, 236–240 (2010).

141. Méndez, A. S. J. *et al.* Bulk modulus of H2 O across the ice VII-ice X transition measured by time-resolved x-ray diffraction in dynamic diamond anvil cell experiments. *Phys. Rev. B* **103**, 064104 (2021).

142. Song, M., Yamawaki, H., Fujihisa, H., Sakashita, M. & Aoki, K. Infrared absorption study of Fermi resonance and hydrogen-bond symmetrization of ice up to 141 GPa. *Phys. Rev. B - Condens. Matter Mater. Phys.* **60**, 12644–12650 (1999).

143. Benoit, M., Marx, D. & Parrinello, M. Tunnelling and zero-point motion in high-pressure ice. *Nat.* **392**, 258–261 (1998).

144. Marques, M., Ackland, G. J. & Loveday, J. S. Nature and stability of ice X. *High Press. Res.* **29**, 208–211 (2009).

145. Meier, T., Petitgirard, S., Khandarkhaeva, S. & Dubrovinsky, L. Observation of nuclear quantum effects and hydrogen bond symmetrisation in high pressure ice. *Nat. Commun.* **9**, (2018).

146. Zha, C. S., Tse, J. S. & Bassett, W. A. New Raman measurements for H_2O ice VII in the range of 300 cm^{-1} to 4000 cm^{-1} at pressures up to 120 GPa. *J. Chem. Phys.* **145**, 124315 (2016).

147. Holzapfel, W. B. On the Symmetry of the Hydrogen Bonds in Ice VII. *J. Chem. Phys.* **56**, 712–715 (1972).

148. Hirsch, K. R. & Holzapfel, W. B. Symmetric hydrogen bonds in ice X. *Phys. Lett. A* **101**, 142–144 (1984).

149. Hirsch, K. R. & Holzapfel, W. B. Effect of high pressure on the Raman spectra of ice VIII and evidence for ice X. *J. Chem. Phys.* **84**, 2771–2775 (1986).

150. Telxelira, J. High-pressure physics: The double identity of ice X. *Nature* **392**, 232–233 (1998).

151. Polian, A. New High-Pressure Phase of H 2 0 : Ice X. **52**, 1312–1314 (1984).

152. Pruzan, P. *et al.* Raman scattering and X-ray diffraction of ice in the megabar range. Occurrence of a symmetric disordered solid above 62 GPa. *J. Phys. Chem. B* **101**, 6230–6233 (1997).

153. Katoh, E. *et al.* Infrared spectroscopic study of mixed ice up to 100 GPa. *Phys. Rev. B - Condens. Matter Mater. Phys.* **62**, 2976–2979 (2000).

154. Flores-Livas, J. A. *et al.* Emergence of superconductivity in doped H2O ice at high pressure. *Sci. Rep.* **7**, 1–10 (2017).

155. Demontis, P., LeSar, R. & Klein, M. L. New High-Pressure Phases of Ice. *Phys. Rev. Lett.* **60**, 2284–2287 (1988).

156. Hemley, R. J., Jephcoat, A. P., Mao, H. K., Zha, C. S., Finger, L. W., Cox, D. E. Static compression of H2O-ice to 128 GPa (1.28 Mbar). *Nature* **330**, 737–740 (1987).

157. Demontis, P., Klein, M. L. & Lesar, R. High-density structures and phase transition in an ionic model of H2O ice. *Phys. Rev. B* **40**, 2716–2718 (1989).

158. Marqués, M., Ackland, G. J. & Loveday, J. S. Nature and stability of ice X. *High Press. Res.* **29**, 208–211 (2009).

159. Militzer, B. & Wilson, H. F. New phases of water ice predicted at megabar pressures. *Phys. Rev. Lett.* **105**, 195701 (2010).

160. Seto, Y., Nishio-Hamane, D., Nagai, T., Sata, N. & Fujino, K. Synchrotron X-ray diffraction study for crystal structure of solid carbon dioxide CO2-V. *J. Phys. Conf. Ser.* **215**, (2010).

161. Aoki, K., Yamawaki, H., Sakashita, M., Gotoh, Y. & Takemura, K. Crystal structure of the high-pressure phase of solid CO2. *Science* **263**, 356–358 (1994).

162. Santoro, M. *et al.* Partially collapsed cristobalite structure in the non molecular phase V in CO2. *Proc. Natl. Acad. Sci. U. S. A.* **109**, 5176–5179 (2012).

163. Sengupta, A. & Yoo, C. S. Raman studies of molecular-to-nonmolecular transitions in

carbon dioxide at high pressures and temperatures. *Phys. Rev. B - Condens. Matter Mater. Phys.* **80**, 1–6 (2009).

164. Liu, L. Dry ice II, a new polymorph of CO2. *Nature* **303**, 508–509 (1983).

165. Zhang, J. S., Shieh, S. R., Bass, J. D., Dera, P. & Prakapenka, V. High-pressure single-crystal elasticity study of CO2 across phase I-III transition. *Appl. Phys. Lett.* **104**, (2014).

166. Yoo, C. S. *et al.* Crystal Structure of Carbon Dioxide at High Pressure: "Superhard" Polymeric Carbon Dioxide. *Phys. Rev. Lett.* **83**, 5527–5530 (1999).

167. Gohr, S., Grimme, S., Söhnel, T., Paulus, B. & Schwerdtfeger, P. Pressure dependent stability and structure of carbon dioxide - A density functional study including long-range corrections. *J. Chem. Phys.* **139**, (2013).

168. Holm, B., Ahuja, R., Belonoshko, A. & Johansson, B. Theoretical investigation of high pressure phases of carbon dioxide. *Phys. Rev. Lett.* **85**, 1258–1261 (2000).

169. Gracia, L., Marqués, M., Beltrán, A., Pendás, A. M. & Recio, J. M. Bonding and compressibility in molecular and polymeric phases of solid CO2. *J. Phys. Condens. Matter* **16**, S1263–S1270 (2004).

170. Park, J. H. *et al.* Crystal structure of bent carbon dioxide phase IV. *Phys. Rev. B - Condens. Matter Mater. Phys.* **68**, 014107 (2003).

171. Bonev, S. A., Gygi, F., Ogitsu, T. & Galli, G. High-Pressure Molecular Phases of Solid Carbon Dioxide. *Phys. Rev. Lett.* **91**, 065501 (2003).

172. Santoro, M. *et al.* Amorphous silica-like carbon dioxide. *Nature* **441**, 857–860 (2006).

173. Yong, X. *et al.* Crystal structures and dynamical properties of dense CO2. *Proc. Natl. Acad. Sci. U. S. A.* **113**, 11110–11115 (2016).

174. Oganov, A. R., Ono, S., Ma, Y., Glass, C. W. & Garcia, A. Novel high-pressure structures of MgCO3, CaCO3 and CO2 and their role in Earth's lower mantle. *Earth Planet. Sci. Lett.* **273**, 38–47 (2008).

175. Santoro, M. & Gorelli, F. A. Constraints on the phase diagram of nonmolecular CO2 imposed by infrared spectroscopy. *Phys. Rev. B - Condens. Matter Mater. Phys.* **80**, 1–5 (2009).

176. Cogollo-Olivo, B. H., Biswas, S., Scandolo, S. & Montoya, J. A. Ab initio Determination of the Phase Diagram of CO2 at High Pressures and Temperatures. *Phys. Rev. Lett.* **124**, 1–5 (2020).

177. Wu, M., Tse, J. S. & Pan, Y. Stability and properties of liquid CO 2 at high pressure and high temperature: Implications for electrical conductivities in Earth's lower mantle. *Geophys. Res. Lett.* **42**, 5820–5827 (2015).

178. Iota, V. & Yoo, C. S. Phase diagram of carbon dioxide: Evidence for a new associated phase. *Phys. Rev. Lett.* **86**, 5922–5925 (2001).

179. Yoo, C. S. *et al.* Crystal structure of pseudo-six-fold carbon dioxide phase II at high pressures and temperatures. *Phys. Rev. B - Condens. Matter Mater. Phys.* **65**, (2002).

180. Datchi, F. *et al.* Structure of liquid carbon dioxide at pressures up to 10 GPa. *Phys. Rev. B* **94**, 1–9 (2016).

181. Tschauner, O., Mao, H. K. & Hemley, R. J. New transformations of CO2 at high pressures and temperatures. *Phys. Rev. Lett.* **87**, 75701 (2001).

182. Scelta, D. *et al.* Extending the Stability Field of Polymeric Carbon Dioxide Phase v beyond the Earth's Geotherm. *Phys. Rev. Lett.* **126**, 65701 (2021).

183. Yoo, C.-S., Sengupta, A. & Kim, M. Carbon Dioxide Carbonates in the Earth's Mantle: Implications to the Deep Carbon Cycle. *Angew. Chemie* **123**, 11415–11418 (2011).

184. Datchi, F. & Weck, G. X-ray crystallography of simple molecular solids up to megabar pressures: Application to solid oxygen and carbon dioxide. *Zeitschrift fur Krist.* **229**, 135–157 (2014).

185. Datchi, F., Mallick, B., Salamat, A. & Ninet, S. Structure of polymeric carbon dioxide CO 2-V. *Phys. Rev. Lett.* **108**, 1–5 (2012).

186. Abd El-Sayed, F. K., Jones, R. & Burgess, I. W. A theoretical approach to the deformation of honeycomb based composite materials. *Composites* **10**, 209–214 (1979).

187. Gibson, L. J., Ashby, M. F., Schajer, G. S. & Robertson, C. I. The Mechanics of Two-Dimensional Cellular Materials. *Proc. R. Soc. A Math. Phys. Eng. Sci.* **382**, 25–42 (1982).

188. Evans, K. E., Alderson, A. & Christian, F. R. Auxetic two-dimensional polymer networks. An example of tailoring geometry for specific mechanical properties. *J. Chem. Soc. Faraday Trans.* **91**, 2671 (1995).

189. Masters, I. G. & Evans, K. E. Models for the elastic deformation of honeycombs. *Compos. Struct.* **35**, 403–422 (1996).

190. Yang, D. U., Lee, S. & Huang, F. Y. Geometric effects on micropolar elastic honeycomb structure with negative Poisson's ratio using the finite element method. *Finite Elem. Anal. Des.* **39**, 187–205 (2003).

191. Bezazi, A., Scarpa, F. & Remillat, C. A novel centresymmetric honeycomb composite structure. *Compos. Struct.* **71**, 356–364 (2005).

192. Sparavigna, A. Phonons in conventional and auxetic honeycomb lattices. *Phys. Rev. B - Condens. Matter Mater. Phys.* **76**, 134302 (2007).

193. Bezazi, A., Remillat, C., Innocenti, P. & Scarpa, F. In-plane mechanical and thermal conductivity properties of a rectangular-hexagonal honeycomb structure. *Compos. Struct.* **84**, 248–255 (2008).

194. Boldrin, L. *et al.* Dynamic behaviour of auxetic gradient composite hexagonal honeycombs. *Compos. Struct.* **149**, 114–124 (2016).

195. Lim, T.-C. A class of shape-shifting composite metamaterial honeycomb structures with thermally-adaptive Poisson's ratio signs. *Compos. Struct.* **226**, 111256 (2019).

196. Lim, T. C. *Auxetic Materials and Structures*. (Springer, 2015). doi:10.1007/978-981-287-275-3

197. Gibson, L. J. & Ashby, M. F. *Cellular Solids: Structure and Properties*. (Cambridge University Press, 1997).

198. Overaker, D. W., Cuitiño, A. M. & Langrana, N. A. Effects of morphology and orientation on the behavior of two-dimensional hexagonal foams and application in a re-entrant foam anchor model. *Mech. Mater.* **29**, 43–52 (1998).

199. Scarpa, F., Panayiotou, P. & Tomlinson, G. Numerical and experimental uniaxial loading on in-plane auxetic honeycombs. *J. Strain Anal. Eng. Des.* **35**, 383–388 (2000).

200. Whitty, J. P. M., Nazare, F. & Alderson, A. Modelling the effects of density variations on the in-plane Poisson's ratios and Young's moduli of periodic conventional and re-entrant honeycombs - Part 1: Rib thickness variations. *Cell. Polym.* **21**, 69–98 (2002).

201. Grima, J. N., Attard, D., Ellul, B. & Gatt, R. An improved analytical model for the elastic

constants of auxetic and conventional hexagonal honeycombs. *Cell. Polym.* **30**, (2011).

202. Henderson, B., Whitty, J. P. M., Myler, P. & Chirwa, C. Crash performance of cellular foams with reduced relative density part 1: Rib thickness variation. *Int. J. Crashworthiness* **12**, 677–688 (2007).

203. Henderson, B., Whitty, J. P. M., Myler, P. & Chirwa, C. Crash performance of cellular foams with reduced relative density part 2: Rib deletion. *Int. J. Crashworthiness* **12**, 689–698 (2007).

204. Miller, W., Smith, C. W. & Evans, K. E. Honeycomb cores with enhanced buckling strength. *Compos. Struct.* **93**, 1072–1077 (2011).

205. Whitty, J. P. M., Alderson, A., Myler, P. & Kandola, B. Towards the design of sandwich panel composites with enhanced mechanical and thermal properties by variation of the in-plane Poisson's ratios. *Compos. Part A Appl. Sci. Manuf.* **34**, 525–534 (2003).

206. Gatt, R. New Structures and Materials Exhibiting Negative Poisson's Ratios and Negative Compressibility. (University of Malta, 2010).

207. Scarpa, F. & Tomlin, P. J. On the transverse shear modulus of negative Poisson's ratio honeycomb structures. *FATIGUE Fract. Eng. Mater. Struct.* **23**, 717–720 (2000).

208. Silva, T. A. A. *et al.* Preliminary investigations on auxetic structures based on recycled rubber. *Phys. Status Solidi Basic Res.* **249**, 1353–1358 (2012).

209. Lira, C., Innocenti, P. & Scarpa, F. Transverse elastic shear of auxetic multi re-entrant honeycombs. *Compos. Struct.* **90**, 314–322 (2009).

210. Sun, Y. & Pugno, N. M. In plane stiffness of multifunctional hierarchical honeycombs with negative Poisson's ratio sub-structures. *Compos. Struct.* **106**, 681–689 (2013).

211. Lim, T. C. Metamaterial honeycomb with sign-toggling expansion coefficients that manifests an Islamic mosaic pattern at the Alhambra Palace. *Adv. Compos. Hybrid Mater.* **4**, 966–978 (2021).

212. Attenborough F.R. The modelling of auxetic polymers. *Ph.D Thesis* (University of Liverpool, United Kingdom, 1997).

213. Sigmund, O. Tailoring materials with prescribed elastic properties. *Mech. Mater.* **20**, 351–368 (1995).

214. Grima, J. N., Alderson, A. & Evans, K. E. Zeolites with negative Poisson's ratios. in *4th Materials Chemistry Conference* P81 (1999).

215. Grima, J. N. & Evans, K. E. Auxetic behavior from rotating squares. *J. Mater. Sci. Lett.* **19**, 1563–1565 (2000).

216. Ishibashi, Y. & Iwata, M. A microscopic model of a negative Poisson's ratio in some crystals. *J. Phys. Soc. Japan* **69**, 2702–2703 (2000).

217. Grima, J. N., Alderson, A. & Evans, K. E. Negative Poisson's Ratios From Rotating Rectangles. *Comput. Methods Sci. Technol.* **10**, 137–145 (2004).

218. Grima, J. N., Alderson, A. & Evans, K. E. Auxetic behaviour from rotating rigid units. *Phys. Status Solidi Basic Res.* **242**, (2005).

219. Grima, J. N., Farrugia, P. S., Gatt, R. & Attard, D. On the auxetic properties of rotating rhombi and parallelograms: A preliminary investigation. *Phys. Status Solidi* **245**, (2008).

220. Attard, D., Manicaro, E. & Grima, J. N. On rotating rigid parallelograms and their potential for exhibiting auxetic behaviour. *Phys. Status Solidi* **246**, (2009).

221. Grima, J. N. & Evans, K. E. Auxetic behavior from rotating triangles. *J. Mater. Sci.* **41**,

3193–3196 (2006).

222. Grima, J. N., Farrugia, P. S., Gatt, R. & Zammit, V. Connected triangles exhibiting negative Poisson's ratios and negative thermal expansion. *J. Phys. Soc. Japan* **76**, (2007).

223. Grima, J. N. *et al.* On the auxetic properties of generic rotating rigid triangles. *Proc. R. Soc. A Math. Phys. Eng. Sci.* **468**, 810–830 (2012).

224. Chetcuti, E. *et al.* Modeling auxetic foams through semi-rigid rotating triangles. *Phys. Status Solidi* **251**, (2014).

225. Attard, D. & Grima, J. N. Auxetic behaviour from rotating rhombi. *Phys. Status Solidi* **245**, (2008).

226. Grima, J. N., Gatt, R., Alderson, A. & Evans, K. E. On the auxetic properties of 'rotating rectangles' with different connectivity. *J. Phys. Soc. Japan* **74**, (2005).

227. Attard, D., Manicaro, E., Gatt, R. & Grima, J. N. On the properties of auxetic rotating stretching squares. *Phys. Status Solidi* **246**, (2009).

228. Grima, J. N., Farrugia, P. S., Caruana, C., Gatt, R. & Attard, D. Auxetic behaviour from stretching connected squares. *J. Mater. Sci.* **43**, (2008).

229. Dmitriev, S. V. Auxetic behavior of crystals from rotational degrees of freedom. *Ferroelectrics* **349**, 33–44 (2007).

230. Grima, J. N., Zammit, V., Gatt, R., Alderson, A. & Evans, K. E. Auxetic behaviour from rotating semi-rigid units. *Phys. status solidi* **244**, 866–882 (2007).

231. Grima, J. N., Alderson, A. & Evans, K. E. An Alternative Explanation for the Negative Poisson's Ratios in Auxetic Foams. *J. Phys. Soc. Japan* **74**, 1341–1342 (2005).

232. Alderson, A. & Evans, K. E. Rotation and dilation deformation mechanisms for auxetic behaviour in the α-cristobalite tetrahedral framework structure. *Phys. Chem. Miner.* **28**, 711–718 (2001).

233. Alderson, A. & Evans, K. E. Molecular origin of auxetic behavior in tetrahedral framework silicates. *Phys. Rev. Lett.* **89**, 225503 (2002).

234. Alderson, A. *et al.* Modelling the deformation mechanisms, structure-property relationships and applications of auxetic nanomaterials. *Phys. Status Solidi* **242**, 499–508 (2005).

235. Rothenburg, L., Berlin, A. I. & Bathurst, R. J. Microstructure of isotropic materials with negative Poisson's ratio. *Nature* **354**, 470–472 (1991).

236. Wojciechowski K.W., Branka, A. C. Auxetics: Materials and Models with Negative Poisson's Ratios. *Molec. Phys. Reports* **6**, 71–85 (1994).

237. Grima, J. N. New Auxetic Materials. *Ph.D thesis* (University of Exeter, United Kingdom, 2000).

238. Wojciechowski, K. W. Two-dimensional isotropic system with a negative poisson ratio. *Phys. Lett. A* **137**, 60–64 (1989).

239. Lakes, R. S. Deformation mechanisms in negative Poisson's ratio materials: structural aspects. *J. Mater. Sci.* **26**, 2287–2292 (1991).

240. Prall, D. & Lakes, R. S. Properties of a chiral honeycomb with a poisson's ratio of -1. *Int. J. Mech. Sci.* **39**, 305–314 (1997).

241. Wu, W. *et al.* Mechanical design and multifunctional applications of chiral mechanical metamaterials: A review. *Mater. Des.* **180**, 107950 (2019).

242. Liu, J. *et al.* A flexible porous chiral auxetic tracheal stent with ciliated epithelium. *Acta Biomater.* **124**, 153–165 (2021).

243. Sigmund, O., Torquato, S. & Aksay, I. A. On the design of 1–3 piezocomposites using topology optimization. *J. Mater. Res.* **13**, 1038–1048 (1998).

244. Sigmund, O. & Torquato, S. Design of smart composite materials using topology optimization. *Smart Mater. Struct.* **8**, 365–379 (1999).

245. Sanchez-Valle, C. *et al.* Brillouin scattering study on the single-crystal elastic properties of natrolite and analcime zeolites. *J. Appl. Phys.* **98**, 053508 (2005).

246. Grima, J. N., Cassar, R. N. & Gatt, R. On the effect of hydrostatic pressure on the auxetic character of NAT-type silicates. *J. Non. Cryst. Solids* **355**, (2009).

247. Keskar, N. R. & Chelikowsky, J. R. Negative Poisson ratios in crystalline SiO2 from first-principles calculations. *Nature* **358**, 222–224 (1992).

248. Keskar, N. R. & Chelikowsky, J. R. Anomalous Elastic Behaviour in crystalline silica. *Condens. Matter* **304**, 297–304 (1993).

249. Grima, J. N., Gatt, R., Alderson, A. & Evans, K. E. Modeling the auxetic behaviour in alpha-cristobalite. in *The 228th ACS National Meeting* (2004).

250. Gatt, R., Mizzi, L., Azzopardi, K. M. & Grima, J. N. A force-field based analysis of the deformation mechanism in α-cristobalite. *Phys. Status Solidi* **252**, (2015).

251. Alderson, A. & Evans, K. E. Deformation mechanisms leading to auxetic behaviour in the alpha-cristobalite and alpha-quartz structures of both silica and germania. *J. Phys. Condens. Matter* **21**, 25401 (2009).

252. Azzopardi, K. M., Brincat, J. P., Grima, J. N. & Gatt, R. Anomalous elastic properties

in stishovite. *RSC Adv.* **5**, 8974–8980 (2015).

253. Azzopardi, K. M., Brincat, J.-P., Grima, J. N. & Gatt, R. Advances in the study of the deformation mechanism of stishovite. *Phys. Status Solidi* **252**, (2015).

254. Du, Y. *et al.* Auxetic Black Phosphorus: A 2D Material with Negative Poisson's Ratio. *Nano Lett.* **16**, 6701–6708 (2016).

255. Jiang, J.-W. & Park, H. S. Negative Poisson's Ratio in Single-Layer Black Phosphorus. *Nat. Commun.* **5**, 1–7 (2014).

256. Grima-Cornish, J. N., Vella-Żarb, L., Grima, J. N. & Evans, K. E. Boron Arsenate and its Pressure-Dependent Auxetic Properties. *Appl. Phys. Lett. Mater.* **(in press)**, (2022).

257. Grima-Cornish, J. N., Vella-Żarb, L., Grima, J. N. & Evans, K. E. A DFT-Based Quantitative and Geometric Analysis of the Effect of Pressure on Boron Arsenate. *Materials (Basel).* **15**, 4858 (2022).

258. Lim, T. C. An anisotropic auxetic 2D metamaterial based on sliding microstructural mechanism. *Materials (Basel).* **12**, 429 (2019).

259. Lim, T. C. A perfect 2D auxetic sliding mechanism based on an Islamic geometric pattern. *Eng. Res. Express* **3**, 015025 (2021).

260. Grima, J. N. *et al.* Tailoring graphene to achieve negative Poisson's ratio properties. *Adv. Mater.* **27**, 1455–1459 (2015).

261. Winczewski, S. & Rybicki, J. Negative Poisson's ratio from pentagons: A new auxetic structure combining three different auxetic mechanisms. *Comput. Mater. Sci.* **201**, 110914 (2022).

262. Winczewski, S. & Rybicki, J. Anisotropic mechanical behavior and auxeticity of penta-

graphene: Molecular statics/molecular dynamics studies. *Carbon N. Y.* **146**, 572–587 (2019).

263. Winczewski, S., Shaheen, M. Y. & Rybicki, J. Interatomic potential suitable for the modeling of penta-graphene: Molecular statics/molecular dynamics studies. *Carbon N. Y.* **126**, 165–175 (2018).

264. Lim, T. C. A 2D auxetikos system based on interconnected shurikens. *SN Appl. Sci.* **1**, 1383 (2019).

265. Lim, T. C. An auxetic system based on interconnected Y-elements inspired by islamic geometric patterns. *Symmetry (Basel).* **13**, 865 (2021).

266. Lim, T. C. Adjustable positive and negative hygrothermal expansion metamaterial inspired by the Maltese cross. *R. Soc. Open Sci.* **8**, 210593 (2021).

267. Lim, T. C. *Mechanics of Metamaterials with Negative Parameters*. (Springer, 2020).

268. Ma, F. *et al.* Half-Auxeticity and Anisotropic Transport in Pd Decorated Two-Dimensional Boron Sheets. *Nano Lett.* **21**, 2356–2362 (2021).

269. Liu, Z., Pan, J., Zhang, Y. F. & Du, S. Half-auxetic effect and ferroelasticity in a two-dimensional monolayer TiSe. *J. Phys. Condens. Matter* **33**, (2021).

270. Nkansah, M. A., Evans, K. E. & Hutchinson, I. J. Modelling the mechanical properties of an auxetic molecular network. *Model. Simul. Mater. Sci. Eng.* **2**, 337–352 (1994).

271. Grima, J. N. *et al.* On the mechanical properties and auxetic potential of various organic networked polymers. *Mol. Simul.* **34**, 1149–1158 (2008).

272. Gibson, L. J. & Ashby, M. F. *Cellular Solids: Structure & Properties*. *Advances in Polymer Technology* (Pergamon Press, 1988). doi:10.1002/adv.1989.060090207

273. Alderson, A. *et al.* Modelling of the mechanical and mass transport properties of auxetic molecular sieves: an idealised organic (polymeric honeycomb) host–guest system. *Mol. Simul.* **31**, 897–905 (2005).

274. Lim, T. C. & Acharya, R. U. Performance evaluation of auxetic molecular sieves with re-entrant structures. *J. Biomed. Nanotechnol.* **6**, 718–724 (2010).

275. Attard, D. & Grima, J. N. Modelling of hexagonal honeycombs exhibiting zero Poisson's ratio. *Phys. Status Solidi* **248**, (2011).

276. Grima, J. N. & Evans, K. E. Self expanding molecular networks. *Chem. Commun.* **15**, 1531–1532 (2000).

277. Grima, J. N., Williams, J. J. & Evans, K. E. Networked calix[4]arene polymers with unusual mechanical properties. *Chem. Commun.* 4065 (2005). doi:10.1039/b505839b

278. Grima, J. N. *et al.* Modelling and testing of a foldable macrostructure exhibiting auxetic behaviour. *Phys. Status Solidi* **248**, 177–122 (2011).

279. Baughman, R. H. & Galvão, D. S. Crystalline networks with unusual predicted mechanical and thermal properties. *Nature* **365**, 735–737 (1993).

280. Gardner, G. B., Venkataramant, D., Mooreh, J. S. & Lee, S. Hinged Coordination Network. *Nature* **374**, 792–795 (1995).

281. He, C., Liu, P., McMullan, P. J. & Griffin, A. C. Toward molecular auxetics: Main chain liquid crystalline polymers consisting of laterally attached para-quaterphenyls. *Phys. status solidi* **242**, 576–584 (2005).

282. Kang, D. *et al.* Pretransitional behavior above the nematic-isotropic phase transition of an auxetic trimer liquid crystal. *Phys. Rev. E - Stat. Physics, Plasmas, Fluids, Relat.*

Interdiscip. Top. **60**, 4980–4982 (1999).

283. Liu, P., He, C., Booth, C. J. & Griffin, A. C. Synthesis and Characterization of Liquid Crystal Trimers Based on Laterally Attached Terphenyls. *Mol. Cryst. Liq. Cryst. Sci. Technol. Sect. A Mol. Cryst. Liq. Cryst.* **332**, 243–250 (1999).

284. He, C., Liu, P., Griffin, A. C., Smith, C. W. & Evans, K. E. Morphology and deformation behaviour of a liquid crystalline polymer containing laterally attached pentaphenyl rods. *Macromol. Chem. Phys.* **206**, 233–239 (2005).

285. He, C., Liu, P. & Griffin, A. C. Toward Negative Poisson Ratio Polymers through Molecular Design. *Macromolecules* **31**, 3145–3147 (1998).

286. Mistry, D. *et al.* Coincident molecular auxeticity and negative order parameter in a liquid crystal elastomer. *Nat. Commun.* **9**, 5095 (2018).

287. Raistrick, T., Zhang, Z., Mistry, D., Mattsson, J. & Gleeson, H. F. Understanding the physics of the auxetic response in a liquid crystal elastomer. *Phys. Rev. Res.* **3**, 023191 (2021).

288. Gunton, D. J. & Saunders, G. A. The Young's modulus and Poisson's ratio of arsenic, antimony and bismuth. *J. Mater. Sci.* **7**, 1061–1068 (1972).

289. Li, Y. The anisotropic behavior of Poisson's ratio, Young's modulus, and shear modulus in hexagonal materials. *Phys. Status Solidi* **38**, 171–175 (1976).

290. Krasavin, V. V. & Krasavin, A. V. Auxetic properties of cubic metal single crystals. *Phys. Status Solidi* (2014). doi:10.1002/pssb.201451129

291. Goldstein, R. V., Gorodtsov, V. A., Lisovenko, D. S. & Volkov, M. A. Negative Poisson's ratio for cubic crystals and nano/microtubes. *Phys. Mesomech.* **17**, 97–115

(2014).

292. Milstein, F. & Huang, K. Existence of a negative Poisson ratio in fcc crystals. *Phys. Rev. B* **19**, 2030–2033 (1979).

293. Ting, T. C. T. & Barnett, D. M. Negative poisson's ratios in anisotropic linear elastic media. *J. Appl. Mech. Trans. ASME* **72**, 929–931 (2005).

294. Tokmakova, S. P. Stereographic projections of Poisson's ratio in auxetic crystals. *Phys. status solidi* **242**, 721–729 (2005).

295. Lethbridge, Z. A. D., Walton, R. I., Marmier, A. S. H., Smith, C. W. & Evans, K. E. Elastic anisotropy and extreme Poisson's ratios in single crystals. *Acta Mater.* **58**, 6444–6451 (2010).

296. Epishin, A. I. & Lisovenko, D. S. Extreme values of the Poisson's ratio of cubic crystals. *Tech. Phys.* **61**, 1516–1524 (2016).

297. Ho, D. T., Park, S.-D., Kwon, S.-Y., Park, K. & Kim, S. Y. Negative Poisson's ratios in metal nanoplates. *Nat. Commun.* **5**, 1–8 (2014).

298. Goldstein, R. V., Gorodtsov, V. A. & Lisovenko, D. S. Classification of cubic auxetics. *Phys. Status Solidi Basic Res.* **250**, 2038–2043 (2013).

299. Gorodtsov, V. A. & Lisovenko, D. S. Auxetics among Materials with Cubic Anisotropy. *Mech. Solids* **55**, 461–474 (2020).

300. Goldstein, R. V., Gorodtsov, V. A. & Lisovenko, D. S. Auxetic mechanics of crystalline materials. *Mech. Solids* **45**, 529–545 (2010).

301. Ji, S. *et al.* Poisson's Ratio and Auxetic Properties of Natural Rocks. *J. Geophys. Res. Solid Earth* **123**, 1161–1185 (2018).

302. Hughes, T. P., Marmier, A. & Evans, K. E. Auxetic frameworks inspired by cubic crystals. *Int. J. Solids Struct.* **47**, 1469–1476 (2010).

303. Branka, A. C., Heyes, D. M. & Wojciechowski, K. W. Auxeticity of cubic materials under pressure. *Phys. Status Solidi* **248**, 96–104 (2011).

304. Baughman, R. H., Shacklette, J. M., Zakhidov, A. A. & Stafström, S. Negative Poisson's ratios as a common feature of cubic metals. *Nature* **392**, 362–365 (1998).

305. Brańka, A. C., Heyes, D. M. & Wojciechowski, K. W. Auxeticity of cubic materials. *Phys. status solidi* **246**, 2063–2071 (2009).

306. Norris, A. N. Poisson's ratio in cubic materials. *Proc. R. Soc. A Math. Phys. Eng. Sci.* **462**, 3385–3405 (2006).

307. Paszkiewicz, T. & Wolski, S. Anisotropic properties of mechanical characteristics and auxeticity of cubic crystalline media. *Phys. Status Solidi* **244**, 966–977 (2007).

308. O'Donnell, W. J. Effective Elastic Constants for the Bending of Thin Perforated Plates With Triangular and Square Penetration Patterns. *J. Eng. Ind.* **95**, 121–128 (1973).

309. Peliński, K. & Smardzewski, J. Static response of synclastic sandwich panel with auxetic wood-based honeycomb cores subject to compression. *Thin-Walled Struct.* **179**, 109559 (2022).

310. Chow, L. *et al.* 3D Printing Auxetic Architectures for Hypertrophic Scar Therapy. *Macromol. Mater. Eng.* **307**, 2100866 (2022).

311. Meeusen, L. *et al.* Auxetic structures used in kinesiology tapes can improve form-fitting and personalization. *Sci. Rep.* **12**, 13509 (2022).

312. Jiang, W. *et al.* Manufacturing, characteristics and applications of auxetic foams: A

state-of-the-art review. *Compos. Part B Eng.* **235**, 109733 (2022).

313. Janus-Michalska, M., Jasińska, D. & Smardzewski, J. Comparison of Contact Stress Distribution for Foam Seat and Seat of Auxetic Spring Skeleton. *Int. J. Appl. Mech. Eng.* **18**, 55–72 (2013).

314. Wang, Y. C. & Lakes, R. Analytical parametric analysis of the contact problem of human buttocks and negative Poisson's ratio foam cushions. *Int. J. Solids Struct.* **39**, 4825–4838 (2002).

315. Chan, N. & Evans, K. E. The Mechanical Properties of Conventional and Auxetic Foams. Part I: Compression and Tension. *J. Cell. Plast.* **35**, 130–165 (1999).

316. Chan, N. & Evans, K. E. Mechanical properties of conventional and auxetic foams. Part II: Shear. *J. Cell. Plast.* **35**, 166–183 (1999).

317. Airoldi, A., Novak, N., Sgobba, F., Gilardelli, A. & Borovinšek, M. Foam-filled energy absorbers with auxetic behaviour for localized impacts. *Mater. Sci. Eng. A* **788**, 139500 (2020).

318. Zhang, Q. *et al.* Impact properties of uniaxially thermoformed auxetic foams. *Int. J. Impact Eng.* **163**, 104176 (2022).

319. Scarpa, F., Yates, J. R., Ciffo, L. G. & Patsias, S. Dynamic crushing of auxetic open-cell polyurethane foam. *Proc. Inst. Mech. Eng. Part C J. Mech. Eng. Sci.* **216**, 1153–1156 (2002).

320. Webber, R. S., Alderson, K. L. & Evans, K. E. A novel fabrication route for auxetic polyethylene, part 2: Mechanical properties. *Polym. Eng. Sci.* **48**, 1351–1358 (2008).

321. Alderson, K. L., Fitzgerald, A. & Evans, K. E. The strain dependent indentation

resilience of auxetic microporous polyethylene. *J. Mater. Sci.* **35**, 4039–4047 (2000).

322. Hu, L. L., Zhou, M. Z. & Deng, H. Dynamic indentation of auxetic and non-auxetic honeycombs under large deformation. *Compos. Struct.* **207**, 323–330 (2019).

323. Hu, L. L. & Deng, H. Indentation resistance of the re-entrant hexagonal honeycombs with negative poisson's ratio. *Mater. Res. Innov.* **19**, S1442–S1445 (2015).

324. Li, T., Liu, F. & Wang, L. Enhancing indentation and impact resistance in auxetic composite materials. *Compos. Part B Eng.* **198**, 108229 (2020).

325. Usta, F., Türkmen, H. S. & Scarpa, F. Low-velocity impact resistance of composite sandwich panels with various types of auxetic and non-auxetic core structures. *Thin-Walled Struct.* **163**, 107738 (2021).

326. Mushtaq, B. *et al.* Core Spun Based Helical Auxetic Yarn: A Novel Structure for Wearable Protective Textiles. *J. Nat. Fibers* 1–13 (2022). doi:10.1080/15440478.2022.2070322

327. Duncan, O. *et al.* Review of Auxetic Materials for Sports Applications: Expanding Options in Comfort and Protection. *Appl. Sci.* **8**, 941 (2018).

328. Shah, I. A. *et al.* Finite Element Analysis of the Ballistic Impact on Auxetic Sandwich Composite Human Body Armor. *Materials (Basel).* **15**, 2064 (2022).

329. Faraci, D., Driemeier, L. & Comi, C. Bending-Dominated Auxetic Materials for Wearable Protective Devices Against Impact. *J. Dyn. Behav. Mater.* **7**, 425–435 (2021).

330. Allen, T. *et al.* Auxetic foams for sport safety applications. in *Procedia Engineering* 104–109 (2015). doi:10.1016/j.proeng.2015.07.183

331. Alderson, A. A triumph of lateral thought. *Chem. Ind.* **10**, 384–391 (1999).

332. Alderson, A. *et al.* An auxetic filter: A tuneable filter displaying enhanced size selectivity or defouling properties. *Ind. Eng. Chem. Res.* **39**, 654–665 (2000).

333. Grima, J. N., Caruana-Gauci, R., Dudek, M. R., Wojciechowski, K. W. & Gatt, R. Smart metamaterials with tunable auxetic and other properties. *Smart Mater. Struct.* **22**, (2013).

334. Alderson, A., Rasburn, J., Evans, K. E. & Grima, J. N. Auxetic polymeric filters display enhanced de-fouling and pressure- compensation properties. *Membr. Technol.* 6–8 (2001).

335. Attard, D., Casha, A. R. & Grima, J. N. Filtration properties of auxetics with rotating rigid units. *Materials (Basel).* **11**, (2018).

336. Wallbanks, M., Khan, M. F., Bodaghi, M., Triantaphyllou, A. & Serjouei, A. On the design workflow of auxetic metamaterials for structural applications. *Smart Mater. Struct.* **31**, 023002 (2022).

337. Ren, X., Shen, J., Tran, P., Ngo, T. D. & Xie, Y. M. Auxetic nail: Design and experimental study. *Compos. Struct.* **184**, 288–298 (2018).

338. Lvov, V. A., Senatov, F. S., Veveris, A. A., Skrybykina, V. A. & Díaz Lantada, A. Auxetic Metamaterials for Biomedical Devices: Current Situation, Main Challenges, and Research Trends. *Materials (Basel).* **15**, 1439 (2022).

339. Choi, J. & Lakes, R. Design of a fastener based on negative Poisson's ratio foam. *Cell. Polym.* **10**, 205–212 (1991).

340. Santulli, C. & Langella, C. Study and development of concepts of auxetic structures in bio-inspired design. *Int. J. Sustain. Des.* **3**, 20–37 (2016).

341. Kim, Y., Son, K. & Lee, J. Auxetic structures for tissue engineering scaffolds and

biomedical devices. *Materials (Basel).* **14**, 1–17 (2021).

342. Shukla, S. & Behera, B. K. Auxetic fibrous materials and structures in medical engineering–a review. *J. Text. Inst.* 1–12 (2022). doi:10.1080/00405000.2022.2116549

343. Wu, W. *et al.* Mechanical properties of anti-tetrachiral auxetic stents. *Compos. Struct.* **185**, 381–392 (2018).

344. Ali, M. N., Busfield, J. J. C. & Rehman, I. U. Auxetic oesophageal stents: structure and mechanical properties. *J. Mater. Sci. Mater. Med.* **25**, 527–553 (2014).

345. Asadi, A. *et al.* Modification of hexachiral unit cell to enhance auxetic stent performance. *Mech. Adv. Mater. Struct.* **22**, 1–15 (2022).

346. Panico, M., Langella, C. & Santulli, C. Development of a biomedical neckbrace through tailored auxetic shapes. *Emerg. Sci. J.* **1**, 105–117 (2017).

347. Moyers, R. E. Dilator for opening the lumen of a tubular organ United States Patent no. 5108413. (1992).

348. Brown, R. H. & Cruikshank, D. P. Determination of the Composition and State of Icy Surfaces in the Outer Solar System. *Annu. Rev. Earth Planet. Sci.* **25**, 243–277 (1997).

349. Sengupta, A., Kim, M., Yoo, C. S. & Tse, J. S. Polymerization of carbon dioxide: A chemistry view of molecular-to- nonmolecular phase transitions. *J. Phys. Chem. C* **116**, 2061–2067 (2012).

350. Lu, C., Miao, M. & Ma, Y. Structural evolution of carbon dioxide under high pressure. *J. Am. Chem. Soc.* **135**, 14167–14171 (2013).

351. Vega, C., Abascal, J. L. F. & Debenedetti, P. G. Physics and chemistry of water and ice. *Phys. Chem. Chem. Phys.* **13**, 19660–19662 (2011).

352. Tse, J. S. & Klug, D. D. Anomalous isostructural transformation in ice VIII. *Phys. Rev. Lett.* **81**, 2466–2469 (1998).

353. Brandenburg, J. G., Maas, T. & Grimme, S. Benchmarking DFT and semiempirical methods on structures and lattice energies for ten ice polymorphs. *J. Chem. Phys.* **142**, (2015).

354. Umemoto, K. & Wentzcovitch, R. M. Theoretical study of the isostructural transformation in ice VIII. *Phys. Rev. B - Condens. Matter Mater. Phys.* **71**, 012102 (2005).

355. Caracas, R. & Gonze, X. Ab Initio Lattice Dynamics and Thermodynamical Properties. *Thermodyn. Prop. Solids Exp. Model.* 291–315 (2010). doi:10.1002/9783527630417.ch8

356. Kawada, S. Dielectric Dispersion and Phase Transition of KOH Doped Ice. *J. Phys. Soc. Japan* **32**, 1442 (1972).

357. Umemoto, K., Wentzcovitch, R. M., Baroni, S. & de Gironcoli, S. Anomalous Pressure-Induced Transition(s) in Ice XI. *Phys. Rev. Lett.* **92**, 2–5 (2004).

358. Bove, L. E. *et al.* Effect of salt on the H-bond symmetrization in ice. *Proc. Natl. Acad. Sci.* **112**, 8216–8220 (2015).

359. Shimizu, H. Elastic Properties of Water and Ice VI Studied by Brillouin Scattering Department of Electronics , Gifu University , 1-1 Yanagido , Gifu 501-11 , Japan. (1998).

360. Tulk, C. A., Gagnon, R. E., Kiefte, H. & Clouter, M. J. Elastic constants of ice III by Brillouin spectroscopy. *J. Chem. Phys.* **101**, 2350–2354 (1994).

361. Tulk, C. A., Kiefte, H., Clouter, M. J. & Gagnon, R. E. Elastic Constants of Ice III, V, and VI by Brilloun Spectroscopy. *J. Phys. Chem. B* **101**, 6154–6157 (1997).

362. Tulk, C. A., Gagnon, R. E., Kiefte, H. & Clouter, M. J. The pressure dependence of the elastic constants of ice III and ice VI. *J. Chem. Phys.* **107**, 10684–10690 (1997).

363. Tulk C. A., Gagnon R. E. , Kiefte H., and C. M. J. Elastic constants of ice VI by Brillouin spectroscopy. *J. Chem. Phys.* **90**, 7014–7016 (1996).

364. Azzopardi, K. M., Brincat, J.-P., Grima, J. N. & Gatt, R. Anomalous elastic properties in stishovite. *RSC Adv.* **5**, 8974–8980 (2014).

365. Vega, C. & Abascal, J. L. F. Simulating water with rigid non-polarizable models: A general perspective. *Phys. Chem. Chem. Phys.* **13**, 19663–19688 (2011).

366. Moore, E. B. & Molinero, V. Is it cubic? Ice crystallization from deeply supercooled water. *Phys. Chem. Chem. Phys.* **13**, 20008–20016 (2011).

367. Stefanutti, E. *et al.* Ice crystallization observed in highly supercooled confined water. *Phys. Chem. Chem. Phys.* **21**, 4931–4938 (2019).

368. French, M., Mattsson, T. R., Nettelmann, N. & Redmer, R. Equation of state and phase diagram of water at ultrahigh pressures as in planetary interiors. *Phys. Rev. B - Condens. Matter Mater. Phys.* **79**, 1–11 (2009).

369. Fang, Y., Xiao, B., Tao, J., Sun, J. & Perdew, J. P. Ice phases under ambient and high pressure: Insights from density functional theory. *Phys. Rev. B - Condens. Matter Mater. Phys.* **87**, 1–6 (2013).

370. Sanz, E., Vega, C., Abascal, J. L. F. & MacDowell, L. G. Phase diagram of water from computer simulation. *Phys. Rev. Lett.* **92**, 23–26 (2004).

371. Pipolo, S. *et al.* Navigating at Will on the Water Phase Diagram. *Phys. Rev. Lett.* **119**, 1–5 (2017).

372. Cai, Y. Q. *et al.* Ordering of hydrogen bonds in high-pressure low-temperature H2O. *Phys. Rev. Lett.* **94**, 1–4 (2005).

373. Grabowska, J. Why is the cubic structure preferred in newly formed ice? *Phys. Chem. Chem. Phys.* **21**, 18043–18047 (2019).

374. Raza, Z. *et al.* Proton ordering in cubic ice and hexagonal ice; A potential new ice phase - XIc. *Phys. Chem. Chem. Phys.* **13**, 19788–19795 (2011).

375. Besson, J. *et al.* Structural Instability in Ice VIII under Pressure. *Phys. Rev. Lett.* **78**, 3141–3144 (1997).

376. Himoto, K., Matsumoto, M. & Tanaka, H. Lattice- and network-structure in plastic ice. *Phys. Chem. Chem. Phys.* **13**, 19876–19881 (2011).

377. Thoeny, A. V., Gasser, T. M. & Loerting, T. Distinguishing ice β-XV from deep glassy ice VI: Raman spectroscopy. *Phys. Chem. Chem. Phys.* **21**, 15452–15462 (2019).

378. Espinosa, J. R. *et al.* Ice Ih: Vs. ice III along the homogeneous nucleation line. *Phys. Chem. Chem. Phys.* **21**, 5655–5660 (2019).

379. Catti, M. *et al.* Ne- and O2-filled ice XVII: A neutron diffraction study. *Phys. Chem. Chem. Phys.* **21**, 14671–14677 (2019).

380. Jiang, L. *et al.* Exotic spectra and lattice vibrations of ice X using the DFT method. *Molecules* **23**, 2780 (2018).

381. Fortes, A. Computational and Experimental Studies of Solids in the Ammonia – Water System. (University College London, 2004).

382. Clark, Stewart J, Matthew D Segall, Chris J Pickard, Phil J Hasnip, Matt I J Prober, K. R. First principles methods using CASTEP. **220**, 567–570 (2005).

383. Zhang, X., Chen, S. & Li, J. Hydrogen-bond potential for ice VIII-X phase transition. *Sci. Rep.* **6**, 37161 (2016).

384. Perdew, J. P., Burke, K. & Ernzerhof, M. Generalized gradient approximation made simple. *Phys. Rev. Lett.* **77**, 3865–3868 (1996).

385. Tkatchenko, A. & Scheffler, M. Accurate molecular van der Waals interactions from ground-state electron density and free-atom reference data. *Phys. Rev. Lett.* **102**, 073005 (2009).

386. Grimme, S. Semiempirical GGA-Type Density Functional Constructed with a Long-Range Dispersion Correction. *J. Comput. Chem.* **27**, 1787–1799 (2006).

387. Perdew, J. P. *et al.* Restoring the Density-Gradient Expansion for Exchange in Solids and Surfaces John. *Phys. Rev. Lett.* **100**, 136406 (2008).

388. Perdew, J. P. *et al.* Atoms, molecules, solids, and surfaces: Applications of the generalized gradient approximation for exchange and correlation. *Phys. Rev. B* **46**, 6671–6687 (1992).

389. Ortmann, F., Bechstedt, F. & Schmidt, W. G. Semiempirical van der Waals correction to the density functional description of solids and molecular structures. *Phys. Rev. B - Condens. Matter Mater. Phys.* **73**, 205101 (2006).

390. Monkhorst, Hendrik J., Pack, J. D. Special points for Brillouin-zone integrations. *Phys. Rev. B* **13**, 5188–5192 (1976).

391. Pack, J. D. & Monkhorst, H. J. special points for Brillouim-zone integration - a reply.

Phys. Rev. B **16**, 1748–1749 (1977).

392. Zha, C. S., Hemley, R. J., Gramsch, S. A., Mao, H. K. & Bassett, W. A. Optical study of H2O ice to 120 GPa: Dielectric function, molecular polarizability, and equation of state. *J. Chem. Phys.* **126**, (2007).

393. Goncharov, A. F., Struzhkin, V. V., Mao, H. & Hemley, R. J. Raman Spectroscopy of Dense H2O and the Transition to Symmetric Hydrogen Bonds. *Phys. Rev. Lett.* **83**, 1998–2001 (1999).

394. Loubeyre, P., LeToullec, R. & Wolanin, E. Modulated phases and proton centring in ice observed by X-ray diffraction up to 170 GPa. *Nature* **397**, 503–506 (1999).

395. Kuriakose, M. *et al.* Longitudinal sound velocities, elastic anisotropy, and phase transition of high-pressure cubic H2 O ice to 82 GPa. *Phys. Rev. B* **96**, 1–13 (2017).

396. Goncharov, A. F., Struzhkin, V. V., Somayazulu, M. S., Hemley, R. J. & Mao, H. K. Compression of ice to 210 gigapascals: Infrared evidence for a symmetric hydrogen-bonded phase. *Science* **273**, 218–220 (1996).

397. Nye, J. F. *Physical Properties of Crystals: Their Representation by Tensors and Matrices*. (Clarendon Press, 1957).

398. Krukau, A. V., Vydrov, O. A., Izmaylov, A. F. & Scuseria, G. E. Influence of the exchange screening parameter on the performance of screened hybrid functionals. *J. Chem. Phys.* **125**, 224106 (2006).

399. Voigt, J. Tetra-Feuerlöscher und Phosgenbildung. *Zeitschrift für Angew. Chemie* **41**, 501–502 (1928).

400. Hill, R. The Elastic Behaviour of a Crystalline Aggregate. *Proc. Phys. Soc. Sect. A* **65**,

349–354 (1952).

401. Reuss, A. Berechnung der Fließgrenze von Mischkristallen auf Grund der Plastizitatsbedingung fur Einkristalle. *Z. Angew. Math. Mech.* **9**, 49–58 (1928).

402. Pugh, S. F. XCII. Relations between the elastic moduli and the plastic properties of polycrystalline pure metals. *London, Edinburgh, Dublin Philos. Mag. J. Sci.* **45**, 823–843 (1954).

403. Chen, S., Xu, Z. & Li, J. The observation of oxygen - Oxygen interactions in ice. *New J. Phys.* **18**, (2016).

404. Sun, C. Q., Zhang, X. & Zheng, W. The hidden force opposing ice compression. *Chem. Sci.* **3**, 1455–1460 (2012).

405. Hohenberg, P. & Kohn, W. Inhomogeneous Electron Gas. *Phys. Rev.* **136**, B864–B871 (1964).

406. Kohn, W. & Sham, L. J. Self-consistent equations including exchange and correlation effects. *Phys. Rev.* **140**, (1965).

407. Hernandez, J. A. & Caracas, R. Proton dynamics and the phase diagram of dense water ice. *J. Chem. Phys.* **148**, (2018).

408. Pettifor, D. G. Theoretical predictions of structure and related properties of intermetallics. *Mater. Sci. Technol.* **8**, 345–349 (1992).

409. Frantsevich, I. N., Voronov, F. F. & Bokuta, S. A. *Elastic constants and elastic moduli of metals and insulator A handbook.* (Naukova Dumka, 1983).

410. Zhou, X., Zhang, L., Zhang, H., Liu, Q. & Ren, T. 3D cellular models with negative compressibility through the wine-rack-type mechanism. *Phys. status solidi* **253**, 1977–

1993 (2016).

411. Bernasconi, M., Silvestrelli, P. L. & Parrinello, M. Ab initio infrared absorption study of the hydrogen-bond symmetrization in ice. *Phys. Rev. Lett.* **81**, 1235–1238 (1998).

412. Wong, P. T. T. & Whalley, E. Raman spectrum of ice VIII. *J. Chem. Phys.* **64**, 2359–2366 (1976).

413. Whale, T. F., Clark, S. J., Finney, J. L. & Salzmann, C. G. DFT-assisted interpretation of the Raman spectra of hydrogen-ordered ice XV. *J. Raman Spectrosc.* **44**, 290–298 (2013).

414. Mason, W. P. Piezoelectric crystals and their application to ultrasonics. *New York, Van Nostrand* (1950).

415. Dong, J., Tomfohr, J. K. & Sankey, O. F. Rigid intertetrahedron angular interaction of nonmolecular carbon dioxide solids. *Phys. Rev. B - Condens. Matter Mater. Phys.* **61**, 5967–5971 (2000).

416. Baur, W. H. & Khan, A. A. Rutile-type compounds. IV. SiO2, GeO2 and a comparison with other rutile-type structures. *Acta Crystolography Section B: Structural Crystallography and Crystal Chemistry* **27**, 2133–2139 (1971).

417. Baur, W. H. The rutile type and its derivatives. *Crystallogr. Rev.* **13**, 65–113 (2007).

418. Sorantin, P. I. & Schwarz, K. Chemical Bonding in Rutile-Type Compounds. *Inorganic Chemistry* **31**, 567–576 (1992).

419. Batyrev, I. G., Golt, M. C. & Sausa, R. C. Modeling and experimental studies of quartz and stishovite and the effects of metal dopants on the quartz-to-stishovite pressure-phase transition. *MRS Commun.* **11**, 317–321 (2021).

420. Yoo, C. S., Iota, V. & Cynn, H. Nonlinear carbon dioxide at high pressures and temperatures. *Phys. Rev. Lett.* **86**, 444–447 (2001).

421. Laniel, D., Geneste, G., Weck, G., Mezouar, M. & Loubeyre, P. Hexagonal Layered Polymeric Nitrogen Phase Synthesized near 250 GPa. *Phys. Rev. Lett.* **122**, 066001 (2019).

422. Kaupp, G. Indentation onto Stishovite (SiO2), MgO, and a Covered Superalloy: "Pop-In" Repair, Phase-Transition Onsets, Polymorph Energies, and Transition-Energies. *Adv. Mater. Phys. Chem.* **10**, 77–95 (2020).

423. Tonauer, C. M., Bauer, M. & Loerting, T. The impact of temperature and unwanted impurities on slow compression of ice. *Phys. Chem. Chem. Phys.* **24**, 35–41 (2022).

424. Mifsud, D. V. *et al.* Laboratory experiments on the radiation astrochemistry of water ice phases. *Eur. Phys. J. D* **76**, (2022).

425. Millot, M. *et al.* Nanosecond X-ray diffraction of shock-compressed superionic water ice. *Nature* **569**, 251–255 (2019).

426. Santoro, M., Lin, J. F., Mao, H. K. & Hemley, R. J. In situ high P-T Raman spectroscopy and laser heating of carbon dioxide. *J. Chem. Phys.* **121**, 2780–2787 (2004).

427. Journaux, B. Salty ice and the dilemma of ocean exoplanet habitability. *Nat. Commun.* **13**, 11–14 (2022).

428. Bove, L. E. & Ranieri, U. Salt- And gas-filled ices under planetary conditions. *Philos. Trans. R. Soc. A Math. Phys. Eng. Sci.* **377**, (2019).

429. Drozdov, A. P., Eremets, M. I., Troyan, I. A., Ksenofontov, V. & Shylin, S. I. Conventional superconductivity at 203 kelvin at high pressures in the sulfur hydride

system. *Nature* **525**, 73–76 (2015).

430. Zarifi, N., Liu, H. & Tse, J. S. Structures of the metallic and superconducting high pressure phases of solid CS2. *Sci. Rep.* **5**, (2015).

431. Freiman, Y. A., Jodl, H. J. & Crespo, Y. Solid oxygen revisited. *Phys. Rep.* **743**, 1–55 (2018).

432. Turnbull, R. *et al.* Unusually complex phase of dense nitrogen at extreme conditions. *Nat. Commun.* **9**, (2018).

433. Monserrat, B., Needs, R. J., Gregoryanz, E. & Pickard, C. J. Hexagonal structure of phase III of solid hydrogen. *Phys. Rev. B* **94**, (2016).

434. Proctor, J. E., Maynard-Casely, H. E., Hakeem, M. A. & Cantiah, D. Raman spectroscopy of methane (CH4) to 165 GPa: Effect of structural changes on Raman spectra. *J. Raman Spectrosc.* **48**, 1777–1782 (2017).

435. Ninet, S. *et al.* Experimental and theoretical evidence for an ionic crystal of ammonia at high pressure. *Phys. Rev. B - Condens. Matter Mater. Phys.* **89**, 174103 (2014).